

Generalised slenderness-based resistance method for the strength prediction of hollow sections

Andrea Toffolon

Vollständiger Abdruck der von der Fakultät für Bauingenieurwesen und Umweltwissenschaften
der Universität der Bundeswehr München zur Erlangung des akademischen Grades eines

Doktor-Ingenieurs [Dr.-Ing.]

genehmigten Dissertation.

Gutachter:

1. Univ.-Prof. Dr.techn. Andreas Taras
2. Univ.-Prof. Dr.-Ing. Markus Knobloch
3. Univ.-Prof. Dr.-Ing. Max Spannaus

Die Dissertation wurde am 26.11.2020 bei der Universität der Bundeswehr München eingereicht und durch die Fakultät für Bauingenieurwesen und Umweltwissenschaften am 23.06.2021 angenommen. Die mündliche Prüfung fand am 09.07.2021 statt.

Abstract

Recent construction practice has seen a rise in the use of structural hollow sections, due to their appealing aesthetics as well as an increased awareness for the advantages in terms of strength and stiffness of this type of section. At the same time, in order to meet increasing demands for more efficient and economic construction typologies and methods, the European steel industry, and particularly the producers of structural hollow sections, are aiming for a reduction of weight through the use of more thin-walled sections and/or higher-strength steel grades (with yield strength $f_y \geq 460\text{MPa}$). These innovations increase the economy and sustainability of construction projects through the reduction of weld volumes, erection times and foundation costs. However, the introduction of more slender construction typologies for hollow sections leads to a number of scientific and engineering challenges. In particular, higher material, with different constitutive laws (shorter or inexistent plastic plateau, diminished ultimate strain) combined with thinner plates leads to an increased significance of instability phenomena, especially of local buckling phenomena and their interaction with the "global" instability mode of flexural buckling.

This thesis addresses the strength and stability of slender, mild- and high-strength-steel hollow sections with flat faces and different cross-sectional geometries and develops a new methodology to be used in structural design and for performance predictions for such elements. The problem of buckling is treated for local, global and interactive local-global buckling phenomena. Most of the described results were developed in the framework of the European (Research Fund for Coal and Steel - RFCS) research project HOLLOSSTAB (grant Nr. RFCS-2015-709892), using a novel design method, called the Generalised Slenderness-based Resistance Method (GSRM), which was developed – in its application to square (SHS) and rectangular (RHS) hollow sections - as part of this thesis work. The new, GSRM design rules cover the cross-sectional and member design checks of hollow sections with various shapes and slenderness ratios. This thesis summarises the experimental and numerical campaign carried out within HOLLOSSTAB and describes the development, validation and application of the new GSRM for the case of the cross-sectional and member resistance of SHS and RHS. It furthermore shows some initial work on an extension of the scope of application of the GSRM. It could be shown that, with the proposed GSRM method, significant gains in accuracy and economy in the design of flat-faced hollow sections can be achieved.

Kurzfassung

In jüngster Zeit werden in der Baupraxis vermehrt Konstruktionshohlprofile verwendet, da diese einerseits ästhetisch ansprechend sind und andererseits auch das Bewusstsein für die Vorteile hinsichtlich Festigkeit und Steifigkeit dieser Art von Profilen gestiegen ist. Gleichzeitig strebt die europäische Stahlindustrie und insbesondere die Hersteller von Konstruktionshohlprofilen eine Gewichtsreduzierung durch den Einsatz dünnwandigerer Profile und/oder höherfester Stahlgüten (mit einer Streckgrenze von $f_y \geq 460 \text{ MPa}$) an, um den steigenden Anforderungen an effizientere und wirtschaftlichere Bautypologien und -methoden gerecht zu werden. Diese Innovationen erhöhen die Wirtschaftlichkeit und Nachhaltigkeit von Bauprojekten durch die Reduzierung von Schweißvolumen, Montagezeiten und Gründungskosten. Die Einführung schlanker Bautypologien für Hohlprofile führt jedoch zu einer Reihe von wissenschaftlichen und ingenieurtechnischen Herausforderungen. Insbesondere führt höherfestes Material mit anderen konstitutiven Gesetzen (kürzeres oder nicht vorhandenes Kunststoffplateau, verminderte Bruchdehnung) in Verbindung mit dünneren Platten zu einer erhöhten Bedeutung von Instabilitätsphänomenen, insbesondere von lokalen Knickphänomenen und deren Wechselwirkung mit dem "globalen" Instabilitätsmodus des Biegeknickens.

Diese Arbeit befasst sich mit der Festigkeit und Stabilität von schlanken Stahlhohlprofilen aus normal- und hochfestem Stahl mit ebenen Flächen und unterschiedlichen Querschnittsgeometrien und entwickelt eine neue Methodik, die bei der Strukturauslegung und für Leistungsvorhersagen für solche Elemente verwendet werden kann. Das Problem des Knickens wird für lokale, globale und interaktive lokal-globale Knickphänomene behandelt. Die meisten der beschriebenen Ergebnisse wurden im Rahmen des europäischen (Research Fund for Coal and Steel - RFCS) Forschungsprojekts HOLLOSSTAB (Grant-Nr. RFCS-2015-709892) entwickelt, wobei eine neuartige Bemessungsmethode, die sogenannte Generalised Slenderness-based Resistance Method (GSRM), verwendet wurde, die - in ihrer Anwendung auf quadratische (SHS) und rechteckige (RHS) Hohlprofile - im Rahmen dieser Dissertation entwickelt wurde. Die neuen GSRM-Bemessungsregeln decken die Querschnitts- und Stabnachweise von Hohlprofilen mit verschiedenen Formen und Schlankheitsverhältnissen ab. Diese Arbeit fasst die im Rahmen von HOLLOSSTAB durchgeführte experimentelle und numerische Kampagne zusammen und beschreibt die Entwicklung, Validierung und An-

wendung der neuen GSRM für den Fall des Querschnitts- und Stabnachweises von SHS und RHS. Darüber hinaus zeigt sie erste Arbeiten zu einer Erweiterung des Anwendungsbereichs des GSRM auf andere Anwendungsfälle. Es konnte in der Arbeit gezeigt werden, dass mit der vorgeschlagenen GSRM-Methode signifikante Genauigkeits- und Wirtschaftlichkeitsgewinne bei der Stabilitätsbemessung von Hohlprofilen erzielt werden können.

Acknowledgements

This work was carried out at the Department of Structural Engineering at Bundeswehr University Munich under the supervision of Prof. Dr. Andreas Taras. I am extremely grateful for the continuous help I received from him over the last years, for the learning process and exchange of ideas. Without his support, encouragement and fundamental contributions this thesis would not be possible.

My gratitude also goes to Prof. Dr. M. Knobloch and Prof. Dr. M. Spannaus for their willingness to take on the task of reviewing this thesis and participating in the examination process.

I express my gratitude for the financial support received throughout my time at Bundeswehr University Munich: first through the Research Fund for Coal and Steel (RFCS), which financed the research project HOLLOSSTAB which made this thesis possible, and later on directly from the Faculty of Civil and Environmental Engineering; I specifically thank Prof. Dr. I. Mangerig and G. Siebert for the contract extension provided during the last year.

I sincerely thank all my colleagues for their technical contributions and personal support. Robert Kroyer and Andreas Müller, among others, helped me in many ways through the various phases of the project. I am also grateful to all technicians at the Laboratory of Structural Engineering at Bundeswehr University Munich for their cooperation. I would also like to thank Christian Merkl and Dr. Michael Kraus for the very pleasant collaboration during the work on common publications.

Finally, I would like to thank my girlfriend, my family and my friends for their patience and support over the years.

Contents

Contents	vii
1 Introduction	1
1.1 General remarks	1
1.2 Motivation and Objectives	2
1.3 Scope	5
1.4 Publication resulting from this thesis	6
2 State of the art	8
2.1 Literature review: design models for local and global buckling	8
2.1.1 Local buckling: critical stresses and design models	8
2.1.2 Column buckling	12
2.1.3 Curve fitting formulae	20
2.2 Eurocode and other standards	22
2.2.1 Cross-sectional strength and local buckling	23
2.2.2 Eurocode rules for column buckling	27
2.2.3 Eurocode rules for beam-columns	29
2.3 Other predictive models	30
2.3.1 The Continuous Strength Method	30
2.3.2 The Direct Strength Method	33
3 Methodology	36
3.1 Introduction	36
3.2 Design approach	37
3.2.1 Cross-section Resistance	38
3.2.2 Member Resistance	40
3.3 Experimental tests	40
3.3.1 Full scale tests	41
3.3.2 Auxiliary tests	45
3.4 FEM modelling	46
3.4.1 FEM discretization and input parameters	47
3.4.2 Geometrically and Materially Non-linear Analyses	47

3.4.3	Validation against experimental tests	50
3.4.4	Calibration of the GMNIA parameters	52
3.5	Analytical formulae	53
3.5.1	Ayrton-Perry format	55
3.5.2	Winter format	57
4	Experimental campaign	60
4.1	Introduction	60
4.2	Auxiliary tests	62
4.2.1	Tensile tests	63
4.3	Imperfection measurement and evaluation	64
4.4	Full-scale tests and validation of the numerical model	70
4.4.1	Stub column tests T1	70
4.4.2	Short beam-column tests T3 and T4	72
4.4.3	Short beam-column tests T2	77
4.4.4	Long beam-column tests T5	77
5	Numerical investigation	79
5.1	Introduction	79
5.2	Calibration of the numerical model used for parametric studies	79
5.3	Scope of the parametric study	83
6	GSRM Design Formulations - Local Buckling	87
6.1	Introduction	87
6.2	Choice of the GSRM representation format	87
6.3	Calibration of the design equations	92
6.3.1	Rules in the elastic range	93
6.3.2	Rules in the stocky range	97
6.4	Comparison with current standards	98
6.5	Reliability aspects, partial factors	103
6.6	Summary of the GSRM design rules for local buckling	104
7	GSRM Design Formulations - Global Buckling	106
7.1	Introduction	106
7.2	Ayrton-Perry formulation and EC3	106
7.3	Derivation of the GSRM design formulae for global buckling of beam-columns	109
7.4	Calibration of the parameters of the Ayrton-Perry formula	113
7.5	Validation and verification with current test standards	119
7.6	Reliability aspects, partial factors	122
7.7	Summary of the GSRM design rules for member buckling	122
8	Further work on the GSRM	124

8.1	Initial numerical study on polygonal sections	124
8.2	AI-based design formulae	128
9	Summary, conclusions and outlook	130
9.1	Summary and conclusions	130
9.2	Outlook on future work	133
	References	135
A	Key facts and deliverables of the RFCS-Project HOLLOSSTAB	142
B	Selected test results	145
C	Sample Abaqus input file for GMNIA	200

Chapter 1

Introduction

1.1 General remarks

This thesis addresses the strength and stability of slender, mild- and high-strength-steel hollow sections with flat faces and different cross-sectional geometries and develops a new methodology to be used in structural design and for performance predictions for such elements. The problem of buckling is treated for local, global and interactive local-global buckling phenomena. Most of the described results were developed in the framework of the European (Research Fund for Coal and Steel - RFCS) research project HOLLOSSTAB (grant Nr. RFCS-2015-709892), using a novel design method, called the Generalised Slenderness-based Resistance Method (GSRM), which was developed – in its application to square (SHS) and rectangular (RHS) hollow sections - as part of this thesis work. The new, GSRM design rules cover the cross-sectional and member design checks of hollow sections with various shapes and slenderness ratios. This thesis summarises the experimental and numerical campaign carried out within HOLLOSSTAB and describes the development, validation and application of the new GSRM for the case of the cross-sectional and member resistance of SHS and RHS. It furthermore shows some initial work on an extension of the scope of application of the GSRM. In the thesis, it is demonstrated that the proposed GSRM method allows for significant gains in accuracy and economy in the design of flat-faced hollow sections.

1.2 Motivation and Objectives

Recent construction practice has seen a rise in the use of structural hollow sections, due to the appealing aesthetics as well as better awareness of the advantages in terms of strength and stiffness of this type of section. In order to meet the increasing demands for more efficient and economic construction typologies and methods, the European steel industry, and particularly the producers of structural hollow sections, are aiming for a reduction of weight through the use of more thin-walled sections and/or higher-strength steel grades (with yield strength $f_y \geq 460MPa$). These innovations increase the economy and sustainability of construction projects through the reduction of weld volumes, erection times and foundation costs. Especially the introduction of higher-strength steel grades into standard construction practice is a relevant industrial goal for the European steel industry, offering chances for new product development, research and innovation, and thus market advantages. However, the introduction of more slender construction typologies for hollow sections leads to a number of scientific and engineering challenges: higher material strength ($R_e/R_{p0,2}$ or f_y ; R_m or f_u), with different constitutive laws (shorter or inexistent plastic plateau, diminished ultimate strain) combined with thinner plates leads to an increased significance of instability phenomena, especially of local buckling phenomena and their interaction with the "global" instability mode of flexural buckling. Preliminary studies had shown that the application of current design codes (e.g. the Eurocodes) is possibly ineffective, uneconomical or – in some cases - altogether impossible for combined instability phenomena in slender, high-strength hollow sections:

1. At the level of cross-sectional resistances, by its definition an increase of yield strength f_y leads to an increase of the (local, "L") normalized slenderness $\bar{\lambda}_L = \sqrt{\frac{f_y}{\sigma_{cr}}}$. This means that more sections will fall into the non-compact (class 3) or slender (class 4) range and are thus more sensitive to local buckling phenomena. The current classification system is quite often not suitable for capturing the actual cross-sectional behaviour in terms of strength: i. it predicts a constant and equal value for both class 1 and 2, and an overly simplified bilinear function for the class 2 to 3 transition, included only in the latest draft version of the planned re-edition of prEN1993-1-1 [1], ii. the classification is based on c/t limits and in turn on bifurcation stresses for individual plates, omitting all mutual supporting effects of adjacent components, iii. plasticity is completely omitted in the non-compact and slender range, while strain hardening

is omitted in the compact range, iv. the strength for class 4 sections is usually calculated by separating the load components (axial force and bending moments) and determining "effective cross-sections" for these individual load cases, creating an artificial separation of the real stress state, and v. for non-standard hollow sections, such as cross-sections with stiffeners and polygonal, point iv is altogether inapplicable, as no definition of effective areas for those sections is given in current design codes such as Eurocode 3, EN 1993-1-1 [1]; standard circular or elliptical cross-sections are also neglected, but are not equally analysed in depth in the following chapters.

2. Beyond the cross-sectional level, instability phenomena become more prevalent also at a global ("G") level (flexural buckling) when interacting with the local ("G") resistance, leading to an ("L+G") instability phenomena. These effects are treated in structural design codes in a manner that is potentially too conservative for the high-strength, slender hollow sections studied in this project.
3. The peculiarities of high-strength materials ($\sigma - \varepsilon$) and sections (lower residual stresses levels relative to strength, different imperfection levels) are only superficially studied and addressed in design codes.
4. Generally, the treatment of local, global, and interactive "L+G" instabilities in the Eurocode and other international design codes is seen as too cumbersome by many designers and does not take full advantage of already-available numerical computational methods.

Combined, these drawbacks represent a hindrance to the further development and market introduction of more slender hollow section members in Europe. In order to overcome them, innovative design methods must be introduced and the corresponding scientific background and knowledge must be gathered. Thereby, the new rules should be combined with software tools ([2]) in order to make the new method simple to use and practical for engineers in design offices and steel construction companies. These were also objectives of the RFCS project HOLLOSSTAB, and were obtained through new design methods, based on a large number of experimental tests and numerical tests. Thereby, the development of a specific type of design rule for SHS and RHS is proposed in this thesis with the denomination of the Generalised Slenderness-based Resistance Method (GSRM). This method, similarly to other recently proposed methods such as the General Method for the design of whole frames ([3, 4]), the Direct Strength Method (DSM, [5, 6, 7, 8, 9, 10, 11, 12]), the Continuous

Strength Method (CSM, [13, 14, 15, 16, 17, 18, 19]) and – in the most directly related way - the Overall Interaction Concept / Overall Method (OIC, [20, 21, 22]) makes use of an "overall" definition of the cross-sectional and member slenderness, generalised to account for combined load cases and the mutual support provided by the various parts of the studied cross-section and member. The generalised definitions of slenderness and resistance make use of load amplification factors to reach a certain defined condition or resistance, and thus termed "R". Thereby, the generalised slenderness is defined as:

$$\bar{\lambda} = \sqrt{\frac{R_{ref}}{R_{cr}}} \quad (1.1)$$

while the ultimate (buckling) resistance is defined as:

$$R_b = \chi R_{ref} \quad (1.2)$$

with the buckling coefficient χ being a function of $\bar{\lambda}$. In detail, this thesis pursues the following objectives:

- In-depth analysis of the GSRM methodology for the design of cross-sectional capacity of slender, innovative mild and high-strength steel (HSS) hollow sections. The GSRM defines a continuous strength representation throughout slenderness ranges - from compact (class 1) to slender (class 4). The cross-sectional slenderness is calculated for the "overall" load-case and the complete cross-section, using numerical methods, thus taking advantage of mutual restraining effects in the different parts of the cross-section and the real stress state. The GSRM expands to applications in beam-columns (members failing in global buckling). This allows the global "G", local "L" and combined "L+G" buckling phenomena to be treated in a uniform format.
- Proposal of new design formulae for RHS and SHS. The formulae predict the cross-section capacity as a continuous function of the cross-section slenderness, providing two different formulations for the stocky range and the elastic range. The obtained functions result into a $\chi - \bar{\lambda}$ curve, which substitutes current classification and design methods of various international standards. Similarly to the cross-section resistance, the GSRM predicts the member resistance as a function of the global slenderness, employing a different predictive curve and inputting a previously calculated cross-section resistance as an fundamental parameter for the determination of the RHS and

SHS member resistance.

- Derivation and validation of the predictive rules on the basis of the experimental and numerical tests. A large database of numerical results for SHS and RHS is used for the validation of the chosen resistance curves for the cross-section capacity. The curves for the member resistance are derived from existing column buckling curves and validated by experimental and numerical tests, as well. Furthermore, a detailed description of the validation of the numerical model (FEM) against the experimental test results is given, focusing also on the calibration of the FEM input parameters.
- Application of the obtained results for SHS and RHS to new cross-sections and future applications with machine learning techniques. For new hollow sections the same methodology and guiding principles of the GSRM are applied, providing promising early results for the prediction of polygonal cross-section strength. Machine learning and deep learning techniques are also employed to predict the SHS and RHS cross-section strength. The results of these techniques are then compared to the GSRM results in terms of precision and reliability.

This thesis should be reviewed as an effort to describe thoroughly each item of the objective list and to propose solutions for them.

1.3 Scope

This thesis focuses on the development and application of the Generalised Slenderness-based Resistance Method (GSRM) for square (SHS) and rectangular (RHS) hollow sections. The thesis is organized in nine chapters. This introductory Chapter 1 contains the motivation and scope of the thesis and identifies the publications that already resulted from the work carried out in the thesis project. It is followed, in Chapter 2, by a review of the current state of the art in the design of sections against local and global buckling in general, with a focus on hollow sections respectively on the phenomena that most affect this type of section. Chapter 3 describes the general methodology used in this thesis, in particular with regards to the considered existing design approaches (used as starting points for own developments), the experimental tests conducted by the author of this thesis at the laboratory of Bundeswehr University Munich, the FEM modelling and the used analytical approaches. In Chapter 4, the experimental campaign and its use as the basis for the validation and verification of

advanced numerical models is described. The numerical campaign made possible by these numerical models is then described in detail in Chapter 5. Chapter 6 and 7 contain the key developments of the thesis: the new GSRM formulations for local and global buckling, respectively, with their background and validation. Some initial work on the expansion of the field of application of the GSRM is presented in Chapter 8. Finally, Chapter 9 contains a summary and conclusions derived from this thesis work. The final pages of the thesis contain the considered references from literature and an Appendix with key facts and deliverables of the project, selected test results and sample input file of the numerical software used in the numerical tests.

1.4 Publication resulting from this thesis

A number of publications already resulted from the work carried out in this thesis. They are listed in the following.

Peer-reviewed Journal Articles

Toffolon, A. & Taras, A. Development of an OIC-Type local buckling design approach for cold-formed unstiffened and groove-stiffened hollow sections. *Thin-Walled Structures* **144**, 106266 (2019)

Toffolon, A. *et al.* The generalized slenderness-based resistance method for the design of SHS and RHS. *Steel Construction* **12**, 327–341 (2019)

Taras, A. & Toffolon, A. Neuartige Bemessungsmethode fuer Hohlprofilquerschnitte und -staebe. *Stahlbau* **89**, 570–584 (2020)

Conference Proceedings

Toffolon, A. & Taras, A. *Numerical investigation of the local buckling behaviour of high strength steel circular hollow sections* in *Proceedings of Eurosteel 2017* **1** (2017)

Toffolon, A. & Taras, A. *Numerical and Experimental Studies for the Development of Direct Strength Design Rules for Locally* in *Proceedings of SSRC Conference 2018* (2018)

Toffolon, A. & Taras, A. *Application of an OIC-type design approach to the buckling design of cold-formed, lip-stiffened hollow sections* in *Proceedings of the International Colloquia on Stability and Ductility of Steel Structures SDSS 2019* (July 2018)

Toffolon, A. & Taras, A. *Proposal of a design curve for the overall resistance of cold formed RHS and SHS members* in *Proceedings of Nordic Steel 2019* **3** (2019)

Toffolon, A. *et al.* *Experimental and numerical analysis of the local and interactive buckling behaviour of hollow sections* in *Proceedings of Nordic Steel 2019* **3** (Sept. 2019)

Toffolon, A. *et al.* *Experimental and numerical analysis of the local and interactive buckling behaviour of hollow sections* in *Proceedings of the International Colloquia on Stability and Ductility of Steel Structures SDSS 2019* (Sept. 2019)

Toffolon, A. & Taras, A. *Proposal of a design curve for the overall resistance of cold formed RHS and SHS members* in *Proceedings of the International Colloquia on Stability and Ductility of Steel Structures SDSS 2019* (Sept. 2019)

Toffolon, A. *et al.* *FEM-based design of hollow sections against local, global and interactive buckling – model verification and calibration against physical tests* in *Proceedings of the 17th International Symposium on Tubular Structures* (Dec. 2019)

Toffolon, A. & Taras, A. *Proposal of generalized slenderness-based resistance curves for the local and interactive buckling of rectangular hollow sections* in *Proceedings of the 17th International Symposium on Tubular Structures* (Dec. 2019)

Toffolon, A. & Taras, A. *New formulations for the cross-sectional strength of high-strength steel rectangular and square hollow sections using a Generalized Slenderness-Strength Method* in *Proceedings of SSRC 2020* (Apr. 2020)

Taras, A. & Toffolon, A. *Development of a generalized slenderness-based resistance method for the design of high-strength steel hollow section beam-columns* in *Proceedings of SSRC 2020* (Apr. 2020)

Awards related to the thesis work

Honorable mention for the Vinnakota Award 2020, Annual Stability Conference of the Structural Stability Research Council SSRC, April 2020, Chicago, Illinois.

Chapter 2

State of the art

2.1 Literature review: design models for local and global buckling

This sections provide a brief historical overview of the design models for local and global buckling and their background, and describe current models for the prediction of the buckling resistance. The first section focuses on the review of the experimental studies and modern design formulae for local buckling of plates. A second section illustrates experimental tests and design methods for members, thus describing the development design formulae for global buckling, introduces different representation formats, and finally mentions briefly the role of the Eurocode in the current design methods. In the last part of the chapter a brief overview of the current methods for the design of local buckling (CSM, DSM) is given.

2.1.1 Local buckling: critical stresses and design models

Early studies on plate buckling investigated the model of a thin rectangular plate (high width to thickness ratio) supported on all sides and subjected to a constant in-plane compression stress σ along two opposite edges. The differential equation governing the state at the initiation of elastic buckling (small deflections) is as follows:

$$\left(\frac{\partial^4 w}{\partial x^4} + 2 \frac{\partial^4 w}{\partial x^2 \partial y^2} + \frac{\partial^4 w}{\partial y^4} \right) - \frac{N_x}{D} \frac{\partial^2 w}{\partial x^2} = 0 \quad (2.1)$$

$$\text{where } D = \frac{Et^3}{12(1-\nu^2)} \quad (2.2)$$

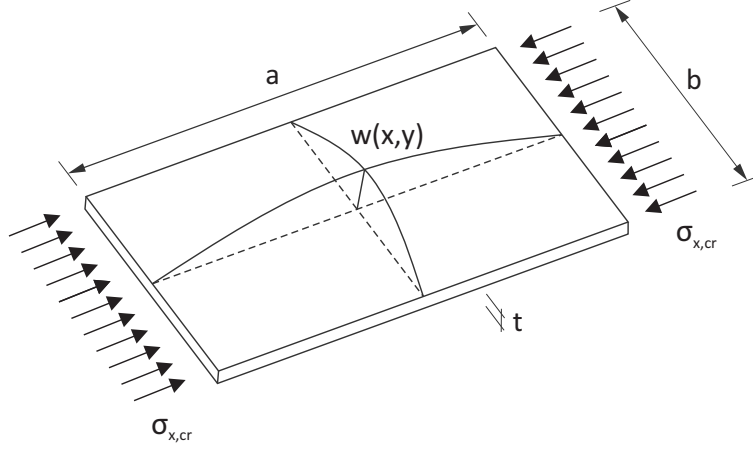


Fig. 2.1. Definition of the parameters for plate buckling.

D is the flexural rigidity of the plate, with the Poisson's ratio $\nu = 0.3$ and Young's modulus E . N_x is the axial force in x -direction, which is defined in equation (2.3). These parameters are shown in figure 2.1.

$$N_x = \sigma_{x,cr}bt \quad (2.3)$$

For the described loading and boundary conditions, the solution of this differential equation can be determined by using the following assumption in equation (2.4) for $w(x,y)$, which describes an approximate shape function for a plate under double curvature.

$$w = f(x,y) = \sin\left(\frac{x}{a}m\pi\right) \sin\left(\frac{y}{b}n\pi\right) \quad (2.4)$$

The solution of equation 2.1 under the assumption shown in (2.4) yields equation 2.5, which is rewritten for the unknown $\sigma_{x,cr}$.

$$D \left(\frac{m^4\pi^4}{a^4} + 2\frac{m^2\pi^2}{a^2} \frac{n^2\pi^2}{b^2} + \frac{n^4\pi^4}{b^4} \right) = \sigma_{x,cr}t \frac{m^2\pi^2}{a^2} \quad (2.5)$$

$$\sigma_{x,cr} = \frac{E\pi^2}{12(1-\nu^2)} \left(\frac{t}{b} \right)^2 \left(\frac{mb}{a} + n^2 \frac{a}{mb} \right)^2 \quad (2.6)$$

$$\text{with } \sigma_e = \frac{E\pi^2}{12(1-\nu^2)} \left(\frac{t}{b} \right)^2 \quad (2.7)$$

$$k_\sigma = \left(\frac{mb}{a} + n^2 \frac{a}{mb} \right)^2 \quad (2.8)$$

Where:

- $\sigma_{x,cr}$ is the elastic critical stress in the x-direction; the index x will be omitted in the following equations.
- k_σ is the boundary and applied stress dependent plate buckling coefficient.
- $\sigma_e = 190000 \left(\frac{t}{b}\right)^2$ for steel material.
- t, b are respectively thickness and width of the plate.

This thesis focuses in large part on the behaviour of rectangular and square hollow sections. These sections produce low constraining moments between the elements of the cross-section due to their symmetrical nature. Their behaviour therefore is often modelled as a composition of simply-supported plates ([36]), and e.g. $k_\sigma = 4.0$ is used in many international standards (e.g. the Eurocodes) to implement design formulae for the case of pure compression. However, in RHS greater edge restraint is applied to the more slender sides of the cross-section by the less slender sides. As a result, values of k_σ obtained from this "hinged plate" model are generally conservative when applied to each side of the hollow section and in general may not describe the overall cross-section behaviour with sufficient precision.

In 1930, von Kármán [37] first formulated the theory underlying the so-called effective width method, based on the assumption that from a certain slenderness level the plate width contributes only partially to the load carrying capacity, and fails where the plate is deflected out-of-plane beyond a certain limit, redistributing stresses in the areas around the corners, which can become higher than σ_{cr} . Thus, for a steel plate supported on all edges and under uniform, monodirectional compression, the following limit compressive force was derived by von Kármán:

$$F_{ult} = C \sqrt{\frac{E}{\sigma}} t^2 f_y \quad (2.9)$$

$$\text{where } C=1.90 \quad (2.10)$$

F_{ult} can be rewritten and set equal to $b_{eff} t f_y$:

$$F_{ult} = C t^2 \sqrt{\frac{E}{f_y}} \sqrt{\frac{f_y}{\sigma_{cr}}} \sqrt{\frac{\sigma_{cr}}{\sigma}} f_y \cong b_{eff} t f_y \quad (2.11)$$

From which the effective width equation according to von Kármán is obtained:

$$b_{eff} = Ct \sqrt{\frac{E}{f_y}} \sqrt{\frac{f_y}{\sigma_{cr}}} \sqrt{\frac{\sigma_{cr}}{\sigma}} \leq b \quad (2.12)$$

where b_{eff} is the portion of width b that “effectively” collaborates to the plate buckling resistance, with the remaining portion of the plate width considered to be ineffective and have zero stress. With this approach, the squash load of the plate $bt f_y$ is reached up to $\sigma = \sigma_{cr}$, while smaller values are obtained for $\sigma > \sigma_{cr}$. Various modifications and adaptations of this approach were the object of several experimental test campaigns. The most important results were obtained by G. Winter [38, 39]. Winter calibrated a modification of the b_{eff} -formula on tests with cold-formed steel. According to Winter’s experiments, the effective width of a supported plate under uniform compression could thus be calculated as follows:

$$b_{eff} = 1.90t \sqrt{\frac{E}{f_y}} \left[1 - 0.574 \left(\frac{t}{b} \right) \sqrt{\frac{E}{f_y}} \right] \quad (2.13)$$

The reduction factor ρ and the plate slenderness $\bar{\lambda}_p$ as defined in modern standards such as EN 1993-1-5 [40] can now be introduced as follows:

$$\rho = \frac{b_{eff}}{b} \quad (2.14)$$

$$\bar{\lambda}_p = \sqrt{\frac{f_y}{\sigma_{cr}}} \quad (2.15)$$

With these, the above formula (2.13) can be rewritten as

$$\rho = \frac{1}{\bar{\lambda}_p} \left(1 - \frac{0.3}{\bar{\lambda}_p} \right) \quad (2.16)$$

The final version of the Winter formula reads as:

$$\rho = \frac{1}{\bar{\lambda}_p} \left(1 - \frac{0.22}{\bar{\lambda}_p} \right) \quad (2.17)$$

Some further modifications were proposed over time in [38, 39]. The strength predictions of Winter are naturally more conservative than von Kármán’s and introduce a correction term proportional to $\bar{\lambda}_p^{-2}$, following the elastic buckling curve. The Winter’s curve with a

value of $c = 0.22$ represents only one example validated against Winter's experimental tests. Equation (2.17) may be thus rewritten in a more general form, as in equation (2.18), which will be analysed in detail in section 3.5.2 and will be designated as the "Winter format".

$$\rho = \frac{1}{\lambda_p} \left(1 - \frac{c}{\lambda_p} \right) \quad (2.18)$$

One key aspect of this thesis will thus be the inclusion of more precise values of k_σ (or rather, of σ_{cr}), determined for the whole section, into Winter-type design formulae, which are described in the following.

2.1.2 Column buckling

A short overview of the literature of different analytical approaches used to describe the ultimate capacity of members in pure compression ("columns") is here presented, not in chronological order, but connecting the most important research approaches over the years. This is done in order to introduce various, often-used methods for the description of buckling knock-down factors for all kinds of member buckling phenomena. They will be considered in this thesis for the description of the general behaviour of members failing in global buckling.

Ayrton-Perry-Robertson approach

The original formula to describe the ultimate strength of columns in flexural (global) buckling was first described by Ayrton and Perry [41] in 1886. This approach – first employed for a practical case by Robertson [42] – proposes to introduce an equivalent imperfection of sinusoidal shape and amplitude e_0 into a second-order analysis and stress design of a pin-ended model column, and to use this imperfection amplitude as a calibration factor to describe the strength of real columns, as observed e.g. in tests. Ayrton and Perry thus derived their formulation from the elastic buckling amplification factor for a pin-ended column under pure compression with an initial imperfection e_0 , leading to the total deflection

$$w = \delta + e_0 = \frac{e_0}{1 - \frac{N_b}{N_{cr}}} \quad (2.19)$$

where:

- e_0 is the initial imperfection.

- δ is the member deflection due to the applied load from the base state.
- w is the total deflection.
- N_b is the applied load N , which finally leads to column failure at N_b .
- N_{cr} is the axial force at the first bifurcation point, or “Euler load”.

Crucially, in the Ayrton-Perry approach a linear cross-sectional failure criterion is introduced, i.e. a linear interaction surface for compression forces and moments is used. The general equation to the limit-state for the case of compression failure of the outermost fibre of the cross-section for a pin-ended column under pure compression reads:

$$\frac{N}{Af_y} + \frac{Nw}{W_y f_y} = 1.0 \quad (2.20)$$

At failure, this leads to the following equation:

$$\frac{N_b}{Af_y} + \frac{N_b e_0}{W_y f_y} \cdot \frac{1}{1 - \frac{N_b}{N_{cr}}} = 1.0 \quad (2.21)$$

where:

- A is the cross-section area.
- W_y the cross-section modulus for bending about the y-axis.
- f_y is the yield stress.
- $N_b w$ is the first order bending moment due to the deflection of the pin-ended column at mid-span.

Ayrton and Perry proceeded with the derivation of the buckling strength in terms of stresses, whereas current design standards such as the Eurocode use equation 2.21 with a reduction factor of the cross-sectional plastic resistance in order to define the member strength, and they plot it as a function of the member slenderness. The elaboration of this approach will be presented in 3.5 both as analytical formula and a new representation format. In the following, the final version of the Ayrton-Perry formulation will be presented and the

calibration made by Robertson will be presented. Equation 2.21 may be rewritten in terms of stress criterion as follows:

$$\frac{N_b}{A} + \frac{N_b e_0}{W_y} \cdot \frac{1}{1 - \frac{N_b}{N_{cr}}} = \sigma_{max} < f_y \quad (2.22)$$

Introducing the following expressions:

$$\sigma_b = \frac{N_b}{A} \quad (2.23)$$

$$m = \frac{e_0 A}{W_y} \quad (2.24)$$

equation 2.22 may be rewritten as follows:

$$\sigma_b \left[1 + \frac{m}{1 - \frac{\sigma_b}{\sigma_{cr}}} \right] = f_y \quad (2.25)$$

which results into a quadratic equation with solution

$$\sigma_b = \frac{1}{2} \left[\sigma_{cr}(1 + m) + f_y - \sqrt{(\sigma_{cr}(1 + m) + f_y)^2 - 4\sigma_{cr}f_y} \right] \quad (2.26)$$

The solution in equation (2.26) represents the design solution according to Ayrton-Perry. According to these authors, a value for m is determined either by fitting the buckling curves to a number of experimental tests, or imposing the dependence on given variable through experimental observations. It is nowadays common practice [1] to impose the imperfection amplitude as a function of the member length; the proposal of Ayrton and Perry implies a linear dependence between m and λ as follows:

$$m = \alpha \lambda \quad (2.27)$$

In figure 2.2a the curves in equation (2.26) are shown according to the original formulation, in which the maximum allowable stress is seen as a reduction of the yield stress f_y . Different values of m indicate the range of application of this formulation. Figure 2.2b shows the application of the input parameters on a rectangular cross-section and the assumption on boundary conditions for the Ayrton-Perry analytical model. A further development of this

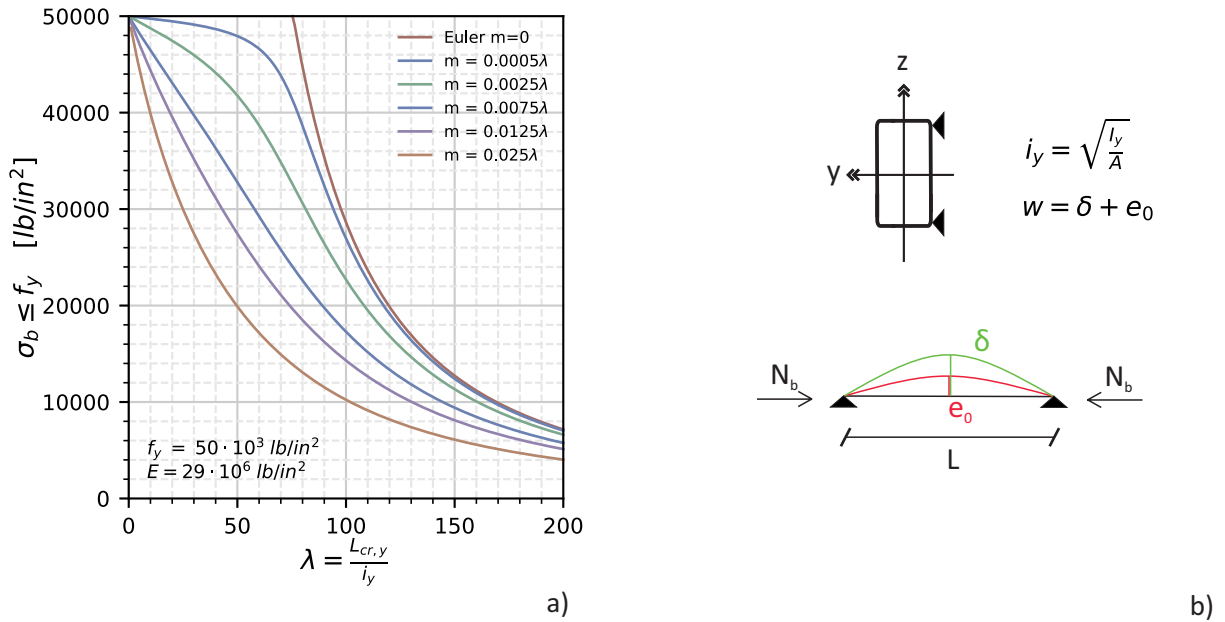


Fig. 2.2. a) shows the Ayrton-Perry design formula 2.26 for various values of m ; b) shows schematically the input parameters, boundary conditions and assumptions of the formulation.

approach was formulated by Robertson [42], who proposed a similar equation for the imperfection changing the parameter notation from m into η (see equation 2.28) and calibrating the values on extensive experimental tests.

$$\eta = \alpha \lambda \quad (2.28)$$

Merchant-Rankine formulation

In the anglophone world, a different approach to the column-buckling was traditionally pursued as well, producing so-called "rational" or "semi-rational" formulae. These formulae, mainly sustained in the early days by practitioners, rely on the empirical assumptions for deformations, critical stresses and thus provide a simplified framework for the application of simple mathematical functions fitting experimental test results. The well-established design formula of Rankine-Gordon is one of the fundamental example of these methods, and is still widely adopted in both research and practice. The formula originates from the beam theory, where the maximum deflection w and tension σ due to the first order moment of a simply

supported beam subjected of pure axial compression can be expressed as:

$$w = c_1 \frac{L^2 M_{y,max}}{I_y} \quad (2.29)$$

$$\sigma_M = c_2 \frac{M_{y,max}}{I_y} z \quad (2.30)$$

$$(2.31)$$

where:

- L, I_y, z are respectively the member length, section inertia and distance to the extreme section fibre.
- $M_{y,max}$ is the mid-span bending moment ought to flexural buckling.
- c_1, c_2 constant parameters.

By substituting σ_M in (2.29) and incorporating σ_M in a new dimensionless constant c , w results in:

$$w = c \frac{L^2}{z} \quad (2.32)$$

which states the proportionality of w to L^2/z for a given elastic stress state defined by σ_M . Equation (2.32) represents the fundamental assumption of the Rankine-Gordon formulation. Thereby, introducing the resulting equation (2.32) for w , the equation at the limit state as in (2.21) becomes:

$$\frac{N_b}{Af_y} + \frac{N_b w}{I_y f_y} z = \frac{N_b}{Af_y} + \frac{N_b c L^2}{I_y f_y} = 1.0 \quad (2.33)$$

In figure 2.2b a schematic representation of the geometric characteristics of the mechanical problem is given. The figure demonstrates the model assumptions (valid for Rankine, as well as for Ayrton-Perry) of pure compression and lateral support in z-direction and the geometric properties. The following definitions of buckling reduction factor and slenderness

are given:

$$\chi_y = \frac{N_b}{Af_y} \quad (2.34)$$

$$\bar{\lambda}_y = \sqrt{\frac{Af_y}{N_{cr,y}}} \quad (2.35)$$

The buckling knock-down factor is a reduction function of the cross-section resistance with domain range of $(0, 1]$, which multiplies the plastic resistance of the section, here represented by the term Af_y , as the considered case is pure compression. The slenderness though is defined as the squared root of the ratio of the plastic resistance and the elastic critical Euler load. Following the definition of $\bar{\lambda}_y$ and χ_y in (2.35) and (2.34), the equation takes the final normalized format as follows

$$\chi_y = \frac{1}{1 + k\bar{\lambda}_y^2} \quad (2.36)$$

where:

$$\bar{\lambda}_y = \frac{\lambda_y}{\lambda_1} \quad (2.37)$$

$$\lambda_1 = \pi \sqrt{\frac{E}{f_y}} \quad (2.38)$$

$$k = c\lambda_1^2 \quad (2.39)$$

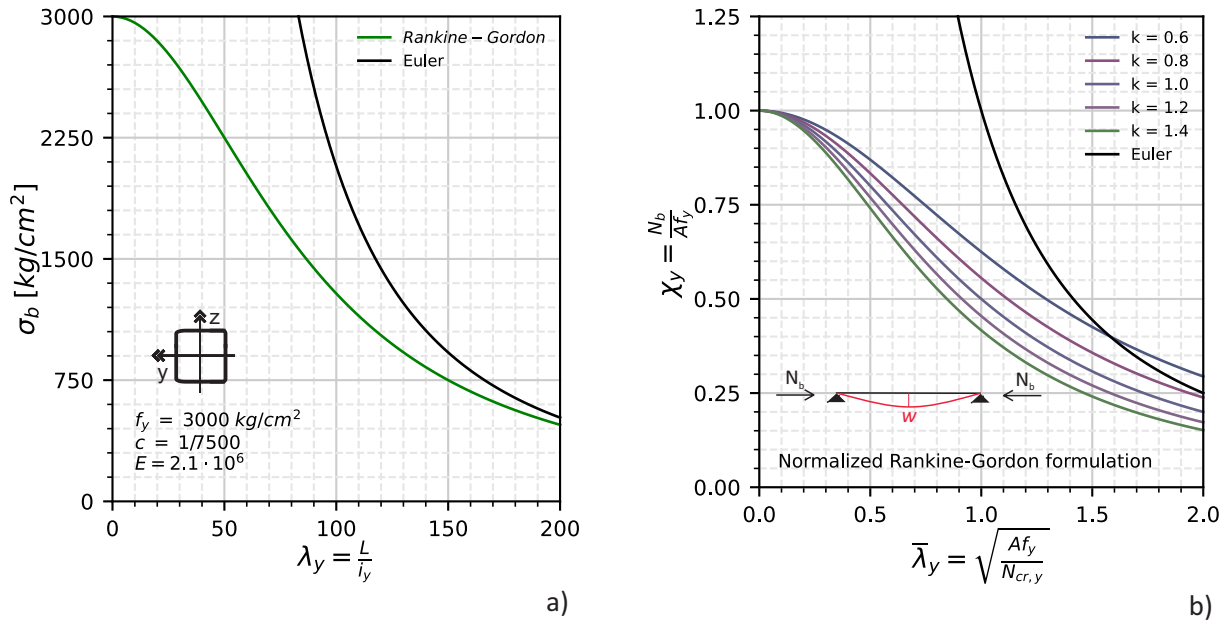


Fig. 2.3. Rankine-Gordon buckling curve in a) the original formulation and b) normalized formulation varying k value comparing curves to the Euler curve.

In figure 2.3a the original form of the Rankine-Gordon curve is represented in the $\chi - \bar{\lambda}_y$ space. Units and dimensions are provided according to the indication of Timoshenko and Lessels [43] as $f_y = 3000 \text{ kg/cm}^2$, $c = 1/75000$ and $E = 2.10 \cdot 10^6$. The curve in green colour reaches the peak of resistance only for very small values of λ_y and tends asymptotically to the Euler critical load for large slenderness. Figure 2.3b shows instead different values of k being explored in the domain of the assumptions of Rankine-Gordon. In this case, a remarkable property of the curves is that they do not necessarily go below the critical Euler load, and only for $k=1.0$ the curve is asymptotic to Euler. This special case is defined as the Ritter's semi-rational formula and was broadly used in North America in the first half of the 20th century. The Rankine-Gordon formula was renewed and rewritten in a different format by Merchant in 1954 [44]. The equation in (2.36) could be rewritten in the following fashion by re-writing $\bar{\lambda}_y$ and χ_y :

$$\frac{N_b}{N_{pl}} = \frac{1}{1 + k \frac{N_{pl}}{N_{cr}}} \quad (2.40)$$

with:

$$\chi_y = \frac{N_b}{N_{pl}} \quad (2.41)$$

$$\bar{\lambda}_y = \sqrt{\frac{N_{pl}}{N_{cr}}} \quad (2.42)$$

Thereby, the equation 2.40 can be re-formulated as follows:

$$\frac{N_b}{N_{pl}} + k \frac{N_b}{N_{cr}} = 1 \quad (2.43)$$

which is the so-called Merchant-Rankine formula. This change of terms does not imply a new content from the Rankine-Gordon formulation. A fundamental contribution of Merchant is a clear visualization of the curve data. In his work the curve corresponding to $k = 1$ is defined as the only rational case. This can be seen from the comparison with two different types of curves, the Euler curve and the Eurocode curve, which were derived from the Ayrton-Perry formulation.

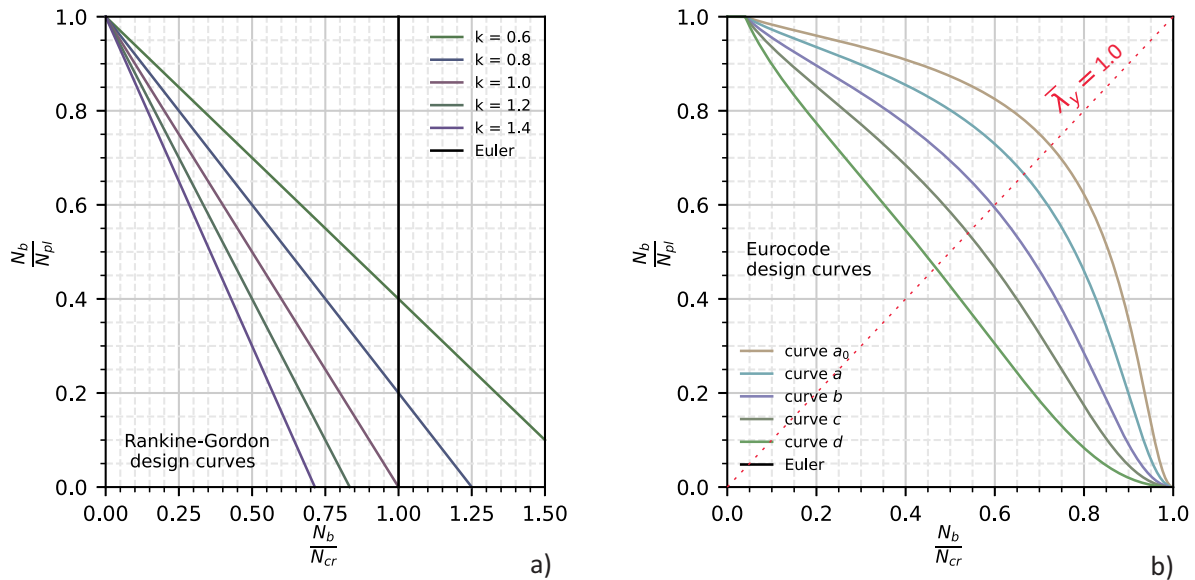


Fig. 2.4. a) Different values of the Rankine-Gordon curves in the Merchant format, b) column-buckling curve from the current Eurocode in the Merchant format of representation.

In figure 2.4a and b a comparison between these two formulations is made in the Merchant representation. The $k=1.0$ curve is shown in 2.4a among other possible values of k and stands out, since it does not predict values greater than the Euler critical load but at the same time fits into a prediction range similar to the Ayrton-Perry predictions, represented in 2.4b. Descending from equation 2.42, the function $\bar{\lambda}_y = 1.0$ is represented as a linear function in the $N_b/N_{pl} - N_b/N_{cr}$ space. Along the $\bar{\lambda}_y = 1.0$ path the Eurocode curves show the highest scatter, which is explained by the interaction of the effects of global slenderness and loss of stiffness of the section with the reserve of plasticity of the cross-section itself. This mechanism is shown in figure 3.11. Thereby, the Merchant formula was modified to account for this type effects by adding an exponent n as follows (for more details see [45, 46, 47]):

$$\frac{N_b}{N_{pl}}^n + k \frac{N_b}{N_{cr}}^n = 1 \quad (2.44)$$

2.1.3 Curve fitting formulae

The representation formats which were analysed in this section show a mechanical background and results into the commonly utilised design formulae of the international standards. E.g. the Winter formulation and the Ayrton-Perry's, determine respectively the currently adopted strength curve for the effective width method (local buckling) and member buckling strength in the Eurocode. These design formulations were derived from design formulae fitting parameters to both experimental and numerical results, by modifying only carefully chosen coefficients. In this section, though, different options for pure curve fitting are explored and examples from other standards will be shown. The buckling reduction factor χ as a function of the slenderness $\bar{\lambda}$ is shown in two possible formats: polynomial/hyperbolic functions and exponential functions.

Polynomial and hyperbolic functions

The general formulation accounting for polynomial and hyperbolic functions reads:

$$\chi = \sum_{i=0}^n A_i \bar{\lambda}_i + \sum_{j=1}^m B_j \bar{\lambda}_j \quad (2.45)$$

In the form of $n = 4$ and $m = 7$, the equation corresponds to the proposal of Lindner [45] for the approximation of the European column buckling curves (see ECCS tabulated curves).

Another fundamental example of these functions is the purely polynomial function, where the parameter $B_j = 0$. These functions may fit with larger accuracy the ECCS curves, and they are indeed adopted in the North-American standard by considering different ranges of application, each with a corresponding polynomial. The approach was applied by Bjorhovde [48] between others (see also Galambos [49] and Ziemian [50] for the most recent publication) and is currently adopted in the SSRC design curves. An example of this formulation is the current SSRC curve 2P (an alternative for the AISC LRFD curve [51]), which is expressed by equations (2.46) to (2.50) using Eurocode notation.

$$\chi = 1.0 \quad \text{for} \quad \bar{\lambda} \leq 0.15 \quad (2.46)$$

$$\chi = \left(1.03 - 0.158\bar{\lambda} - 0.206\bar{\lambda}^2\right) \quad \text{for} \quad 0.15 \leq \bar{\lambda} \leq 1.0 \quad (2.47)$$

$$\chi = \left(-0.193 + \frac{0.803}{\bar{\lambda}} + \frac{0.056}{\bar{\lambda}^2}\right) \quad \text{for} \quad 1.0 \leq \bar{\lambda} \leq 1.80 \quad (2.48)$$

$$\chi = \left(0.018 + \frac{0.815}{\bar{\lambda}^2}\right) \quad \text{for} \quad 1.80 \leq \bar{\lambda} \leq 3.20 \quad (2.49)$$

$$\chi = \left(\frac{1}{\bar{\lambda}^2}\right) \quad \text{for} \quad \bar{\lambda} \geq 3.20 \quad (2.50)$$

The equations are represented in figure 2.5a, and compared with the current Eurocode column buckling curves derived from the Ayrton-Perry formulation described above. The buckling strength N_b is normalised by the section plastic resistance in compression and as a reduction factor for the weak y-axis. The SSRC curve follows a smooth path inside each range and shows a point of discontinuity at $\lambda_y = 0.15$ and $\lambda_y = 1.0$. The values lie between the curve *a* and *b* of the Eurocode, thus providing consistency with both formulations, and were calibrated by the authors against experimental and numerical tests, resulting in the assessment of a level of reliability for each curve. Thereby, the curve fitting approach by polynomial demonstrates that it may effectively replace other mechanically sound approaches.

Exponential functions

Another possible function of the curve-fitting approach may be the adoption of the exponential function. The equation is also utilized in North-America [51] and in the most general

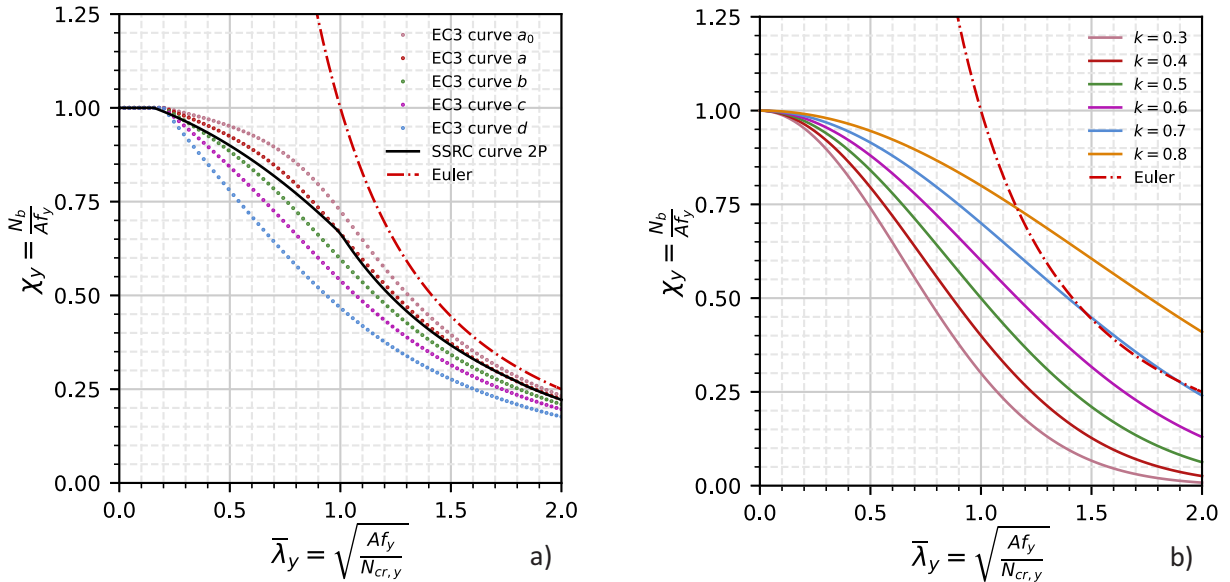


Fig. 2.5. a) comparison of the current EC3 column buckling curves and the SSRC curve 2P; b) evaluation of the exponential function curve fitting for various values of k .

form it presents a coefficient k multiplying $\bar{\lambda}$ as follows.

$$\chi = k \bar{\lambda}^n \quad (2.51)$$

In the AISC specification presents the equation (2.51) with $k = 0.658$ and $n = 2$. Figure 2.5b shows the exponential function of the slenderness as defined in (2.51). For lower values of k the function is describes lower, which are monotonically decreasing as any buckling strength function of the slenderness requires. With values of k larger than 0.7 the curves the values results larger than the Euler curve, which is mechanically not plausible.

2.2 Eurocode and other standards

In this section, the current design methods in the European Eurocodes [1, 40] will be presented, focusing on rules for the calculation of cross-section and member resistance.

2.2.1 Cross-sectional strength and local buckling

For the determination of the cross-sectional strength and the consideration of local buckling, Eurocode 3 [1] divides sections into 4 classes, and proposes a different strength function for each class. The ultimate strength of cross-sections in class 1 and 2 corresponds to the plastic resistance R_{pl} for an SHS or RHS loaded by a general combination of axial force and bending. Class 3 sections can be loaded up to their elastic resistance R_{el} , which corresponds to the first occurrence of yielding in a fibre of the section. In Class 4 sections, the elastic resistance cannot be reached because the onset of local buckling phenomena precedes the reaching of yielding in a nominal stress calculation. In this case, local buckling is accounted for directly in the design calculations, by the use of either the "effective width method" or of the "reduced stress method", both of which are to be found e.g. in EN 1993-1-5 [40]. An overview of the classes and corresponding cross-sectional capacity is given in figure 2.6. In the following, each class design method is analysed in detail.

The ultimate strength of cross-sections in class 1 and 2 corresponds to R_{pl} , which is calculated according to equations (2.52) to (2.56), found in Eurocode 3.

$$\left(\frac{M_{y,Ed}}{M_{N,y,Rd}} \right)^\alpha + \left(\frac{M_{z,Ed}}{M_{N,z,Rd}} \right)^\beta \leq 1.0 \quad (2.52)$$

$$\text{where } M_{N,y,Rd} = M_{pl,y,Rd} \frac{1-n}{1-0.5a_w} \leq M_{pl,y,Rd} = \frac{W_{pl,y} f_y}{\gamma_{M0}} \quad (2.53)$$

$$M_{N,z,Rd} \leq M_{pl,z,Rd} \frac{1-n}{1-0.5a_f} \leq M_{pl,z,Rd} = \frac{W_{pl,z} f_y}{\gamma_{M0}} \quad (2.54)$$

$$n = \left(\frac{N_{Ed}}{N_{pl,Rd}} \right) \quad a_w = \frac{A-2bt}{A} \leq 0.5 \quad a_f = \frac{A-2ht}{A} \leq 0.5 \quad (2.55)$$

$$\alpha = \beta = \frac{1.66}{1-1.13n^2} \leq 6 \quad (2.56)$$

where:

- α and β are the parameters introducing the effects of biaxial bending.
- n is the ratio of design normal force to design plastic resistance to normal forces of the gross cross-section.
- a_w and a_f are respectively the ratio of web and flange area to gross area.

- $M_{N,y,Rd}$ is the reduced design values of the resistance to bending moments making allowance for the presence of normal forces.

Figure 2.6 shows the class 3 strength function both of the current version EN1993-1-1:2005 [1] and the new version prEN1993-1-1:2020 [52]. The current Eurocode version assesses a pure elastic resistance design value R_{el} for class 3 sections, producing an unrealistic drop in the class 2 to 3 transition. The project SEMI-COMP [53] introduced a more effective and realistic linear transition between class 2 and 4, instead of a sudden drop of strength at the border between class 2 and 3. prEN1993-1-1:2020 took on board these changes and introduced a new elasto-plastic modulus W_{ep} , a new parameter β_{ep} , depending on ε and the cross-section width-to-thickness ratio, and a new formula for biaxial bending. The equations for SHS and RHS of this design method are reported in (2.57) to (2.65).

$$W_{ep,y} = W_{pl,y} - (W_{pl,y} - W_{el,y}) \beta_{ep,y} \quad (2.57)$$

$$W_{ep,z} = W_{pl,z} - (W_{pl,z} - W_{el,z}) \beta_{ep,z} \quad (2.58)$$

$$\text{where } \beta_{ep,y} = \max \left(\frac{\frac{c}{t_f} - 34\varepsilon}{4\varepsilon}; \frac{\frac{c}{t_w} - 83\varepsilon}{38\varepsilon}; 0 \right) \leq 1.0 \quad (2.59)$$

$$\beta_{ep,z} = \max \left(\frac{\frac{c}{t_w} - 34\varepsilon}{4\varepsilon}; 0 \right) \leq 1.0 \quad (2.60)$$

$$\left(\frac{M_{y,Ed}}{M_{N,ep,y,Rd}} \right)^{\alpha_y} + \left(\frac{M_{z,Ed}}{M_{N,ep,z,Rd}} \right)^{\alpha_z} \leq 1.0 \quad (2.61)$$

$$\text{where } M_{N,ep,y,Rd} = \frac{W_{ep,y} f_y}{\gamma_{M0}} (1 - n) \quad M_{N,ep,z,Rd} = \frac{W_{ep,z} f_y}{\gamma_{M0}} (1 - n) \quad (2.62)$$

$$n = \left(\frac{N_{Ed}}{N_{pl,Rd}} \right) \quad (2.63)$$

$$\alpha_y = \alpha_z = \frac{1.66}{1 - 1.33n^2} \quad \text{when } n \leq 0.8 \quad (2.64)$$

$$\alpha_y = \alpha_z = 6.0 \quad \text{when } n > 0.8 \quad (2.65)$$

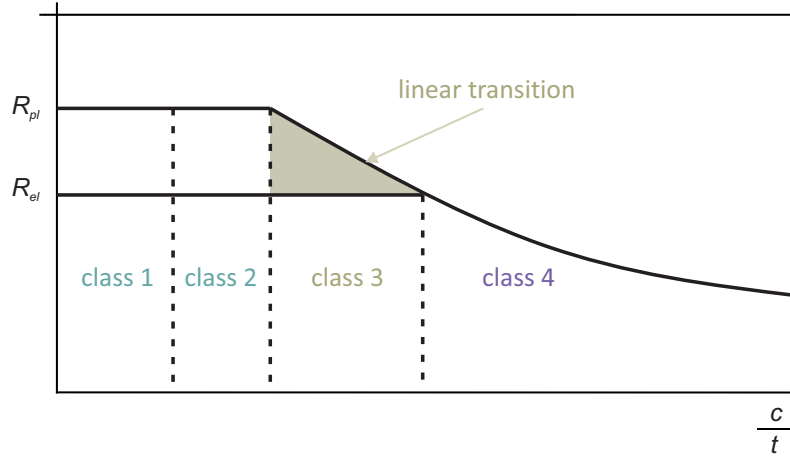


Fig. 2.6. Schematic representation of the EC3 classes in terms of cross-section strength versus c/t ratio.

Class 4 accounts for the effects of local buckling of the plates, thus obtaining a cross-section strength lower than R_{el} . The Eurocode provides different options for the calculation of the strength of class 4 cross-sections. Here the effective width method is presented, since it originates from the literature presented in section 2.1. The effective width method for plate buckling applies the findings of Winter and assesses separately ρ for each cross-sectional plate by introducing the parameter ψ , as the ratio between the stress along each plate centre line. The reduction factor ρ and the plate slenderness $\bar{\lambda}$ are defined as follows:

$$\rho = \frac{1}{\bar{\lambda}_p} \left(1 - 0.22 \frac{3 + \psi}{\bar{\lambda}_p} \right) \quad (2.66)$$

$$\bar{\lambda}_p = \sqrt{\frac{b_{eff}}{b}} = \frac{\frac{\bar{b}}{t}}{28.4 \sqrt{\frac{235}{f_y}} \sqrt{k_\sigma}} \quad (2.67)$$

k_σ is once again the buckling coefficient and can be obtained from table 4.1 and table 4.2 in EN1993-1-5 [40], here shown in figure 2.7.

Table 4.1: Internal compression elements

Stress distribution (compression positive)				Effective ^b width b_{eff}		
				$\psi = 1:$ $b_{eff} = \rho \bar{b}$ $b_{e1} = 0,5 b_{eff} \quad b_{e2} = 0,5 b_{eff}$		
				$1 > \psi \geq 0:$ $b_{eff} = \rho \bar{b}$ $b_{e1} = \frac{2}{5 - \psi} b_{eff} \quad b_{e2} = b_{eff} - b_{e1}$		
				$\psi < 0:$ $b_{eff} = \rho b_c = \rho \bar{b} / (1 - \psi)$ $b_{e1} = 0,4 b_{eff} \quad b_{e2} = 0,6 b_{eff}$		
$\psi = \sigma_2 / \sigma_1$	1	$1 > \psi > 0$	0	$0 > \psi > -1$	-1	$\frac{AC_1}{AC_4} - 1 > \psi \geq -3 \frac{AC_1}{AC_4}$
Buckling factor k_{σ}	4,0	$8,2 / (1,05 + \psi)$	7,81	$7,81 - 6,29\psi + 9,78\psi^2$	23,9	$5,98 (1 - \psi)^2$

Table 4.2: Outstand compression elements

Stress distribution (compression positive)				Effective ^b width b_{eff}		
				$1 > \psi \geq 0:$ $b_{eff} = \rho c$		
				$\psi < 0:$ $b_{eff} = \rho b_c = \rho c / (1 - \psi)$		
$\psi = \sigma_2 / \sigma_1$	1	$1 > \psi > 0$	0	-1	$1 \geq \psi \geq -3$	
Buckling factor k_{σ}	0,43	0,57	0,85	$0,57 - 0,21\psi + 0,07\psi^2$		
				$1 > \psi \geq 0:$ $b_{eff} = \rho c$		
				$\psi < 0:$ $b_{eff} = \rho b_c = \rho c / (1 - \psi)$		
$\psi = \sigma_2 / \sigma_1$	1	$1 > \psi > 0$	0	$0 > \psi > -1$	-1	
Buckling factor k_{σ}	0,43	$0,578 / (\psi + 0,34)$	1,70	$1,7 - 5\psi + 17,1\psi^2$	23,8	

Fig. 2.7. Table 4.1 and 4.2 from EN1993-1-5

2.2.2 Eurocode rules for column buckling

In the Eurocode 3, following the Ayrton and Perry's approach, the general term η is replaced by a formula that makes this imperfection a function of slenderness, of a plateau value to account for stocky columns not failing before the squash load, and of a calibration factor α which accounts for residual stresses and production differences, here denoted as α_{EC3} :

$$\eta_{imp} = \alpha_{EC3} (\bar{\lambda}_y - 0.2) \quad (2.68)$$

Thereby, the member slenderness and buckling reduction factor read:

$$\bar{\lambda} = \sqrt{\frac{Af_y}{N_{cr}}} \quad (2.69)$$

$$\text{where } N_{cr} = \frac{\pi^2 EI}{L^2} \quad (2.70)$$

$$\chi = \frac{1}{\phi + \sqrt{\phi^2 - \bar{\lambda}^2}} \leq 1.0 \quad (2.71)$$

$$\text{with } \phi = 0.5 \left[1 + \alpha_{EC3} (\bar{\lambda} - 0.2) + \bar{\lambda}^2 \right] \quad (2.72)$$

The buckling verification of a pin-ended member subjected to axial compression is finally written as:

$$\frac{N_{Ed}}{N_{b,Rd}} \leq 1.0 \quad (2.73)$$

$$\text{where } N_{b,Rd} = \chi N_{pl,Rd} \quad \text{for class 1,2,3} \quad (2.74)$$

$$N_{b,Rd} = \frac{\chi A_{eff} f_y}{\gamma_{M1}} \quad \text{for class 4} \quad (2.75)$$

A_{eff} is the effective area of the cross-section calculated from the gross area with the effective width method. The table 2.1 and table 6.2 from EN1993-1-1 [1] summarise the values and conditions for α_{EC3} .

Buckling curve	a_0	a	b	c	d
Imperfection factor α	0.13	0.21	0.34	0.49	0.76

Table 2.1: EN 1993-1-1. Imperfection factors for the determination of the buckling curve.

Table 6.2: Selection of buckling curve for a cross-section

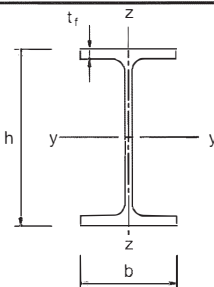
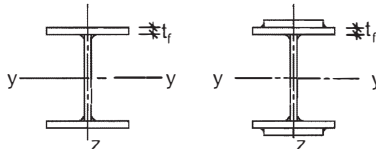
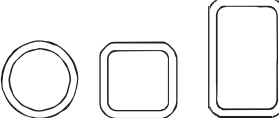
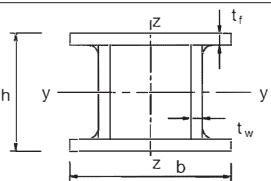
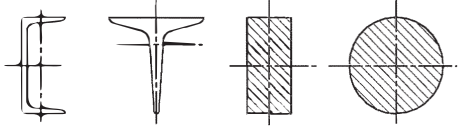
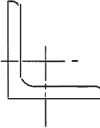
Cross section	Limits	Buckling about axis	Buckling curve	
			S 235 S 275 S 355 S 420	S 460
Rolled sections 	$h/b > 1,2$	$t_f \leq 40 \text{ mm}$	y-y	a
			z-z	b
	$h/b \leq 1,2$	$40 \text{ mm} < t_f \leq 100$	y-y	b
			z-z	c
	$t_f \leq 100 \text{ mm}$	y-y	b	
		z-z	c	
	$t_f > 100 \text{ mm}$	y-y	d	
		z-z	d	
Welded I-sections 	$t_f \leq 40 \text{ mm}$	y-y	b	
		z-z	c	
Hollow sections 	hot finished	any	a	
	cold formed	any	c	
Welded box sections 	generally (except as below)	any	b	
	thick welds: $a > 0,5t_f$ $b/t_f < 30$ $h/t_w < 30$	any	c	
U-, T- and solid sections 		any	c	
L-sections 		any	b	

Fig. 2.8. Table 6.2 from EN1993-1-1

2.2.3 Eurocode rules for beam-columns

According to the current Eurocode 3 [1], SHS and RHS members which are subjected to combined bending and axial compression should satisfy equation (2.76) and (2.77).

$$\frac{N_{Ed}}{\chi_y N_{Rk}} + k_{yy} \frac{M_{y,Ed} + \Delta M_{y,Ed}}{M_{y,Rk}} + k_{yz} \frac{M_{z,Ed} + \Delta M_{z,Ed}}{M_{z,Rk}} \leq 1.0 \quad (2.76)$$

$$\frac{N_{Ed}}{\chi_z N_{Rk}} + k_{zy} \frac{M_{y,Ed} + \Delta M_{y,Ed}}{M_{y,Rk}} + k_{zz} \frac{M_{z,Ed} + \Delta M_{z,Ed}}{M_{z,Rk}} \leq 1.0 \quad (2.77)$$

where:

- N_{Ed} , $M_{y,Ed}$ and $M_{z,Ed}$ are the design values of the compression force and the maximum moments about the y-y and z-z axis along the member, respectively.
- $\Delta M_{y,Ed}$, $\Delta M_{z,Ed}$ are the moments due to the shift of the centroidal axis for class 4 sections.
- k_{yy} , k_{zy} , k_{yz} , k_{zz} are the interaction factors.

Interaction factors	Design assumptions	
	elastic cross-sectional properties class 3, class 4	plastic cross-sectional properties class 1, class 2
k_{yy}	$C_{my} \left(1 + 0,6 \lambda_y \frac{N_{Ed}}{\chi_y N_{Rk} / \gamma_{M1}} \right)$ $\leq C_{my} \left(1 + 0,6 \frac{N_{Ed}}{\chi_y N_{Rk} / \gamma_{M1}} \right)$	$C_{my} \left(1 + (\bar{\lambda}_y - 0,2) \frac{N_{Ed}}{\chi_y N_{Rk} / \gamma_{M1}} \right)$ $\leq C_{my} \left(1 + 0,8 \frac{N_{Ed}}{\chi_y N_{Rk} / \gamma_{M1}} \right)$
k_{yz}	k_{zz}	$0,6 k_{zz}$
k_{zy}	$0,8 k_{yy}$	$0,6 k_{yy}$
k_{zz}	$C_{mz} \left(1 + 0,6 \lambda_z \frac{N_{Ed}}{\chi_z N_{Rk} / \gamma_{M1}} \right)$ $\leq C_{mz} \left(1 + 0,6 \frac{N_{Ed}}{\chi_z N_{Rk} / \gamma_{M1}} \right)$	$C_{mz} \left(1 + (\bar{\lambda}_z - 0,2) \frac{N_{Ed}}{\chi_z N_{Rk} / \gamma_{M1}} \right)$ $\leq C_{mz} \left(1 + 0,8 \frac{N_{Ed}}{\chi_z N_{Rk} / \gamma_{M1}} \right)$

Fig. 2.9. Table B.1 from EN1993-1-1 Annex B

The values for the interaction factors k_{yy} , k_{zy} , k_{yz} can be taken from figure 2.9. The $C_{m,y}$ and $C_{m,z}$ parameters account for the effects of the different bending moment diagrams in both y and z direction. In equation 2.78 to 2.81 the $C_{m,y}$ and $C_{m,z}$ functions for the case of linear bending moment along the beam-column length are displayed.

$$C_{my} = 0.6 + 0.4\psi_M \geq 0.4 \quad (2.78)$$

$$C_{mz} = 0.6 + 0.4\psi_M \geq 0.4 \quad (2.79)$$

$$\text{where } M_{y,Ed,right-end} = \psi_M M_{y,Ed,left-end} \quad (2.80)$$

$$M_{z,Ed,right-end} = \psi_M M_{z,Ed,left-end} \quad (2.81)$$

2.3 Other predictive models

2.3.1 The Continuous Strength Method

The Continuous Strength Method (CSM), developed by the research group of professor L. Gardner at Imperial College (see [13, 15, 54, 17, 19, 14, 16]), was created with the intent of obtaining design formulae which define the cross-section strength as a continuous function of the slenderness of the constituent plate elements of a cross-section. Similarly to currently developed design methods, the CSM discards the concept of classes (as in the Eurocode for example), and makes use of the definition of cross-section (or local) slenderness and the strain-hardening behaviour of the material, in order to predict the buckling strength of any section. The inclusion of the strain-hardening relationship into the analysis allows to capture effectively the deformation capacity of the section, both in term of end shortening δ_u and rotation capacity ϕ . The CSM determines a fundamental function, expressing the deformation capacity of the section both for plates and circular sections, shown in equation (2.82) and (2.83) in the original form from [13].

$$\frac{\varepsilon_{cr}}{\varepsilon_y} = \frac{1}{\lambda_p^2} \quad \text{for plates} \quad (2.82)$$

$$\frac{\varepsilon_{cr}}{\varepsilon_y} = \frac{1}{\lambda_c} \quad \text{for CHS} \quad (2.83)$$

where ε_{cr} is the critical buckling strain and $\varepsilon_y = f_y/E$. A more generalised version of these functions accounts for the effects due to the chosen load case and the section geometry and

is defined as the CSM base curve, demonstrated in equation (2.84).

$$\frac{\varepsilon_{csm}}{\varepsilon_y} = \frac{A}{\bar{\lambda}_p^n} \quad (2.84)$$

where the parameters A and n are coefficient calibrated against a number of numerical simulations. In more recent papers [18] [55] Yun et al. proposed the following parameters for the base curve for plated sections, adapting it both to cold-formed and hot-rolled steel:

$$\frac{\varepsilon_{csm}}{\varepsilon_y} = \frac{0.25}{\bar{\lambda}_p^{3.6}} \leq \min \left(15, \frac{C_1 \varepsilon_u}{\varepsilon_y} \right) \quad \text{for } \bar{\lambda}_p \leq 0.68 \quad (2.85)$$

$$(2.86)$$

where:

- ε_u is the ultimate strain.
- an upper bound for the $\frac{\varepsilon_{csm}}{\varepsilon_y}$ ratio was found as constant value 15 or a parameter depending on ε_u and C_1 , a factor changing according to the manufacturing process, e.g. $C_1 = 0.4$ for cold-formed steels.
- for $\lambda > 0.68$ the cross-section enters the slender range and different formulations could apply, e.g. Winter's.

These curves define the strain level as a function of the slenderness and well describe non-slender and stocky sections, since they show large deformation capacity, which can be easily captured with the CSM. The strain-hardening material model account for the correspondent maximum stresses in the cross-section. Thereby, the strain hardening material is inserted into the formulation with f_{csm} as the maximum allowable stress, which is a function of ε_{csm} and other material properties shown in equation (2.87).

$$f_{csm} = f_y + E_{sh} \varepsilon_y \left(\frac{\varepsilon_{csm}}{\varepsilon_y} - 1 \right) \quad (2.87)$$

Figure 2.10a shows the base-curve of the CSM for different values of A and n , corresponding to equation (2.82), (2.83) and (2.85). In figure 2.10b two diagrams describe advanced formulation for strain-hardening of the CSM according to Yun and Gardner ([56], [57]), fitting an extensive number of coupon tests. The curve for hot-rolled steels is a bilinear function with

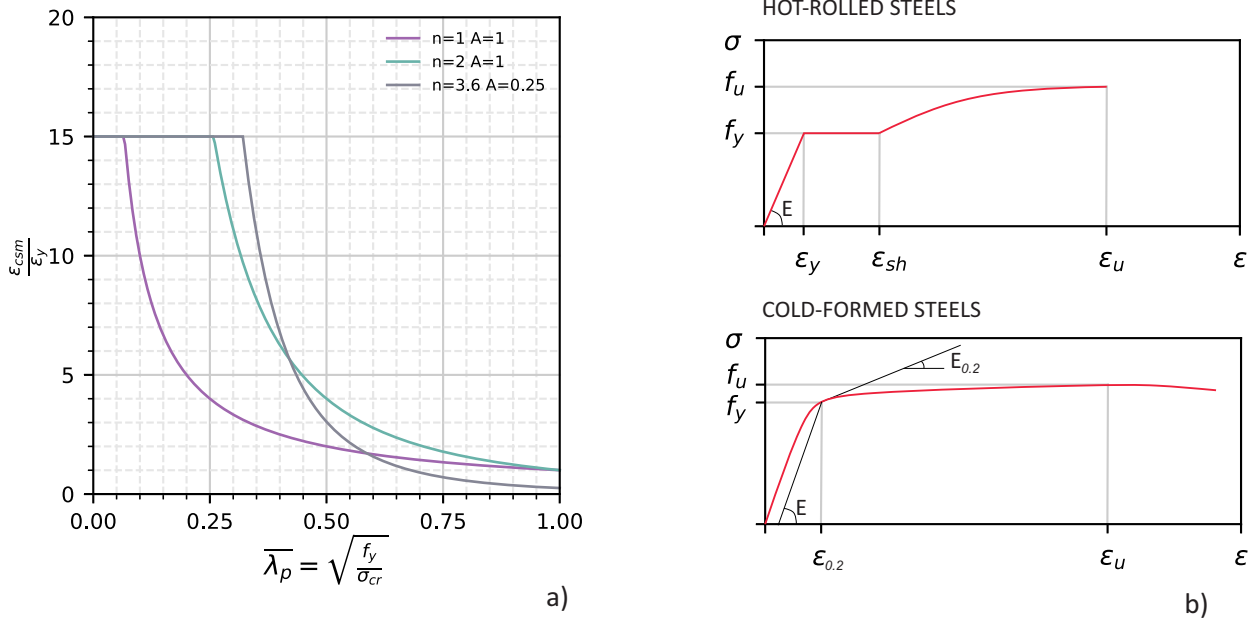


Fig. 2.10. a) CSM curve shapes obtained by varying A and n ; b) stress-strain model for cold-formed and hot-rolled sections.

non-linear model from the typical plateau line to the ultimate strain; the stress-strain curve for the cold-formed steel is built on a two-stage Ramberg-Osgood [58] model. Both representations will be analysed in detail for modelling codified steel grades from S235 to S890 and serve as the fundamental material model also for the GSRM design rules of this work, developed from chapter 6. The Continuous Strength Method already provides examples of very precise predictive design rules for certain load cases and cross-sections primarily with a focus on the stocky range. As equation (2.87) predicts the compression resistance for the case of pure compression, for non-slender ($\bar{\lambda}_p \leq 0.68$) cold-formed SHS/RHS the bending moment resistance on the y-axis (see [55]) reads :

$$M_{csm,y,Rd} = \frac{W_{pl,y} f_y}{\gamma_{M0}} \left[1 + \frac{E_{sh}}{E} \frac{W_{el,y}}{W_{pl,y}} \left(\frac{\varepsilon_{csm}}{\varepsilon_y} - 1 \right) - \left(1 - \frac{W_{el,y}}{W_{pl,y}} \right) / \left(\frac{\varepsilon_{csm}}{\varepsilon_y} - 1 \right)^2 \right] \quad (2.88)$$

The complex formulation in equation (2.88) poses - similarly to equation (2.87) - the cross-section resistance at pure bending $M_{csm,y,Rd}$ as a function of the strain parameters and E-modulus values of the strain-hardening model. Geometrical properties and an exponent are added to fit the curve to numerical results. This formulation is limited to singular (and usually simplified) load cases. When there is an interaction of pure compression and

pure bending, the method follows the approach of the Eurocode interaction formulae for the cross-section resistance for combined bending moment in both axes and compression; for members, the Eurocode formulation is chosen again. The CSM still needs further research for the application to more load cases and other types of stocky sections, but seems an excellent method for the determination of the resistance of stocky hollow sections.

2.3.2 The Direct Strength Method

The Direct Strength Method (DSM) method was developed by the research group of professor B.W. Schafer at John Hopkins University [59, 11, 12], and it is integrated in the North-American AISI/AISC standard [51] [60]. Similarly to the CSM, the method defines a strength curve for the overall section, as opposed to the effective width method, which reduces each section plate contributing to the overall section resistance (described as the Eurocode approach in section 2.2). While the CSM is focused mainly on stocky hollow sections and members, the DSM focuses on slender open sections and members, such as channel sections and Z-shape sections. Thereby, the Winter formulation represents the perfect background for the development of the DSM design formulae at a local level in the slender range. The core of the method consists in the definition of the slenderness with a similar approach to the Winter formulation and Ayrton-Perry shown in sections 2.1 and 3.5. As a starting point, the DSM defines the slenderness and strength as the member slenderness (i.e. global slenderness) and then accounts for the cross-section reduction due to local and distortional buckling. The global slenderness thus reads (for a similar approach see equation (2.42) in this section under the description of the global buckling approaches):

$$\bar{\lambda}_{dsm,N} = \sqrt{\frac{Af_y}{N_{cr}}} \quad (2.89)$$

$$\bar{\lambda}_{dsm,M_y} = \sqrt{\frac{W_{el,y}f_y}{M_{cr,y}}} \quad (2.90)$$

Where N_{cr} and $M_{cr,y}$ refer respectively to the Euler elastic critical load and the critical bending moment for lateral-torsional buckling, which are both cases of global buckling. A graphic representation of the slenderness and strength curve is given in figure 2.11b. The global buckling reduction factor of the AISI is plotted against the corresponding slenderness and compared to the other DSM curves for local buckling and distortional buckling for the case of pure compression of a lipped C-section. The global buckling strength curve consists

in a reduction factor of the squash load, the local and the distortional buckling curves represent a reduction of the global buckling strength. The reduction factor is defined here as χ continuing to use the European notation, while the DSM uses a different character. Similarly to global buckling, the elastic critical load for local and distortional buckling is represented in figure 2.11a.

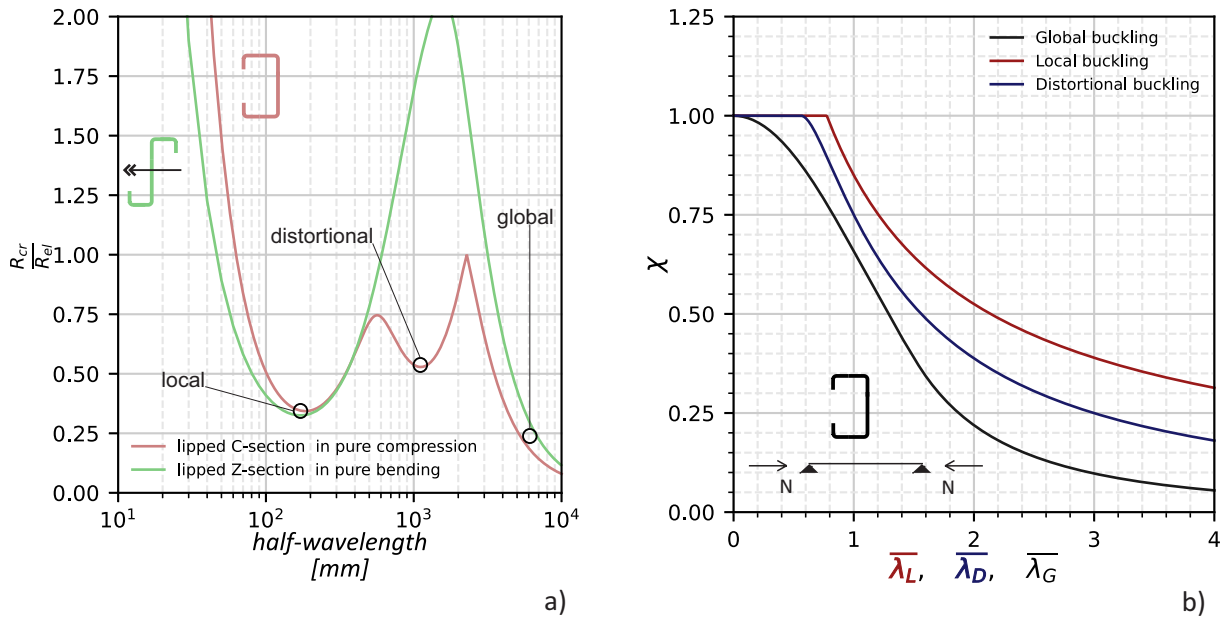


Fig. 2.11. a) signature curve of a section under pure compression and a section under pure bending; b) strength curves for local, distortional and global buckling.

In the figure the signature curves of two cases are displayed: a lipped C-section under pure compression and a lipped-Z-section under pure bending. A function connecting a large number of numerical results obtained with the CUFSM software (finite strip method, [61]) is plotted against each half-wave length of the corresponding numerical model. The function local points of minimum represent the critical loads for both distortional and local buckling for the case of pure compression and pure bending of the sections. In the y-axis the critical load is normalised by the elastic resistance and is thus defined as amplification factor R coherently to the GSRM methodology, described in detail in chapter 3. Each point in the signature curve defines a corresponding slenderness, and provides the buckling strength following the curves shown in figure 2.11b. For the exact formulation of the local, distortional and global buckling curves of the DSM the reader may refer to the Appendix 1 of the AISI [60] and DSM publications ([59], [11]). Equations (2.91) (2.92) (2.93) describe the buckling

strength curves for a lipped channel member under pure compression respectively for the case of global, distortional and local buckling, and they are represented in figure 2.11b. Coherently with the scope of this work, these DSM design rules are formulated in the GSRM format, closer to the European parameter definition.

$$\chi_G = 0.658\bar{\lambda}_G^2 \text{ for } \bar{\lambda}_G \leq 1.5 \quad \chi_G = \frac{0.877}{\bar{\lambda}_G^2} \text{ for } \bar{\lambda}_G > 1.5 \quad (2.91)$$

$$\chi_D = 1 \leq 0.561 \quad \chi_D = \left(1 - \frac{0.25}{\bar{\lambda}_D^{1.2}}\right) \frac{1}{\bar{\lambda}_D^{1.2}} \text{ for } \bar{\lambda}_D > 0.561 \quad (2.92)$$

$$\chi_L = 1 \leq 0.776 \quad \chi_L = \left(1 - \frac{0.15}{\bar{\lambda}_L^{0.8}}\right) \frac{1}{\bar{\lambda}_L^{0.8}} \text{ for } \bar{\lambda}_L > 0.776 \quad (2.93)$$

where G , D and L are the indices for global (flexural or lateral torsional buckling for channel sections), distortional and local.

Chapter 3

Methodology

3.1 Introduction

This chapter provides an overview of the methodology employed for the development of the GSR-Method. The section then follows a detailed description of the methodology adopted for the experimental tests, introducing the concepts of validation and calibration of FEM models against experimental tests. Finally, the last part describes the methodology for capturing predictive curves and functions according to the GSRM. The aim of this chapter is to provide GSR based methods for the prediction of the cross-section and beam-column resistance of SHS and RHS and other compression elements. In the following, the background for the development of the GSRM rules and predictive models is laid. Section 3.2 presents the general scientific methodology for the attainment of predictive rules in the following research areas:

- Conduction of full scale experimental tests for a background of the experimental tools.
- Measurement techniques and auxiliary tests.
- Validation of the numerical model for the extensive parametric study.
- Definition of analytical formulae for the prediction of the section and member resistance

The design formulae are the final outcome of the development of a predictive method. The formulae are generally mathematical functions fitting a large pool of numerical data. The numerical model is validated on the experimental test results, calibrating the necessary FEM model parameters. In the next section this general approach of the GSRM is described, in

order to clarify the objectives of this predictive methods and make it easy to follow the steps the methodology in each research areas, which are explained in the next section starting from 3.3.

3.2 Design approach

The development of a specific type of design rule, termed the Generalised Slenderness-based Resistance Method (GSRM), represents the main objective of this thesis and of the project HOLLOSSTAB. This method, similarly to other recently proposed methods such as the General Method for the design of whole frames ([3, 4]), the Direct Strength Method (DSM, see section 2.3.2), the Continuous Strength Method (CSM, see section 2.3.1) and – in the most directly related way - the Overall Interaction Concept / Overall Method (OIC, [20, 21]) makes use of an “overall” definition of the cross-sectional and member slenderness, generalised to account for combined load cases and the mutual support provided by the various parts of the studied cross-section and member. This requires the development of bespoke software tools for a straightforward use.

The generalised definitions of slenderness and resistance make use of load amplification factors to reach defined condition or resistance, and thus termed R . Thereby, the generalised slenderness is defined in equation (3.1), and the ultimate (buckling) resistance in equation (3.2):

$$\bar{\lambda} = \sqrt{\frac{R_{ref}}{R_{cr}}} \quad (3.1)$$

$$R_b = \chi \cdot R_{ref} \quad (3.2)$$

where the buckling coefficient χ is a function of $\bar{\lambda}$. In the following, the general idea behind the GSRM will be described in its application to determining the cross-sectional and member resistance.

3.2.1 Cross-section Resistance

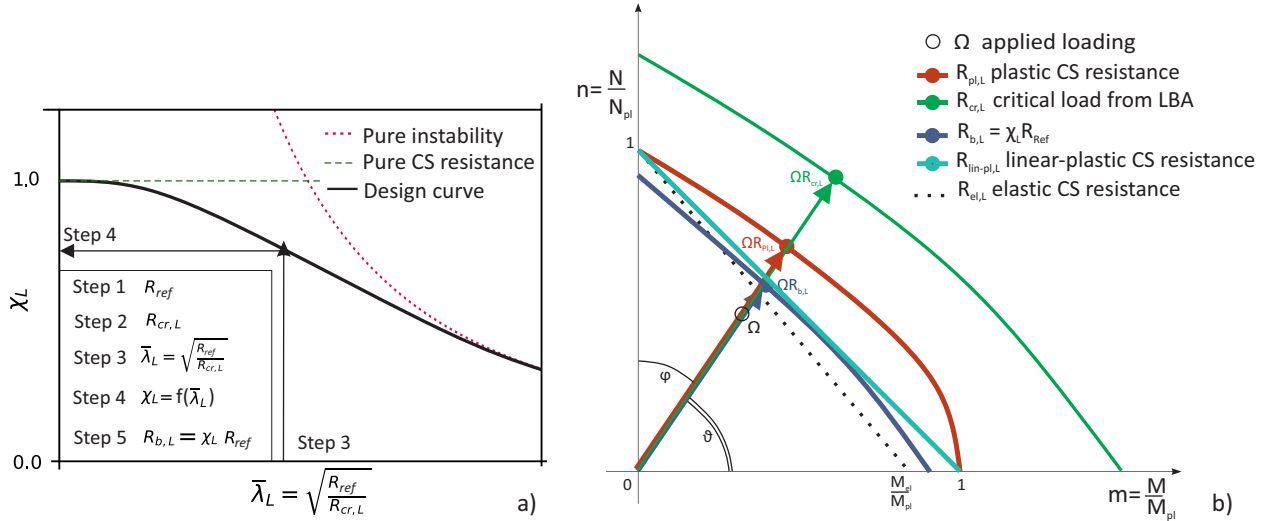


Fig. 3.1. Graphical representation of the GSRM design approach steps and procedures concerning the determination of the member cross-section resistance: a) strength curves in the $\chi - \bar{\lambda}$ plane and b) $n-m$ interaction curves.

The Generalised Slenderness-based Resistance Method (GSRM) belongs to the methods which associate a slenderness (λ) value depending on cross-section properties and applied load to the local resistance of the cross-section itself. The CSM and DSM share this general concept, as shown in section 2.3. Similarly to the Eurocode, the GSRM then introduces these steps in its own set of formulae for beam-column buckling, based on the Ayrton-Perry formulation described in detail in the following section 2.1.2. The proposed design methodology requires the sequential performance of two groups of steps and procedures, the first associated with the cross-section and the second with the member resistance. The steps and procedures concerning the determination of the cross-section resistance are shown in figure 3.1a and 3.1b. At a cross-section level the steps may be summarised as follows:

1. Determination of the cross-section resistance factor, termed R_{ref} , calculated by the stress resultants stemming from the applied loading under consideration, which is a combination of axial force and bending defined by an amplitude Ω and an angle φ in the $n-m$ plane (see figure 3.1b - n and m are the axial force and bending moment normalised with respect to the corresponding plastic resistances). For instance, in figure 3.1b, the applied loading has the amplitude given by the distance between the circle and the origin, measured along a direction making an angle φ with the n -axis,

defined by

$$\varphi = \arctan\left(\frac{m}{n}\right) \quad (3.3)$$

2. Calculation of the cross-section (local) critical elastic bifurcation/buckling load factor, termed $R_{cr,L}$, also associated with the same stress resultant profile defined in the previous item (see figure 3.1b).
3. On the basis of the two values calculated in the two previous items, calculate the cross-section (local) slenderness, defined as

$$\bar{\lambda}_L = \sqrt{\frac{R_{ref}}{R_{cr,L}}} \quad (3.4)$$

4. Calculation of a reduction factor of the cross-section resistance, termed χ_L , by means of a previously developed design curve, thus providing the cross-section (local) buckling resistance factor $R_{b,L} = \chi_L R_{ref}$ (see 3.1a), which constitutes the output required by the first of the aforementioned two groups of steps and procedures. Figure 3.1a shows the interaction curve associated with $\Omega R_{b,L}$, which is the final design value of the cross-section resistance.

The applied load determining the Ω point in the $n - m$ diagram may be determined by the interaction of a compressive or tensile axial load and biaxial bending moment, moving the $R_{cr,L}$ curve to very large or even infinite values. Both R_{ref} and $R_{cr,L}$ are calculated by means of available analytical expressions, for simple loadings, or through numerical analysis, for general loadings. Moreover, the value of $R_{cr,L}$ may be obtained for a simply supported member with a very short length (stub-member) acted by uniform stress resultant diagrams with the maximum values caused by the loading under consideration - i.e., it is not necessary to consider the particular end support conditions and stress resultant diagrams. The set of design curves $\chi_L = f(\bar{\lambda}_L)$ account for all the relevant aspects influencing the cross-section collapse (e.g., local geometrical imperfections and residual stresses) and cover all possible stress resultant combinations - currently, such curves are only available for pure compression or bending in similar methods.

3.2.2 Member Resistance

Since hollow section members are doubly symmetric and not susceptible to lateral-torsional buckling, the member (global) resistance involves exclusively flexural buckling, whenever axial compression is present. Therefore, regardless of the stress resultant combination, the member (global) critical elastic bifurcation/buckling load factor, termed $R_{cr,G}$, has a flexural nature. The above steps and procedures, simpler than their cross-section counterparts, are listed as follows.

1. Calculation of the member (global) critical elastic bifurcation/buckling load factor, termed $R_{cr,G}$ - in the particular case of hollow section members, it is a flexural bifurcation/buckling load factor associated with uniform compression.
2. Using the previously calculated cross-section (local) resistance factor ($R_{b,L} = \chi_L R_{ref}$) and the $R_{cr,G}$ value obtained in the previous step, calculate the member (global) slenderness, defined as

$$\bar{\lambda}_G = \sqrt{\frac{R_{b,L}}{R_{cr,G}}} \quad (3.5)$$

3. Calculation of a cross-section resistance reduction factor, termed χ_G , by means of the appropriate existing EC3 column strength curve, thus providing the member/overall resistance factor $R_{b,G} = \chi_G R_{b,L}$, i.e., $R_{b,G} = \chi_G \chi_L R_{ref}$, which constitutes the final output required.
4. Lastly, the member safety check merely consists of verifying the condition

$$\frac{R_{b,G}}{\gamma_M} \leq 1.0 \quad (3.6)$$

where γ_M is the appropriate partial safety factor. This means that the member stress resultant values at collapse must exceed those stemming from the applied loading.

3.3 Experimental tests

Cold-formed SHS and RHS (in addition to several derived sections such as hexagonal sections and groove-stiffened SHS) were studied at the structural laboratory of Bundeswehr University Munich. The section outer dimensions and wall thicknesses were chosen by keeping in mind

the general objective of the HOLLOSSTAB project, which was to provide design rules that lead to improvements particularly for more slender sections, i.e. mainly class 3 and 4 sections according to Eurocode 3. Of the six RHS/SHS tested at the laboratory, four were made of S355 steel, while two were cold-formed higher strength steel sections with measured values of the yield stress of above $R_{p0,2} = 700\text{N/mm}^2$.

3.3.1 Full scale tests

Stub column tests

The full-scale experimental tests on local buckling comprised two test setups: stub-column tests and short beam-column tests. Figure 3.2 gives an overview of the chosen setup. Part a) of the figure shows the configuration used for stub-column tests (pure axial compression), while parts b) to d) show the configuration and stiff lever arm used to introduce the plane stress field due to compression and bending in eccentrically loaded short beam-columns. The tests were carried out using an MFL Type UPS 1000V test rig. The actuator used for the vertical load transfer in this rig is a servo-hydraulic device with a maximum compression force capacity of 10 MN and a maximum tensile force capacity of 6 MN. The actuator is controlled by a servo-hydraulic valve of type Moog 508K03DOJNO D101. A hydraulic load cell is used for measuring the actuator force, using a pressure transducer of type HBM P3MB-350bar. The load cells also incorporate a linear variable displacement transducer (LVDT). All experimental tests were displacement controlled, with a given total displacement (accounting for setup stiffness) ranging from 10.0 mm to 20.0 mm for stub-column tests and from 10.0 mm to 60.0 mm for the beam-column tests. A constant, slow test velocity was applied in order to simulate a static problem. The velocity varied between 0.01 mm/s to 0.06 mm/s. A digital image correlation system (DIC) produced by GOM was used to monitor deformations and rotations of the specimen surfaces and of the test rig itself, see the reference points and speckle patterns in figure 3.2a and 3.2b for the definition of the angle α . The DIC recording rate was set to 1 Hz, providing around 1000 pictures and measurements for each specimen for a complete test.

Strain gauges were attached to the specimen surfaces in order to confirm the DIC measurement system, which showed more reliable and efficient results. A precise measurement of the overall specimen deformation and the deformation field for the DIC surface were recorded; thus, an additional LVDT measurement was not necessary. The overall machine stiffness was taken into account and eliminated from the measurement through a calibration

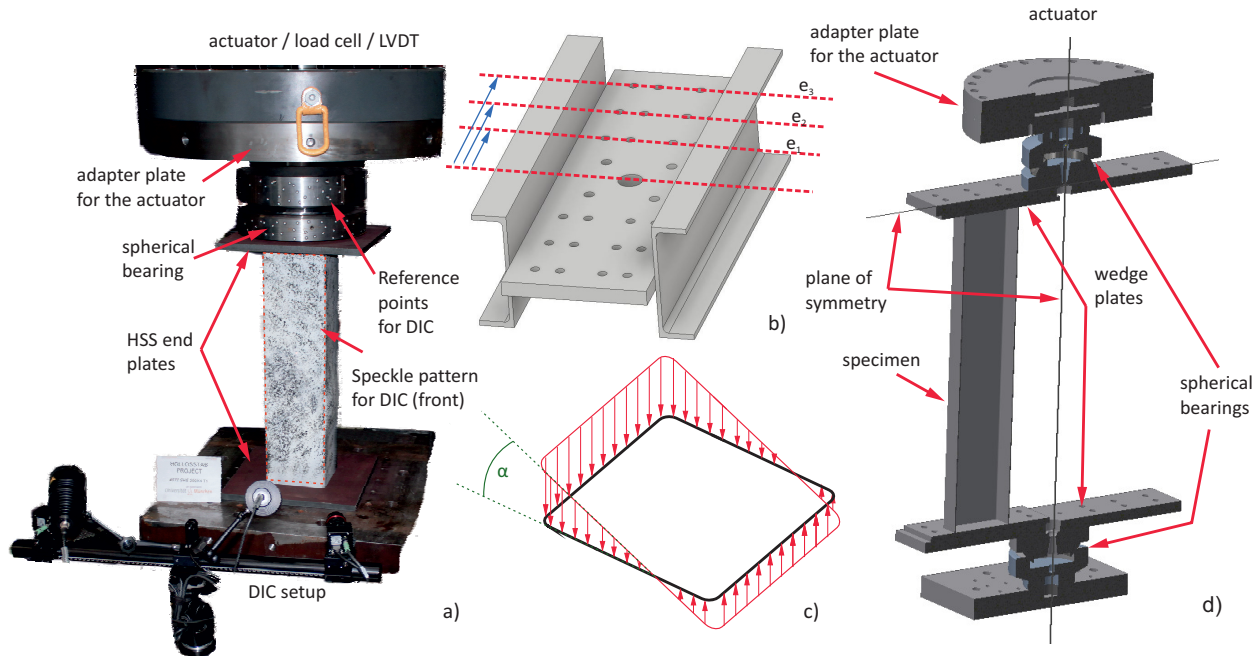


Fig. 3.2. a) test setup for the stub-column test, b) eccentricity levels, c) tensional field induced by $N+M$ and corresponding angle (α) of rotation, d) scheme of the $N+M$ test setup.

test, whereas the rest of the test setup stiffness results in additional 10 MN machine LVDT deformation than DIC deformation. Due to the large load range, the same test setup was positively applied for the different cross-sections. The stub-columns load capacity for the tested specimens ranges from 0.5 to 7 MN. Each specimen was accurately positioned, so that the specimen axis and the test rig axis coincided using the calibration measurement of the distance between specimen side and spherical bearing. A once time test on the accuracy of this procedure was conducted with the DIC measurement of the reference points on the spherical bearing and its adapter. The results showed precision around 0.1 mm. Failure of all the tested stub columns featured local buckling, with the failure modes for the stub column tests shown in figure 3.3. Each cross section is representatively displayed, and in the Appendix more details of the experimental tests can be found. The ID number of the stub column tests is composed of a test denomination “T1” and a number from 1 to 12.

Short beam column tests

Short beam column tests were performed to investigate the local buckling behaviour of cross-sections under the $N+M$ load case. In total, 36 compression plus uniaxial bending tests with different eccentricity values were carried on. The compression tests on T3-1 to

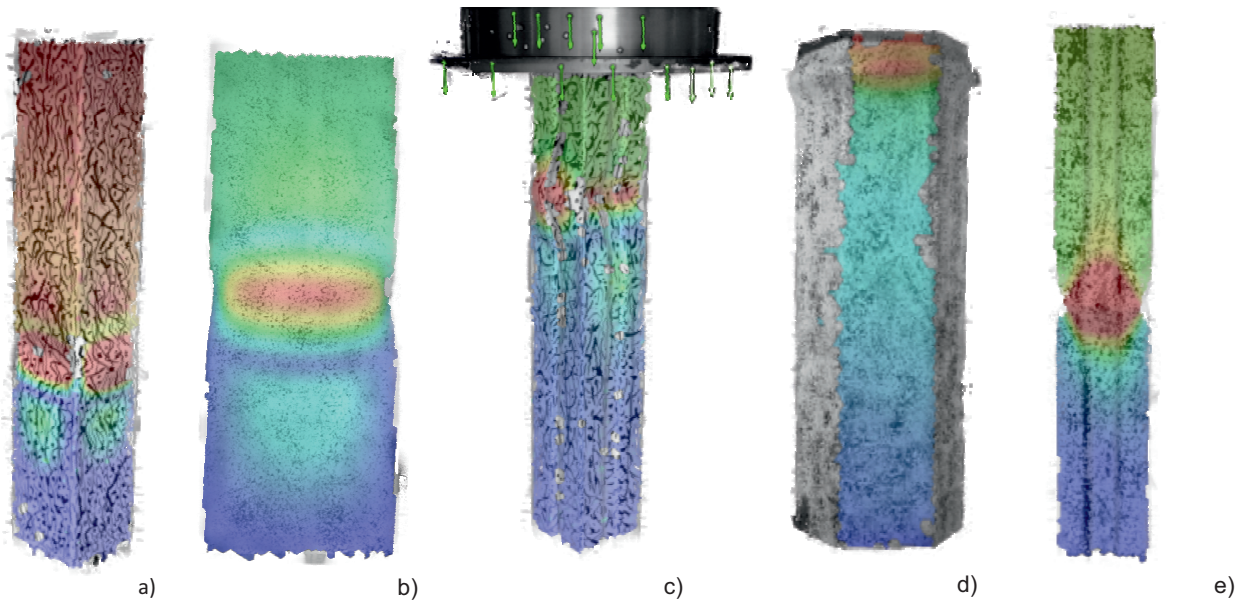


Fig. 3.3. Failure modes for the stub column tests measured with the DIC system. The scale shows the maximum displacement in red and the minimum in blue; in the figure a) SHS T1-1, b) RHS T1-6, c) SHS-S T1-9, d) hexagonal T1-10, e) SHS-T T1-11 cross-sections are shown.

T3-12 and T4-1 to T4-12 were conducted on the same 10 MN servo-hydraulic test rig built by MFL, where the T1 stub-column tests were conducted. Other important test setup aspects remained unchanged, such as the speckle pattern and its positioning to the camera, the use of the DIC system itself, the load and displacement measurement of the test rig load cell. The most important changes in the test setup regard the introduction of the load. For T3 and T4 a constant uniaxial bending moment was introduced by adding an eccentricity to the compression force on both ends of the specimen. A schematic representation of the test setup is given in figure 3.2d and 3.4a. With three different eccentricity steps, a wide variety of combinations of pure compression and bending moment were possible. T3 were always positioned in the first step with eccentricity, e_1 in figure 3.2b, and T4 specimens either in position e_2 or e_3 . The measurement of the deformation remained unchanged, since the DIC system produced the best results, compared to other options. A determining change in the measurement and setup was represented by the rotation measurement. The first direct measurement was given by the measurement of the rotation angles in degree from two inclinometers, on the top and bottom wedge plates. These values – similarly to the machine stroke measurement – contain additional deformation due to the test setup stiffness. Thus, a second option for the evaluation of the inclination was found as the angle α , as defined in figure 3.2c. While the measurement with the inclinometers can be directly compared to the

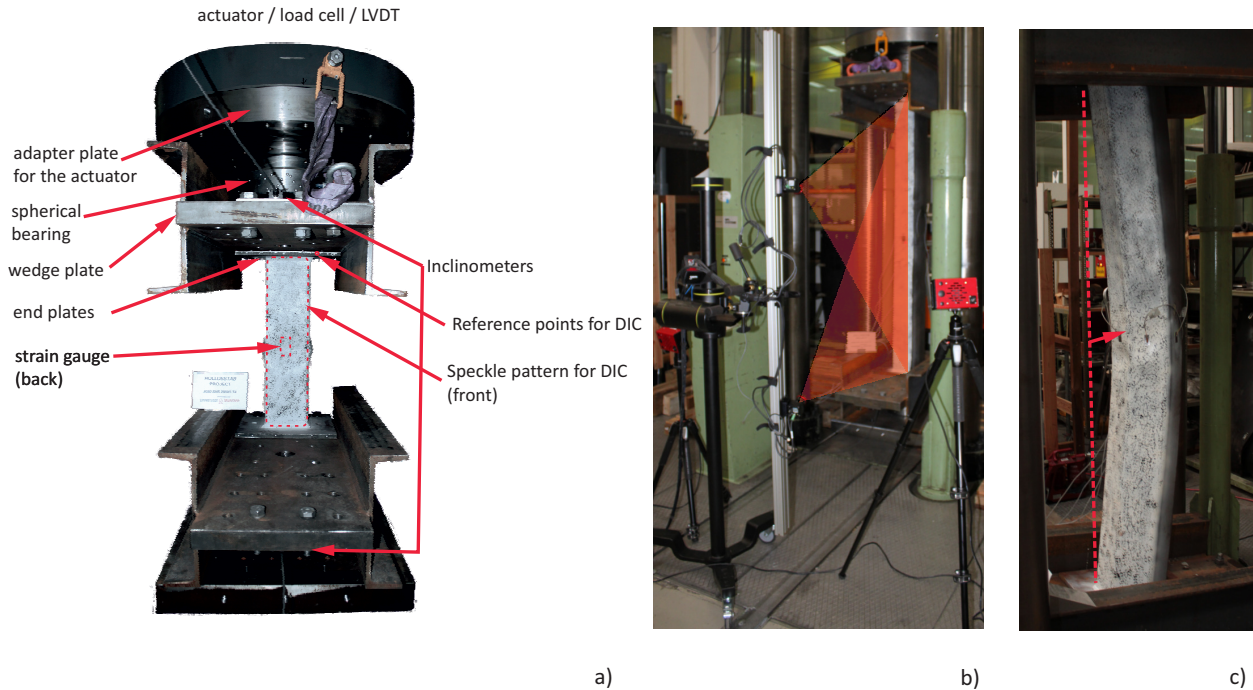


Fig. 3.4. a) Scheme and representation of a T3 and T4 test measurement systems; b) adaptation of the DIC measuring system to large deformation fields, a schematic representation of the cameras views is marked in red; c) large mid-span displacement for T5-7 hexagonal beam-column test.

end rotation of a numerical GMNIA-MEAS simulation, the angle α is grasping the overall rotation of the specimen and it is valid exclusively in the elastic field. Figure 3.4a represents a typical test setup for the combined N and M load, T3 and T4.

Long beam column tests

T5 long beam column tests were performed to investigate the interaction between the local buckling and the global buckling behaviour of hollow sections under the N+M load case. In total, 7 compression plus uniaxial bending tests with different eccentricity values were carried on at the laboratory of the chair structural engineering at the University of the Bundeswehr Munich. The specimens consisted of a sample of different cross-sections, which were already tested in other load combinations, but a different specimen length was introduced to investigate the effects of the global buckling. The compression tests on T5-1 to T5-7 were conducted on the same 10 MN servo-hydraulic test rig, and the test setup remained mostly unchanged. The main challenge of these experimental tests consisted in the bigger measuring field for the DIC system. To reach acceptable results, the Aramis GOM system was adapted to this special task with new calibration sticks and a different setup, but the

logic of DIC and results remained unchanged. An important result of the use of the DIC is the measurement of the mid-span deflection in order to estimate accurately the second order moment at the mid-span level, shown in a tested specimen in figure 3.4c.

3.3.2 Auxiliary tests

While the purpose of a full scale test is the direct determination of the ultimate capacity of realistically sized specimens, auxiliary tests are used to obtain certain input parameters for analytical or numerical models (such as material models, or imperfection models), and help reduce the scatter in the results of the full-scale tests. These tests give additional information compared to the full-scale test, thereby enhancing the accuracy in the reproduction of the full-scale test by numerical models. For each specimen, the experimental campaign included auxiliary tests such as tensile coupon tests and imperfection measurements. Owing to the number and the quality of the tests that were carried out, they provided sufficient information on each test to perform an accurate validation of numerical models, described in the next section 3.4.

Tensile coupon tests

The tensile coupon tests were taken from both the flat faces and the corners of the SHS and RHS and tested in a standard hydraulic testing rig produced by Zwick-Röll. The specimens of the experimental test campaign were chosen between mild-steel (S355) and high-strength steel (up to S890). Special care was given to the cutting process of the high-strength steel by cutting the steel elements with high-pressure water jet, thus not altering the original material properties. The results of the coupon tests were load-deformation curves, converted to engineering stress-strain relations, which were then transformed to true stress-strain functions according to equations 3.7 and 3.8.

$$\sigma_{true} = \sigma_{engineering} (1 + \varepsilon_{engineering}) \quad (3.7)$$

$$\varepsilon_{true} = \ln(1 + \varepsilon_{engineering}) \quad (3.8)$$

Imperfection measurement

A 3D scanning technique was employed to measure the distribution of local geometric imperfections in each test specimen. After cleaning of the specimens' surfaces, the outer sur-

face of the specimens was scanned using a Zeiss 3D scanner and recorded as point cloud. The scanned data was initially processed using the software “Colin3D” [62]; a typical pre-processed 3D model for a groove-stiffened, cold-formed SHS is displayed in figure 3.2 as point cloud. The 3D spline curves in figure 3.2b are laid on the measured points of the cloud and then used in the numerical simulation as the input geometry of the FEM model. Additionally, the 3D scan data were statistically evaluated with respect to shape deviations and tolerances from the nominal geometry (figure 3.2c and d).

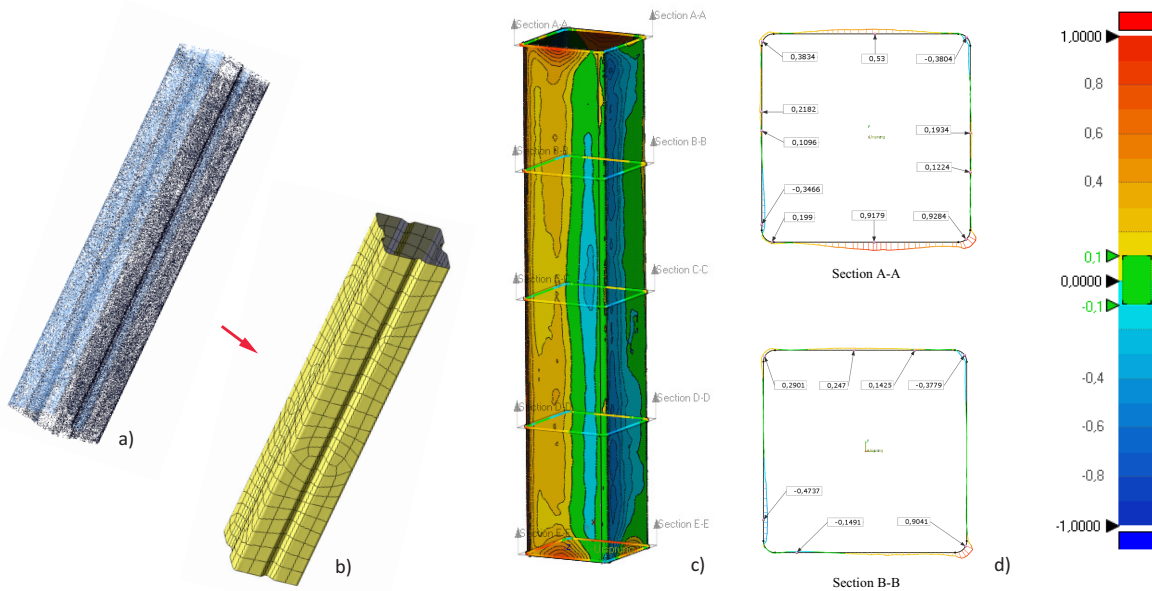


Fig. 3.5. a) point cloud of the 3D scan data; b) spline curves approximating the real geometry c) 3D results of measuring system of a SHS specimen, d) exemplary evaluation of two cross-sections of the specimen in c) (imperfection values in [mm]).

3.4 FEM modelling

The Finite Element Method (FEM) model is the numerical model used for the simulation of the mechanical problems within the scope of this work. The principal aim of the experimental campaign was to provide the basis for the validation of advanced FEM models that use Geometrically and Materially Non-Linear Analyses with Imperfections (GMNIA) to realistically and accurately simulate the behaviour of the studied sections loaded in com-

pression and bending. The proprietary software Simulia ABAQUS (2016) [63] was used for all numerical simulations.

3.4.1 FEM discretization and input parameters

In this thesis, the numerical analysis of hollow sections was carried out using the Finite Element Method (FEM) and a shell-element type discretization. Shell elements can be used advantageously for 3-dimensional bodies with a thickness significantly smaller than the other dimensions and whose topology allow for a two-dimensional (surfaced based) mathematical description. The assumption for the stress state of this type of elements is that the stress in the direction of the thickness are negligible. Linear isoparametric shell elements with reduced integration (element type S4R) were employed in Abaqus. These shell elements have six degrees of freedom associated with each node, three translations and three rotations. Each element presents 5 section points along the thickness in order to calculate the behaviour at selected points through numerical integration.

3.4.2 Geometrically and Materially Non-linear Analyses

The Finite Element Method (FEM) models were created with the aim of comparing the numerical results with the experimental tests. Abaqus provides the option of carrying out a non-linear analysis with both geometrical and material non-linearity. The material is defined as elastic plastic according to:

$$\boldsymbol{\varepsilon}_{total} = \boldsymbol{\varepsilon}_{el} + \boldsymbol{\varepsilon}_{pl} \quad (3.9)$$

which postulates the additive strain rate decomposition. The stress-strain relation input consists of a multi-linear function of $\sigma - \varepsilon$ and is based on the incremental plasticity theory. The Abaqus FEM model produces small increments of the applied load (in this case meaning either imposed deformation or force load) typically starting at 5% of the final applied load and increasing by smaller values. The non-linear problem is history-dependent, so at each new increment the software finds a new equilibrium point with the Newton's method as numerical technique to find convergence. The iteration process used in the FEM models applies load or displacement control, and the results shown in the next chapter are derived from this type of analysis, but several tests on different simulation configurations used RIKS analysis (iteration based on arc-control length), which produced similar results, showing that

no local minima were missed during the iterations. Example of such problems related to the buckling analysis are snap-through problems.

The accurate reproduction of an experimental test is defined as *reverse engineering process*, and uses Geometrically and Materially Non-linear Imperfection Analyses (GMNIA) with the measured geometrical shape of the sections and an accurate material model. This leads to very small (<3%) deviations to the ultimate load of the buckling tests, if the meshing and modelling of boundary conditions are accurate. This type of GMNIA, which uses measured input data and was performed during the reverse engineering and model validation phase, is denoted by “GMNIA-MEAS” in the following section. In the GMNIA-MEAS model the true stresses and true strains were introduced for the validation of each full-scale experimental test. The stress-strain curve was simplified by dividing the true strain range into 50-100 points and each point of the corresponding stress was utilised in the FEM material model. The imperfections were introduced as spline curve and meshed directly in the Abaqus software. Both real imperfections and real material model improved significantly the accuracy of the FEM model outcome.

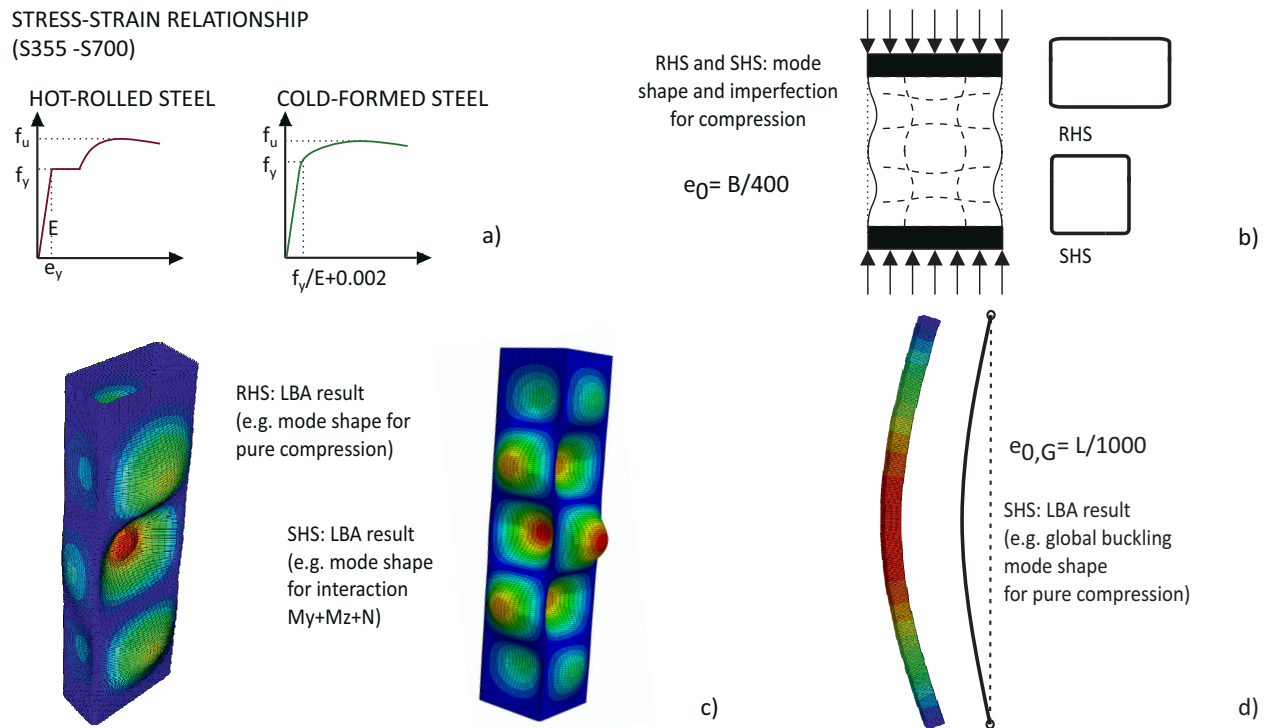


Fig. 3.6. a) Material model; b) buckling shape and imperfection amplitude; c) LBA results of two sections under different applied load; d) first global eigenmode and global imperfection amplitude in a LBA analysis.

As a result of the GMNIA model validation, a mesh density with a minimum of 60 elements in circumferential and 200 elements in longitudinal direction was found to lead to converging results of high accuracy. While the purpose of the GMNIA-MEAS is to reproduce accurately the experimental tests, the aim of a parametric study is to produce a large number of numerical values for the curve fitting procedure during the development of the design formulae. This is not practical with a large number of unknowns and degrees of freedom as in a GMNIA-MEAS, and more importantly, the GMNIA-MEAS may not generalise well, if nominal geometric or material values from the standards were applied. For these reasons, an equivalent FEM model was developed, here defined as GMNIA. Thereby, a GMNIA is a simplified model with equivalent material models and imperfections. These properties are shown in figure 3.6. Figure 3.6c shows a typical GMNIA mesh, presenting a lower number of degrees of freedom than a GMNIA-MEAS and showing the buckling shape for the modelling of the imperfections. The imperfections in the model are given by the shape of the first eigenmode of a linear buckling analysis (LBA), scaled by a multiplying factor e_0 , defined as imperfection amplitude.

The material model provides a stress-strain relation equivalent to the measured stress-strain values from the tensile coupons. Figure 3.6a shows the two material models from Yun and Gardner [57] [56]. These material models correspond to the stress-strain function described in the CSM in section 2.3 figure 2.10 and are adopted in the GMNIA model for the GSRM in the following cases:

- in the analysis of cold-formed sections, modelled by a linear-elastic range up to the yield stress and by a Ramberg-Osgood model in the plastic range.
- in the analysis of hot-rolled sections, modelled by a bilinear function up to ε_{sh} and a non-linear function up to f_u .

Applying nominal values for the yield stress to both models, the GMNIA obtains a material model equivalent to the stress-strain relation from the coupon tests in the GMNIA-MEAS. The residual stresses are not introduced in the model since the stress-strain formulation of Yun-Gardner is calibrated against a large pool of experimental results to account for the effects of residual stresses. A more detailed description of the Yun-Gardner curves is found in section 2.3.

3.4.3 Validation against experimental tests

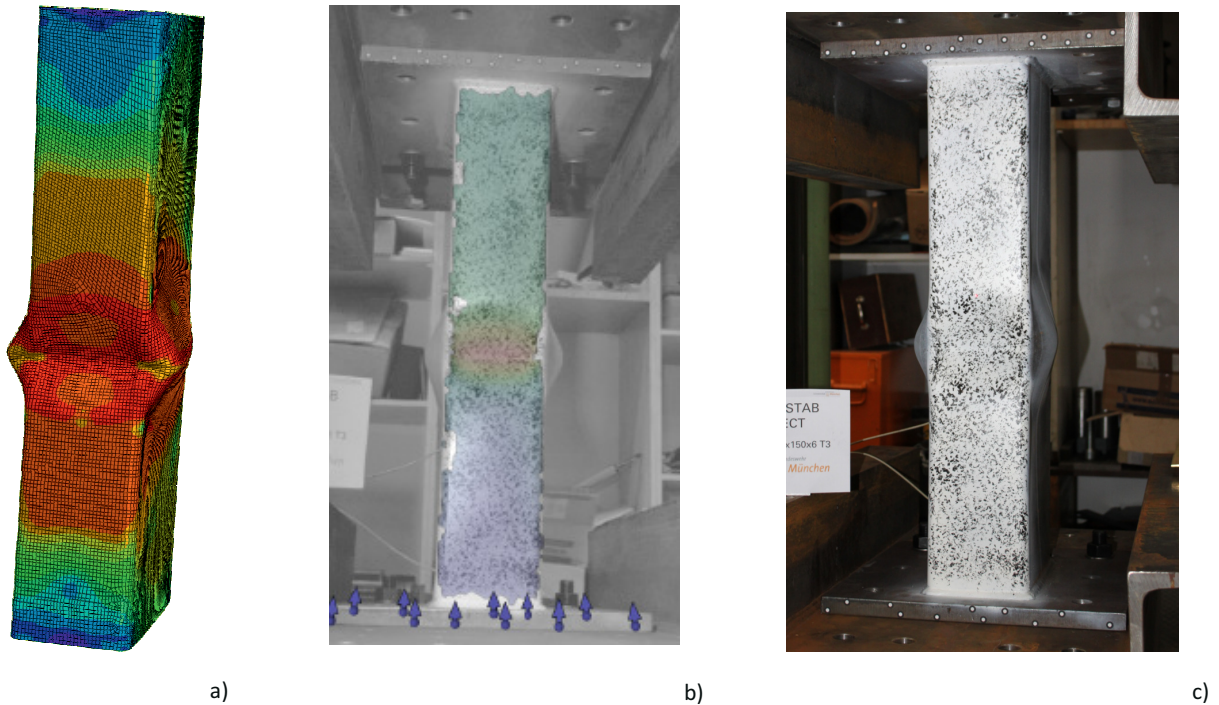


Fig. 3.7. GMNIA-MEAS model vs. test results, specimen deformed shape measured with DIC.

An example of a GMNIA-MEAS model validation is shown in figure 3.7. The RHS specimen deformed shape in a) was caused by an eccentric compressive load and the deformations were measured by a GOM (Aramis) Digital Correlation Image (DIC) system. The DIC method tracks simultaneously images of the on-going experimental test and captures the changes in the image producing a full-field of displacements of the registered experiment. The DIC necessitates of a painted stochastic grid of black and white colours, isolates single cells in the stochastic grid and recognises them during the experiment. Thereby, during the experimental test the single cell displacement may be tracked, and provided that the full external surface of the specimen is painted in a black-and-white stochastic grid, the DIC recollects the deformation field of the specimen surface. The evaluation of the DIC deformations in a colour scale is shown in figure 3.7b and figure 3.7c represents the deformed specimen with the painted stochastic grid for the DIC. While the comparison of the deformation shape between the GMNIA-MEAS and the full-scale experimental test shows qualitatively the accuracy of the numerical model, the direct comparison of the peak load in both experimental measure the accuracy of the GMNIA-MEAS and the experimental test. The comparison is

shown in terms of accuracy of the load-deformation and load-rotation plots. In figure 3.8 the GMNIA-MEAS reproduces both the position and shape of the post-buckling deformations as well as the peak load itself quite accurately, see figure 3.8. As illustrated in the figure, the load-shortening and load-rotation paths obtained from the FE models were typically too stiff up to the peak load and descended more rapidly than in the experimental observation. For the purposes of the project, these deviations in the load-deformation paths were not of concern, as the peak value of resistance was the main value against which the models were validated. In summary, the following statistics of the model validation were obtained for the experimental tests conducted at Bundeswehr University Munich:

- for the 12 stub-column tests (pure axial compression) considered, the average of the ratio between the peak load in the validated GMNIA-MEAS models and the experimental tests was $F_{max,FEM}/F_{max,test} = 0.99$, with a standard deviation of 3.2%.
- for the total of 48 stub-column and short beam-column tests on RHS/SHS and derived section shapes, an average value of $F_{max,FEM}/F_{max,test} = 0.99$ was obtained, with 4.2% standard deviation.

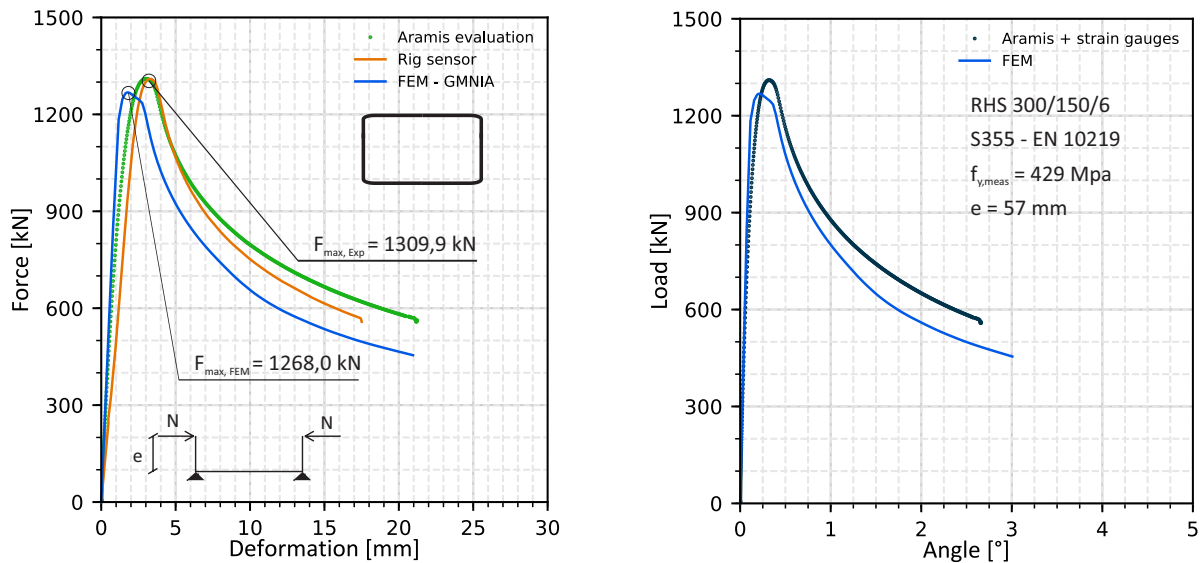


Fig. 3.8. Load-deformation and load-rotation plots.

3.4.4 Calibration of the GMNIA parameters

As was shown in chapter 2, most the formulation of a design rule undergoes a "calibration" phase, which consists in a process of fine-tuning arbitrary input parameters of the model. For both the Winter approach and Ayrton-Perry approach a determining parameter is the shape and amplitude of the imperfections. The imperfection shape relies on the mechanical analysis of the structural element, and in the scope of this work the imperfection model requires an approach at a local level, where the Winter formulation is chosen, and a different approach at a global level, where the Ayrton-Perry formulation is chosen. The work of Winter on local buckling represents an extensive source of experimental data and provides design curves for the prediction of the buckling strength, that are mechanically sound and are applied in chapter 6 for the development of GSRM curves. The imperfection in the literature of plate buckling [38, 39] is commonly referred to as:

$$e_{0,L} = B/400 \quad (3.10)$$

where $e_{0,L}$ is the imperfection amplitude, B the plate width and 400 is a value calibrated from experimental and numerical tests. The Eurocode 3 [1] provides a similar approach for the imperfection amplitude and utilises the value of 200. In chapter 5 the calibration of the imperfection amplitude against the HOLLOSSTAB experimental test results is described and analysed in detail.

The approach for imperfections for the global buckling is derived from the Ayrton-Perry formulation. Global imperfections of the whole member determine a second order bending moment and influence the behaviour for global buckling. The shape of the imperfection is given by the first global eigenmode of the LBA and is scaled by the imperfection amplitude calculated with equation (3.11).

$$e_{0,G} = L/1000 \quad (3.11)$$

where L is the member length and 1000 a calibrated parameter found in the literature for column buckling (see [48] and [50]) and code provisions. More details on the model validation and calibration may be found in chapter 5 and in [64, 22, 29].

3.5 Analytical formulae

Whether at a local level or at a global level, a buckling curve is defined as any kind of representation of buckling strength R_b as a function of its cross section resistance R_{CS} and critical bifurcation load R_{cr} :

$$R_b = f(R_{CS}; R_{cr}) \quad (3.12)$$

With:

- R_b buckling resistance, i.e. the load level at which the peak of a load-deformation (F-u) curve would be measured in tests, see figure 3.9.
- R_{CS} resistance at a cross-sectional level. This can for instance be the plastic or elastic capacity, or a reduced elastic capacity owing to local buckling effects.
- R_{cr} elastic bifurcation load from analytical formulae (e.g. Euler load) or an LBA.

This function f is defined by an analytical formula developed for the prediction of the buckling strength, and this section reports the most common formats for the development of analytical formulae within the scope of this thesis.

In figure 3.9 the elastic bifurcation load is represented as a constant load-value independent from the deformation of the member. The real resistance value in case of member buckling is always lower and is defined as the buckling resistance R_b in 3.9 at the peak level of each load-deformation curve. The imperfection amplitude e_0 is applied to local and global imperfection shapes. With increasing e_0 , member length L and effects due to the material non-linearity, the peak loads are progressively reduced, but these effects are not clearly visible in this type of representation. The formulation of the design function and parameters inherently depends on the chosen representation format, since same numerical results could assume different shapes and tendency according to the chosen representation. A basic representation of the single numerical or experimental results is the load-deformation curve, which was here analysed as an introduction to the different formats for the analytical formulae both for plate and member buckling.

A common representation format for the cross-section resistance is the normalised $m_y - n$ plot. This plot shows the applied normalised pure compression n and the applied normalised bending moment m_y , defined as follows:

$$n = \frac{N}{N_{pl}} \quad m_y = \frac{M_y}{M_{y,pl}} \quad (3.13)$$

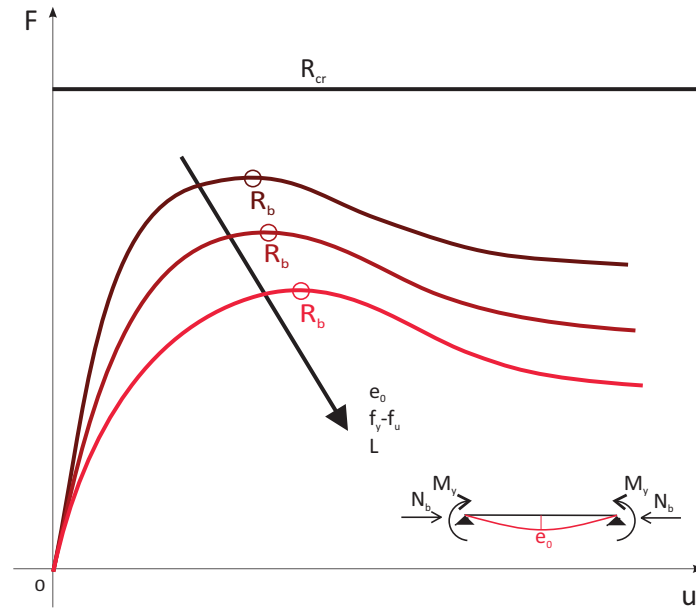


Fig. 3.9. Load-deformation curve comparing the beam-column resistance with increasing imperfection amplitude, member length and with real material models.

Similarly to m_y , m_z may be added if the cross-section is not bi-symmetrical. Figure 3.10 serves to illustrate the concept with example. The $n - m_y - m_z$ diagram shows the numerical results of the plastic resistance on a RHS section with an H/B ratio of 2. The continuous surface shown in the figure is a reference load, which was given in the $n - m_y - m_z$ space by the equation of a sphere:

$$n^2 + m_y^2 + m_z^2 = 1 \quad (3.14)$$

The dots in the plot show the points corresponding to the full plastic resistance of the section, which is asymmetrical with respect to the origin and thus has a markedly varying distance from the reference load surface. Generally speaking for SHS and RHS cross-sections, the R_{pl} points are found mostly inside the reference load surface, in some cases exactly on the surface, and sometimes somewhat outside the reference load surface, as is shown in figure 3.10.

In the following part of the section several design formats corresponding to analytical formulae for the development of a design curve are presented: the Ayrton-Perry and the Winter format methodologies will be presented in detail.

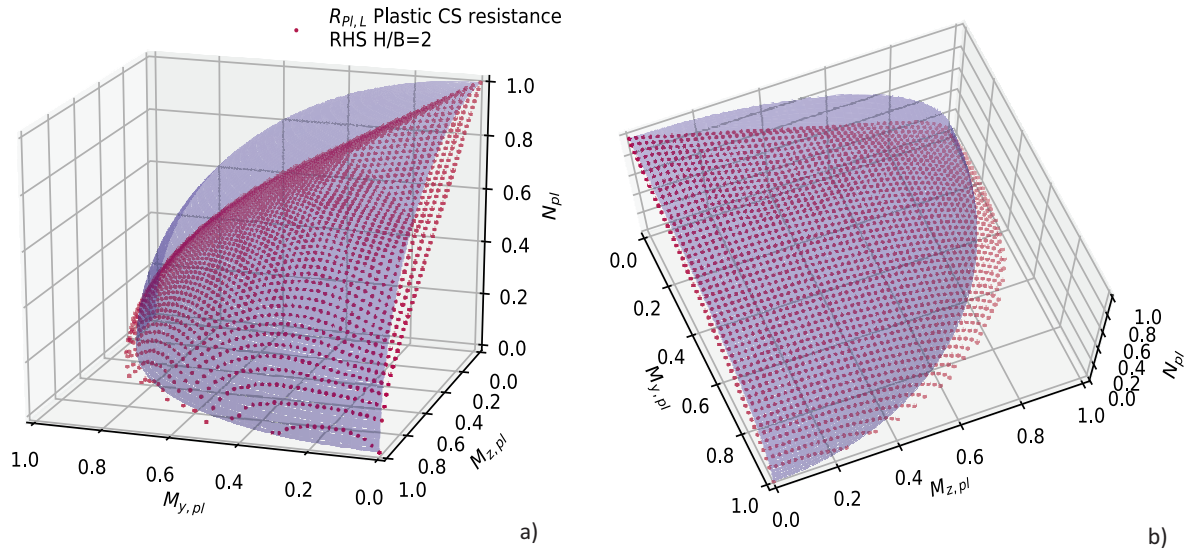


Fig. 3.10. normalised pure compression and biaxial bending moment diagram shown in two different views a) and b).

3.5.1 Ayrton-Perry format

Starting from the approach of Ayrton and Perry defined in section 2.1.2, the equation to the limit state and a formulation for the imperfections were introduced. Current design standards such as the Eurocode use equation (2.21) to the limit state with a reduction factor of the cross-sectional plastic resistance in order to define the member strength, and they plot it as a function of the member slenderness, obtaining:

$$\chi_y + \frac{Ae_0}{N_{cr}} \cdot \frac{\chi_y}{1 - \chi_y \bar{\lambda}_y^2} = 1.0 \quad (3.15)$$

where χ_y and $\bar{\lambda}_y$ are, respectively, the knock-down factor and normalized slenderness for buckling about the y-axis. In this section, the y-axis will be used as a reference for a simplified explanation of the Ayrton-Perry model, but the formulae and formats may be extended to 3D models including buckling along the z-axis. Thereby, the following variable may be introduced:

$$\eta_{imp} = \frac{Ae_0}{N_{cr}} \quad (3.16)$$

where η_{imp} is a normalization of e_0 by the section core width. The η_{imp} value is the correspondent parameter for the imperfection derived by Robertson and shown in section 2.1.

Introducing this definition in the equation (3.15) results in:

$$\chi_y + \eta_{imp} \cdot \frac{\chi_y}{1 - \chi_y \bar{\lambda}_y^2} = 1.0 \quad (3.17)$$

The quadratic equation may be rewritten in the reduced quadratic form as follows:

$$\chi_y^2 - \frac{\chi_y}{\bar{\lambda}_y^2} \left(1 + \eta_{imp} + \bar{\lambda}_y^2\right) + \frac{1}{\bar{\lambda}_y^2} = 0 \quad (3.18)$$

The solution for equation (3.18) reads:

$$\chi_y = \frac{\varphi_y}{\bar{\lambda}_y^2} - \sqrt{\frac{\varphi_y^2}{\bar{\lambda}_y^4} - \frac{1}{\bar{\lambda}_y^2}} = \frac{1}{\bar{\lambda}_y^2} \left(\varphi_y - \sqrt{\varphi_y^2 - \bar{\lambda}_y^2} \right) \quad (3.19)$$

$$\text{with } \varphi_y = \frac{1}{2} \left(1 + \eta_{imp} + \bar{\lambda}_y^2\right) \quad (3.20)$$

The expression (3.19) leads to the well-known solution:

$$\chi_y = \frac{1}{\varphi_y + \sqrt{\varphi_y^2 - \bar{\lambda}_y^2}} \quad (3.21)$$

Figure 3.11 shows possible buckling curves applying different values of a constant value of η_{imp} . Still, this equation does not predict accurately any real cross-section, since the η_{imp} is not defined in a practical manner. Rondal and Maqui in 1979 [65] proposed a formulation for this parameter, which later would be used by the Eurocode and it is still the current version in use:

$$\eta_{imp} = \alpha (\bar{\lambda}_y - \bar{\lambda}_0) \quad (3.22)$$

where η_{imp} is a linear function of the relative slenderness in the y-axis $\bar{\lambda}_y$ and α a newly introduced constant value accounting for manufacturing process and cross-section type, and $\bar{\lambda}_0$ is a constant value equal to 0.2 and representing the end of the plateau of $\chi_y = 1.0$. In figure 3.11b the curves for column-buckling are represented from curve a_0 to d . The corresponding values of α are shown in table 3.1, corresponding to the values calibrated by Rondal and Maquoi against experimental tests. These values are still adopted in the current version of the European standard.

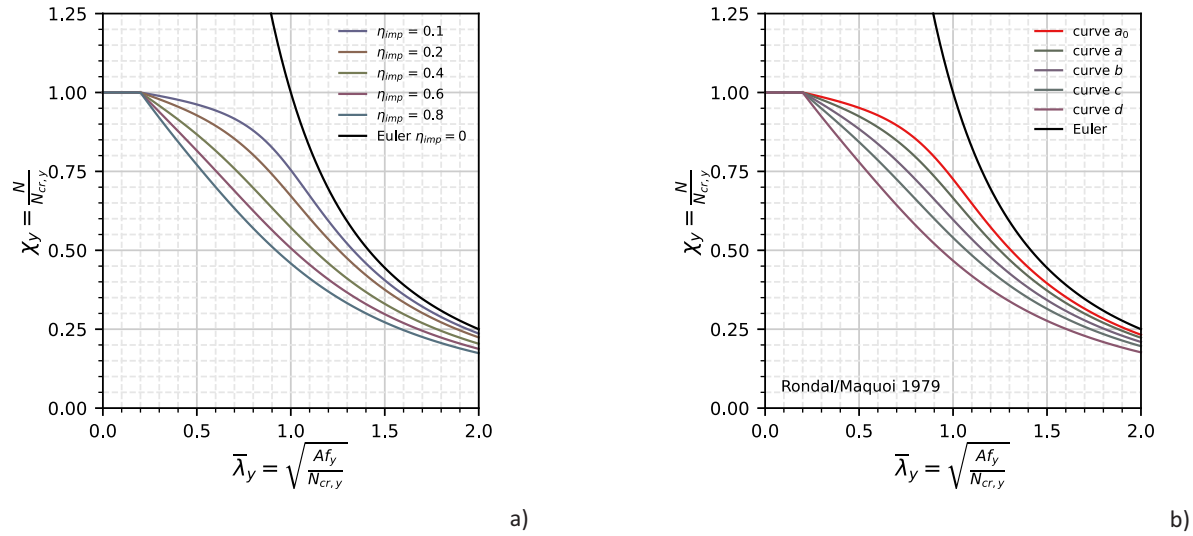


Fig. 3.11. a) different buckling curves varying η_{imp} ; b) EC3 buckling curves.

Buckling curve	a ₀	a	b	c	d
Imperfection factor α	0.13	0.21	0.34	0.49	0.76

Table 3.1: EN 1993-1-1. Imperfection factors for the determination of the buckling curve.

3.5.2 Winter format

The description of the formulations for local buckling by Winter ended in section 2.1 with equation 2.18. This formula predicts values on precise assumptions on load and boundary conditions. This formulation may though be extended to a general case by introducing calibration factors. Following existing proposals and currently developed design methods ([11], [66], [60]), equation (2.17) may be rewritten as follows:

$$\rho = \frac{1}{\bar{\lambda}_L^{n_1}} \left(1 - \frac{A}{\bar{\lambda}_L^{n_2}} \right) \quad (3.23)$$

where:

- n_1 and n_2 are the exponent of $\bar{\lambda}_L$.
- A is generally a constant value.

In general, $n_1 = n_2$ is often the chosen as it is consistent with the Winter formulation. The Winter format is currently in use to predict very different effects of buckling not only related to local buckling, but distortional and global buckling, too.

$$\rho = \frac{1}{\lambda_L^{0.6}} \left(1 - \frac{0.25}{\lambda_L^{0.6}} \right) \quad (3.24)$$

$$\rho = \frac{1}{\lambda_{LG}^{0.8}} \left(1 - \frac{0.15}{\lambda_{LG}^{0.8}} \right) \quad (3.25)$$

Equations (3.24) and (3.25) are two powerful examples of the Winter format. Equation (3.24) represents the formula for the prediction of buckling strength for open channel sections found in the current version of the AISI [60] with calibration values $n_1 = n_2 = 0.6$ and $A = 0.25$, derived from numerical and experimental results. In equation (3.25) the predictive formula for the interaction of local and global buckling of open channel members from the same design provisions is shown. The member strength is calculated as a reduction factor of the cross-section resistance. In order for the GSRM to benefit from the Winter formula and design approach the effects on the parameter A are studied, whereas the choice of different values than $n_1 = n_2 = 1$ is neglected, since it is not consistent with Winter plate buckling and does not show substantial improvement in result accuracy. In fact, this same approach for plate buckling is adopted in the Eurocode [40] and described in 2.2. Figure 3.12a shows the domain of the Winter curve with values of A ranging from $A = 0.11$ to $A = 0.22$; consistently with the Eurocode approach $A = 0.22$ corresponds to the buckling curve for the case of pure compression, resulting in the same equation as in (3.23). $A = 0.11$ results into the load case of pure bending. A graphic representation of a general stress distribution is shown in figure 3.12b. The Eurocode approach is to consider each plate singularly in case of a cross-section, and as is shown in 3.12b, each of the 4 plates of the RHS applies a different A value. The parameter ψ , defined as the ratio of the stress at both plate ends, follows directly the stress state of the plate. For the case of a hollow section A may become a function of each plate ψ value as follows:

$$A = f(\psi_1, \psi_2) \quad \text{with} \quad \psi_1 \geq \psi_2 \quad (3.26)$$

where only two sides of the represented section govern the value of the parameter A , which are the most 2 compressed sides of the cross-section. This relationship is applied to a single

type of cross-section such as the RHS and SHS, and it is proven to be effective, as will be demonstrated in the verification of the GSRM design curves in chapter 6.

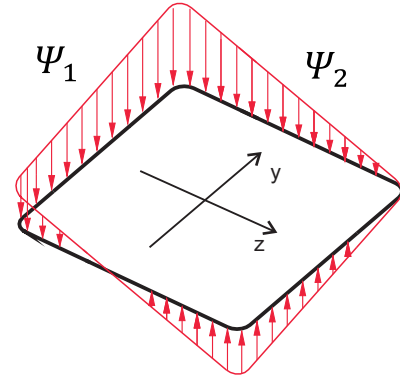
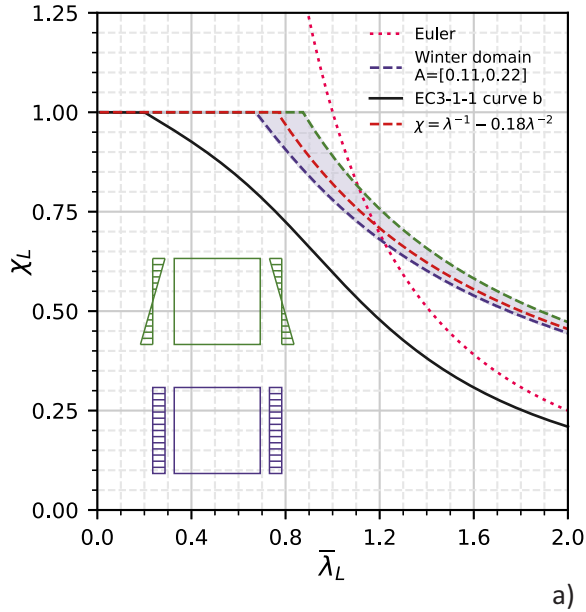


Fig. 3.12. a) range of application for the parameter A in the Winter format of representation, compared with the curve b for column-buckling and the Euler curve; b) graphic representation of ψ_1 and ψ_2 .

Chapter 4

Experimental campaign

4.1 Introduction

A comprehensive experimental programme was conducted in the Structural Laboratory at Bundeswehr University Munich to investigate the cross-sectional behaviour of cold formed square and rectangular hollow sections (SHS and RHS), of stiffened RHS and hot-rolled hexagonal cross-sections. Two grades of mild and high strength steel – S355 and S500 - and twelve section sizes – four SHS, two RHS, covering all four cross-section classes according to the slenderness limits in the Eurocode [1], were examined. The cross-section sizes, material grades, and classes are represented in figure 4.1. This experimental investigation consisted of twelve tensile coupon tests, twelve stub column tests, twenty-four short beam-column tests, along with measurement of geometric imperfections for each specimen. This chapter presents a summary of the results of this experimental test campaign and a detailed description of each experimental test category. A comprehensive and detailed overview of the results of the experimental test campaign conducted during the HOLLOSSTAB project is given in [64].

The full scale tests were divided in 5 categories according to load case and length. In the first 4 categories local buckling was analysed, the categories are numbered from 1 to 4 (T1, T2, T3, T4) with increasing eccentricity of the test. T1 includes solely pure compression stub column tests; T2 category presents a small eccentricity at the top and a gradient that brings the eccentricity equal to zero at the bottom, showing mostly compression on the specimen; T3 has a medium eccentricity, which models N+M interaction; T4 shows high eccentricity that brings the specimen almost no compression and simulates a load case very closely to pure bending. The T5 is equivalent to T3 but the chosen length of 2000 mm for

Cross-section dimensions	dimen-	Grade	EC3 Class	Standard
SHS 140×140×4		S355	3	EN10219
SHS 200×200×5		S355	4	EN10219
SHS 200×200×8		S355	1	EN10219
SHS 200×200×4		S500	4	EN10219
SHS 200×200×5		S500	4	EN10219
RHS 300×150×6		S355	1-4	EN10219.
RHS 300×150×8		S355	1-4	EN10219
SHS-S 140×140×2.5		S355GD	-	-
SHS-S 140×140×3.5		S355GD	-	-
SHS-T 140×140×2.5		HX460	-	-
SHS-T 140×140×4.0		HX460	-	-
HEX250×8.5		S355	-	EN10210

Table 4.1: Overview of the tested cross-sections.

the specimens decreased the specimen resistance and displayed global phenomena during the test. Table 4.2 offers an overview of the test specimen properties.

Test denomination	Top eccentricity	Bottom eccentricity	Length
-	[mm]	[mm]	[mm]
T1	0	0	800
T2	9-64	0	800
T3	57-196	equal to top	800
T4	232-457	equal to top	800
T5	57-196	equal to top	2000

Table 4.2: Overview of test type and corresponding test properties.

The ID test number is composed of the test type denomination and an increasing number (e.g. T1-1, T1-2 etc.). For the stub-column tests, the ID number goes from T1-1 to T1-12, for the short beam-column test with constant moment, it ranges from T3-1 until T3-12, from T4-1 until T4-12. The short beam-columns with compression on all sides and a bending moment gradient (see T2 special section for more details) span from T2-1 to T2-12 as well. Long beam-columns are 7 in total, from T5-1 to T5-7. Figure 4.1 displays an overview of the cross sections and a 3D representation.

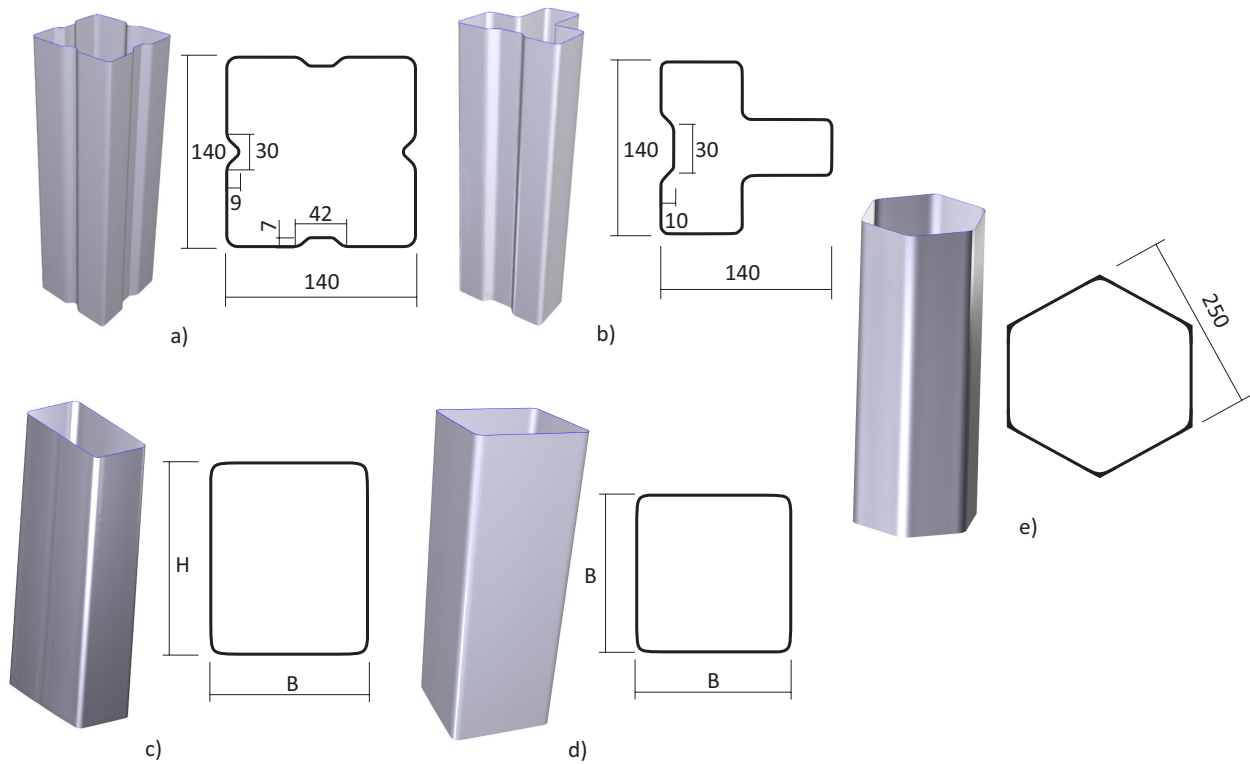


Fig. 4.1. Tested sections: a) square hollow section with stiffeners (SHS-S); b) square hollow section with stiffeners and T-shape (SHS-T); c) rectangular hollow section (RHS); d) square hollow section (SHS); e) hexagonal hollow section (HEX).

4.2 Auxiliary tests

Auxiliary tests provide information to the main experimental test, which are not measurable during the test.

4.2.1 Tensile tests

Tensile coupon tests were initially conducted to obtain the key mechanical properties and full stress-strain responses of the test materials. In total, more than twelve flat tensile coupon tests were conducted, and here one test sample for each cross sections is represented. In case of more tensile tests for cross-section the more representative coupon and test was chosen. The coupon specimens were dimensioned and tested in accordance with EN ISO 6892 [67] and machined longitudinally from adjacent faces of the section. The extracted coupons were in some cases sand blasted prior to dimension measurements being taken to remove the mill scale from their surfaces. The tensile tests were conducted at room temperature using a Zwick und Röll 400 kN hydraulic testing machine, and for the high strength specimens a Doli 600 kN testing rig. The tensile tests were displacement controlled with different velocities according to the specimen dimensions, while the deformation was measured with extensometer attachments on both specimen sides and the tension was measured with an internal load cell, connected to the hydraulic grips.

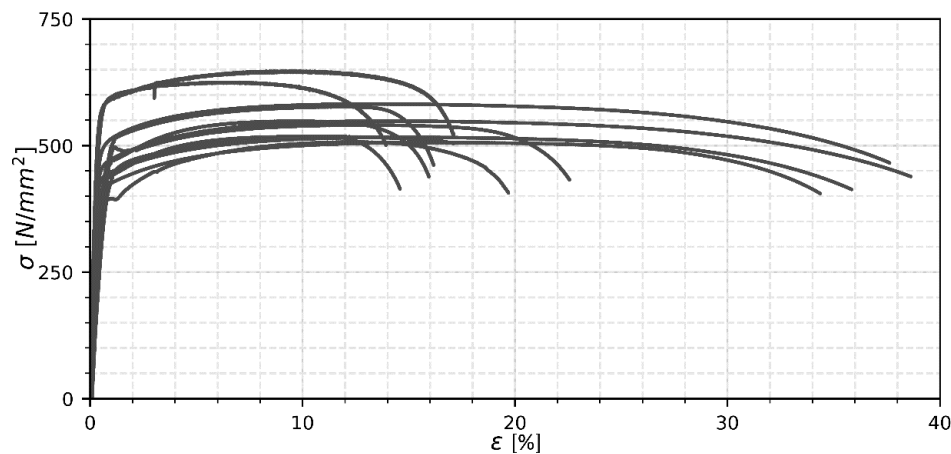


Fig. 4.2. Overview of the engineering stress-strain curves obtained from tensile coupon tests.

An overview of the engineering stress-strain curves obtained from the tensile tests is plotted in figure 4.2, and the material properties for each section, including the yield strength f_y , ultimate tensile strength f_u and ultimate strain at the ultimate tensile strength ϵ_u are summarised in table 4.3. The majority of the obtained test stress-strain curves displayed the typical characteristics of cold-formed steels, with a non-defined shift from the elastic range to the strain-hardening range similar to the Ramberg-Osgood model; SHS-S showed

a behaviour similar to the cold-formed tests and SHS-T a different behaviour, in one case with a sharply defined yield point and a yield plateau, followed by strain hardening until fracture.

Cross-section	f_y	f_u	ϵ_u	f_u/f_y
SHS 140×140×4	430	517	10.8	1.20
SHS 200×200×5	401	506	16.0	1.26
SHS 200×200×8	475	582	13.2	1.22
SHS 200×200×4	563	647	9.6	1.15
SHS 200×200×5	557	625	7.0	1.12
RHS 300×150×6	429	516	14.3	1.20
RHS 300×150×8	451	548	13.9	1.21
SHS-S 140×140×2.5	409	548	9.6	1.34
SHS-S 140×140×3.5	463	551	12.8	1.19
SHS-T 140×140×2.5	420	500	14.0	1.19
SHS-T 140×140×4.0	480	533	13.6	1.11
HEX250×8.5	395	507	13.0	1.28

Table 4.3: Average measured material properties of tested cross-sections from tensile coupon tests.

4.3 Imperfection measurement and evaluation

Cold steel manufacturing introduces geometric imperfections and residual stresses by bending the steel coils and welding the cross-section parts into the final shape. An additional source of imperfections is the preparation of the specimens by cutting and welding the steel tubes for the experimental test. This can significantly influence the structural responses including the onset of buckling, initiation of plasticity and ultimate load-carrying capacity [68]. An investigation of the local geometric imperfections in cold-formed steel SHS, RHS, SHS-T and SHS-S and hot-rolled hexagonal cross-sections is described in this subsection. A 3D laser-scanning technique was employed to measure the distribution of local geometric imperfections in each test specimen. Firstly, the specimens were cleaned, the outer surface of the specimens was then scanned using a Zeiss 3D scanner and recorded as point clouds. The scanned data was initially processed in the software Colin3D [62], whereby a typical pre-processed

3D model is displayed in 4.3a as point cloud. Then, 3D spline curves were laid over the point cloud with a with Geomagic [69], a Computer-Aided Deseign software which sets the sensitivity and roughness of the spline mesh. The spline surface may be imported without further process in the Abaqus FEM Software (figure 4.3c), since it disposes of CAD interface, and then converted into a precise mesh (figure 4.3d). The mesh is composed of shell elements, described in 3.4, and the target mesh size for the numerical model originated from the spline curves (GMNIA-MEAS) is 5 mm.

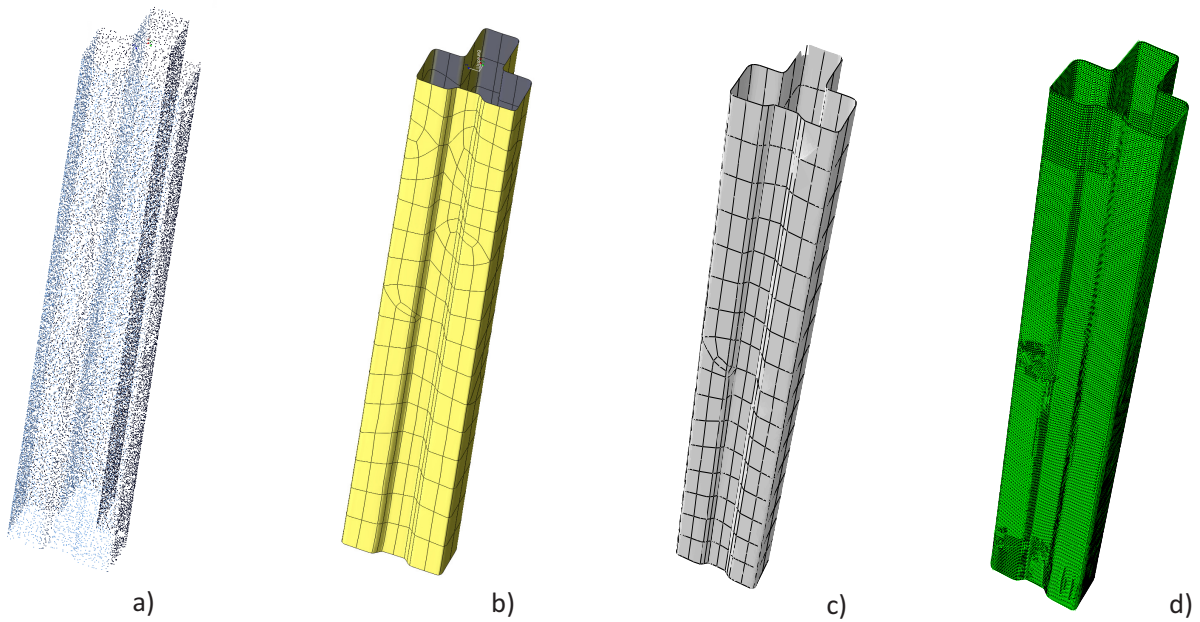


Fig. 4.3. a) point cloud of the 3D scan data; b) spline curves approximating the real geometry; c) spline surface directly imported into the Abaqus FEM Software; d) shell element mesh discretization in Abaqus.

SHS 200/200/5 T1-2

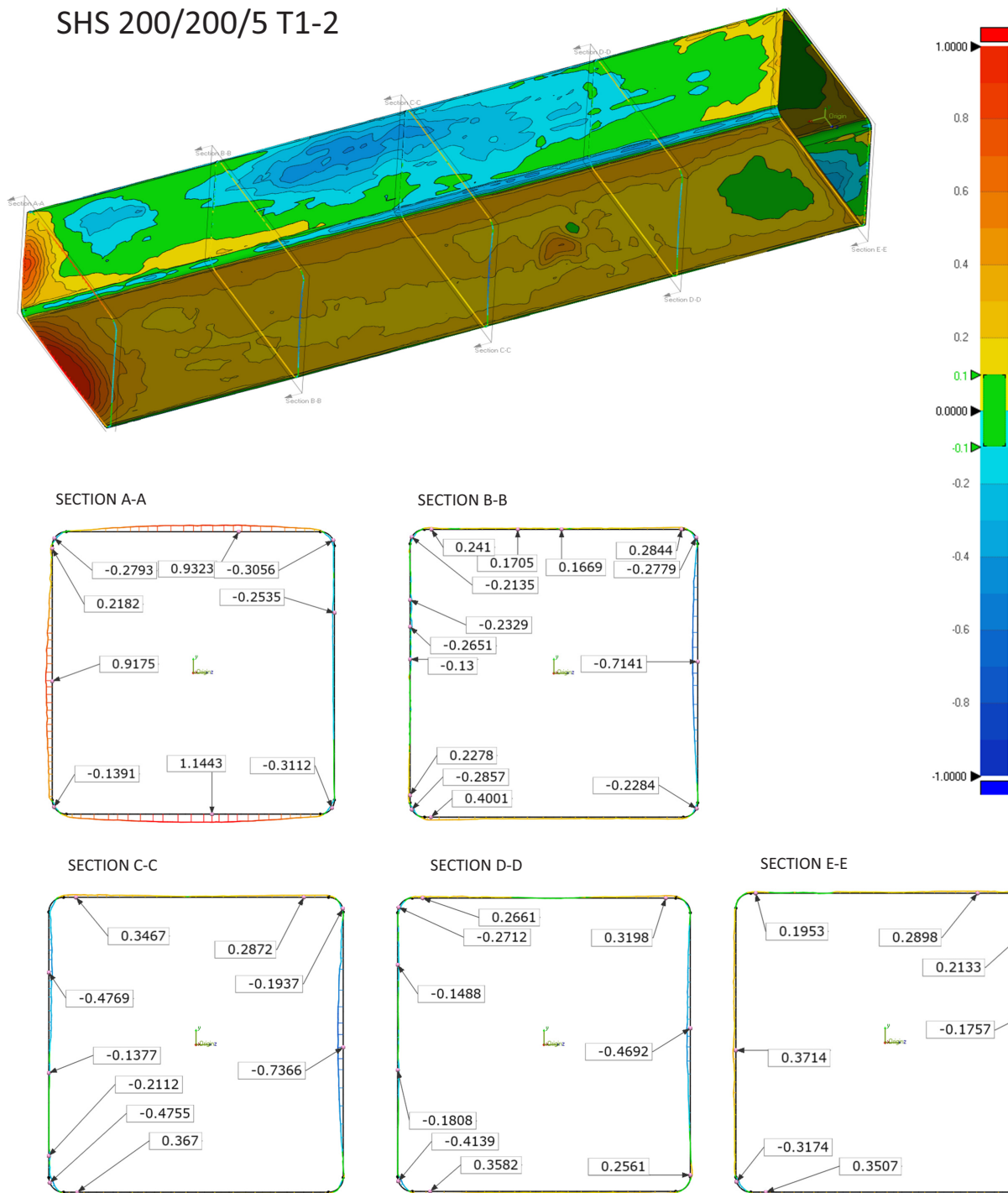


Fig. 4.4. Example of imperfection measurement in mm for an SHS, displaying imperfection data at various sections (A to E).

The imperfection amplitude represents a fundamental parameter and input for the FE model. The local imperfection distribution of a sample of specimens, as obtained from the local imperfection scanning and analysis described above, is provided in the Appendix. The primary finding of the imperfection analysis is that the highest values of imperfections are consistently observed at the specimen ends. This is due to the cutting process or welding in order to fabricate the specimen. Thus, in the Appendix the values at the specimen ends near the cover plate or near the cut edge are neglected. In figure 4.4 a full imperfection analysis of a case study showing sample values of 5 different specimen sections is shown. The chosen specimen is a SHS with 200 mm width and 5 mm plate thickness, 800 mm length and had a cold-formed manufacturing process. The study of the imperfections locates the largest imperfection at the ends where the specimen was machined and welded, and at the mid-span plate centre, where the cold-formed process caused both corner bends and mid-plate imperfections. This thorough analysis of the real geometry of the specimens for the experimental tests is one of the broadest in the literature for local buckling for number of tested specimens and accuracy of the collected data. The statistics of these data is collated in table 4.4, showing test ID and ideal geometrical properties and the mean value and standard deviation of the imperfection data points compared to the ideal geometry.

ID	Cross-Section	Mean Imperfection [mm]	Standard Deviation [mm]
T1-1	SHS 140X140X4	0.18	0.164
T2-1	SHS 140X140X4	0.18	0.152
T1-8	SHS-S 140X140X2.5	1.544	1.13
T2-8	SHS-S 140X140X2.5	1.536	1.176
T1-9	SHS-S 140X140X3.5	0.841	0.362
T2-9	SHS-S 140X140X3.5	0.844	0.45
T1-12	SHS-T 140X140X4	0.662	0.438
T2-12	SHS-T 140X140X4	0.668	0.444
T1-11	SHS-T 140X140X2.5	0.865	0.669

ID	Cross-Section	Mean Imperfection	Standard Deviation
-	-	[mm]	[mm]
T2-11	SHS-T 140X140X2.5	0.797	0.561
T4-8	SHS-S 140X140X2.5	1.727	1.239
T3-9	SHS-S 140X140X3.5	0.803	0.457
T4-9	SHS-S 140X140X3	0.785	0.433
T3-11	SHS-T 140X140X2.5	0.89	0.575
T4-12	SHS-T 140X140X2.5	0.87	0.585
T3-1	SHS 140X140X4	0.168	0.186
T4-1	SHS 140X140X4	0.187	0.19
T3-12	SHS-T 140X140X4	0.69	0.45
T4-12	SHS-T 140X140X4	0.685	0.404
T1-6	RHS 300X150X6	0.273	0.294
T1-7	RHS 300X150X8	0.633	0.585
T2-7	RHS 300X150X8	0.659	0.589
T1-2	SHS 200X200X5	0.199	0.156
T2-2	SHS 200X200X5	0.208	0.159
T1-3	SHS 200X200X8	0.432	0.433
T3-6	RHS 300X150X6XT3	0.385	0.478
T4-6	RHS 300X150X6XT4	0.339	0.429
T5-1	SHS 140X140X4	0.173	0.187
T5-5	SHS-S 140X140X2.5	1.696	1.269
T5-7	SHS-T 140X140X2.5	0.797	0.561
T5-4	RHS 300X150X6	0.246	0.261
T3-7	RHS 300X150X8	0.814	0.67
T4-7	RHS 300X150X8	0.836	0.691
T3-2	SHS 200X200X5	0.192	0.168
T4-2	SHS 200X200X5	0.206	0.24

ID	Cross-Section	Mean Imperfection [mm]	Standard Deviation [mm]
-	-		
T3-3	SHS 200X200X8	0.503	0.493
T4-3	SHS 200X200X8	0.499	0.481
T5-6	HEX 250X8.5	0.552	0.474
T3-10	HEX 250X8.5	0.48	0.436
T4-10	HEX 250X8.5	0.511	0.462
T1-10	HEX 250X8.5	0.518	0.474
T2-10	HEX 250X8.5	0.557	0.478
T1-4	SHS 200X200X4	0.301	0.247
T2-4	SHS 200X200X4	0.32	0.242
T3-4	SHS 200X200X4	0.369	0.337
T4-4	SHS 200X200X4	0.323	0.279
T5-2	SHS 200X200X4	0.335	0.278
T1-5	SHS 200X200X5	0.186	0.151
T2-5	SHS 200X200X5	0.196	0.165
T3-5	SHS 200X200X5	0.257	0.214
T4-5	SHS 200X200X5	0.217	0.191
T5-3	SHS 200X200X5	0.217	0.191

Table 4.4: Statistics of the imperfection measurement.

4.4 Full-scale tests and validation of the numerical model

4.4.1 Stub column tests T1

As was described in section 3.3 and 3.4, the reverse engineering process consists in replicating the experimental test in a GMNIA-MEAS with the highest possible accuracy, since the overarching objective of the experimental test campaign is the validation of such a numerical model. A FEM model of the stub-column test with the measured geometrical shape of the sections and real strain-stress relation gathered in the auxiliary tests led to minimum (3%) deviations to the ultimate load of the buckling tests if the meshing and modelling of boundary conditions is accurate and representative.

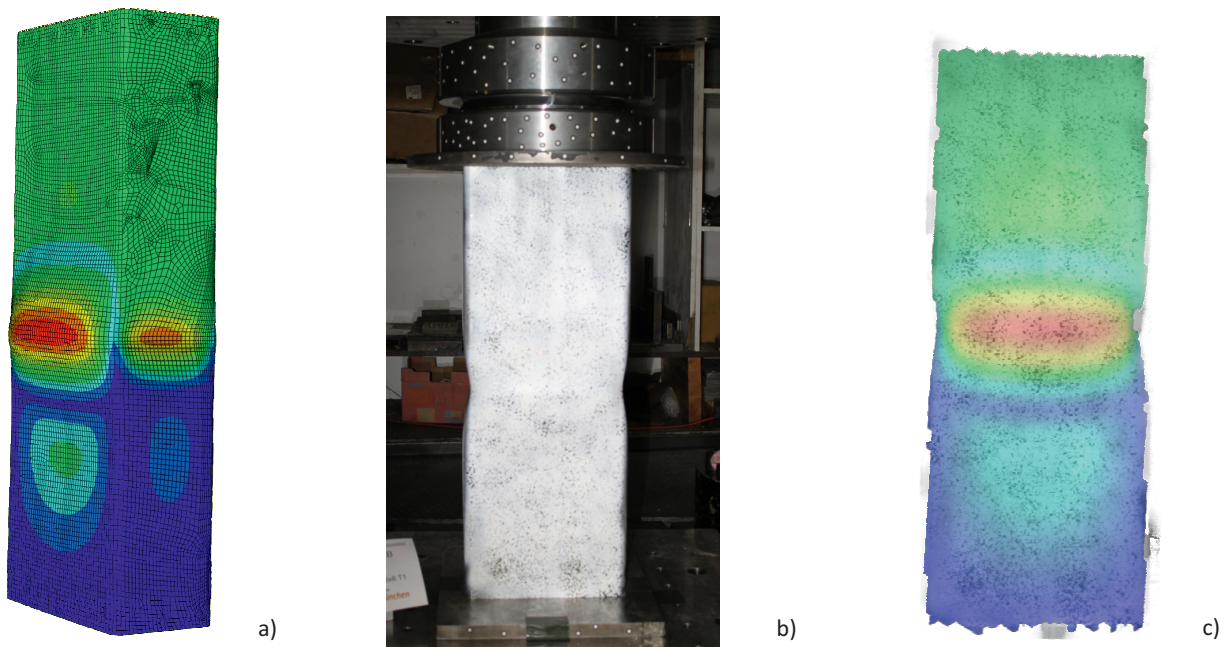


Fig. 4.5. a) deformed shape of the T1-6 RHS stub-column test of a GMNIA-MEAS numerical analysis with Abaqus; b) specimen deformed shape of the corresponding experimental test measured by the DIC system.

A thorough validation of the GMNIA-MEAS numerical model defined and explained is given in the Appendix. Each experimental test displays a load deformation curve plotted against the GMNIA-MEAS corresponding outcome. The estimated numerical load capacity values reproduce fairly well the experiment ultimate load, and in most cases follow quite precisely the shape of the load-deformation curve. Figure 4.5 shows a comparison between

the experimental test on the T1-6 experimental test (RHS 300/150/6 S355) and the numerical model buckling shape. Both tests showed similar buckling shapes, validating the GMNIA-MEAS model, which predicts with large accuracy the location and the amplitude of the buckling shape.

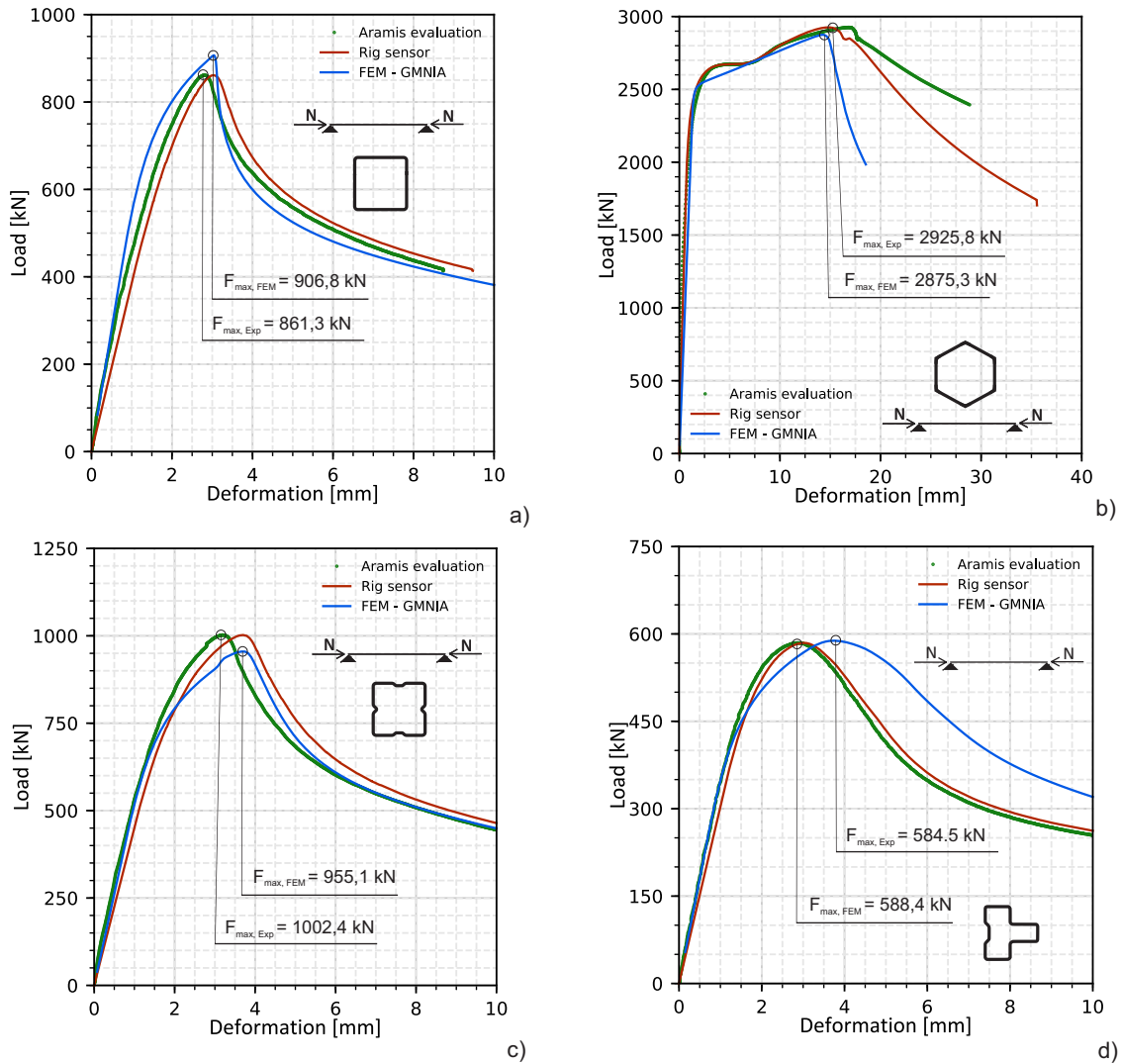


Fig. 4.6. Exemplary results for all different cross-section shapes; a) SHS T1-1, b) hexagonal T1-10, c) SHS-S T1-9, d) SHS-T T1-11 cross-sections are shown.

Figure 4.6 shows a sample of the validation results for the stub-column tests of 4 different cross-sections, where the validation is conducted by comparing the peak load and shape of the load-deformation curve of the experimental tests and the GMNIA-MEAS. A summary of all results for stub-column tests is given in table 4.5.

Cross-section	Steel grade	Specimen ID	$N_{u,Exp}$ [kN]	$N_{u,Exp}/N_{u,FEM}$
-	-	-	-	-
SHS 140×140×4	S355	T1-1	861.3	0.950
SHS 200×200×5	S355	T1-2	1227.9	0.943
SHS 200×200×8	S355	T1-3	2917.9	0.967
SHS 200×200×4	S500	T1-4	1111.2	0.971
SHS 200×200×5	S500	T1-5	1736.1	0.977
RHS 300×150×6	S355	T1-6	1582.0	0.962
RHS 300×150×8	S355	T1-7	2806.8	1.001
SHS-S 140×140×2.5	S350GD	T1-8	623.1	0.988
SHS-S 140×140×3.5	S350GD	T1-9	1002.4	1.050
HEX250×8.5	S355	T1-10	2925.8	1.018
SHS-T 140×140×2.5	HX460	T1-11	584.5	0.993
SHS-T 140×140×4.0	HX460T1-	1098.1	1.034	

Table 4.5: Summary of stub column test results. $N_{u,Exp}$ is the experimental test load capacity, and $N_{u,Exp}/N_{u,FEM}$ is experimental load capacity vs the expected value from the numerical simulation.

4.4.2 Short beam-column tests T3 and T4

For the short-beam column tests another simplified GMNIA-MEAS model was developed. From the basis of the reverse engineering process, a model with simplified boundary conditions (such as pinned connectors at both end plates) was developed. The underlying numerical model corresponds to the one developed for the stub column case (3.3), where isoparametric SR4 elements and real imperfections from 3D spline curves are used in Abaqus and the strain-stress relation comes from the tensile tests. Different conditions apply here for the boundary as well as for the load. The axial force is applied with a fixed eccentricity, which combined with second-order effects results in a slightly non-constant bending moment over the specimen length.

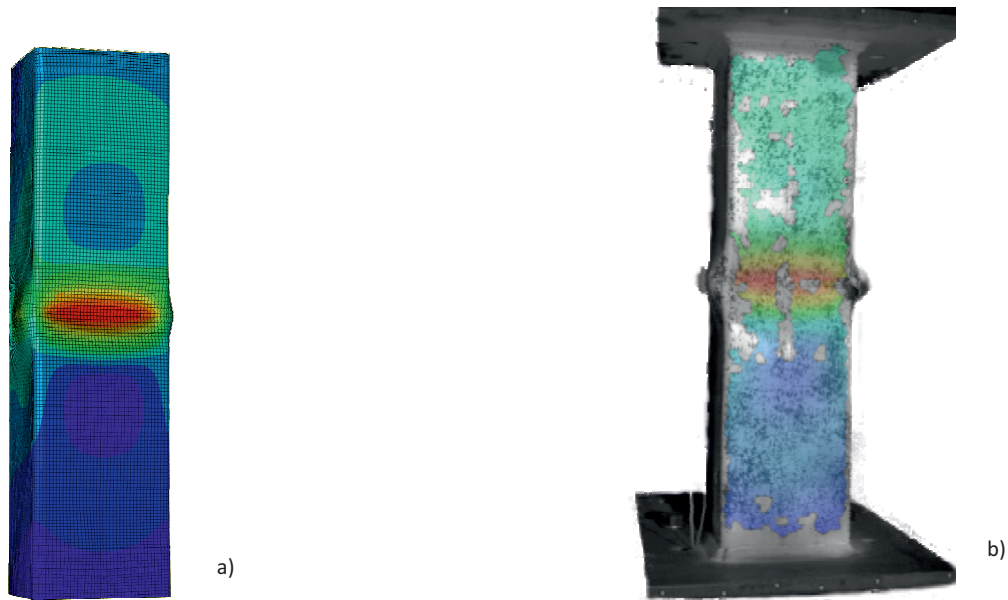


Fig. 4.7. Exemplary result for the T3-T4 numerical model validation a) deformed shape of a SHS $200 \times 200 \times 4$ S500 T3-4 test of a GMNIA-MEAS numerical analysis with Abaqus; b) specimen deformed shape of the corresponding experimental test measured by the DIC system.

Models with simplified boundary conditions generally explain with sufficient accuracy the load-deformation path for specimens with large eccentricity tests (T4), as well as some of the tests with smaller eccentricity (T3). When the load capacity outcome of the numerical simulation did not provide satisfying results, a more precise numerical model was developed. The objective of this more refined model was to reproduce with more accuracy the interaction between the test setup parts and the specimen, simulating the reciprocal effect of the spherical bearing on the specimen and vice-versa. Thus, a model with a simulation of the contact behaviour between the two elements of the spherical bearing was created. The upper part of the bearing consists of a perfectly rigid element, which models the axial load introduction from the 10 MN machine actuator, and a contact interaction with a fairly rigid part, representing the bottom part of the spherical bearing, assumed to show a stiffer behaviour than the specimen by being modelled by shell elements with thickness of 100 mm. This simulates the spherical bearing surface contact, where the bottom surface is connected through perfectly rigid elements to the specimen. The simulation of the wedge plate was neglected. This model will be called hereinafter GMNIA-CONTACT, and solely represents a more precise evaluation of the load capacity in terms of load-deformation curves.

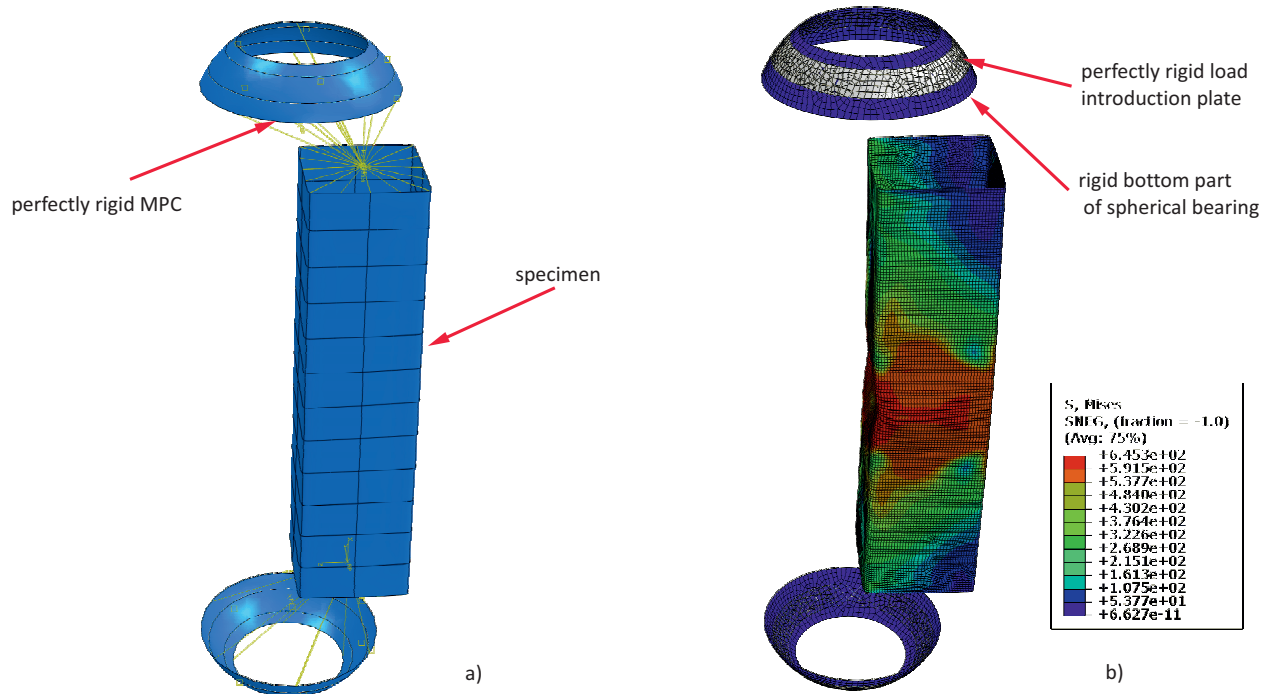


Fig. 4.8. a) Input model of the real geometry of SHS 200×200×4 S500 in Abaqus, consisting of 3D spline curves and 3D surface for the spherical bearing; b) deformed shape and stress results of the same model with displacement control.

For all models, considering that the deflection at specimen mid-height increases the test eccentricity, a second order moment was calculated to compare cross-sectional resistance in the OIC-format, as in:

$$M_u^{II} = M^I + N_u e^{II} \quad (4.1)$$

An overview of the validation of a sample of experiments is given in figure 4.9, and an overview of the result values for the load capacity is given in table 4.6.

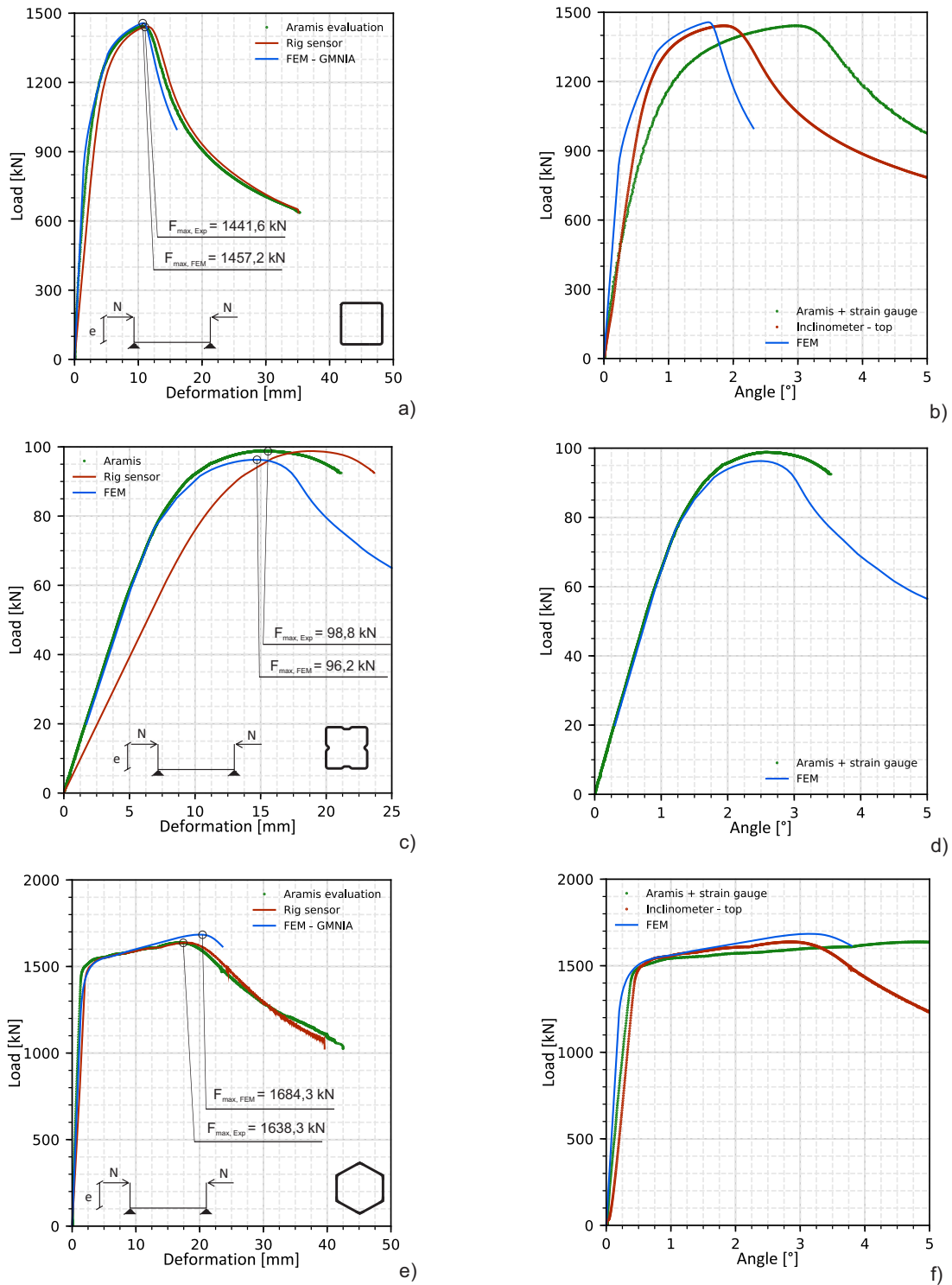


Fig. 4.9. Exemplary result for the T3-T4 numerical model validation with the comparison of the load-deformation curve and peak loads in a) , c) and e), and the load-end plate rotation in b), d), and f). The analysed experimental tests are a) b) SHS 200×200×8 S355 T3; c) d) SHS-S 140×140×2.5 S350GD T4; e) f) HEX 250×8.5 S355 T3.

Cross-section	Steel grade	Specimen ID	$N_{u,Exp}$ [kN]	$N_{u,Exp}/N_{u,FEM}$
-	-	-	-	-
SHS 140×140×4	S355	T3-1	291.7	1.032
SHS 200×200×5	S355	T3-2	615.4	1.004
SHS 200×200×8	S355	T3-3	1441.6	0.989
SHS 200×200×4	S500	T3-4	622.6	0.887
SHS 200×200×5	S500	T3-5	895.8	0.926
RHS 300×150×6	S355	T3-6	1309.9	1.033
RHS 300×150×8	S355	T3-7	2119.0	0.973
SHS-S 140×140×2.5	S350GD	T3-8	205.4	1.020
SHS-S 140×140×3.5	S350GD	T3-9	309.8	0.944
HEX 250×8.5	S355	T3-10	1638.3	0.973
SHS-T 140×140×2.5	HX460	T3-11	63.2	1.055
SHS-T 140×140×4.0	HX460	T3-12	225.0	0.955
SHS 140×140×4	S355	T4-1	141.3	1.027
SHS 200×200×5	S355	T4-2	194.3	1.023
SHS 200×200×8	S355	T4-3	453.8	1.017
SHS 200×200×4	S500	T4-4	212.1	1.017
SHS 200×200×5	S500	T4-5	294.5	0.967
RHS 300×150×6	S355	T4-6	584.7	1.047
RHS 300×150×8	S355	T4-7	1080.4	0.995
SHS-S 140×140×2.5	S350GD	T4-8	98.8	1.027
SHS-S 140×140×3.5	S350GD	T4-9	155.5	1.002
HEX 250×8.5	S355	T4-10	457.1	0.972
SHS-T 140×140×2.5	HX460	T4-11	63.2	1.055
SHS-T 140×140×4.0	HX460	T4-12	118.1	1.050

Table 4.6: Summary of short beam-column test results. $N_{u,Exp}$ is the experimental test load capacity, and $N_{u,Exp}/N_{u,FEM}$ is experimental load capacity vs the expected value from the numerical simulation.

4.4.3 Short beam-column tests T2

Short beam column tests with one-sided were performed to investigate the effect of a linear bending moment over the member length for local buckling. The numerical model presents an eccentric load on the top and shows fix connection on the bottom. For this reason, T2 numerical model can be derived from the GMNIA-MEAS or GMNIA-CONTACT, applying a fixed connection on the bottom. Table 4.7 summarises the validation results for the T2 test. A detailed description of the general model is given in 3.4, and a detailed description of each experimental test may be found in the Appendix.

Cross-section	Steel grade	Specimen ID	$N_{u,Exp}$ [kN]	$N_{u,Exp}/N_{u,FEM}$
-	-	-	-	-
SHS 140×140×4	S355	T2-1	868.3	1.010
SHS 200×200×5	S355	T2-2	1224.8	0.969
SHS 200×200×8	S355	T2-3	2800.2	0.956
SHS 200×200×4	S500	T2-4	865.1	0.967
SHS 200×200×5	S500	T2-5	1334.6	0.957
RHS 300×150×6	S355	T2-6	1507.7	0.921
RHS 300×150×8	S355	T2-7	2533.4	0.933
SHS-S 140×140×2.5	S350GD	T2-8	614.8	1.016
SHS-S 140×140×3.5	S350GD	T2-9	995.5	1.013
HEX250×8.5	S355	T2-10	2117.7	0.997
SHS-T 140×140×2.5	HX460	T2-11	591.4	1.048
SHS-T 140×140×4.0	HX460	T2-12	1098.1	1.027

Table 4.7: Summary of the resulting load capacity values for T2 short beam-column tests with linear bending moment distribution.

4.4.4 Long beam-column tests T5

Long beam-column experimental tests investigate the interaction of the local+global buckling effects. The chosen numerical model for the validation is a particular case of the T3-T4 model, described in this section. Table 4.8 summarises the results of the experimental test

campaign. A fundamental remark is that - from the perspective of the GSRM formulation for cross-sectional capacities - long beam-columns may be considered as a special case of the short beam-column cases. The necessary requirement is that the second order eccentricity is available and the applied second order moment can be calculated. A short specimen (stub-column wise) is then extracted from the real geometry 2000 mm long beam-column specimen; by doing so, all global effects are excluded. As a result, a local buckling short model problem with the applied second order moment is equivalent to the GMNIA-MEAS model of the long beam-column tests. All results shown in the GSRM format for the experimental test results are obtained following this method and are shown in the Appendix.

Cross-section	Steel grade	Specimen ID		$N_{u,Exp}$ [kN]	$N_{u,Exp}/N_{u,FEM}$
-	-	-	-	-	-
SHS 140×140×4	S355	T5-1	25	262	1.009
SHS 200×200×4	S355	T5-2	13	569.6	1.056
SHS 200×200×5	S355	T5-3	16	852.7	0.966
RHS 300×150×6	S500	T5-4	8	1289.8	1.013
SHS-S 140×140×2.5	S350GD	T5-5	25	199.6	1.024
HEX 250×8.5	S355	T5-6	14	1484.8	1.029
SHS-T 140×140×2.5	S350GD	T5-7	36	109.7	1.065

Table 4.8: Summary of short beam-column test results. δ_u is the mid-span, $N_{u,Exp}$ is the experimental test load capacity, and $N_{u,Exp}/N_{u,FEM}$ is the experimental load capacity vs the expected value from the numerical simulation.

Chapter 5

Numerical investigation

5.1 Introduction

In the previous chapter, physical tests (full-scale and auxiliary) were used as the basis for the validation and verification of advanced (GMNIA) numerical models. These models need to be further simplified in order to carry out an extensive numerical investigation of the behaviour of hollow sections under the full range of possible compression and biaxial bending loading configurations, both for local and global buckling. The calibration of imperfection and material input parameters for this purpose is carried out in section 5.2. Subsequently, these scope of the parametric studied performed in the context of this thesis is described in section 5.3.

5.2 Calibration of the numerical model used for parametric studies

This section investigates the possible values for the imperfection amplitudes. In order to carry out an extensive parametric study, it was decided to further simplify the validated and verified numerical models used in chapter 4. Thereby, nominal geometric and material Input Parameters were used in combination with a calibrated value of geometric imperfections. Thereby, the first eigenmode shape for local and global buckling was chosen as reference and scaled. Additionally, a standardized strain-stress relation for hot-rolled and cold-formed profiles developed by Yun-Gardner [57, 56] was applied, as mentioned in section 3.4, using

input values of f_y and f_u .

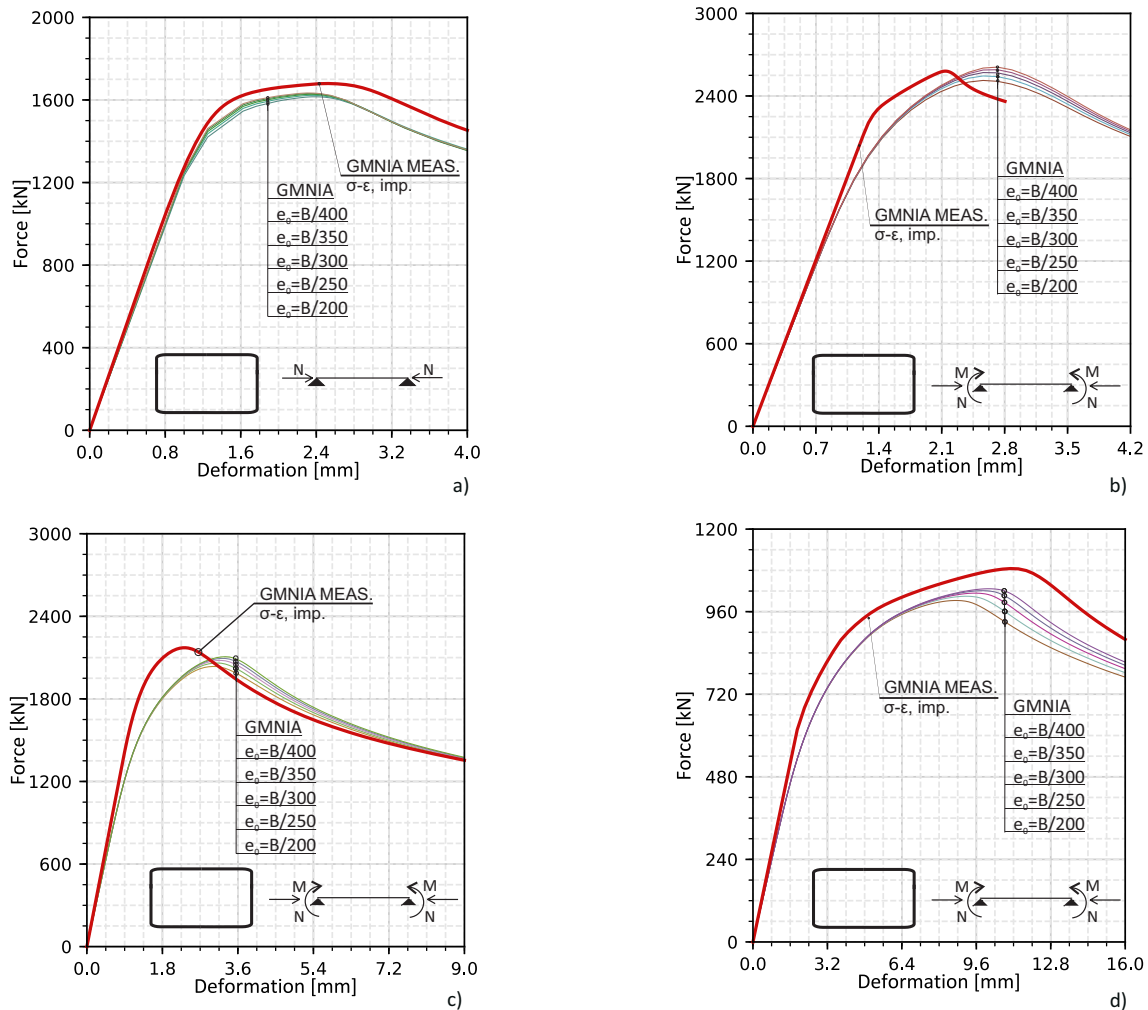


Fig. 5.1. Calibration of the imperfection amplitude for a) RHS 300×150×8 S355 T1-6, for b) RHS 300×150×8 S355 T2-6, for c) RHS 300×150×8 S355 T3-6 and for d) RHS 300×150×8 S355 T4-6.

With the chosen FEM modelling technique and discretization, described in section 3.4, the GMNIA-MEAS model approximate the resulting maximum force of the experimental test with an average error of less than 3% in terms of ultimate load. In most observed cases, the deformation curve follows the test curve very closely. For the purpose of calibrating numerical models for the extensive parametric study, these same GMNIA-MEAS models were compared to GMNIA-models with nominal geometry, eigenmode-based imperfections and the Yun-Gardner material model with the input of f_y and f_u from the tensile coupon test.

The GMNIA-MEAS load-deformation curve is thus compared in the following to different GMNIA calculations with varying equivalent imperfection amplitudes, see figure 5.1 and 5.2.

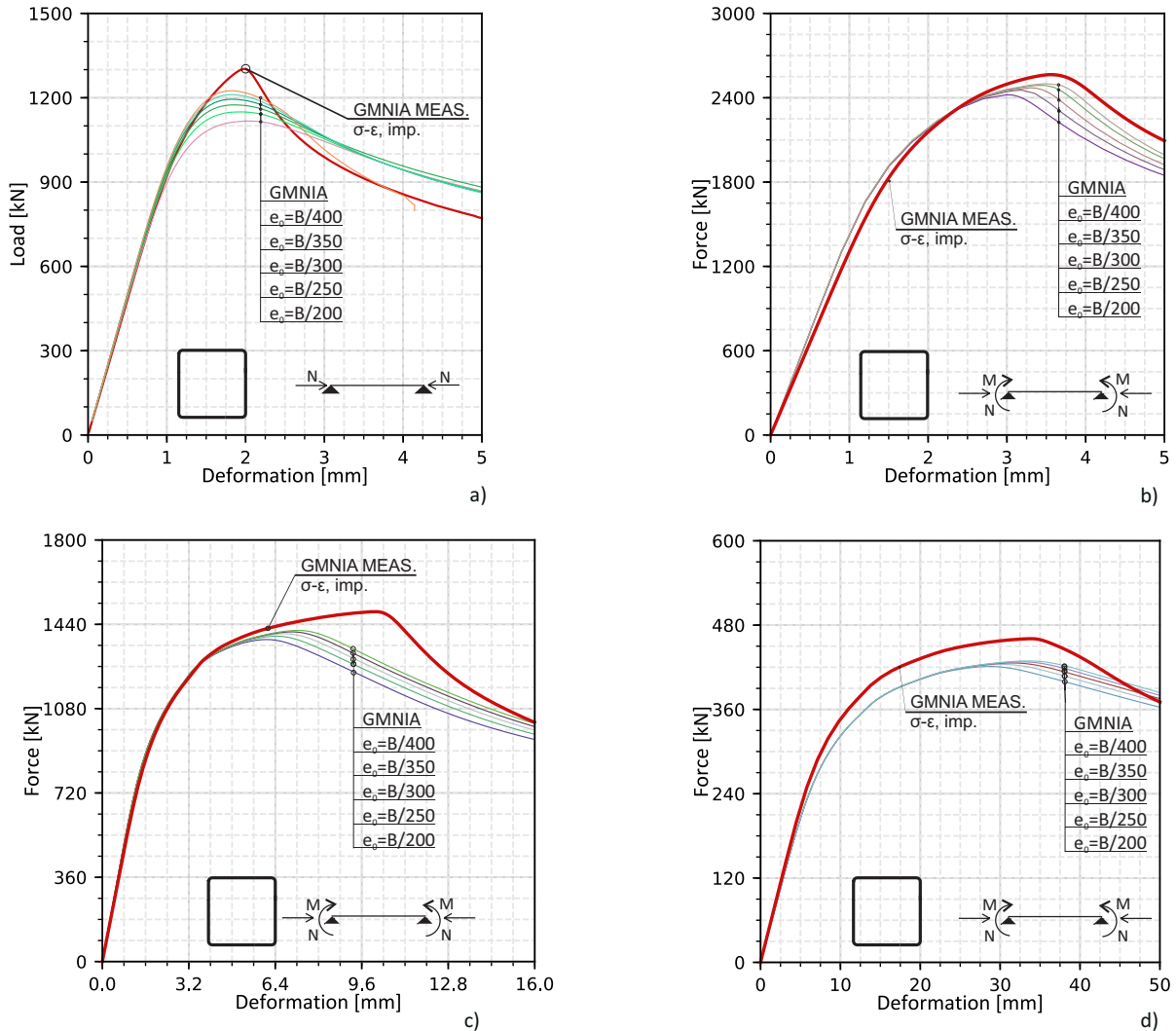


Fig. 5.2. Calibration of the imperfection amplitude for a) SHS 200x200x5 S355 T1-5, for b) SHS 200x200x8 S355 T2-3, for c) SHS 200x200x5 S355 T3-3 and for d) SHS 200x200x5 S355 T4-3.

The imperfection amplitudes range from $B/400$ up to $B/200$, where B is the largest cross-section part subjected to compression. Finally, a value of $B/400$ was chosen, matching what is mentioned in various literature references as an accurate description for the Winter-type buckling, see e.g. [38, 39, 70].

For the calibration of the numerical model for the global analysis a different approach was chosen. Similarly to the local buckling, the equivalent imperfection shape derive from

the first non-global eigenmode of a LBA analysis. The difference lies in the calibration of the amplitude. Figure 5.3 compares the well-established buckling curve “a” (for hot-rolled sections) and “c” (for cold-formed sections) from EC3-1-1 [1] with the results of the GMNIA model with different imperfection amplitudes. At each level of global slenderness $\lambda_G = \sqrt{\frac{R_{pl,G}}{R_{cr,G}}}$ several GMNIA models of a SHS 200/200/10 S355 section were calculated varying only the global imperfection amplitude. The value of $L/850$ for the amplitude minimizes the distance of the GMNIA result points to EC curve pattern.

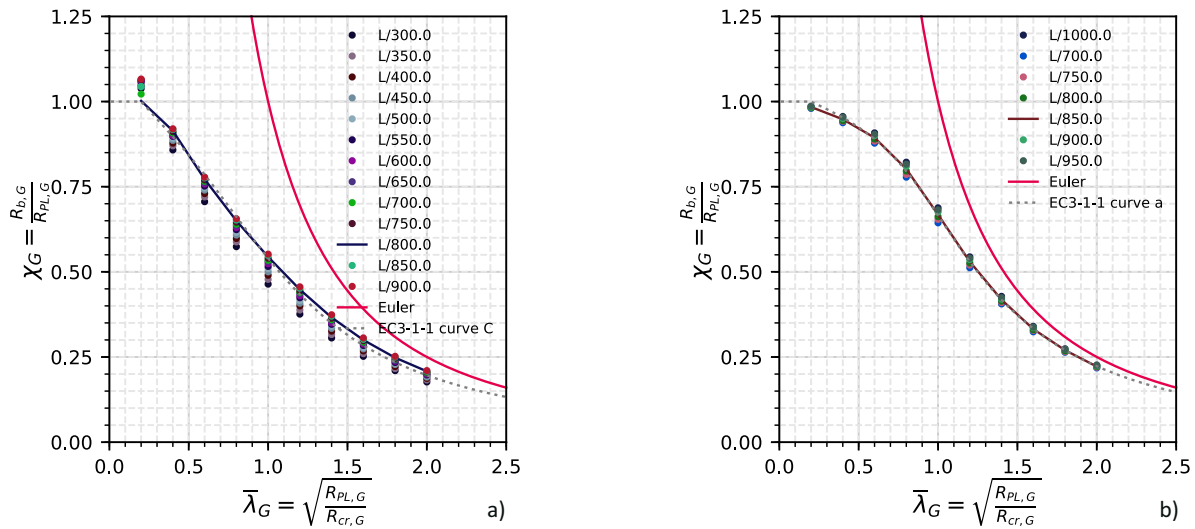


Fig. 5.3. Calibration of the imperfection for global buckling model. In a) the results for the hot-rolled EN10210 cross-sections are shown, and similarly for cold-formed according to EN10219 in b).

Finally, the value of $L/1000$ was chosen as equivalent global imperfection. This imperfection amplitude accounts for the safety factors implied by the Eurocode and corresponds to various proposals in the scientific literature and in the international codes [48, 10, 56], and as is shown in figure 5.3, $L/1000$ does not produce significantly higher results than $L/850$ or $L/800$. In fact, this study of the global imperfection amplitude may be seen as a sensitivity analysis of the desired GMNIA outcome (output variable) with respect to the parameter imperfection amplitude (input variable), and it corroborates the use of value of $L/1000$ as equivalent imperfection for the GSRM as well, confirmed by the review of the literature on global buckling.

5.3 Scope of the parametric study

The numerical test campaign consisted of around 43000 individual numerical tests. As a first step, around 30000 numerical tests (LBA+GMNIA) were conducted for the study of local buckling, the parameters of which are shown in table 5.1 in form of a numerical test matrix. All shown parameters were combined with all other given parameters.

Thickness	L/L_{cr}	Steel grade	$e_{0,L}$	ϕ_y	ϕ_z	h/b	Manufacturing standard
[mm]	[-]		[mm]	[°]	[°]	[-]	
2.0	0.1	S355	B/400	0	0	1	EN10219
2.5	0.15	S460		15	15	1.5	EN10210
3.0	0.2	S550		30	30	2	
3.5		S700		45	45		
4.0				60	60		
5.0				75	75		
6.3				90	90		
8.0							
10.0							
12.0							

Table 5.1: Parameters for the SHS and RHS local buckling numerical campaign.

The following parameters

$$e_{0,L} \quad \phi_y \quad \phi_z \quad n \quad m_y \quad m_z \quad (5.1)$$

were defined in section 3.2 as the GSRM incorporates them in the design methodology. The values of the applied loads in the $\phi_y - \phi_z$ space is given by the sphere points of equation 3.14 in section 3.5 and bending moments were applied at both specimen ends, defining a constant bending diagram along the length. The sole new parameter to be defined here is the length

of the specimen L , defined by equation (5.2).

$$\frac{L}{L_{cr}} = \min\left(\frac{I_y}{A}; \frac{I_z}{A}\right) \pi \sqrt{\frac{E}{f_y}} \quad (5.2)$$

The aim of an extensive parametric study on the local buckling behaviour of slender and non-slender cross-sections is the precise determination of the cross-section capacity under different load combinations. For this reason, a large number of thicknesses and load combinations was employed in order to evaluate with accuracy the effects of plate buckling.

In the study of global buckling the number and type of chosen parameters is different. In figure 5.4 the different load combinations for global buckling are shown. Around 13000 numerical calculations were conducted for the study of global buckling, the parameters of which are shown in table 5.2. Figure 5.4a represents the constant bending moment case, 5.4b and 5.4c a linear distribution of the bending moment, 5.4c and 5.4e illustrate the distribution corresponding to uniformly distributed load and mid-span concentrated load.

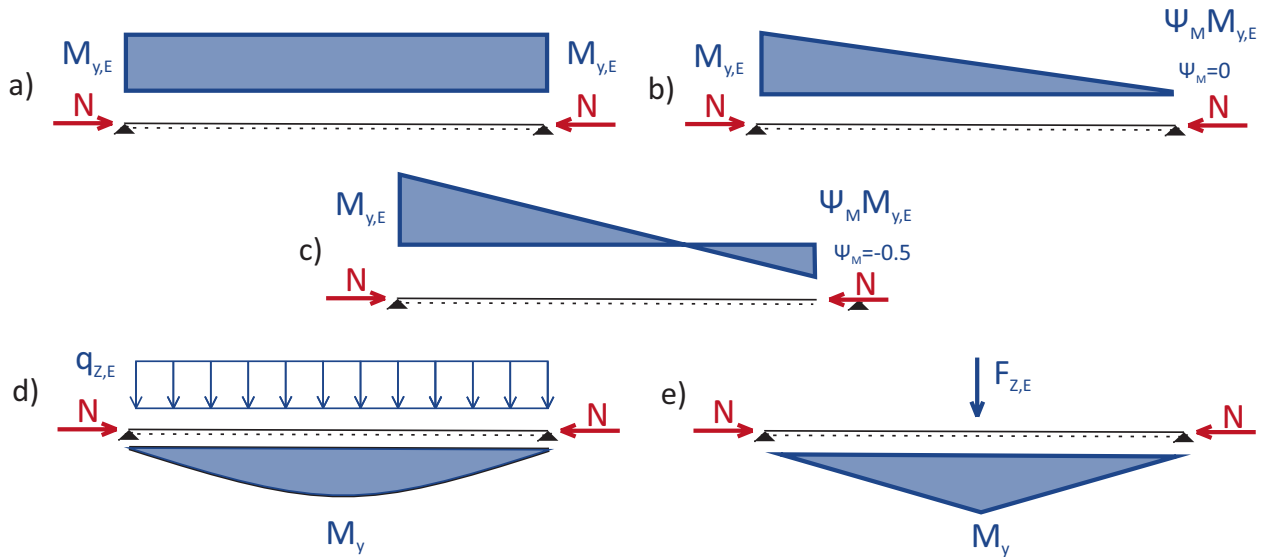


Fig. 5.4. Different bending moment diagrams for the parametric study on global buckling.

The new variables η_y and η_z are defined in equations (5.3) and (5.4).

$$\eta_y = \frac{m_y}{n} \quad (5.3)$$

$$\eta_z = \frac{m_z}{n} \quad (5.4)$$

$\bar{\lambda}_p$	L/L_{cr}	Steel grade	$e_{0,L}$	η_y	η_z	h/b	Manufacturing standard	Load case
[-]	[-]		[mm]	[-]	[-]	[-]		
0.3	0.2	S355	B/400	0	0	1	EN10219	$\psi_M = 0$
0.6	0.4	S700	L/1000	0.5	0.5	1.5	EN10210	$\psi_M = -0.5$
0.9	0.6			1.0	1.0	2		$\psi_M = 1$
1.2	0.8			2.0				$F_y - F_z$
	1.0			60				$q_y - q_z$
	1.2							
	1.4							
	1.6							
	1.8							
	2.0							

Table 5.2: Parameters for the SHS and RHS local buckling numerical campaign.

The remaining new variables in table 5.2 are defined as follows:

- $\bar{\lambda}_p$ is defined following equation 2.67 in section 2.2 in accordance with the definition of EN 1993-1-5 [40].
- ψ_M is the coefficient applied to one end of the member to the applied bending moment, as in (5.5)

$$M_{y,E, \text{right-end}} = \psi_M M_{y,E, \text{left-end}} \quad (5.5)$$

- $F_y - F_z$ indicates a mid-span concentrated load in y and/or z direction.
- $q_y - q_z$ indicates a distributed load along the member length.

In the parametric study for global buckling, the SHS and RHS thickness was defined by the choice of a certain $\bar{\lambda}_p$ for the section. For the case of global (and combined global+local) buckling, a large number of member lengths was considered. The probability of the simultaneous occurrence of the maximum values of both the local and global imperfection is much lower than the probability of occurrence of an individual maximum. This is also

reflected in standardized procedures for FEM-based design of steel structures, such as the one found in Annex C of EN 1993-1-5. Following the basic concepts described therein, in the present parametric study two different imperfection models were adopted for each GMNIA calculation:

1. A model with an amplitude of 100% of $L/1000$ for the global buckling shape and 70% of $B/400$ for the local (plate) imperfection.
2. A model with an amplitude of 70% of $L/1000$ for the global buckling shape and 100% of $B/400$ for the imperfection at a local level.

In order to consistently apply the imperfection at a global and local level, the corresponding shapes for local and global buckling were chosen as scaled buckling modes derived from an LBA analysis, described in section 3.2. Since the global buckling can affect both axes, the imperfections were applied in both directions simultaneously, and were additionally reduced to equations (5.6) (5.7) when applied simultaneously.

$$e_{0,G,y} = \frac{L}{1000} \cos \frac{\pi}{4} \approx 0.7 \frac{L}{1000} \quad (5.6)$$

$$e_{0,G,z} = \frac{L}{1000} \sin \frac{\pi}{4} \approx 0.7 \frac{L}{1000} \quad (5.7)$$

Chapter 6

GSRM Design Formulations - Local Buckling

6.1 Introduction

The chosen approach for the GSR Method as applied to describing local buckling makes use of Winter's formula, generalising it to describe the behaviour of the entire cross-section as observed in the physical and numerical tests. The slenderness and the reduction factors refer to the cross-section properties (geometry and steel grade) and to the applied load and derive from simple analytical formulae (cross-section resistance) and from a linear buckling analysis (elastic bifurcation load). The chosen representation format was developed by comparing different definitions of the cross-section resistance and is presented in section 6.2, then the Winter format for the development of a design curve is applied and calibrated against the database of numerical results (section 6.3). Section 6.4 compares the GSRM prediction with the current international standards.

6.2 Choice of the GSRM representation format

The discussion on the most suitable representation format started in section 3.2 and 3.5, where design approach, representation in 2D or 3D diagrams and analytical formulae were described. In figure 6.1 a sample of numerical results is shown in the $n - m_y$ plot, as the first type of traditional representation for the local buckling resistance of sections. The figure illustrates the resistance of SHS-S sections as observed for some representative examples and

parameter variations. The GMNIA results are represented by the dots, while the continuous lines represent reference resistances. The (ideal) plastic and elastic cross-sectional resistances are independent of code provisions, while the *N-M-EC3* lines represent the simplified rules for plastic cross-sectional resistances of rectangular and square hollow sections found in Eurocode 3 [1]. Figure 6.1a shows the influence of the (constant) wall thickness, with otherwise equal member length ($L=800$ mm), steel grade (S355) and imperfection amplitude $e_{0,L} = B/400$. As could be expected, the resistances lie between the elastic and plastic cross-sectional capacities, with the thinner cross-section getting closer to the elastic (class 3) cross-section capacity line. Figure 6.1b shows the influence of the steel grade. A higher-strength steel grade (S460) leads to a relative (but obviously not absolute) reduction of strength in comparison to the plastic cross-sectional resistance.

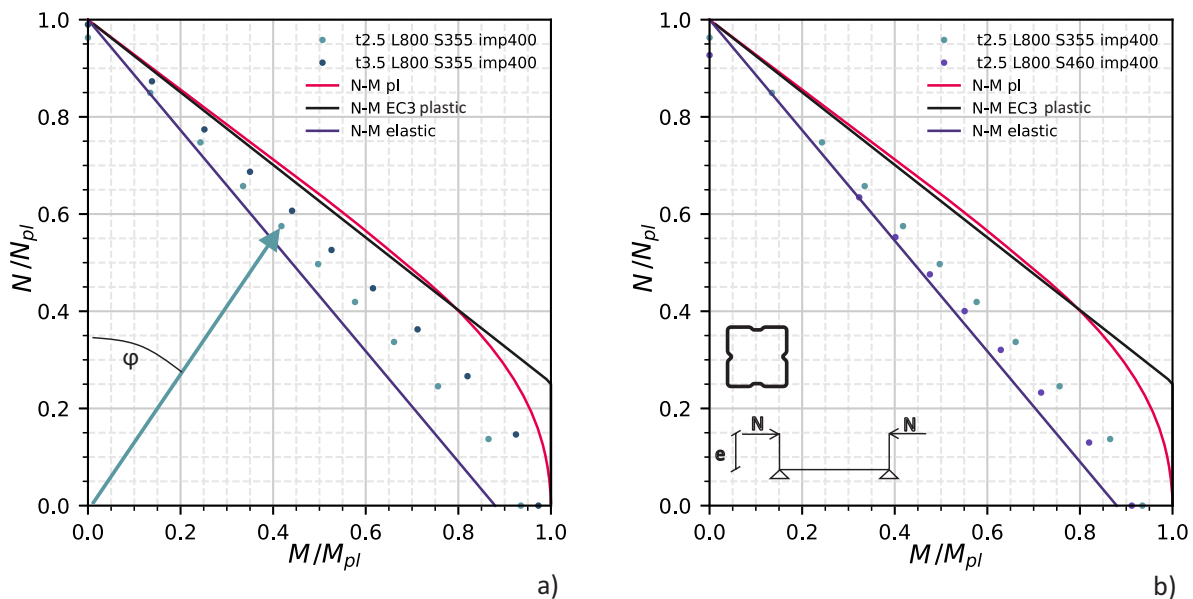


Fig. 6.1. a) GMNIA results in the $n - m_y$ diagram of a SHS-S specimen with a) two thickness values and b) two steel grades.

The $n - m_y$ diagram seems to be a powerful tool for the understanding of the effects of parameters on the resistance, for standard SHS/RHS and even for a non-standard section as the SHS-S. This format, though, is not suited to determine a general design concept, which may capture the GMNIA results varying the section slenderness. For this, the $\bar{\lambda}_L - \chi_L$ diagram is a better representation format: it plots the buckling resistance $R_{b,L}$ as a function of the overall cross-section slenderness. As was stated in section 3.2, the slenderness and the

buckling resistance (as multiplier of a reference load) are defined as follows:

$$\bar{\lambda}_L = \sqrt{\frac{R_{ref}}{R_{cr,L}}} \quad (6.1)$$

$$R_{b,L} = \chi_L R_{ref} \quad (6.2)$$

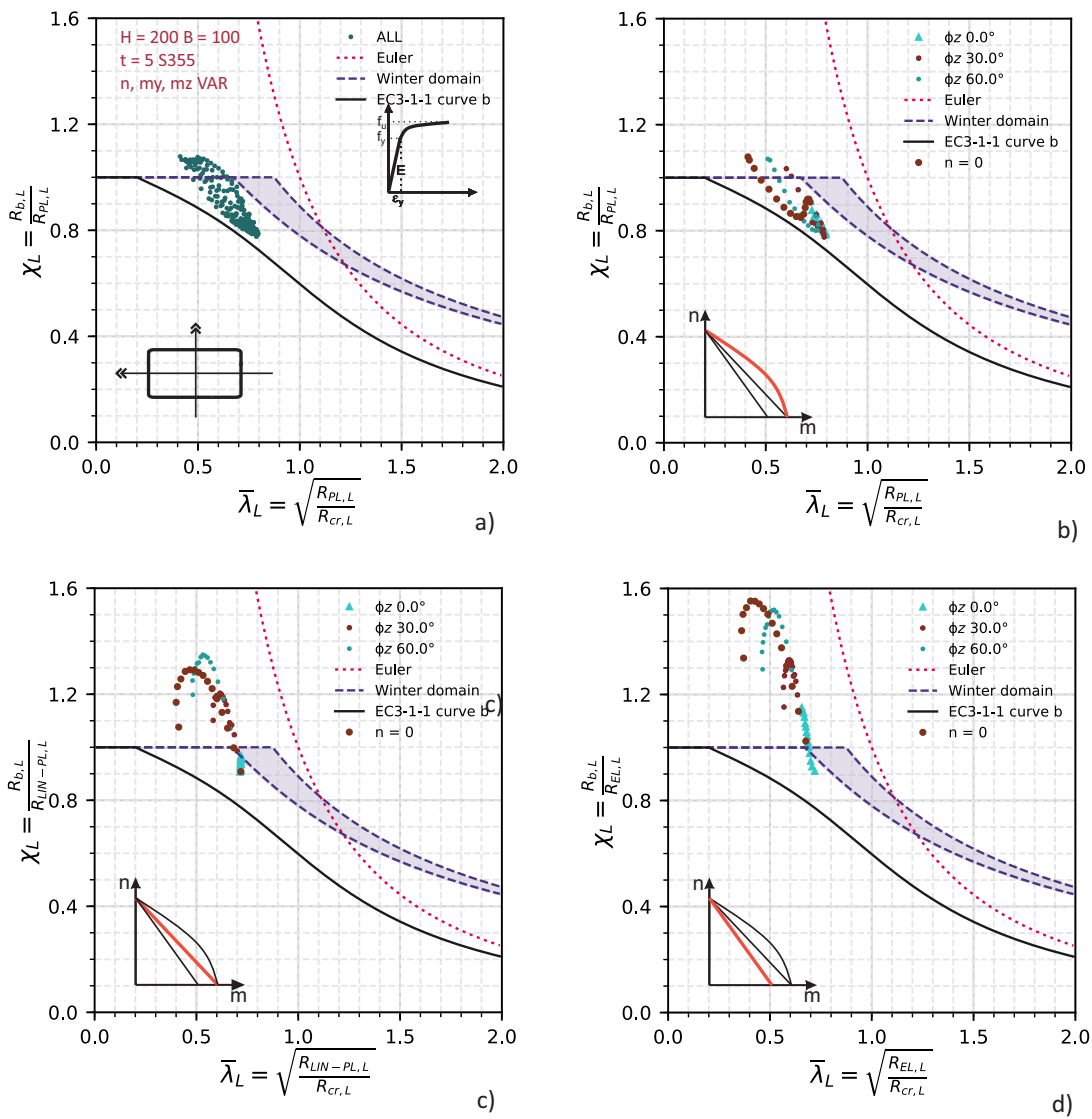


Fig. 6.2. a) a $H/B=2$ CS with a few ϕ_y ϕ_z combinations in the GSRM R_{pl} method for cold-formed RHS; b) results of a) for $\phi_z = 0, \phi_z = 30, \phi_z = 60$ and $n = 0$; c) results of b) with CS resistance R_{LIN-pl} ; d) results of b) with CS resistance R_{EL} .

In equation (6.1) and (6.2) R_{ref} is a reference resistance measure defined by analytical formulae from the geometry and material. R_{el} and R_{pl} are respectively the well-known elastic resistance and plastic resistance. Another possible definition of R_{ref} is $R_{LIN,pl}$, consisting in a linear function in the $n - m_y$ plot passing through the points ($n = 1, m_y = 0$) and ($n = 0, m_y = 1$). The following figure 6.2 shows results of the numerical study for an individual section, an RHS with $H=200$, $B=100$ mm, wall thickness of $t=5mm$ and steel grade S355, loaded by variable combinations of axial compression and biaxial bending. In the various sub-figures, the results based on the different reference cross-sectional resistances (full non-linear plastic R_{pl} , linear plastic $R_{LIN,pl}$, elastic R_{el}) are illustrated. It should be noted that, as is indicated in the figure, a non-linear stress-strain curve was employed in these calculations in accordance with the recommendations in the methodology section 3. Figure 6.2a shows the totality of the obtained results for all considered combinations of n , m_y and m_z , while figure 6.2b shows a selection with only 3 “angles” ϕ_z (and all combinations of n and m_y) as well as the case with pure bending ($n=0$) with various degrees of double-axiality. In this latter plot, a characteristic, “U-shaped” distribution of the results for each the four considered cases is obtained. The mentioned “U-shape” is thereby given by the distribution of the values of χ_L plotted over the slenderness, since these start and end at a higher value at each end of the considered spectrum of loading parameters than many values that are obtained from intermediate combinations of parameters. In all cases, loading scenarios with more eccentricity and biaxiality lead to lower values of χ_L . It may thereby be noted that this behaviour is only typical, if a representation based on the full non-linear plastic cross-sectional resistance is chosen. This can further be seen in figure 6.2c and d, where the same results as in 6.2b are plotted on the bases of the linear-plastic and the elastic cross-sectional resistances. In this case, the resistances first increase (in terms of χ_L) with increasing eccentricity e_z (i.e. causing bending about the y-axis), only to later decrease after a peak value is achieved. The scatter of these results is fairly large, both in terms of slenderness and values of the buckling resistance. In order to be able to develop design equations that conservatively, yet sufficiently accurately cover the full range of possible combinations of loading for all RHS and SHS sections in the context of the GSRM design philosophy, it is useful to plot the entirety of the results of the numerical test campaign. In figure 6.3 both $R_{ref} = R_{el}$ and $R_{ref} = R_{pl}$ are adopted. The plots clearly illustrate that quite different values of χ_L are obtained depending on the definition of R_{ref} . At first glance, figure 6.3 seems to indicate a relatively compact scatter band in the R_{pl} -based representation. However, the differences between various χ_L values for a particular slenderness are still

pronounced, and a simple lower-bound curve would underestimate many capacities by up to 50%. The most common load cases, such as pure compression or bending moments, are positioned in the higher range of the scatter band for this type of representation, with the pure compression case exhibiting a similar pattern to that of the pure bending case. This implies that conservative design rules based on R_{pl} would mostly be governed by less common cases with high load eccentricities. Different results are obtained if the cross-section reference resistance is given by R_{el} , with the corresponding changes in the definitions of slenderness and knock-down factor. At first, the scatter in the corresponding figure 6.3b appears wider, since very high χ_L values are reached, mainly due to the large difference between R_{el} and R_{pl} in biaxially bent sections. However, as was observed during the development of GSRM design rules, much clearer patterns emerge if R_{el} is chosen as the reference resistance. Very advantageously for the development of practical design curves, a description with “Winter-type formulae” is made possible, since most of the results follow the general pattern of the Winter curve. Conveniently, the standard cases of pure compression and pure bending are near the lower bound of resistances. For this reason, among others, $R_{ref} = R_{el}$ was finally chosen in the GSRM to represent the results of the numerical parametric study and the design rules developed from it.

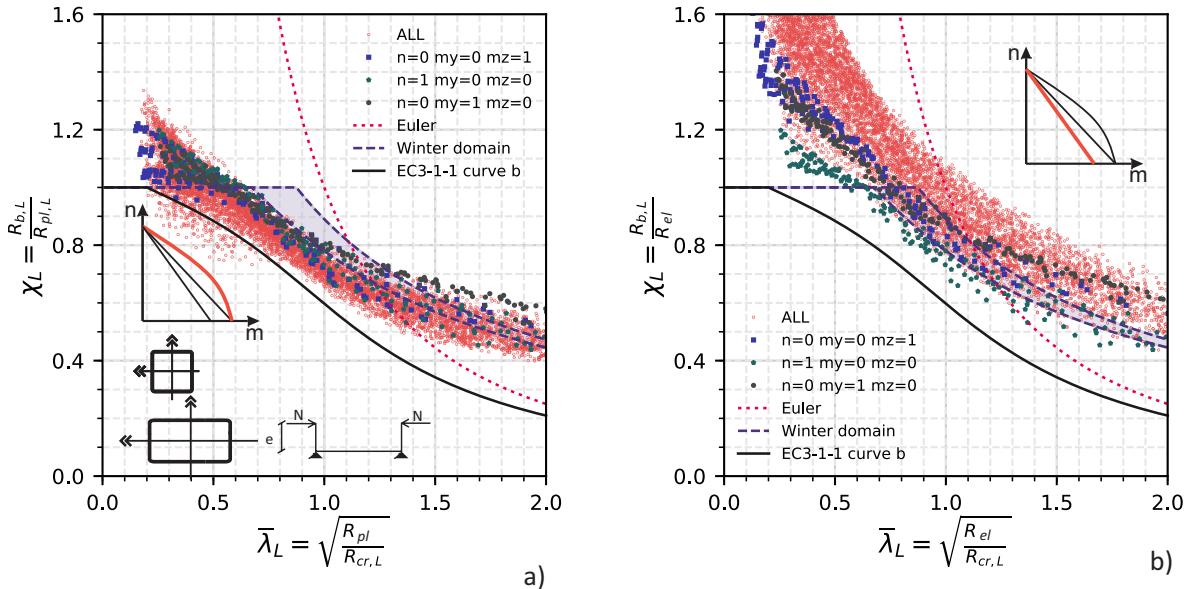


Fig. 6.3. Overview of all results from the parametric study of the cross-sectional (local buckling) strength of cold-formed SHS and RHS; a) representation of GSRM buckling knock-down factor using R_{pl} as reference resistance, and b) representation using R_{el} .

6.3 Calibration of the design equations

The Winter formulation is the format chosen for the development of local buckling reduction curves for flat-faced hollow sections, as it naturally provides a shape that is suited to this task, by its very background. The steps for the development of the Winter design curves and a final format of representation of the resistance were described in section 2.1, while in 3.5 equation (3.23) describes the general format of the Winter curve. The GSRM defines a section-based $\chi_L = f(\bar{\lambda}_L)$ function, which assumes the form of the generalised Winter-curve of equation (3.23). Thus, in order to use the Winter formulation and fit it to the results of the parametric study, the results in the GSRM format can be rewritten in equation (6.3), where n_1 and n_2 are set to 1.0.

$$\rho = \frac{1}{\bar{\lambda}_L} \left(1 - \frac{A}{\bar{\lambda}_L} \right) \quad (6.3)$$

In doing so, the parameter A was calibrated to the results of the extensive numerical parametric study of local buckling. In this calibration it was seen to be conducive to good results to define A as a function of ψ_1 and ψ_2 , in partial reference to the EN1993-1-5 [40] Table 4.1 and 4.2 approach, shown in figure 2.7 in section 3.5.2.

$$A = f(\psi_1; \psi_2) \quad (6.4)$$

ψ_1 and ψ_2 are the stress ratios in the two plates adjacent to the corner with the highest compressive stress in the section, see figure 3.12. They may be determined in a simplified manner, discounting the presence of the typical rounding at the edges of SHS and RHS, or more precisely, without significantly changing the accuracy of the method. This is justified by the small difference in the actual stress state and the increased ease of use of the formulations.

Equation (6.5) defines the parameters with analytical formulae.

$$\psi_1 = MAX \left(\frac{N}{A} + \frac{M_y}{W_y} - \frac{M_z}{W_z}, \frac{N}{A} - \frac{M_y}{W_y} + \frac{M_z}{W_z} \right) \quad (6.5)$$

$$\psi_2 = MIN \left(\frac{N}{A} + \frac{M_y}{W_y} - \frac{M_z}{W_z}, \frac{N}{A} - \frac{M_y}{W_y} + \frac{M_z}{W_z} \right) \quad (6.6)$$

6.3.1 Rules in the elastic range

In an initial step, a formulation for the parameter A was sought which describes the cases with compression and mono-axial (or “in-plane”) bending about either axis. This corresponds to all cases where the stress ratio $\psi_1 = 1.0$ (pure compression in one of the plates). For cold-formed (EN 10219, [71]) and hot-finished (EN 10210, [72]) sections, the linear functions in equations (6.7) and (6.8) were determined through calibration and the final choice of practical, easy-to-use functions and coefficients.

$$A = 0.225 + 0.025\psi_2 \quad \text{cold-formed sections} \quad (6.7)$$

$$A = 0.20 + 0.02\psi_2 \quad \text{hot-finished sections} \quad (6.8)$$

A general overview of some of the calibrated curves is given in figure 6.4, for cases with in-plane bending only. The pure compression case for cold-formed sections was accepted as being less conservative than other cases, thus allowing continuity of the chosen formulation, while diverging as little as appeared to be acceptable from the current Eurocode 3 levels of accuracy and safety. The results of this curve fitting is shown in figure 6.5a e.g. for cold-formed sections. In the figure, the horizontal segments represent GMNIA results of the single load cases of the numerical campaign, which lie at different levels of ψ_2 . Each load case corresponds to a value of A , adopted in the Winter curve to fit the GMNIA results, as is shown in each load case of figure 6.4. The resulting range of possible design curves for cold-formed sections loaded in compression and with any level of in-plane bending is shown in figure 6.5b; the pure compression case $\psi_2 = \psi_1 = +1$ and the pure in-plane bending case $\psi_2 = -1$ $\psi_1 = +1$ are displayed in different colours, and the area between the lines corresponds to the various $N + M_y$ combinations.

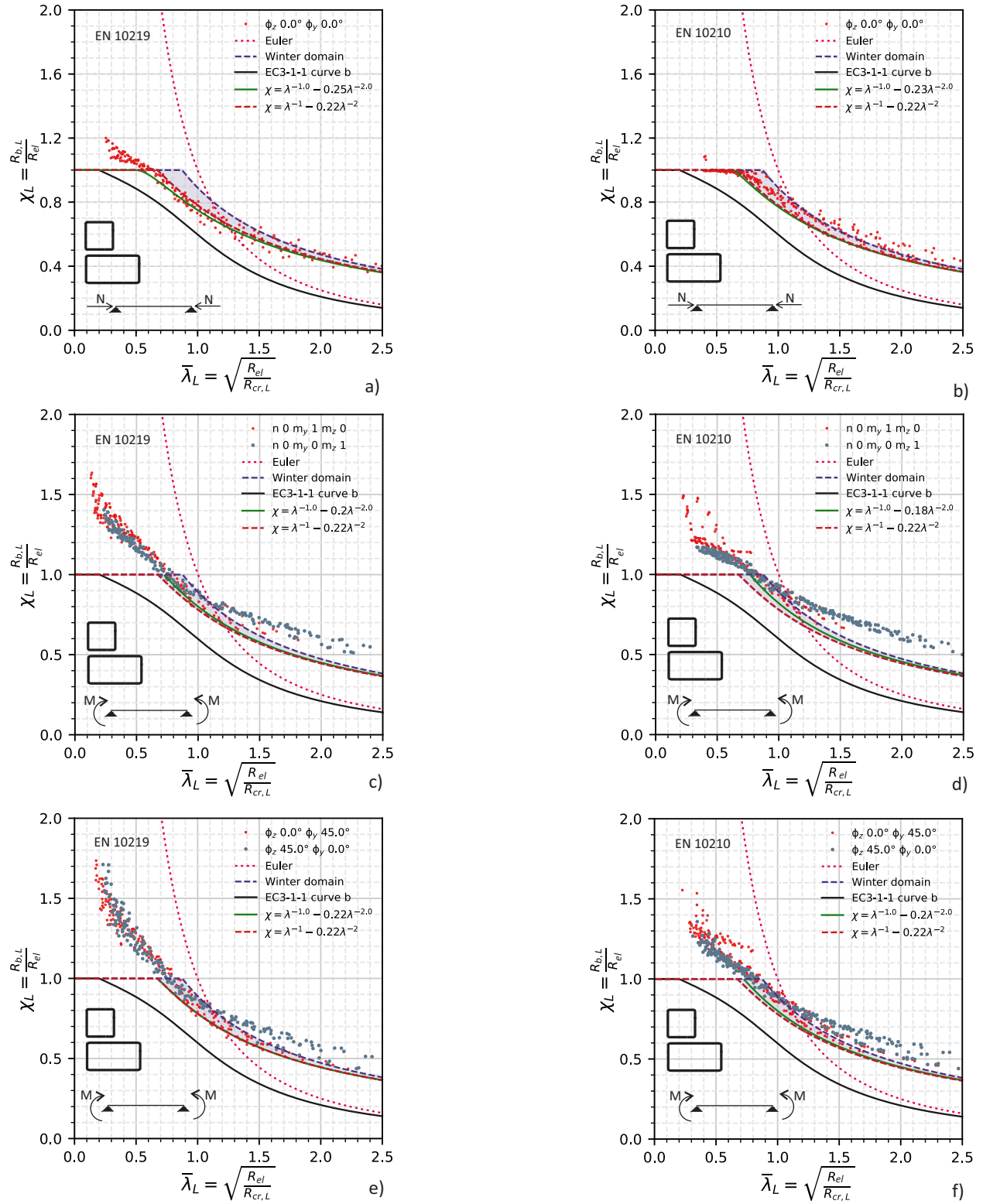


Fig. 6.4. Calibration of the Winter-type curve varying ψ_2 for the following cases: a) pure compression of cold-formed sections; b) pure compression of hot-finished sections; c) pure bending on the minor axis of cold-sections and d) hot-finished sections; pure bending on the major axis for e) cold-formed and f) hot-finished sections.

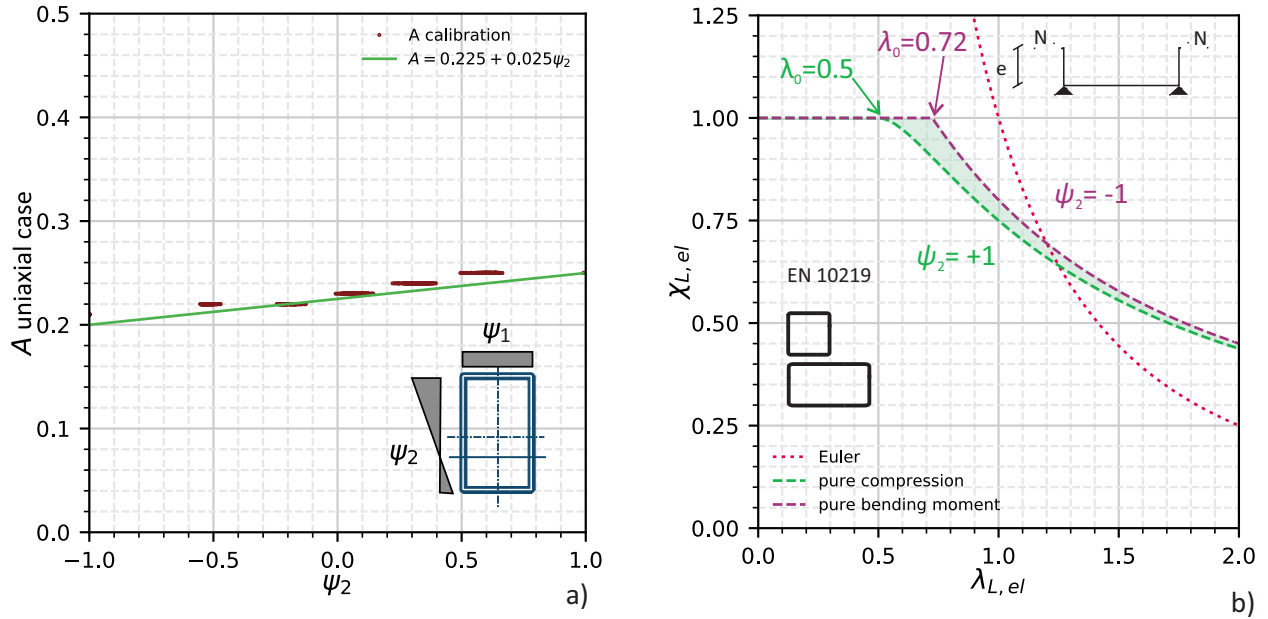


Fig. 6.5. a) overview of the fitted values of A plotted against ψ_2 , and b) overview of GSRM design curve (mono-axial case) for cold-formed sections.

An additional multiplier $f(\psi_1)$ for the ψ_1 dependency covers the biaxial load case and is formulated in equation (6.9) as a generalised equation of the one found in EN 1993-1-5 for linear stress fields in an individual plate.

$$f(\psi_1) = \frac{c + \psi_1}{c + 1} \quad (6.9)$$

In the Eurocode the value $c = 3$ is applied. Multiple integer values of c were attempted during the calibration of the Winter formula coefficient A to the numerical test data. Finally, a value of $c = 1$ was found to best fit the data, while maintaining ease of use (non-integer values were avoided) and a relation to the EC3 practice. Thus, in summary, for the general (biaxial) case, A is defined in equations

$$A = 0.225 + 0.025\psi_2 \frac{1 + \psi_1}{2} \quad \text{cold-formed sections} \quad (6.10)$$

$$A = 0.20 + 0.02\psi_2 \frac{1 + \psi_1}{2} \quad \text{hot-finished sections} \quad (6.11)$$

If $\psi_1 = 1$ the formula results equal to the in-plane banding cases.

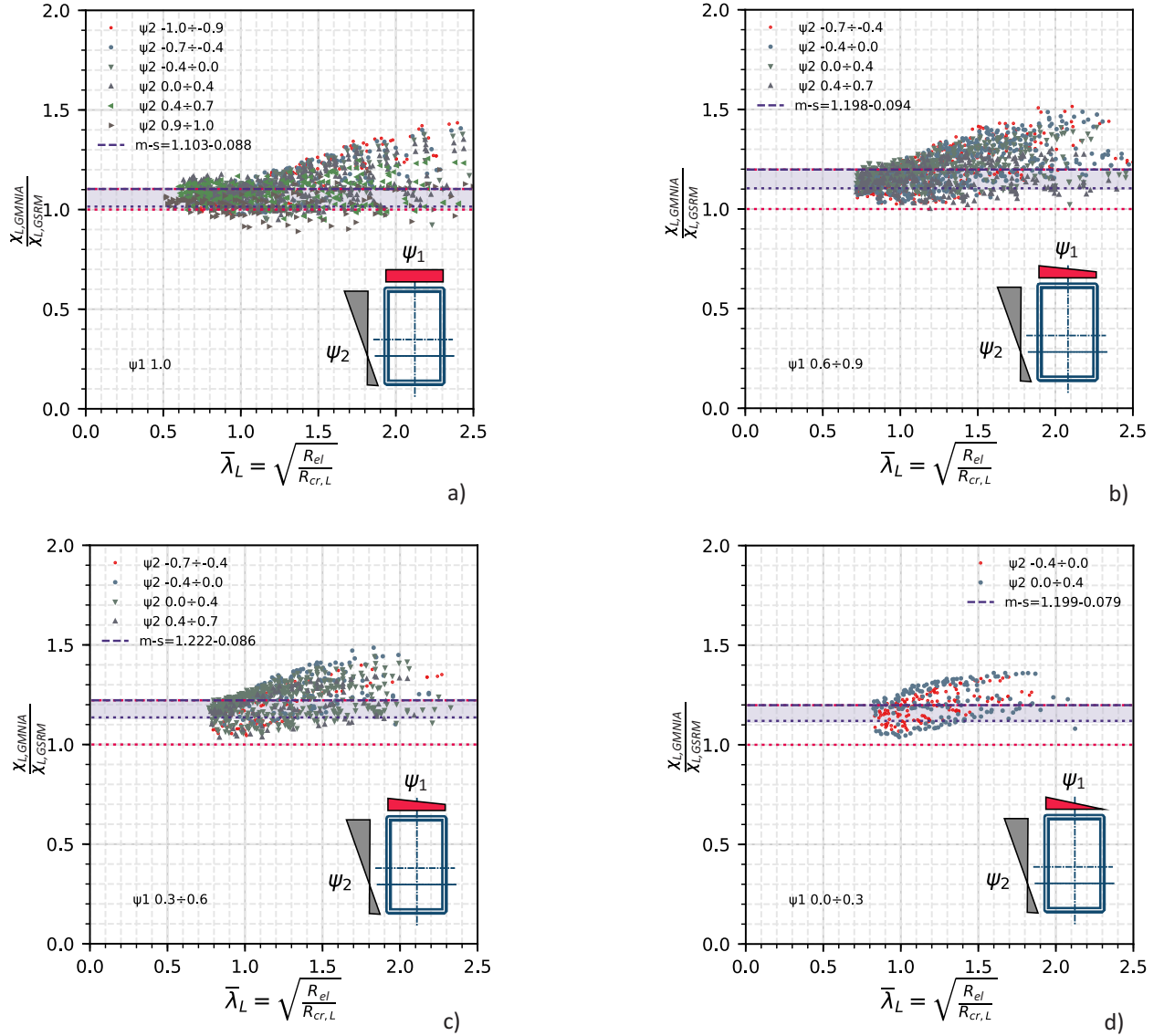


Fig. 6.6. Overview of the calibration of cold formed sections. In a) the in-plane case. In b) c) and d) different values of ψ_1 are illustrated.

The point where the slender range ends is denoted as the *elastic limit slenderness* $\bar{\lambda}_0$ and reads

$$\bar{\lambda}_0 = 0.5 + \sqrt{0.25 - A} \quad (6.12)$$

In figure 6.6 an overview of the numerical results for cold-formed sections in the Winter-type formulation is shown. The GMNIA results divided by the GSRM prediction are plotted against the local slenderness. Figure 6.6a represents the in-plane case, and in Figure 6.6b,

c and d the level of biaxial load increases as ψ_1 decreases. The plots demonstrate the accuracy of the chosen formulation for A in the elastic range, and show a fairly low scatter of the results, positioning the average GMNIA results between 10% and 22% higher than the predictions with different levels of biaxial bending. The scatter is also fairly homogenous along the slenderness with a slight tendency of increasing with larger values of the local slenderness, approximately from $\bar{\lambda}_L \approx 1.5 - 2$, which is a range of very slender cross-sections ($\gg t$ or $\gg f_y$), which are not common.

6.3.2 Rules in the stocky range

For the plastic (stocky) range, a simplified bilinear function is used for the modelling of the cross-section resistance in the GSRM. A more complex and precise method based on the CSM was developed by Meng et al. [54]. The GSRM function is based on a simple expansion of the stress-based design to the stocky range used in the elastic range, while the CSM is a strain-based approach.

In the GSRM, the bilinear relation is chosen to represent the resistance in the stocky range, where the cross-sectional capacity exceeds R_{el} . A linear function which intersects two points is unique, thereby two anchor points are necessary for the definition of the bilinear function in the $\bar{\lambda}_L - \chi_L$ plot, defined in equation 6.13 and 6.14.

$$\chi_L = 1 \quad \text{at} \quad \bar{\lambda}_0 \quad (6.13)$$

$$\alpha_{pl} \quad \text{at} \quad \bar{\lambda}_L = \bar{\lambda}_{pl} = 0.3 \quad (6.14)$$

The proposed formulation for predicting the cross-sectional capacity for the stocky range is as follows, with the values for $\bar{\lambda}_{pl}$ and the maximum value α_{pl} , see (6.14), taken to represent the data with acceptable safety and accuracy. Equations (6.15) and (6.16) summarise the GSRM design proposal for the stocky range.

$$\bar{\lambda}_L \leq \bar{\lambda}_0 : \quad \chi_L = 1 + (\alpha_{pl} - 1) \left(\frac{\bar{\lambda}_0 - \bar{\lambda}_L}{\bar{\lambda}_0 - \bar{\lambda}_{pl}} \leq \alpha_{pl} \right) \quad (6.15)$$

$$\text{where:} \quad \bar{\lambda}_{pl} = 0.3 \quad \alpha_{pl} = \frac{R_{pl}}{R_{el}} \leq 1.5 \quad (6.16)$$

Figure 6.7 illustrates the method and the resulting location of the design values for the cross-sectional (local buckling) strength $R_{b,L,GSRM}$ for all cross-sections and load combinations

studied in the numerical campaign described in chapter 4.

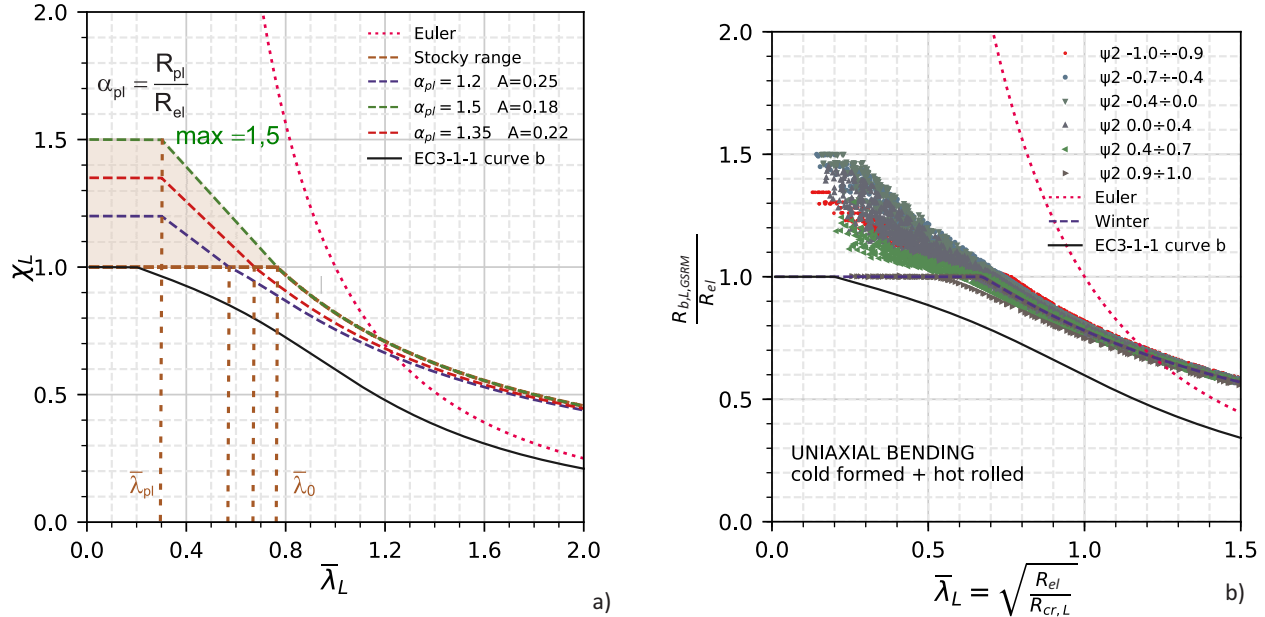


Fig. 6.7. a) Representation of the simplified bilinear relation in the stocky range and Winter formulation in the slender range, and b) evaluation of the hot-finished and cold-formed sections dataset for the uniaxial bending case ($\psi_1 = 1$, ψ_2 varies from -1 to 1).

6.4 Comparison with current standards

In figure 6.8, an overview of the results of the parametric study are plotted over the GSRM slenderness and knock-down factor definition. The figure shows the results of the parametric study – in terms of GMNIA resistance divided by the reference resistance R_{el} – plotted against the GSRM slenderness and definition. The same is also done for the predictions of the GSRM in figure 6.8c and 6.8d. The figures show that the method captures the general position of the GMNIA results in the $\bar{\lambda}_L - \chi_L$ plot, particularly in the slender range. The GSRM results appear to be positioned somewhat lower than the GMNIA results throughout all slenderness ranges, indicating a degree of conservatism, although the degree of conservatism is not easily assessed in this type of representation. Thus, in order to achieve a better overview of the accuracy and safety of the new GSRM design rules, the resistance values from GMNIA calculations are normalized in figure 6.9 by the predicted value of the GSRM (see figure 6.9a). For the validation of the design rule in the GSRM, the results of the design method are compared with the GMNIA results and then compared with the EC3 design method.

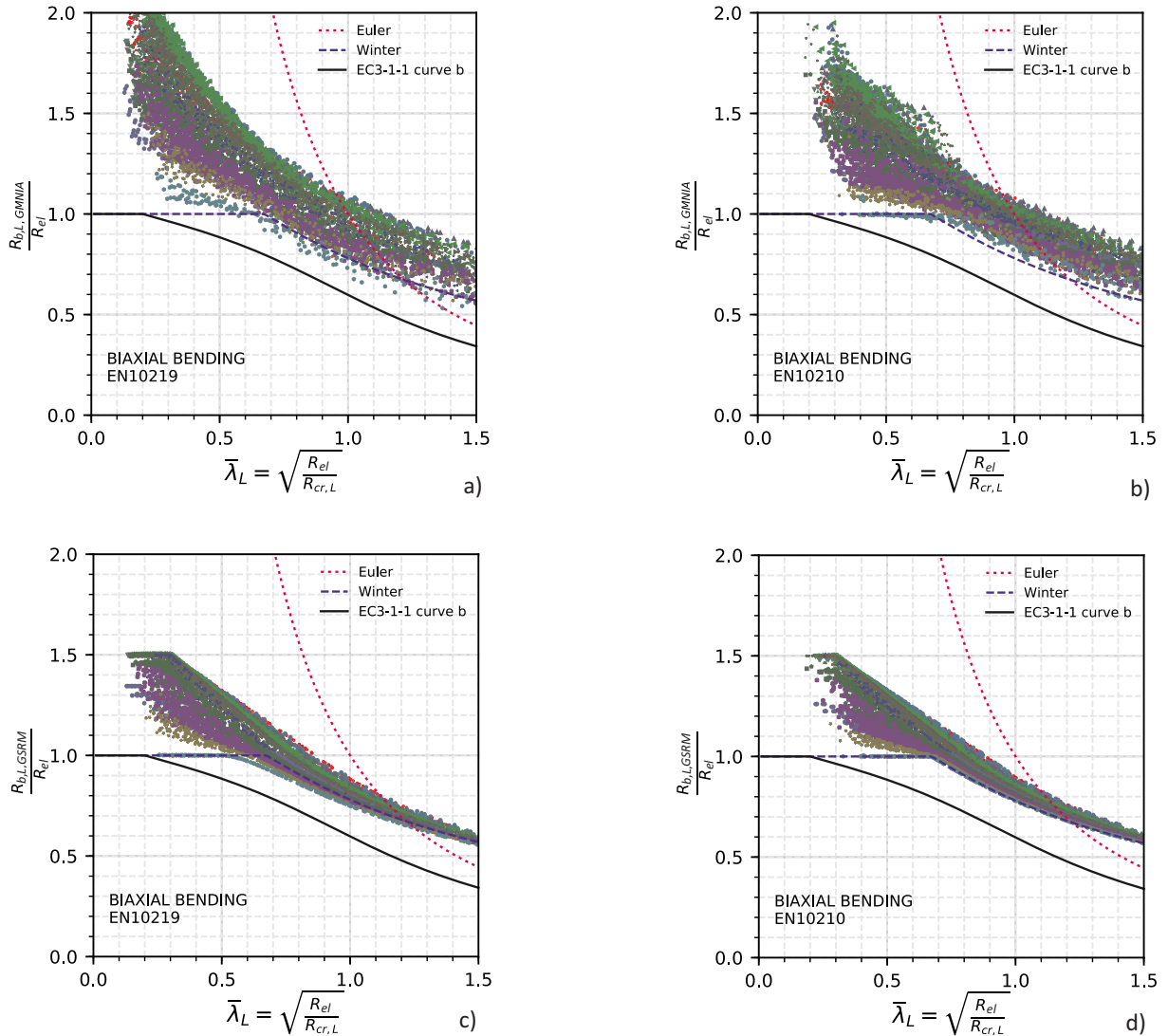


Fig. 6.8. Representation of the GMNIA results for a) cold-formed sections and b) hot-finished sections in the case of biaxial bending, where each colour represents a different ψ_1 and ψ_2 combination; in c) and d) the corresponding values according to the GRSM proposal are represented.

The results of the GMNIA calculations are in most of the cases higher than the GSRM results, but fall in a range fairly close to the design values, providing generally low values of scatter, see figure 6.9. The scatter is represented in the plots by the horizontal lines for each class of cross-section (classes 1+2, class 3 and class 4 in the figures) by indicating the mean value (upper line) and the $m - 2s$ value, whereby s is the calculated standard deviation for the considered cross-sectional class. Thereby, as can be seen in figure 6.9, the proposed formulation leads to a relatively stable degree of scatter and thus a fairly homogenous (and

low) level of average conservatism throughout slenderness classes, for all load cases and cross-sectional shapes. In figure 6.9a and b the load cases of uniaxial bending and compression are shown and marked with different colours, identifying possible paths for load cases, but in the figure the different cases are homogeneously distributed in slenderness and resistance, and the statistical evaluation of the data in terms of mean value and variance is largely unchanged from cold-formed steels to hot-finished. Similarly, figures 6.9c and d show a similar analysis for the parametric study including biaxial bending.

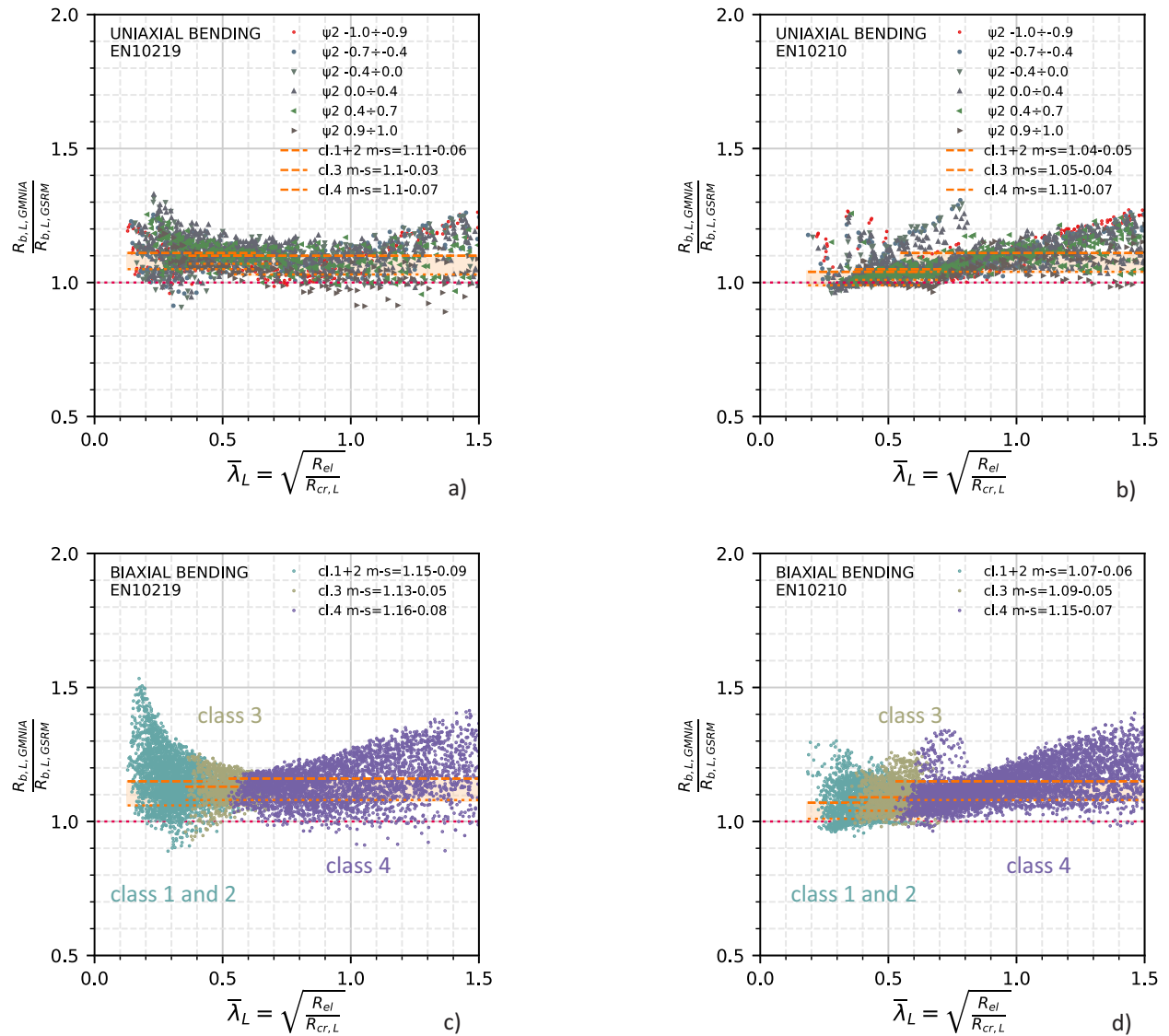


Fig. 6.9. Graphical validation of uniaxial bending + compression cases for a) cold-formed and b) hot-finished sections; c) and d): cases with compression and biaxial bending, categorized by EC3 classes.

Colours of sub-figure c and d refer to the Eurocode 3 classes, the same m and s value are shown and cold-formed and hot-finished steels are treated separately. While the average value of the GMNIA results falls between is 5-10% higher than the design results for the uniaxial case, in the biaxial case 7% up to 15% higher (on average) are found. This produces a satisfactory initial safety assessment. The standard deviation of the result cloud in this format is also fairly low. A minimum of 3% for the uniaxial bending case of cold-formed sections is found, and 4% for hot-finished sections, showing the highest effectiveness of the method in the class 3 section range. The scatter of the results is also low in the more stocky and more slender range, reaching values between 6% to 9%. This outcome is an initial validation of the GSRM predictive formulae and leads to the comparison with the current design formulae. In order to visualize the improvement of accuracy and safety obtained through the GSRM, a comparison with the EC3 predictions is shown in figure 6.10. The current EC3 version includes some changes in the cross-sectional classification for SHS/RHS sections, as well as specific design rules for the cross-sectional strength of class 3 cross-sections with double-symmetric section, developed during the RFCS project SEMICOMP. As the plots in the figure 6.10 show, while the GSRM design shows consistent accuracy and comparable average distance from „real“ (GMNIA) resistance across slenderness ranges and EC3 classes, the Eurocode design rule shows much larger inconsistencies and larger scatter in the results for classes 1 to 4. Gains in strength through the use of the GSRM are noticeable, compared to EC3, particularly for class 4 sections and in cases with a pronounced level of biaxial bending, the gains are even higher. A consciously accepted lower resistance is found for class 1 and 2 sections, in order to compensate for an apparent lack of conservatism of the Eurocode rules in this range. For class 3 sections, the methods are on average equivalent in their strength predictions. In all cases, particularly those that involve load cases with combined compression and bending, the GSRM design method employs a much more straightforward procedure and avoids the cumbersome determination of effective cross-sections (class 4 sections) or multi-step design strengths for combined loading (classes 1 to 3). The statistics of these data, which are also represented in figure 6.10, are summarized in table 6.1.

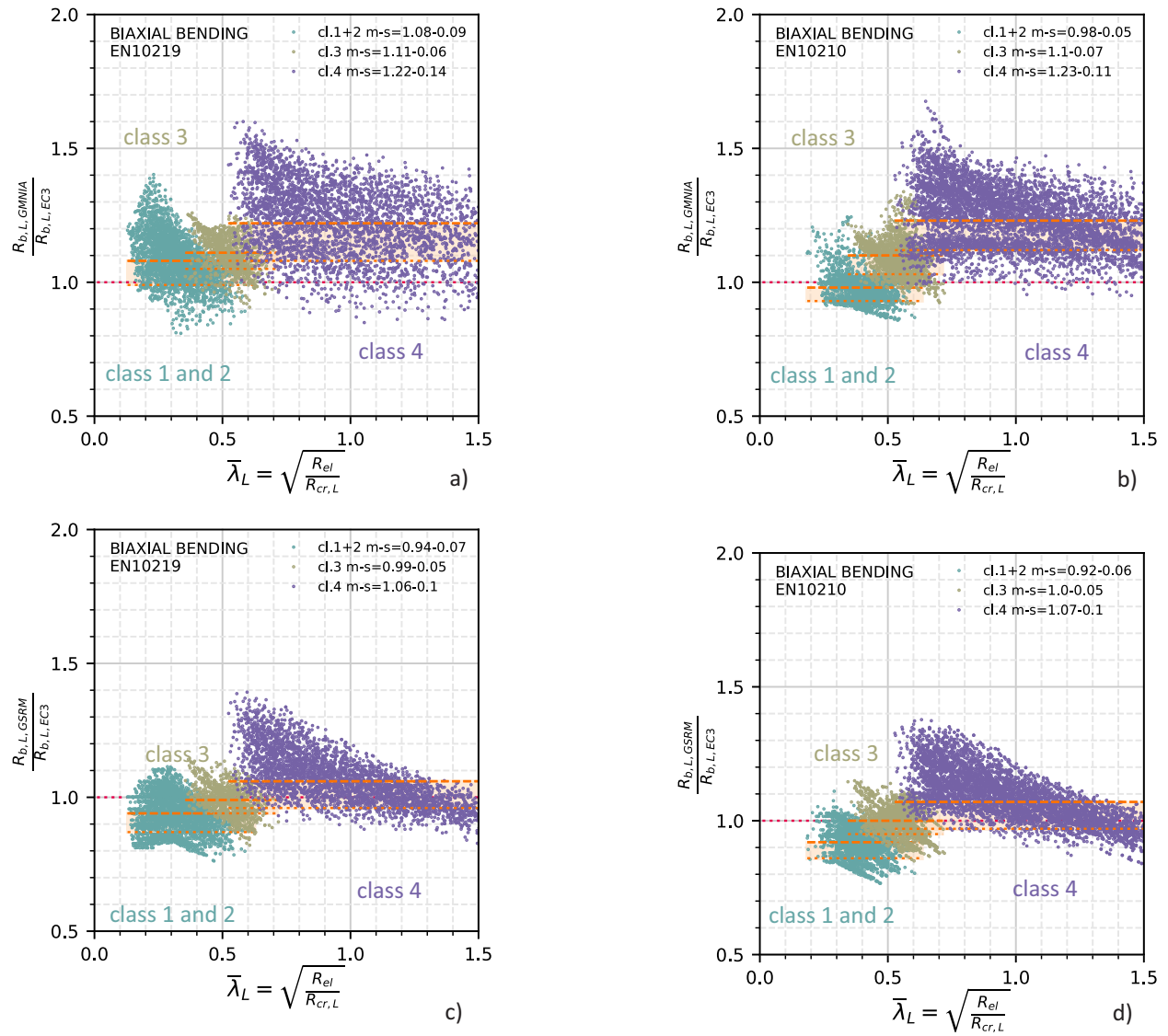


Fig. 6.10. a) and b): GMNIA results divided by the EC3 resistance prediction, plotted against the cross-section slenderness; a) cold-formed and b) hot-finished sections; c) and d): direct comparison of the proposed GSRM formulation results with EC3 [1].

			Class 1 and 2	Class 3	Class 4
$\frac{R_{b,L,GMNIA}}{R_{b,L,GSRM}}$	EN10219	m s	1.15 0.09	1.13 0.05	1.16 0.08
$\frac{R_{b,L,GMNIA}}{R_{b,L,GSRM}}$	EN10210	m s	1.07 0.06	1.09 0.05	1.15 0.07
$\frac{R_{b,L,GMNIA}}{R_{b,L,EC3}}$	EN10219	m s	1.08 0.09	1.11 0.06	1.22 0.14
$\frac{R_{b,L,GMNIA}}{R_{b,L,EC3}}$	EN10210	m s	0.98 0.05	1.10 0.07	1.23 0.11
$\frac{R_{b,L,GSRM}}{R_{b,L,EC3}}$	EN10219	m s	0.94 0.07	0.99 0.05	1.06 0.10
$\frac{R_{b,L,GSRM}}{R_{b,L,EC3}}$	EN10210	m s	0.92 0.06	1.00 0.05	1.07 0.10

Table 6.1: Summary of average values m and standard deviations s of the results.

6.5 Reliability aspects, partial factors

While questions of reliability and the necessary values of the partial factors of safety (γ_{Mi} in Eurocode terminology) was not the focus of this thesis, this topic was treated in the HOLLOSSTAB project, see [73]. For the purposes of this thesis, it shall only be mentioned that the derived formulations for the GSRM for local buckling were shown to have a very consistent level of reliability and to require a partial factor of $\gamma_{M0} = 1.0$.

6.6 Summary of the GSRM design rules for local buckling

In chapter 6 the GSRM design formulations for local buckling was described. Section 6.2 introduced the GSRM representation format, which employs the $\bar{\lambda}_L - \chi$ diagram and the Winter curve. In section 6.3 the calibration of the parameters for the Winter curve were determined, defining two different design rules for the stocky range and the elastic range of the curve. In section 6.4 the newly developed design rules for the cross-sectional strength were compared with the current Eurocodes design rules, evaluating advantages and improvements of the method. Figure 6.11 represents schematically the developed design rules for SHS and RHS.

GSRM Proposal for local buckling	
<p>$R_{b,L} = R_{el} \cdot \chi_L$ with: $R_{b,L}$... load amplifier to reach the cross-sectional resistance R_{el} ... load amplifier to reach compressive first yield in the section χ_L ... buckling coefficient to account for elastic or plastic local buckling</p>	<p style="text-align: center;">$\bar{\lambda}_L = \sqrt{\frac{R_{el}}{R_{cr,L}}}$</p> <p style="text-align: center;">Cross-section check: $\frac{R_{b,L}}{\gamma_{M0}} \geq 1$ with $\gamma_{M0}=1,0$.</p>
GSRM rules for RHS/SHS	
<p style="text-align: center;">$\bar{\lambda}_0 = 0.5 + \sqrt{0.25 - A}$</p> <p>$A = (0.2 + 0.02\psi_2) \frac{(1+\psi_1)}{2}$ for hot-finished sections $A = (0.225 + 0.025\psi_2) \frac{(1+\psi_1)}{2}$ for cold-formed sections $B_2 = 1$</p>	<p>$\psi_1 = \text{MAX} \left(\frac{\frac{N}{A} + \frac{M}{W_y} + \frac{W_z}{M}; \frac{N}{A} + \frac{M}{W_x} + \frac{W_z}{M} \right)$ $\psi_2 = \text{MIN} \left(\frac{\frac{N}{A} + \frac{M}{W_y} + \frac{W_z}{M}; \frac{N}{A} + \frac{M}{W_x} + \frac{W_z}{M} \right)$</p>
<p style="text-align: center;">$\chi_L = (1 - \frac{A}{\bar{\lambda}_L B_2}) \cdot \frac{1}{\bar{\lambda}_L B_2}$</p>	<p style="text-align: center;">$\chi_L = 1 + (\alpha_{pl} - 1) \cdot \frac{\bar{\lambda}_0 - \bar{\lambda}_L}{\bar{\lambda}_0 - 0,25} \leq \min(\alpha_{pl}; 1,5)$</p>
<p>Elastic range $\bar{\lambda}_L > \bar{\lambda}_0$</p>	<p>Plastic range $\bar{\lambda}_L < \bar{\lambda}_0$</p> <p style="text-align: center;">$\alpha_{pl} = \frac{R_{pl}}{R_{el}}$</p>

Fig. 6.11. GSRM design rules for local buckling.

Chapter 7

GSRM Design Formulations - Global Buckling

7.1 Introduction

The following sections present predictive methods for the design of members against global buckling in the GSRM format. The formulation developed in the GSR method is based entirely on second order theory and basic mechanics, thereby using the basic principles of the Ayrton-Perry concept but expanding it to include external bending moments. In a final step, some calibration factors are introduced, which help to adapt the mechanically derived formulation to better describe the real, elasto-plastic non-linear behaviour as observed in physical and numerical tests.

7.2 Ayrton-Perry formulation and EC3

As discussed in detail in section 2.1.2, a widely used formula to describe the behaviour of columns in flexural (global) buckling was first described by Ayrton and Perry in 1886 (see [41]). This approach uses an equivalent imperfection of sinusoidal shape and amplitude e_0 in combination with a second-order analysis and stress design of a pin-ended model column, to calibrate a buckling reduction factor χ_y describing the strength of real columns, as observed e.g. in tests. The following variables are used in the Ayrton-Perry formulation found in the

Eurocode (flexural buckling about y-y):

$$\chi_y = \frac{N_b}{Af_y} \quad (7.1)$$

$$\bar{\lambda}_y = \sqrt{\frac{Af_y}{N_{cr,y}}} \quad (7.2)$$

$$\eta_{imp} = \frac{Ae_0}{W_y} \quad (7.3)$$

Where N_b is the applied load, which finally leads to column failure, N_{cr} is the axial force at the first bifurcation point, or "Euler load", A is the cross-section area, W_y the cross-section modulus for bending about the y-axis, f_y is the yield stress. By introducing the aforementioned variables (see section 3.5.1 for the complete derivation) and applying the findings of Ayrton-Perry, the limit state equation (3.17) may be solved, leading to the well-known equation found e.g. in EN1993-1-1:

$$\chi_y = \frac{1}{\phi_y + \sqrt{\phi_y^2 - \bar{\lambda}_y^2}} \quad (7.4)$$

$$\text{with } \phi_y = 0.5 \left(1 + \eta_{imp} + \bar{\lambda}_y^2 \right) \quad (7.5)$$

In Eurocode 3, following Ayrton and Perry's original idea, the still-general term η_{imp} is replaced by a formula that makes this imperfection a function of:

- slenderness $\bar{\lambda}_y$.
- a plateau value 0.2, accounting for stocky columns not failing before the squash load.
- calibration factor α which accounts for residual stresses and production differences, here denoted as α_{EC3} .

Thereby, η_{imp} reads as follows:

$$\eta_{imp} = \alpha_{EC3} (\bar{\lambda}_y - 0.2) \quad (7.6)$$

This solution is valid for the case of pure flexural column buckling without any applied bending moment. In figure 7.1b the different values of α_{EC3} and the corresponding Eurocode buckling curves are shown.

The GSRM formulation developed in this thesis and in the RFCS project HOLLOSSTAB derives the rules for global-buckling from the same principles as the Ayrton-Perry and the Eurocode method, accounting for applied bending moments and global buckling in both y- and z-axis. Column buckling curves are represented in a slightly different format, shown in figure 7.1a. The member capacity is illustrated by the $\chi_G - \bar{\lambda}_G$ plot, defined in equation (7.7) and (7.8).

$$\bar{\lambda}_G = \sqrt{\frac{R_{b,L}}{R_{cr,G}}} \quad (7.7)$$

$$\chi_G = \frac{R_{b,G}}{R_L} \quad (7.8)$$

where:

- χ_G is the global buckling resistance defined as a reduction factor of the local, cross-sectional resistance R_L .
- $\bar{\lambda}_G$ is defined in terms of cross-sectional resistance and critical bifurcation load of the first global buckling mode $R_{cr,G}$.

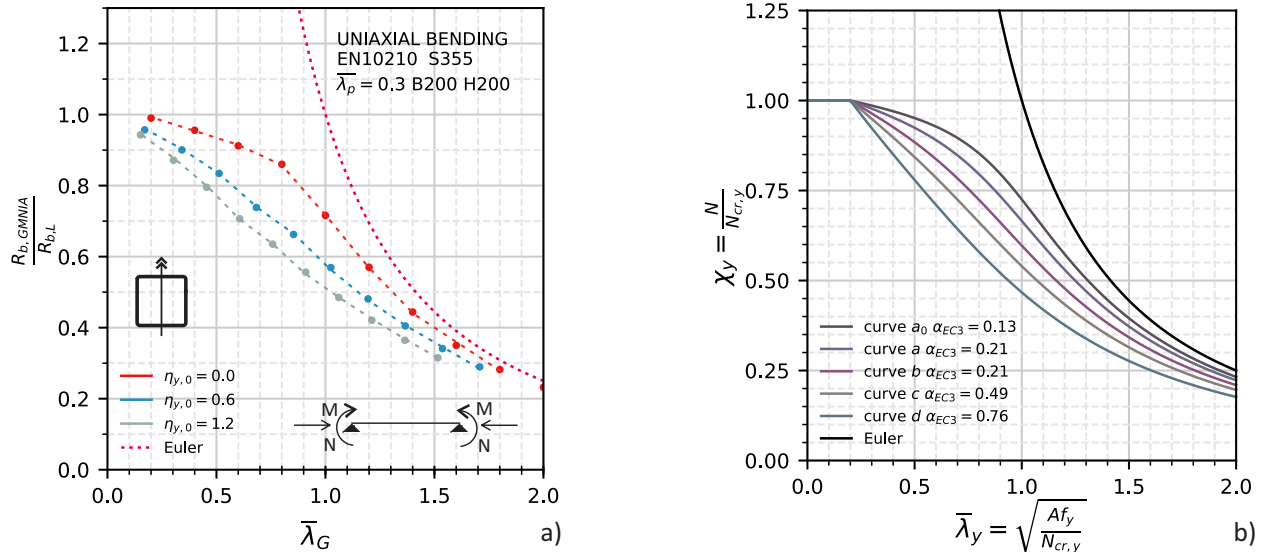


Fig. 7.1. a) GMNIA results of pure compression with uniaxial bending on a SHS; b) EC3 buckling curves.

Figure 7.1a shows some relevant GMNIA results from the numerical study on SHS and RHS member with different level of applied bending moment and compression on the same

column. The GMNIA points confirm the Ayrton-Perry approach and curve formulation. The numerical results with equal level of bending moment η_y lie in the same ideal curve, which appears to be very similar to the Ayrton-Perry curves. This intuitive fact will be demonstrated in the next section with a formal derivation of the Ayrton-Perry curves for global buckling.

7.3 Derivation of the GSRM design formulae for global buckling of beam-columns

The following derivation for beam-columns is based on and makes use of the the Ayrton-Perry derivation for the column described in 3.5. A linear cross-sectional failure criterion is used, in combination with a normalized representation of the *global imperfections* of the load eccentricity represented by the bending moment. Initially discounting the imperfection effect (which will be reintroduced later), the bending moment eccentricity M_y/N can be normalized by the section core width, as is defined in equation (7.6). This is similar to equation (3.16) in section 3.5.1, where η_{imp} is a normalization of e_0 by the section core width. Taking into account also the preceding step of the determination of the cross-sectional capacity, and introducing the assumption that the linear failure surface of any surface can be described with sufficient accuracy (for the intended purpose) as being parallel to the elastic, first-yield failure surface in the $m_y - m_z - n$ diagram), the compression resistance and the bending moment resistance in y (in-plane bending) are a function of χ_L (7.9) (7.10).

$$N_L = \chi_L A f_y \quad (7.9)$$

$$M_{y,L} = \chi_L W_{y,el} f_y \quad (7.10)$$

Thereby, η_y may be rewritten in equation (7.11).

$$\eta_y = \frac{\frac{M_y}{N}}{\overline{N}_L} \quad (7.11)$$

Figure 7.2 shows that the behaviour of a beam-column member on global buckling without imperfection is comparable to the column buckling behaviour with imperfections by using

the relative eccentricity η_y .

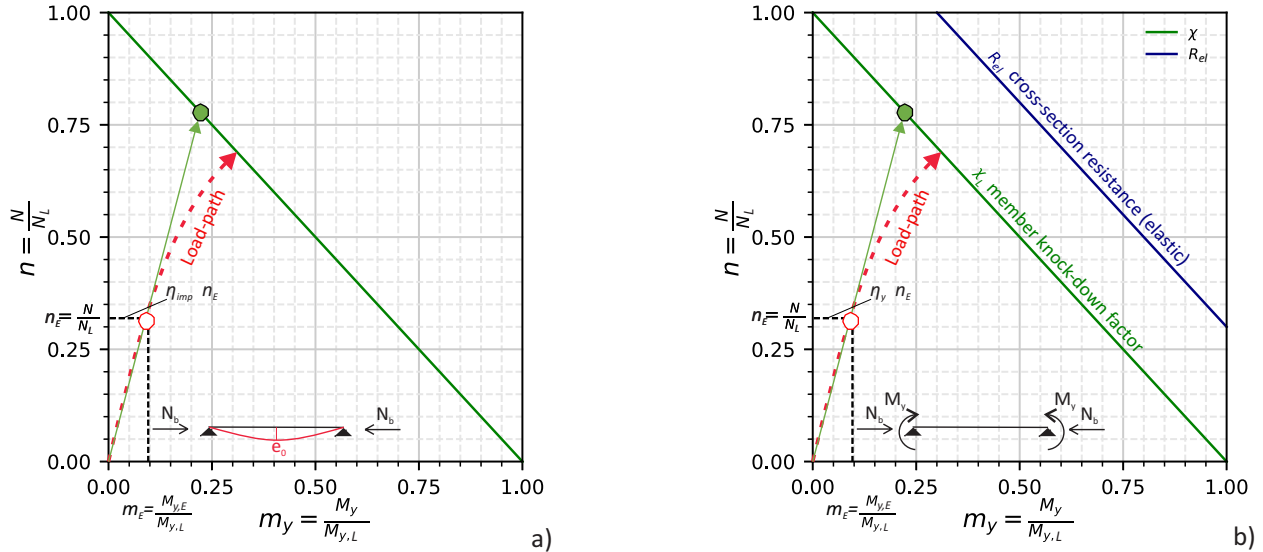


Fig. 7.2. Equivalence of an imperfection effect in a column a) and bending effect in a beam-column b).

In figure 7.2 the beam-column behaviour for in-plane bending is represented in terms of normalized bending moment m_y and normalised compression n , as was seen in the analysis of the representation formats in section 3.5. Introducing equation (7.9) and (7.10), the normalised applied loads read:

$$m_{y,E} = \frac{M_{y,E}}{M_{y,L}} \quad (7.12)$$

$$n_E = \frac{N_E}{N_L} \quad (7.13)$$

The $m_{y,el} - n$ format is introduced, similarly to the normalised $m_{y,pl} - n$, by dividing the applied bending moment $M_{y,E}$ by $M_{y,el}$. Equation (7.14) shows the function of elastic resistance in this format.

$$n_{el} = 1 - m_{y,el} \quad (7.14)$$

Under the assumption described for equations (7.9) and (7.10), in the $m_{y,E} - n_E$ diagram equation (7.14) yields:

$$R_L n_E = 1 - R_L m_{y,E} \quad (7.15)$$

Moving terms and introducing η_y results in (7.16)

$$R_L = \frac{1}{n_E \left(1 + \frac{m_{y,E}}{n_E}\right)} = \frac{1}{n_E (1 + \eta_y)} \quad (7.16)$$

R_L may be rewritten as

$$R_L = \frac{1}{n_E c_0} \quad (7.17)$$

$$\text{where } c_0 = (1 + \eta_y) \quad (7.18)$$

Since the formulation of the critical load R_{cr} of a SHS/RHS member subjected to flexural buckling the effects of lateral torsional buckling can be neglected, it follows:

$$R_L = \frac{N_{cr}}{N_E} \quad (7.19)$$

A new definition of relative slenderness $\bar{\lambda}_y^*$ is introduced in (7.21) as opposed to the classic (7.20).

$$\bar{\lambda}_y = \sqrt{\frac{Af_y}{N_{cr,y}}} \quad (7.20)$$

$$\bar{\lambda}_y^* = \sqrt{\frac{N_L}{N_{cr,y}}} = \sqrt{\frac{\chi_L Af_y}{N_{cr,y}}} \quad (7.21)$$

$$\bar{\lambda}_G = \sqrt{\frac{R_{b,L}}{R_{cr,G}}} \quad (7.22)$$

Equation (7.22) rewrites the slenderness in a more generalised format. $R_{b,L}$ is the cross-section capacity and $R_{cr,G}$ is the critical load for flexural buckling. $R_{cr,G}$ includes more than one global buckling mode in y and z direction, but the rules for global buckling are here derived for the in-plane bending case around the y-axis, i.e. the mode referred to as FB_{y-y} . Thus, $R_{cr,G}$ is rewritten in equation (7.23). By introducing $\bar{\lambda}_y^*$ in the $\bar{\lambda}_G$ definition and after

few algebraic steps equation (7.24) is obtained.

$$R_{cr,G} = \frac{N_{cr}}{N_E} = \frac{\frac{N_{cr}}{N_L}}{\frac{N_E}{N_L}} = \frac{1}{n_E \bar{\lambda}_y^{*2}} \quad (7.23)$$

$$\bar{\lambda}_G = \frac{\bar{\lambda}_y^*}{\sqrt{c_0}} \quad (7.24)$$

Similarly to the slenderness, the definition of the global buckling resistance $R_{b,G}$ in the GSRM is given in equation (7.25), where $R_{b,G}$ is the global buckling resistance and R_L is the cross-section resistance. χ_{y,η_y} in (7.26) is the buckling reduction factor for the axial force (compression) component of the cross-sectional strength obtained by the Ayrton-Perry formulation, which considers again the non-linear elastic second-order load path displayed in figure 2.2. Equation (7.27) follows from (7.25) and (7.26).

$$\chi_G = \frac{R_{b,G}}{R_L} \quad (7.25)$$

$$\chi_{y,\eta_y} = \frac{N_b}{N_L} \quad (7.26)$$

$$\chi_G = \frac{R_{b,G}}{R_L} = \chi_{y,\eta_y} c_0 \quad (7.27)$$

The derivation of the global buckling formulae for the GSRM starts with the derivation of χ_{y,η_y} , and is similar to the derivation of $\chi_{y,EC3}$ in section 3.5.1, adding however terms to account for the effect of the external (first-order) bending moments. The limit-state equation (2.21) in the quadratic format can be transformed into the formula in (7.28) by introducing N_L and differentiating the applied first order bending moment M_b^I from the bending moment caused by the imperfection eccentricity $N_b e_0$. After few algebraic steps and by introducing $\bar{\lambda}_y^*$ and η_{imp} , equation (7.30) to the limit-state is obtained in the final form.

$$\frac{N_b}{N_L} + \frac{M_{y,b}^I + N_b e_0}{W_y f_y} \cdot \frac{1}{1 - \frac{N_b}{N_{cr}}} = 1.0 \quad (7.28)$$

$$\text{where } M_{y,b}^I = N_b \eta_y \quad (7.29)$$

$$\chi_{y,\eta_y} + (\eta_y + \eta_{imp}) \cdot \frac{\chi_{y,\eta_y}}{1 - \chi_{y,\eta_y} \bar{\lambda}_y^{*2}} = 1.0 \quad (7.30)$$

$$\text{where } \eta_{imp} = \frac{N_L e_0}{M_{y,L}} \quad (7.31)$$

Equation (7.30) leads to the well-known solution shown in (7.32) and (7.33).

$$\chi_{y,\eta_y} = \frac{1}{\phi_y + \sqrt{\phi_y^2 - \bar{\lambda}_y^{*2}}} \quad (7.32)$$

$$\text{with } \phi_y = \frac{1}{2} \left(1 + \eta_{imp} + \eta_y + \bar{\lambda}_y^{*2} \right) \quad (7.33)$$

The format of the GSR method uses global slenderness $\bar{\lambda}_G$ and global resistance χ_G . Applying the results in (7.22) and (7.25) equation (7.32) is thus rewritten as

$$\chi_G = \frac{1}{\phi_G + \sqrt{\phi_G^2 - \beta_{LG} \bar{\lambda}_G^2}} \quad (7.34)$$

$$\phi_G = \frac{1}{2} \left(\beta_{LG} (1 + \eta_{imp} + \eta_y) + \bar{\lambda}_G^2 \right) \quad (7.35)$$

$$\text{with } \beta_{LG} = \frac{1}{c_0} \quad (7.36)$$

The approach of Rondal and Maquoi [65] is also utilised for the calibration of η_{imp} (7.37) in the column buckling curves, introducing the same parameters α_{EC3} from the Eurocode formulation and $\bar{\lambda}_G$.

$$\eta_{imp} = \alpha_{EC3} (\bar{\lambda}_G \sqrt{c_0} - 0.2) \quad (7.37)$$

7.4 Calibration of the parameters of the Ayrton-Perry formula

In the last section the effects of global buckling were presented accounting only for the elastic behaviour of the SHS and RHS members. As was conducted in other recent studies (see [74, 75]), in this section the interaction between local and global buckling will be analysed in detail, expanding the formulation obtained so far. In the elastic analysis of the previous section the geometric non-linearities are accounted for only as long as they are small, and material non-linearities are included only partially and with unreliable accuracy, through the chosen cross-sectional resistance surface. In particular, the derivation does not include effects caused by the deterioration of stiffness once yielding sets on in the outermost fibres. Accordingly, in order to account for the typical effects of the SHS and RHS cross-sections,

additional parameters were added in the GSRM framework. This is relevant and necessary for all sections that reach a higher cross-sectional capacity than the one given by a first-yield criterion, i.e. for all cases where $\chi_L > 1$. Thus, a new term ξ_{LG} was introduced to account for the effects of the cross-section in the plastic range ($\chi_L > 1$). It may be interpreted as a reduction of the originally valid cross-sectional capacity surface, leading to the use of a new, “transition” surface for these cases. The procedure is schematically shown in figure 7.3 for the in-plane beam-column buckling case. As can be seen in the figure, the linear approximation of the cross-sectional resistance (represented by “ $N_L - M_{y,L}$ ” as well as χ_L) is reduced to a new transition surface in the bent red line load path, so that in the original space the limit for the achievable axial force is now given by equation (7.38).

$$\frac{N}{\text{”}N_L\text{”}} = \frac{1}{\xi_{LG}} \quad (7.38)$$

The numerical parametric study has shown that it is indeed necessary to account for this effect in stocky sections. For the representation of the transition behaviour it was chosen to define the term ξ_{LG} as a linear function of the generalised global slenderness $\bar{\lambda}_G$, with an additional factor ρ to act as a calibration factor for different types of section. Equation (7.39) expresses ξ_{LG} in the GSRM format.

$$1.0 \leq \xi_{LG} = 1 + (\chi_L - 1) \rho \bar{\lambda}_G \leq \chi_L \quad (7.39)$$

For SHS and RHS, it was found that the effect could be limited to a transition from the plastic range to the elastic range; this is represented by limiting ξ_{LG} by χ_L . With the added term ξ_{LG} , the Ayrton-Perry’s quadratic equation is modified and results into equation (7.40) with solution shown in equations (7.41) and (7.42).

$$\xi_{LG} \chi_{y,\eta_0} + (\eta_y + \eta_{imp}) \cdot \frac{\xi_{LG} \chi_{y,\eta_0}}{1 - \chi_{y,\eta_0} \bar{\lambda}_y^2} = 1.0 \quad (7.40)$$

$$\chi_G = \frac{1}{\phi_G + \sqrt{\phi_G^2 - \beta_{LG} \bar{\lambda}_G^2}} \quad (7.41)$$

$$\phi_G = \frac{1}{2} \left(\beta_{LG} (1 + \eta_{imp} + \eta_y) + \bar{\lambda}_G^2 \right) \quad (7.42)$$

$$\text{with } \beta_{LG} = \frac{\xi_{LG}}{c_0} \quad (7.43)$$

For the spatial case, i.e. for compression and biaxial buckling of SHS and RHS beam-columns, two paths of buckling are considered as possible buckling modes, corresponding to the two axes of bending, as in figure 7.3. The “in-plane” case treated in the previous section is one of the two possible paths for flexural buckling and is defined as $FB_{y,y}$ for bending about the major axis. The equation is only modified to account for the simultaneous presence of a weak-axis bending moment. Similarly, the basic equation (i.e. the failure criterion) for the out-of-plane buckling case is very similar to the in-plane case, provided that the out-of-plane (weak-axis) flexural buckling slenderness is considered. The resulting limit state equation is shown in (7.44).

$$\xi_{LG}\chi_{z,\eta_0} + (\eta_z + \eta_{imp}) \cdot \frac{\xi_{LG}\chi_{z,\eta_0}}{1 - \chi_{z,\eta_0}\bar{\lambda}_z^2} + \xi_{LG}\eta_y\chi_{z,\eta_0} = 1.0 \quad (7.44)$$

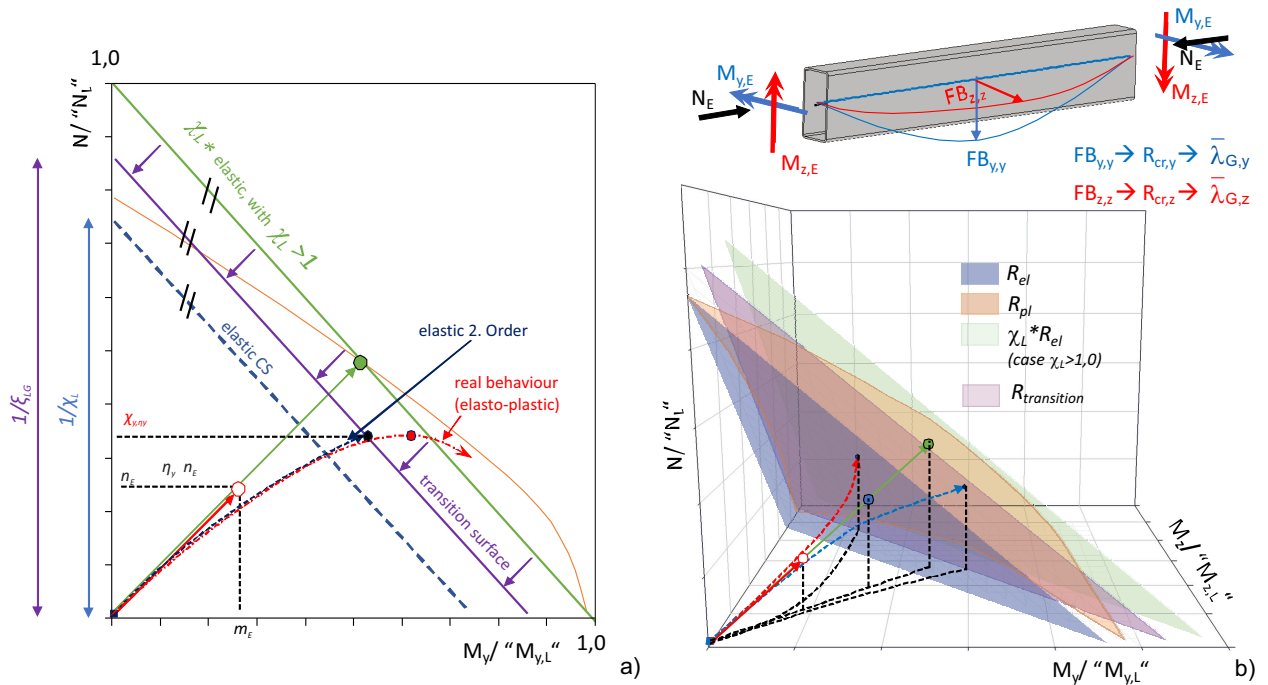


Fig. 7.3. a) Representation of the “transitional behaviour” for beam-columns with elasto-plastic, stocky sections in the $n - m_y$ space and b) in the $n - m_y - m_z$ space.

The accuracy of this calibration factor may be assessed by comparing the accuracy of the GSRM prediction and the GMNIA results of the parametric study on global buckling, described in section 5.3. The GMNIA results shall be represented in the GSRM format. Thereby, the ratio $R_{b,GMNIA}/(R_{el}\chi_L)$ is compared to the GSRM- χ_G from above.

As is illustrated in figure 7.4, the behaviour of the GMNIA results is consistently described by the GSRM formulation. 7.4a shows a class 1 SHS subjected to in-plane loading, with three different eccentricity levels and a uniform bending moment diagram. The points represent the GMNIA results while the curve shows the corresponding buckling curve according to the developed and calibrated GSRM. In sub-plot b, similar results for a class 3 SHS subjected to in-plane loading are shown. For the in-plane case, the combined accuracy of χ_G and χ_L generally leads to quite precise results. The conservatism is more pronounced for HSS cold-formed sections, where the EC3 imposes $\alpha_{EC3} = 0.49$.

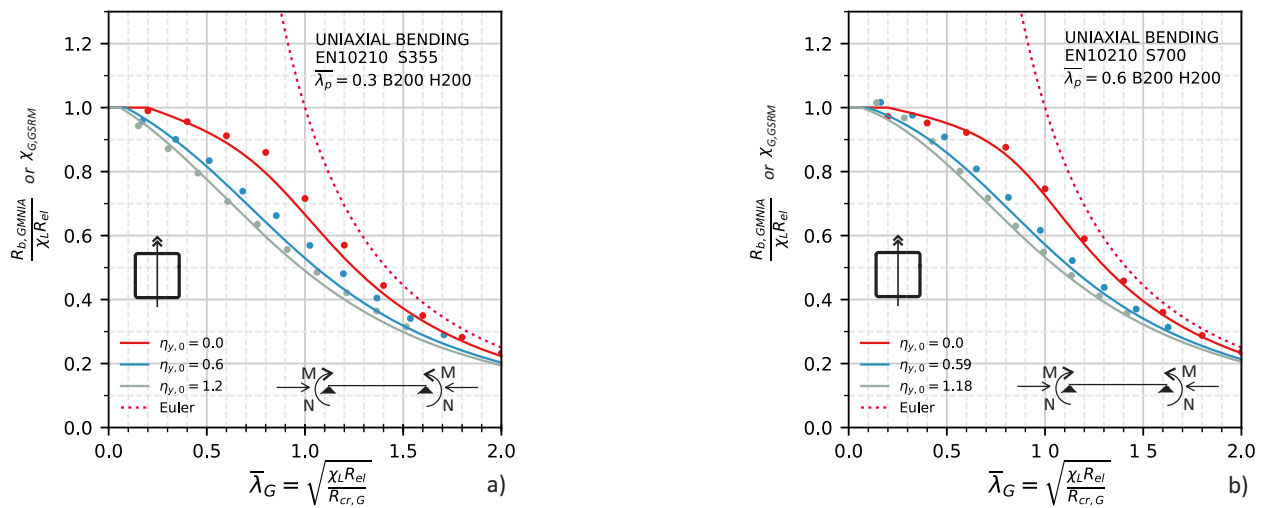


Fig. 7.4. Comparison of GMNIA results (dots) and calibrated GSRM predictions (continuous lines) for various levels of eccentricity and hot-finished SHS with various plate thickness values; a) plate slenderness $\lambda_p = 0.3$ (class 1 section); b) $\lambda_p = 0.6$ (class 3 section).

Through calibration and the selection of satisfactorily safe and accurate strength predictions, the following values of ρ were selected:

- $\rho = 0.6$ for hot-finished section
- $\rho = 0.5$ for cold-formed sections

The calibration of the GSRM parameters also produced accurate and satisfactorily safe-sided results for RHS, both for the in-plane and out-of-plane cases. A few exemplary cases are illustrated in figure 7.5. In sub-plot b), the effect of the local buckling conservatism is eliminated from the representation by using a slightly different format of χ_G as defined in equation (7.45). In this case, the value of the each GMNIA result is divided by the value of the shortest member of the corresponding load case, and it can be noticed that the rather

high conservatism of the GSRM predictions of the value in the global case of figure 24 a) is mostly due to the predicted value of the cross-section capacity, which happens to be quite conservative (by around 20%) for this particular cross-section.

$$\chi_G = \frac{R_{b,GMNIA}}{R_{b,GMNIA,SHORT}} \quad (7.45)$$

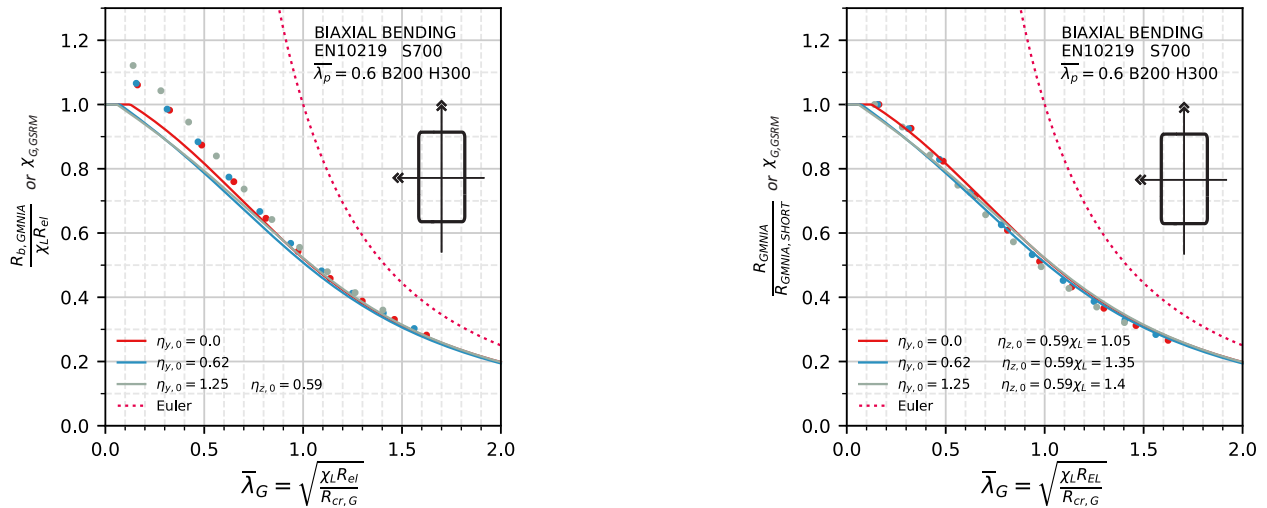


Fig. 7.5. Class 3-4 RHS subjected to biaxial bending. In a) the traditional representation of the GMNIA results in the GSRM format is shown; b) shows the results without the effects of the cross-section conservatism of χ_L .

Finally, the last parameter that needed to be introduced for a more general implementation of the method accounts for the cases where the bending moment is not constant along the member length. In the extensive parametric study several combinations of the bending moment diagrams along the member length were applied, and a bending moment factor C_m was introduced, in correspondence with the common use in Eurocode 3. This is shown by example in the following. In 7.6a, the GMNIA results for the application of an exemplary non-constant, linear bending moment diagram are plotted in the GSRM format. In an attempt to diverge as little as possible from established EC3 design rules, the existing formulae and tables for C_m were adapted, leading to the use of $C_{m,y}$ for this particular case. A schematic overview of the resulting accuracy for an SHS section and various levels of bending is given in the figure. Figure 7.6b contains the proposed values for some simple bending moment cases. The final version of the global buckling calibrated formulation includes coefficients $C_{m,y}$ and $C_{m,z}$, taken from EN1993-1-1, to account for the effects of the different

bending moment diagrams in both directions. They enter the formulae by directly reducing the maximum value of the bending moment along the member. In equation 7.46 and 7.48 the final versions of the GSRM formula for global buckling are given with the adoption of all calibration factors, such as ρ , $\xi_{LG,y}$, $\xi_{LG,z}$, $\beta_{LG,y}$, $\beta_{LG,z}$, $\eta_{EC3,y}$, $\eta_{EC3,z}$, $C_{m,y}$ and $C_{m,z}$.

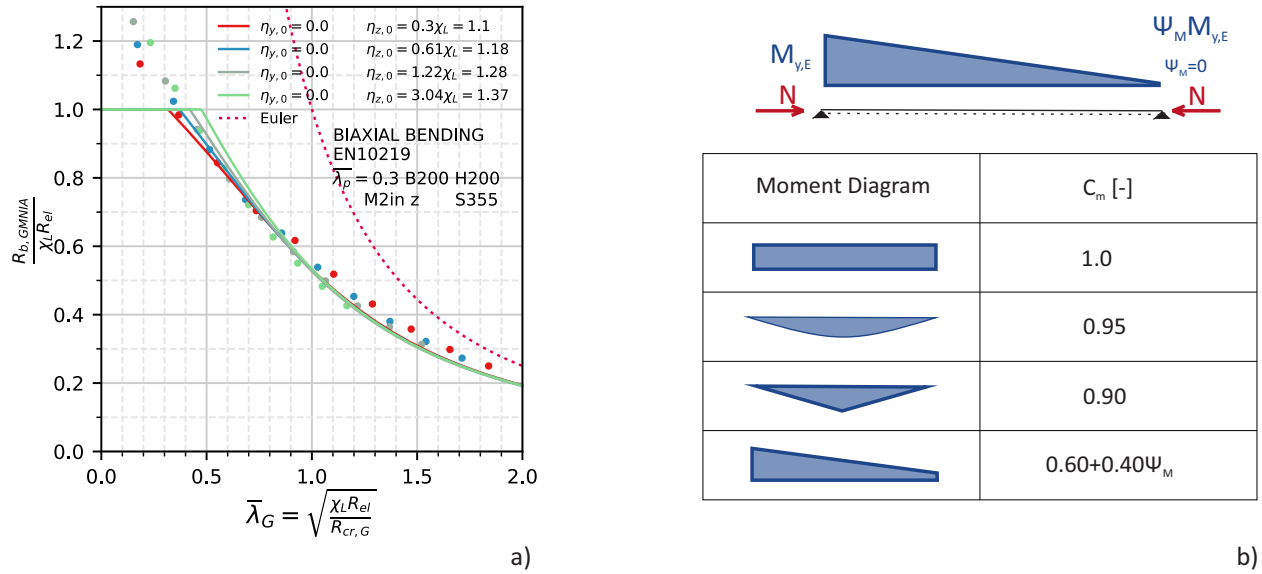


Fig. 7.6. In a) class 1 SHS subjected to in-plane linear bending moment (M_2) over the length; in b) an overview of the evaluated applied bending moment and a schematic representation of the ψ_M factor.

$$\chi_{G,y} = \frac{1}{\phi_{G,y} + \sqrt{\phi_{G,y}^2 - \beta_{LG,y} \bar{\lambda}_{G,y}^2}} \leq 1.0 \quad (7.46)$$

$$\phi_{G,y} = \frac{1}{2} \left(\beta_{LG,y} (1 + \eta_{EC3,y} + \eta_y C_{m,y} + \eta_z C_{m,z}) + \bar{\lambda}_{G,y}^2 \right) \quad (7.47)$$

$$\chi_{G,z} = \frac{1}{\phi_{G,z} + \sqrt{\phi_{G,z}^2 - \beta_{LG,z} (1 + \eta_y C_{m,y}) \bar{\lambda}_{G,z}^2}} \leq 1.0 \quad (7.48)$$

$$\phi_{G,z} = \frac{1}{2} \left(\beta_{LG,z} (1 + \eta_{EC3,z} + \eta_z C_{m,z} + \eta_z C_{m,z}) + \bar{\lambda}_{G,z}^2 \right) \quad (7.49)$$

7.5 Validation and verification with current test standards

An overview of the results of the parametric study is necessary in order to validate the GSRM formulation with respects to accuracy and safety, as well as to compare and verify the efficiency of the method with the current European design standard. A much larger set of points is used in the following, representative results, which will be grouped for members of equal flexural buckling slenderness about the weak axis $\bar{\lambda}_Z$, where:

$$\bar{\lambda}_Z = \sqrt{\frac{Af_y}{N_{cr,Z}}} \quad (7.50)$$

The chosen representation format is the so-called box plot format, which allows a graphical evaluation of the statistical parameters in the plot. A box in red colour is used to represent the area that contains 50% of the data for a certain slenderness, while the whiskers show the 5% upper and lower bound of the data, and the “outliers” beyond this range are shown as small black points. In figure 7.7a and b, the results of the GMNIA numerical campaign on global buckling with constant bending moment along the member length are divided by the strength prediction of the new GSRM formulation. The corresponding scatter bands are shown for a) cold-formed sections and b) hot-finished sections. The scatter is higher for cold-formed sections, reaching consistently about the same resistance of the GSRM prediction with the 5% lower bound and 25% higher results with the 5% upper bound. Hot-finished sections instead behave differently on the upper bound of the result distribution, with a maximum of 20% of higher resistance for $\bar{\lambda}_Z = 1.2$. Similar but slightly lower scatter is found in figure 7.7c and d for both cold-formed and hot-finished sections, where the ratio between the GSRM prediction over EC3 design value is shown. In general, the GSRM results are fairly above the EC3 predictions except few points located in low slenderness range for the cold-formed sections, where also the effect of the cross-section capacity is higher and the prediction of the GSRM at a local level is on purpose lower than the Eurocode. On hot-finished sections low predictions of the GSRM are uniformly distributed and the 5% lower bound of the GSRM consistently lies on 97% of the Eurocode prediction. In figure 7.7e and f, the GMNIA results of non-constant bending moment diagrams are shown. Both cold-formed and hot-finished sections demonstrate a higher scatter, owing to the diversity of the diagrams of the applied bending moments. Nevertheless, the GSRM still predicts

the GMNIA resistance fairly consistently over the slenderness and with sufficient accuracy. Table 7.1 shows an overview of the mean values and standard deviation of both cases.

Sub-plot	Mean	Standard De- viation
Figure 7.7a	1.092	0.074
Figure 7.7b	1.067	0.51
Figure 7.7c	1.079	0.069
Figure 7.7d	1.054	0.071
Figure 7.7e	1.164	0.129
Figure 7.7f	1.159	0.141

Table 7.1: *Overview of the tested cross-sections.*

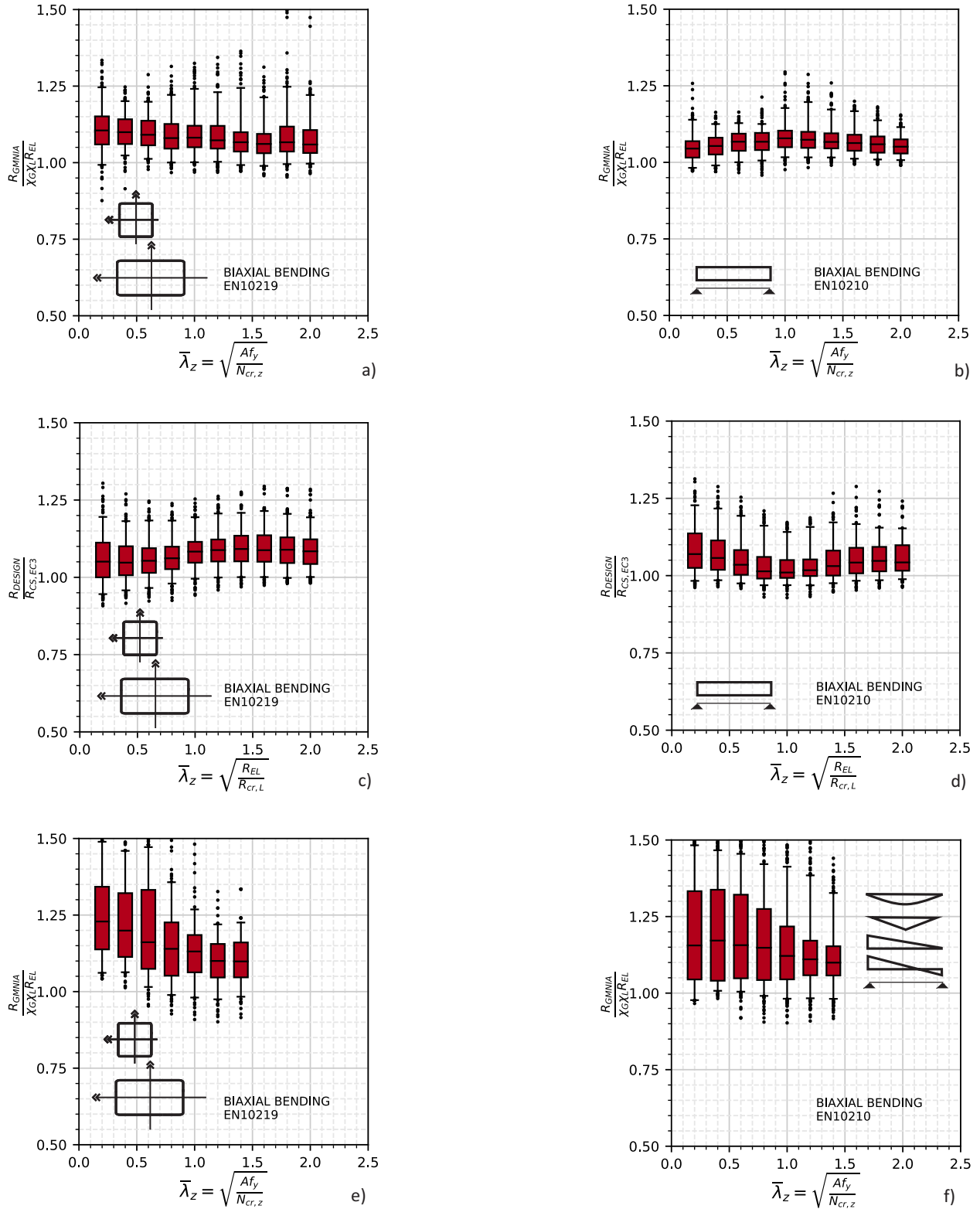


Fig. 7.7. Comparison of results through box plots; a) and b): GMNIA vs GSRM, compression and biaxial uniform bending; c) and d): GSRM vs EC3 rules, biaxial uniform bending; e) and f): GMNIA vs GSRM, compression and various bending moment diagrams.

7.6 Reliability aspects, partial factors

As was already said in the previous chapter for the GSRM design rules for local buckling, a detailed assessment of the reliability level and the necessary values of the partial factors of safety (γ_{Mi} in Eurocode terminology) was not the focus of this thesis. It shall only be mentioned that the derived formulations for the GSRM for global buckling were shown to have a consistent level of reliability and a partial factor of $\gamma_{M1} = 1.0$ could be accepted, see [73].

7.7 Summary of the GSRM design rules for member buckling

In chapter 7 the GSRM design formulations for global buckling was described. Section 7.2 introduced the Ayrton-Perry and Eurocodes formulation, in section 7.2 GSRM design formulae for global buckling of beam-columns were derived. New parameters were introduced, in order to calibrate the new formulae against the numerical test campaign. Finally, a verification and comparison with the current standard was conducted, showing the advantages and improvements of the GSRM rules. Figure 7.8 represents schematically the developed design rules for SHS and RHS members.

Proposals for global buckling – RHS /SHS											
COMMON SYMBOLS FOR ALL BUCKLING DIRECTIONS											
	$M_{y,E,max} \frac{M_{z,E,max}}{M_{el,z}} \frac{M_{y,E,max}}{M_{el,y}} \frac{M_{z,E,max}}{M_{el,z}} ; \eta_z = \frac{N_E}{N_{el}} \frac{M_{z,E,max}}{M_{el,z}}$ $\eta_y = \frac{N_E}{N_{el}} \frac{M_{y,E,max}}{M_{el,y}} ; \eta_z = \frac{N_E}{N_{el}} \frac{M_{z,E,max}}{M_{el,z}}$ $c_0 = 1 + \eta_y + \eta_z$										
$R_{b,L} = \chi_L R_{el}$ $\alpha_{EC3} = 0,21$ (hot-finished, S235 to S420) $\alpha_{EC3} = 0,13$ (hot-finished, S460 and higher) $\alpha_{EC3} = 0,49$ (cold-formed) // 0,34 for S460 and higher	$M_{el,y} = W_{el,y} f_y$ $M_{el,z} = W_{el,z} f_y$ $N_{el} = A f_y$										
ξ_{LG} : for $\chi_L \leq 1,0$: $\xi_{LG} = 1$ for $\chi_L > 1,0$: $\xi_{LG} = 1 + (\chi_L - 1) \cdot \rho \cdot \bar{\lambda}_{G,y} \cdot C_m \leq \chi_L$ with $\rho = 0,5$ for cold-formed; $\rho = 0,6$ for hot-finished sections $\beta_{LG} = \frac{\xi_{LG}}{c_0}$	<table border="1"> <thead> <tr> <th>Moment diagram</th> <th>C_m</th> </tr> </thead> <tbody> <tr> <td></td> <td>1.0</td> </tr> <tr> <td></td> <td>0.95</td> </tr> <tr> <td></td> <td>0.9</td> </tr> <tr> <td>M</td> <td>$\psi_{y,M}$</td> </tr> </tbody> </table>	Moment diagram	C_m		1.0		0.95		0.9	M	$\psi_{y,M}$
Moment diagram	C_m										
	1.0										
	0.95										
	0.9										
M	$\psi_{y,M}$										
FB-y-y: 2nd order effect mostly in z-direction	FB-z-z: 2nd order effect mostly in y-direction										
$N_{cr,y} = \frac{\pi^2 E I_y}{L^2}$ $R_{cr,y} = \frac{N_{cr,y}}{N_E}$ $\bar{\lambda}_{G,y} = \sqrt{\frac{R_{b,L,min}}{R_{cr,y}}}$ $\beta_{LG,y} = \frac{\xi_{LG,y}}{c_0}$ with $\xi_{LG,y}$: for $\chi_L \leq 1,0$: $\xi_{LG,y} = 1$ for $\chi_L > 1,0$: $\xi_{LG,y} = 1 + (\chi_L - 1) \cdot \rho \cdot \bar{\lambda}_{G,y} \cdot C_{my} \leq \chi_L$ $\chi_{G,y} = \frac{1}{\Phi_{G,y} + \sqrt{\Phi_{G,y}^2 - \beta_{LG,y} \cdot \bar{\lambda}_{G,y}^2}} \leq 1,0$ $\Phi_{G,y} = \frac{1}{2} \left[\beta_{LG,y} (1 + \eta_z C_{m,z} + \eta_y C_{m,y} + \eta_{EC3,y}) + \bar{\lambda}_{G,y}^2 \right]$ $\eta_{EC3,y} = \alpha_{EC3} (\bar{\lambda}_{G,y} \sqrt{c_0 - 0,2})$	$N_{cr,z} = \frac{\pi^2 E I_z}{L^2}$ $R_{cr,z} = \frac{N_{cr,z}}{N_E}$ $\bar{\lambda}_{G,z} = \sqrt{\frac{R_{b,L,min}}{R_{cr,z}}}$ $\beta_{LG,z} = \frac{\xi_{LG,z}}{c_0}$ with $\xi_{LG,z}$: for $\chi_L \leq 1,0$: $\xi_{LG,z} = 1$ for $\chi_L > 1,0$: $\xi_{LG,z} = 1 + (\chi_L - 1) \cdot \rho \cdot \bar{\lambda}_{G,z} \cdot C_{mz} \leq \chi_L$ $\chi_{G,z} = \frac{1}{\Phi_{G,z} + \sqrt{\Phi_{G,z}^2 - \beta_{LG,z} (1 + \eta_y C_{m,y}) \bar{\lambda}_{G,z}^2}} \leq 1,0$ $\Phi_{G,z} = \frac{1}{2} \left[\beta_{LG,z} (1 + \eta_z C_{m,z} + \eta_y C_{m,y} + \eta_{EC3,z}) + \bar{\lambda}_{G,z}^2 \right]$ $\eta_{EC3,z} = \alpha_{EC3} (\bar{\lambda}_{G,z} \sqrt{c_0 - 0,2})$										
$\chi_G = \min(\chi_{G,y}; \chi_{G,z})$ $R_{p,G+L} = \chi_G \cdot \chi_L \cdot R_{el}$											

Fig. 7.8. GSRM design rules for global buckling, as given in [76].

Chapter 8

Further work on the GSRM

A brief summary of the previous chapter topics shows in this paragraph the chosen structure of the presented work and may easily introduce the necessary steps for further work on the GSRM. Chapter 3 described the approach and methodology of the GSRM. The format of the design is only the last step in a methodology work-flow, where the experimental tests were designed in order to provide sufficient data for the creation of an accurate and robust FEM-model. The GMNIA results of a large experimental and numerical campaign described in 4 served as database for the derivation of mechanically-sound analytical formulae, and were used to calibrate the design formulae in the GSRM format (chapters 6 and 7). Thus, a similar approach is carried on for polygonal cross-sections, which were described in chapter 4, but were not analysed in detail for the development of a GMNIA model and for the development of predictive formulae calibrated on the results of a numerical campaign. Section 8.1 presents a GMNIA model calibrated on the basis of the experimental tests and a parametric study for the analysis of the cross-section behaviour of the polygonal sections. Section 8.2 proposes a new and different approach for SHS and RHS, which is purely numerical and based on machine learning techniques, and compares it with the GSRM in terms of accuracy and reliability.

8.1 Initial numerical study on polygonal sections

The validation of a GMNIA-MEAS model for hexagonal sections was conducted in chapter 4, providing results for SHS, SHS-S, SHS-T and hexagonal sections. The validated GMNIA-MEAS models had to be simplified with regards to the modelling of imperfections and

material laws. Thus, a more generalized model, with a simplified definition of the material law and the geometrical imperfections, yet the same FEM mesh size and element types as the ones validated through the calibration to the experimental tests, was developed similarly to the GMNIA model developed for the other cross-sections. Figure 8.1 shows the first main assumption for the imperfection shape of the GMNIA model. This shape is derived from a linear buckling analysis (LBA), to which a scaling factor is applied. The type of the buckling shape is local and distortional, since the first buckling mode can occur at both levels, affecting a single plate in case of local buckling or contiguous plates in case of distortional. The choice of the imperfection is defined in equation (8.1) as the maximum between both buckling modes.

$$\max\left(\frac{B}{400}; 0.1\sqrt{D_e t}\right) \quad (8.1)$$

$\frac{B}{400}$ is the amplitude for local buckling, as was found all plated sections in the SHS/RHS numerical campaign; $0.1\sqrt{D_e t}$ corresponds to the imperfection amplitude for distortional buckling [54]. The latter formulation is derived from the analysis of circular hollow sections (CHS), where D is the outer diameter, corresponding to the polygon circumcircle diameter. In polygonal sections, the distortional buckling effect is more pronounced with an increasing number cross-section sides. As the number of sides becomes smaller, the effect of distortional buckling becomes larger and approximate better CHS, in terms of geometry and behaviour. Different buckling types, local and distortional, are shown in figure 8.1a with the LBA shape of two different polygonal sections subjected to different applied load combinations. Figure 8.1b shows the analysed cross-sections in the parametric study and compares them graphically. Figure 8.1c introduces graphically the material model assumption chosen for the steel sections, the same models for cold-formed and hot-finished steels described in chapter 3. Detailed information regarding the GMNIA-MEAS predictions can be found in the Appendix.

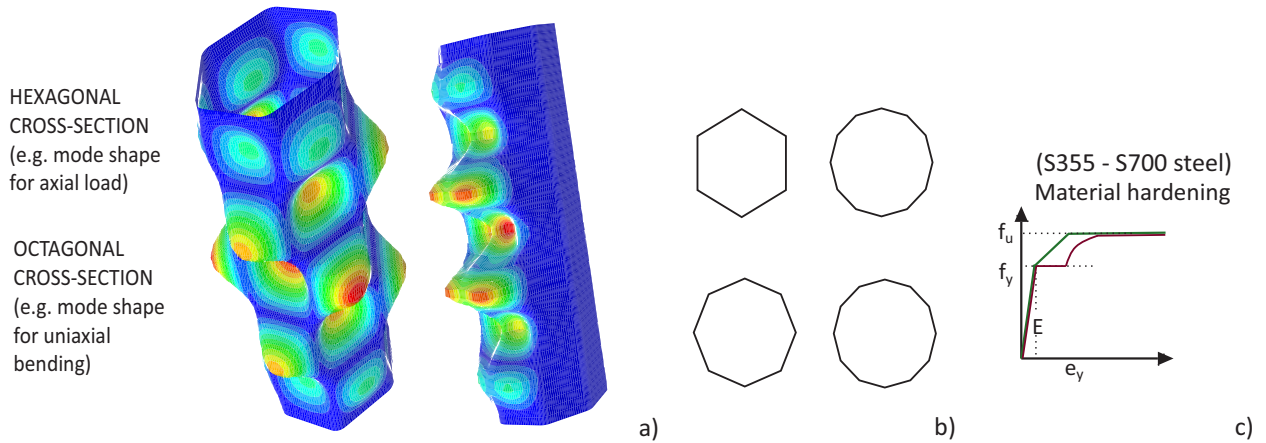


Fig. 8.1. LBA shape for the numerical input of the imperfections; b) cross-sections applied in the parametric study; c) schematic representation of the material model.

With these calibrated, equivalent input parameters for the GMNIA, a numerical parametric study was conducted. An overview of the parameters for the numerical test campaign is given in table 8.1, where the parameters were defined as in section 5.3.

Parameter	Variable number	Range
Thickness [mm]	7	0.5 - 12.0
L/L_{cr}	2	0.1 - 0.15
Steel Grade	2	S355 - S700
ϕ_y [°]	3	0 - 45 - 90
ϕ_z [°]	0	-
D [mm]	1	100
Manufacturing standard	1	EN10219

Table 8.1: Parameters of the parametric study on local buckling expressed in terms of number of used variables for each parameters and range of application.

More than 600 numerical simulations (GMNIA+LBA) were conducted and were used as the database for the development of the deep learning models and the GSRM design rules. In figure 8.2 the results of the parametric study are represented. Sub-plot 8.2a illustrates the results, differentiated by section, showing each section with a different colour and ranging

the side number from 6 to 20. The scatter is homogeneous along the slenderness and the different sections spread uniformly in the plot. Sub-plot 8.2b shows the three analysed load cases, demonstrating a clear path for both the pure compression case $\phi = 0$ and pure bending $\phi = 90$ around the y-axis. For the case of combined compression and bending the scatter increases considerably, but a descending pattern for these results is still discernible. The results are remarkably unaffected by the geometrical properties of the section. For the

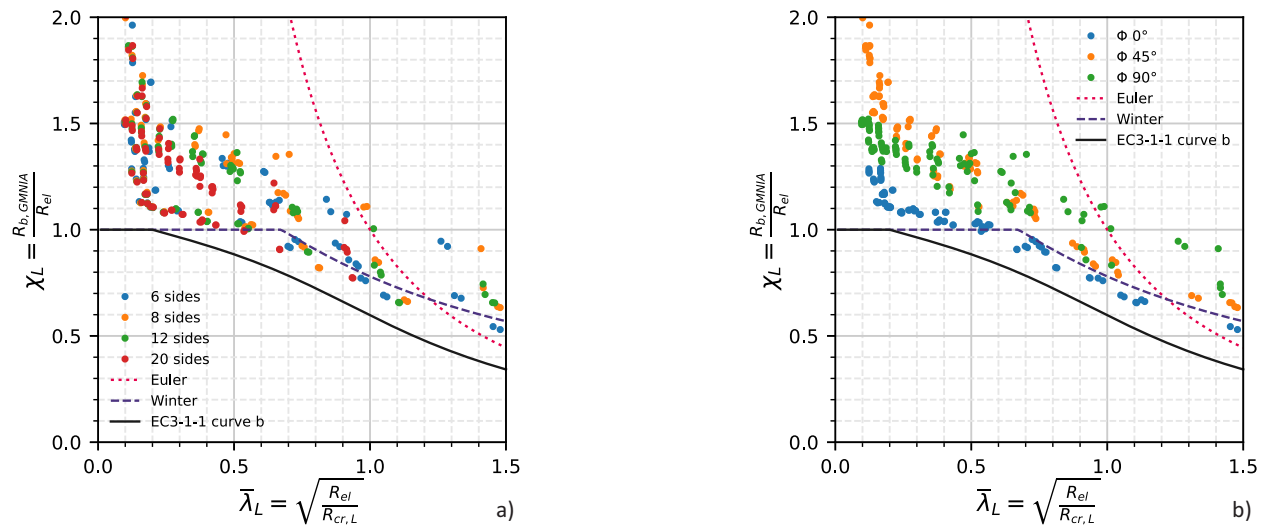


Fig. 8.2. Results of the parametric study on polygonal sections; sub-plot a) highlights the sections, and b) the load-cases of pure compression, pure bending and combined compression and bending

cases of pure compression and pure bending the scatter of the results is low and a clear pattern is shown. The GMNIA points lie respectively below and above the Winter-curve, which is consistent with the results for SHS and RHS sections. The consistency and the overall low scatter of the results divided into load cases is ought to the choice of the GSRM representation. In general, these first results are encouraging, since they fit into the GSRM design format of the Winter curve for the elastic range and show similar behaviour in the stocky range, when compared to SHS and RHS. A possible design proposal may account for a larger number of sections, with uneven side numbers, and more input parameter. Finding a general design rule, which accounts for all effects of local buckling and all polygonal sections, appears to be a feasible task.

8.2 AI-based design formulae

The latest approach to mention, which received in recent years increasingly attention in all engineering fields, is machine learning, and its most developed techniques defined by the general term of deep learning [77]. Machine Learning (ML) is a subgroup of algorithms belonging to Artificial Intelligence (AI), which enables systems to learn from given data and not just to execute or make actions, commands or decisions by explicit programming. DL initially was a subgroup of ML dealing with Artificial Neural Nets (ANN). Deep learning uses so-called artificial neural networks to recognize patterns and highly non-linear relationships in data, providing a series of non-linear functions fitted to the input data, called *train set*. The Deep Neural Network (DNN) is "trained" on the train set, learn with complex algorithm in a very efficient way to minimise the error between the DNN predictions and the data set. After the training the DNN is applied to a new *test set*, to verify the prediction accuracy. This kind of approach falls into the category of curve fitting formats, described in section 3.5.

Different DNN architectures were tested, and here only the results of one DNN architecture, which minimizes the mean square root of the error between local buckling GMNIA results and predictions, will be presented. A prefixed architecture with one input layer of 24 dimensions (features from the FEM study), 5 dense hidden deep layers with dimensionality of 150 nodes each and 1 output layer (ultimate load amplification factor) of dimension 1 was chosen. This type of structure is defined as dense (all nodes of consecutive layers are connected), and all nodes share the same activation function type, for this case *tanh* was chosen. For the training, the mean-squared-error (MSE) loss function was used together with a L2-norm regulariser with scaling factor $\lambda = 10^{-5}$ on the parameters of the DNN to avoid overfitting. In figure 8.3 the predictions of the DNN model are shown and compared to the GSRM predictions. The gains in accuracy are extremely high, when compared to every developed method for the prediction of SHS and RHS resistance. The higher accuracy of the predictions – measured through the standard deviation of the data – is in general one order of magnitude greater than the previously described GSRM results. Figure 8.3a shows very low scatter over the whole slenderness ranges, and extremely high accuracy. The average values and the standard deviation values are very similar, with differences between the classes of 0.1%. Most importantly, the consistency of the results is valid throughout every Eurocode class and slenderness range, even though in the DNN model inputs there was no data describing the mechanical behaviour of the numerical results (e.g. Winter function,

slenderness, elastic bifurcation load, etc.), as the model entirely relied on basic geometrical and material input data. Even though the GSRM predictions in 8.3b are more accurate than the Eurocode, they show larger scatter than the DNN results and a less uniform distribution along the slenderness.

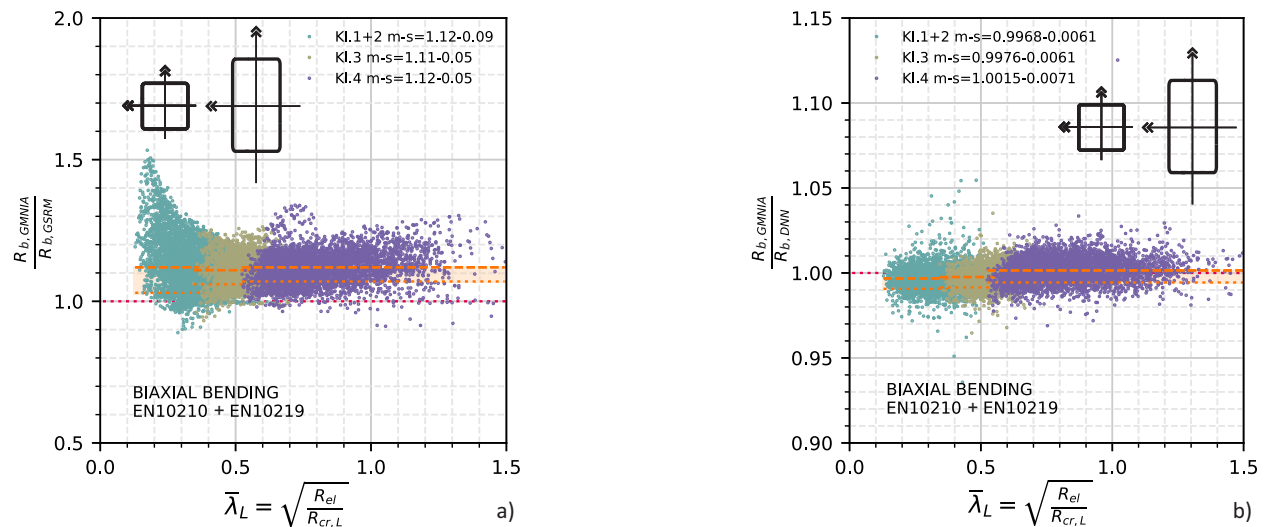


Fig. 8.3. a) GMNIA results on local buckling normalized by the GSRM predictions, and by the b) DNN predictions.

This study represents only a first step, which shows the potential of the DNN architectures, which demonstrate better results and very fast implementation. These methods are not new, machine learning and curve fitting methods were continuously applied in various fields of engineering for decades, but the developments of developer friendly libraries (such as Tensorflow) and increasing processor capacity made DNN a very handy solution for problems with a large database, providing robust algorithms and rapidly decreasing implementation time. This positive note on DNN shall also put emphasis on the recommendation to use these methods with extreme caution. The lack of a mechanical background for the development of these methods may result into non-physical result predictions, which may decrease the assessed safety. For this reason extensive research is recommended for the development of any method based on DNN or ML.

Chapter 9

Summary, conclusions and outlook

9.1 Summary and conclusions

Current steel design codes are based on methods for the determination of the cross-section and member resistance, that are not always sufficiently efficient or accurate. The effective section method for the prediction of the resistance of slender sections is robust, but complicated by several calculation steps and is made less efficient, since it does not analyse the overall cross-section resistance, but considers the plate-by plate resistance. The Eurocode 3 provides robust and efficient rules for member buckling, based on the Ayrton-Perry approach, but the interaction of the member resistance with the local buckling effects is neglected. The primary objective of this thesis was therefore to develop a more rational and efficient design method for SHS and RHS sections and members, while maintaining the consistency with the Eurocode approach. This method was termed the "Generalised Slenderness-based Resistance Method" - GSRM. As the name implies, it is a method that formulates resistance as a functions of a more general definition of slenderness. Where it was possible, similar representation formats to the Eurocode were used, and the Ayrton-Perry and Winter representation formats respectively for members and sections were adopted.

The process of developing the proposed design method involved:

- reviewing existing design rules and current design methods for local buckling and global buckling.
- conducting an extensive experimental test campaign.
- validating and calibrating numerical models reproducing the experimental test results by focussing on key input parameters.
- creating an equivalent FEM-model for the generation of a large numerical dataset.
- developing design rules on the basis of the GSRM representation format.

These steps are described in detail in the thesis, which is organized in nine chapters and 3 Appendices. Chapter 1 contains the motivation and scope of the thesis and identifies the publications that already resulted from the work carried out in the thesis project. It is followed, in Chapter 2, by a review of the current state of the art in the design of sections against local and global buckling in general, with a focus on hollow sections respectively on the phenomena that most affect this type of section. Chapter 3 describes the general methodology used in this thesis, in particular with regards to the considered, existing design approaches (used as starting points for own developments), the experimental tests conducted by the author of this thesis at the laboratory of Bundeswehr University Munich, the FEM modelling and the used analytical approaches. In Chapter 4, the experimental campaign and its use as the basis for the validation and verification of advanced numerical models is described. The numerical campaign made possible by these numerical models is then described in detail Chapter 5. Chapter 6 and 7 contain the key developments of the thesis: the new GSRM formulations for local and global buckling, respectively, with their background and validation. Some initial work on the expansion of the field of application of the GSRM is presented in Chapter 8. Finally, Chapter 9 contains a summary and conclusions derived from this thesis work. The Appendices contain further information on the physical tests and the numerical analyses, including a sample input file.

The following conclusions can be drawn from the work presented in this thesis:

1. The GSRM is able to capture some key aspects of the buckling resistance of hollow sections that are not covered in a straightforward manner by other design rules. This includes the fact that a cross-section level slenderness is far better able to describe the susceptibility to local buckling than plate-by-plate methods as currently used e.g. in the Eurocode. Furthermore, the method can accurately take into account the fact that the buckling strength is actually continuous over slenderness, as opposed to behaving distinctly in the three ranges described by the Eurocode cross-sections classes 1, 2, 3 and 4. Both of these aspects lead to predictions of the buckling strength that are far more consistent and generally more economical than traditional approaches. Finally, in the case of global buckling phenomena, the method's ability to capture the precise onset of the first yielding and include this point in the design methodology leads to advantages in accuracy and consistency also in the case of member buckling.
2. At the same time, the development of new design rules carried out in this thesis demonstrated that traditional formulations, such as the Winter curves for plate buckling and the Ayrton-Perry approach for members, can be fruitfully used as the basis for design also in newer concepts, such as the GSRM. This is inherent in the mechanical background of the method, but could be demonstrated quite effectively in the calibrations carried out for the development of the GSRM.
3. More generally, the work carried out in this thesis has shown both the continuous relevance of carrying out extensive physical test campaigns to understand buckling phenomena, while nevertheless demonstrating the accuracy that can be achieved through advanced numerical analyses, provided that one has insight in the material used and can represent the specimens' true geometry. Huge advances are currently taking place in this field, so that it can be foreseen that advanced, non-linear numerical analysis will take on increasing significance in practice as well in the near future.

9.2 Outlook on future work

The GSRM has the potential for new and more general GSRM design rules to be developed in the future. A similar investigation conducted for hollow sections may be done for open cross-section, including also torsion and lateral torsional buckling effects in the experimental and numerical models. New, robust and more efficient GSRM design rules could be easily developed, thanks to the methodology described in this thesis and implemented during the HOLLOSSTAB project. Rules for Circular Hollow Sections (CHS) were also developed during the project [78]. Other sections, such as sections with grooves and polygonal sections, were analysed in this thesis and described for promising future studies. A new course of studies could be developed by focusing on open sections. The promising results of the GSRM for this thesis could be applicable also for torsion-prone cross-sections, where lateral torsional buckling plays an important role. The approach in this case should be tailored to the specific sections: one aspect of the GSRM which could significantly change is the role of the Linear Buckling Analysis (LBA), with regard to the determination of the critical buckling load and imperfection shape. In fact, new buckling eigenmodes could be introduced, such as distortional buckling and lateral torsional buckling at a global level, impacting significantly the outcome of the analysis. Completing this necessary set of rules for a broad set of sections could provide the background for a future implementation in the Eurocodes, possibly integrating the method with other set of rules, such as the CSM design rules.

Another promising research area could be the implementation of the GSRM rules, while accounting for the rotation capacity of the sections. The present thesis did not focus on describing the rotation capacity of SHS and RHS. Integrating this parameter, both in the numerical analysis and design curves could open up new applications, especially in the stocky range, where plastic redistributions are possible. Further studies could bring to the implementation of these rules into finite elements. In this thesis, a direct relation between slenderness and cross-section and member resistance was found, and could be applied in a fast and more efficient FEM model, combining GMNIA and GSRM design checks. Furthermore, if the rotation capacity could be assessed as a function of the GSRM slenderness and implemented as a parameter in a finite element, new GSRM-based numerical models could be developed, improving significantly the design efficiency.

If new methods could be explored, certainly machine learning techniques represent a subject of debate. The recent increase in computation efficiency and the enormous growth of open source material for machine and deep learning techniques, have made the development

of predictive "tools", based on these techniques, quite an easy task. In many areas, researchers produce what could be called "fast-tools", tailored to the given set of data, which predict with exceptional accuracy the target/design data. In the field of structural engineering this could be an enormous advancement in developing predictive methods, such as the GSRM, but it is currently hindered by the lack of precise assessment of the reliability of these machine learning techniques. Unfortunately, these techniques, especially deep learning, which is mostly used in AI and in more complex problems, work in many as a "black-box". Convergence to the desired minima points is not generally guaranteed, and thus the reliability of the results is hindered in terms of safety assessment. This should not stop the research for structural engineers in this area, but should direct the efforts towards feasible solutions, which account for possible application such as the Eurocodes.

References

1. *Eurocode 3: Design of steel structures - Part 1-1: General rules and rules for buildings* Standard EN 1993-1-1 (CEN – European Committee for Standardization, Brussels, 2005).
2. Taras, A., Toffolon, A., Niko, I., Gardner, L., Meng, X., Camotim, D., Silvestre, N., Goncalves, R., Bureau, A., Beyer, A. & Dehan, V. *Innovative buckling design rules for structural hollow sections* Deliverable 9.1 (HOLLOSSTAB, RFCS Grant No. 2015-709892, Munich, 2019).
3. Szalai, J. & Papp, F. *THEORY AND APPLICATION OF THE GENERAL METHOD OF EUROCODE 3 PART 1-1* in *Proceedings of EUROSTEEL 2011* (Jan. 2011).
4. Tankova, T., Marques, L., Andrade, A. & Simões da Silva, L. A consistent methodology for the out-of-plane buckling resistance of prismatic steel beam-columns. English. *Journal of Constructional Steel Research* **128**, 839–852 (2017).
5. Yu, C. & Schafer, B. W. Distortional Buckling Tests on Cold-Formed Steel Beams. *Journal of Structural Engineering* **132**, 515–528 (2006).
6. Li, Z. & Schafer, B. Application of the finite strip method in cold-formed steel member design. *Journal of Constructional Steel Research* **66**, 971–980 (2010).
7. Moen, C. D. & Schafer, B. W. *Extending Direct Strength Design to Cold-formed Steel Beams with Holes* in *International Specialty Conference on Cold-Formed Steel Structures*. (2010).
8. Moen, C. D. & Schafer, B. W. Direct Strength Method for Design of Cold-Formed Steel Columns with Holes. *Journal of Structural Engineering* **137**, 559–570 (2011).
9. Torabian, S., Zheng, B. & Schafer, B. W. *Development of a New Beam-Column Design Method for Cold-Formed Steel Lipped Channel Members* in *International Specialty Conference on Cold-Formed Steel Structures* (2014).
10. Taras, A. Derivation of DSM-type resistance functions for in-plane global buckling of steel beam-columns. *Journal of Constructional Steel Research* **125**, 95–113 (Oct. 2016).
11. Schafer, B. *Advances in the direct strength method of thin-walled steel design* in *Proceedings of the Eighth International Conference on Thin-Walled Structures* (2018).
12. Schafer, B. W. Advances in the Direct Strength Method of cold-formed steel design. *Thin-Walled Structures* **140**, 533–541 (2019).

13. Gardner, L. The Continuous Strength Method. *Proceedings of The Institution of Civil Engineers-structures and Buildings - PROC INST CIVIL ENG-STRUCT B* **161**, 127–133 (Jan. 2008).
14. Afshan, S. & Gardner, L. The continuous strength method for structural stainless steel design. *Thin-Walled Structures* **68**, 42–49 (2013).
15. Su, M.-N., Young, B. & Gardner, L. The continuous strength method for the design of aluminium alloy structural elements. *Engineering Structures* **122**, 338–348 (2016).
16. Buchanan, C., Gardner, L. & Liew, A. The continuous strength method for the design of circular hollow sections. *Journal of Constructional Steel Research* **118**, 207–216 (2016).
17. Zhao, O., Afshan, S. & Gardner, L. Structural response and continuous strength method design of slender stainless steel cross-sections. *Engineering Structures* **140**, 14–25 (2017).
18. Yun, X., Gardner, L. & Boissonnade, N. The Continuous Strength Method for The Design of Hot-Rolled Steel Cross-Sections. *Engineering Structures* (Jan. 2018).
19. Theofanous, M., Profsert, T., Knobloch, M. & Gardner, L. The continuous strength method for steel cross-section design at elevated temperatures. *Thin-Walled Structures* **98**. Elevated temperature performance of thin-walled structures, 94–102 (2016).
20. Boissonnade, N., Nseir, J. & Saloumi, E. *The Overall Interaction Concept: an Alternative Approach to the Stability and Resistance of Steel Sections and Members* in (Apr. 2013).
21. Boissonnade, N., Hayeck, M., Saloumi, E. & Nseir, J. An Overall Interaction Concept for an alternative approach to steel members design. *Journal of Constructional Steel Research* **135**, 199–212 (2017).
22. Toffolon, A. & Taras, A. Development of an OIC-Type local buckling design approach for cold-formed unstiffened and groove-stiffened hollow sections. *Thin-Walled Structures* **144**, 106266 (2019).
23. Toffolon, A., Meng, X., Taras, A. & Gardner, L. The generalized slenderness-based resistance method for the design of SHS and RHS. *Steel Construction* **12**, 327–341 (2019).

24. Taras, A. & Toffolon, A. Neuartige Bemessungsmethode fuer Hohlprofilquerschnitte und -staebe. *Stahlbau* **89**, 570–584 (2020).
25. Toffolon, A. & Taras, A. *Numerical investigation of the local buckling behaviour of high strength steel circular hollow sections* in *Proceedings of Eurosteel 2017* **1** (2017).
26. Toffolon, A. & Taras, A. *Numerical and Experimental Studies for the Development of Direct Strength Design Rules for Locally* in *Proceedings of SSRC Conference 2018* (2018).
27. Toffolon, A. & Taras, A. *Application of an OIC-type design approach to the buckling design of cold-formed, lip-stiffened hollow sections* in *Proceedings of the International Colloquia on Stability and Ductility of Steel Structures SDSS 2019* (July 2018).
28. Toffolon, A. & Taras, A. *Proposal of a design curve for the overall resistance of cold formed RHS and SHS members* in *Proceedings of Nordic Steel 2019* **3** (2019).
29. Toffolon, A., Müller, A., Niko, I. & Taras, A. *Experimental and numerical analysis of the local and interactive buckling behaviour of hollow sections* in *Proceedings of Nordic Steel 2019* **3** (Sept. 2019).
30. Toffolon, A., Taras, A., Müller, A. & Niko, I. *Experimental and numerical analysis of the local and interactive buckling behaviour of hollow sections* in *Proceedings of the International Colloquia on Stability and Ductility of Steel Structures SDSS 2019* (Sept. 2019).
31. Toffolon, A. & Taras, A. *Proposal of a design curve for the overall resistance of cold formed RHS and SHS members* in *Proceedings of the International Colloquia on Stability and Ductility of Steel Structures SDSS 2019* (Sept. 2019).
32. Toffolon, A., Niko, I. & Taras, A. *FEM-based design of hollow sections against local, global and interactive buckling – model verification and calibration against physical tests* in *Proceedings of the 17th International Symposium on Tubular Structures* (Dec. 2019).
33. Toffolon, A. & Taras, A. *Proposal of generalized slenderness-based resistance curves for the local and interactive buckling of rectangular hollow sections* in *Proceedings of the 17th International Symposium on Tubular Structures* (Dec. 2019).
34. Toffolon, A. & Taras, A. *New formulations for the cross-sectional strength of high-strength steel rectangular and square hollow sections using a Generalized Slenderness-Strength Method* in *Proceedings of SSRC 2020* (Apr. 2020).

35. Taras, A. & Toffolon, A. *Development of a generalized slenderness-based resistance method for the design of high-strength steel hollow section beam-columns* in *Proceedings of SSRC 2020* (Apr. 2020).
36. Timoshenko, S. & Gere, J. M. *Theory of elastic stability*. (McGraw-Hill International Book Company, New York, 1985).
37. Von Kármán, T., Sechler, E. E. & Donnell, L. The strength of thin plates in compression. *Transactions of the American Society of Mechanical Engineers* **11**, 53–57 (1932).
38. Winter, G. Strength of thin steel plates compression flanges. *Transactions of the American Society of Mechanical Engineers* **112**, 527–554 (1946).
39. Winter, G. *Theoretical solutions and test results* in *8th Congress International Association for Bridge and Structural Engineering* (Cornell, 1968), 101–112.
40. *Eurocode 3: Design of steel structures - Part 1-5: General rules - Plated structural elements* Standard EN 1993-1-5 (CEN – European Committee for Standardization, Brussels, 2006).
41. Ayrton, W. & Perry, J. On Struts. *The Engineer* **62**, 464–465, 513–515 (1886).
42. Robertson, A. The Strength of Struts. *The Institution of Civil Engineers - Selected Engineering Papers* **28** (1925).
43. Timoshenko, S. & Lessels, I. *Festigkeitslehre* German (Springer, Berlin, 1928).
44. Merchant, W. The Failure Load of Rigidly Jointed Frameworks as Influenced by Stability. *Structural Engineer* **32**, 185–190 (1954).
45. Lindner, J. Näherungen für die Europäischen Knickspannungskurven. *die Bautechnik* **10**, 344–347 (1978).
46. Murzewski, J. Joint probability of elastic and plastic instability modes. *Proc. of the Regional Coll. on Stability of Steel Structures*, 249–268 (1977).
47. Unger, B. Ein Konzept zur Berechnung der Traglast von biegedrillknickgefährdeten Stäben unter Berücksichtigung des Einflusses geometrischer und werkstofflicher Imperfektionen. *der Stahlbau* **46**, 329–338 (Nov. 1977).
48. Bjorhovde, R. *Deterministic and probabilistic approaches to the strength of steel columns* dissertation (Fritz Laboratory Reports., 1972).

49. Galambos, T. *Stability Design Criteria for Metal Structures* English (Wiley and Sons, New York, 1998).
50. Ziemian, R. D. *GUIDE TO STABILITY DESIGN CRITERIA FOR METAL STRUCTURES* English (Wiley and Sons, New York, 2010).
51. *ANSI/AISC: Specification for Structural Steel Buildings* Standard ANSI/AISC 360-16 (American Institute of Steel Construction, Chicago, IL, 2016).
52. *Eurocode 3: Design of steel structures - Part 1-1: General rules and rules for buildings* Standard prEN1993-1-1:2020 (CEN – European Committee for Standardization, Brussels, 2018).
53. Greiner, R., Kettler, M., Lechner, A., Freytag, B., Linder, J., Jaspert, J.-P., Boissonnade, N., Bortolotti, E., Weynand, K., Ziller, C. & Oerder, R. *Final Report: SEMI-COMP: Plastic Member Capacity of Semi-Compact Steel Sections - a more Economic Design. 2008* English (., 2008).
54. Meng, X., Toffolon, A., Gardner, L. & Taras, A. The generalised slenderness-based resistance method for the design of CHS and EHS. *Steel Construction* **12**, 342–353 (2019).
55. Yun, X. & Gardner, L. The continuous strength method for the design of cold-formed steel non-slender tubular cross-sections. *Engineering Structures* **175**, 549–564 (Nov. 2018).
56. Gardner, L. & Yun, X. Description of stress-strain curves for cold-formed steels. *Construction and Building Materials* **189**, 527–538 (Nov. 2018).
57. Yun, X. & Gardner, L. Stress-strain curves for hot-rolled steels. *Journal of Constructional Steel Research* **133**, 36–46 (June 2017).
58. Ramberg, W. & Osgood, W. R. Description of stress-strain curves by three parameters. *Technical Note No. 902, National Advisory Committee for Aeronautics* (1943).
59. Schafer, B. Review: The Direct Strength Method of cold-formed steel member design. *Journal of Constructional Steel Research* **64**, 766–778 (July 2008).
60. *AISI: North American Specification for the Design of Cold-Formed Steel Structural Members* Standard AISI S100-16 (American Iron and Steel Institute, Washington, D.C., 2016).

61. Li, Z. & Schafer, B. W. *Buckling analysis of cold-formed steel members with general boundary conditions using CUFSM: conventional and constrained finite strip methods* in *Proc. 20th Int'l Spec Conf Cold-Form. Steel Struct. St Louis MO* (Nov. 2010).
62. Carl Zeiss Optotechnik GmbH. *Zeiss colin3D* Neubeuern, 2017.
63. Dassault Systèmes, Simulia Corporation. *Abaqus* version 2016. United States, 2016.
64. Taras, A., Toffolon, A., Niko, I., Gardner, L., Meng, X. & Silvestre, N. *Cross-sectional resistance and local buckling of RHS & SHS, HOLLOSSTAB* Deliverable 4.2 (HOLLOSSTAB, RFCS Grant No. 2015-709892, Munich, 2019).
65. Ayrton, W. & Perry, J. Formulations d'Ayrton-Perry pour le Flambement des Barres Métalliques. *Construction Metallique* **4**, 41 –53 (1979).
66. Hancock, G. J., Kwon, Y. B. & Bernard], E. S. Strength design curves for thin-walled sections undergoing distortional buckling. *Journal of Constructional Steel Research* **31**, 169 –186 (1994).
67. *Metallic materials — Tensile testing Part 1: Method of test at room temperature* Standard EN ISO 6892-1:2016 (CEN – European Committee for Standardization, Brussels, 2016).
68. Zhao, W.-B. *Behaviour and design of cold-formed steel hollow flange sections under axial compression* PhD thesis (Queensland University of Technology, 2006).
69. 3D Systems Inc. *Geomagic Design X - Geomagic Control X* Rock Hill, South Carolina, United States, 2017.
70. Rusch, A. & Lindner, J. Überprüfung der grenz (b/t)-Werte für das Verfahren Elastisch-Plastisch. *Stahlbau* **70**, 857–868 (2001).
71. *EN10219: Cold formed welded structural hollow sections of non-alloy and fine grain steels* Standard (CEN – European Committee for Standardization, Brussels, 2006).
72. *EN10210: Hot finished structural hollow sections of non-alloy and fine grain steels* Standard (CEN – European Committee for Standardization, Brussels, 2006).
73. Beyer, A., Bureau, A., Taras, A. & Toffolon, A. *Reliability Analysis of the Design Proposals and Determination of Partial Factors, HOLLOSSTAB* Deliverable 7.2 (HOLLOSSTAB, RFCS Grant No. 2015-709892, Munich, 2019).

74. Knobloch, M., Fontana, M. & Frangi, A. *On the Interaction of Global and Local Buckling of Square Hollow Sections* in *Proceedings of the Fifth International Conference on Coupled Instabilities in Metal Structures. 1* (2008).
75. Degee, H., Detzel, A. & Kuhlmann, U. Interaction of global and local buckling in welded RHS compression members. *Journal of Constructional Steel Research - J CONSTR STEEL RES* **64**, 755–765 (July 2008).
76. Taras, A., Toffolon, A., Niko, I., Gardner, L., Meng, X. & Silvestre, N. *Cross-sectional resistance and local buckling of RHS & SHS, HOLLOSSTAB* Deliverable 8.2 (HOLLOSSTAB, RFCS Grant No. 2015-709892, Munich, 2019).
77. Goodfellow, I., Bengio, Y. & Courville, A. *Deep Learning* (MIT Press, 2016).
78. Meng, X., Gardner, L., Toffolon, A. & Taras, A. *Background on the development of Overall-Slenderness based design rules for CHS and EHS, HOLLOSSTAB* Deliverable 8.3 (HOLLOSSTAB, RFCS Grant No. 2015-709892, Munich, 2019).

Appendix A

Key facts and deliverables of the RFCS-Project HOLLOSSTAB

Project overview table

Title	Overall-Slenderness Based Direct Design for Strength and Stability of Innovative Hollow Sections
Research Fund	Research Fund for Coal and Steel - RFCS
Category of research	Steel
Technical group	TGS8
Grant agreement no.	RFCS-2015-709892
Project Partners	<ol style="list-style-type: none"> 1) Universität der Bundeswehr München, “UniBW”, Germany 2) Imperial College of Science Technology and Medicine, “ICL”, United Kingdom 3) Instituto Superior Técnico, “IST”, Portugal 4) European Convention for Constructional Steelwork, “ECCS”, Belgium 5) Centre Technique Industriel de la Constr. Metallique, “CTICM”, France 6) CONDESA SA, “Condesa”, Spain 7) Université Laval, “ULaval”, Canada
Total Budget	1.74 millions
Commencement date	1 July 2016
Completion date	30 June 2019

Deliverables

No.	Title	Date completed/ submitted
D1.1	Meetings, Workplans, Correspondence	Y3Q4
D2.1	Document containing current market trends	Y1Q4
D2.2	Document describing the benchmark cases	Y2Q1
D2.3	Benchmark cases	Y3Q4
D3.1	Re-examine tests data on CHS	Y2Q3
D3.2	Full Reporting of “numerical test” results - CHS	Y3Q3
D3.3	Procurement / Delivery of test specimens - CHS	Y1Q4
D4.1	Re-examine test data on RHS/SHS	Y2Q3
D4.2	Full Reporting of “numerical test” results - RHS/SHS	Y3Q3
D4.3	Procurement / Delivery of test specimens - RHS/SHS	Y1Q4
D5.1	Reporting of re-examined experimental data - Beam-columns	Y2Q3
D5.2	Full Reporting of “numerical test” results - Beam-columns	Y3Q3
D5.3	Procurement / Delivery of test specimens - beam-columns	Y1Q4
D6.1	Report on elastic buckling of SHS and RHS	Y2Q3
D6.2	Report on elastic buckling of CHS and EHS	Y3Q4
D6.3	Report on elastic buckling of RPHS	Y2Q3
D7.1	Report on statistical data	Y3Q4
D7.2	Report on the safety evaluation	Y3Q4
D8.1	Guidelines for development of strength curves	Y2Q3
D8.2	Report on proposals for SHS/RHS	Y3Q4
D8.3	Report on proposals for CHS/EHS	Y3Q4
D8.4	Report on Software tools	Y3Q4
D9.1	Design Guidelines and Background Doc.	Y3Q4
D9.2	Final Workshop	Y3Q4
	Final Report	Y3Q4

Appendix B

Selected test results

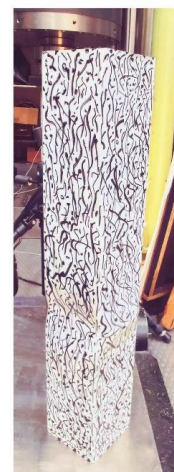
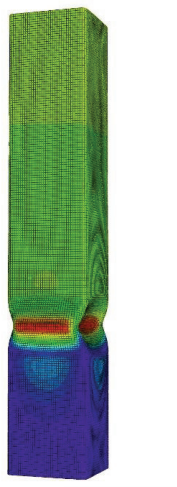
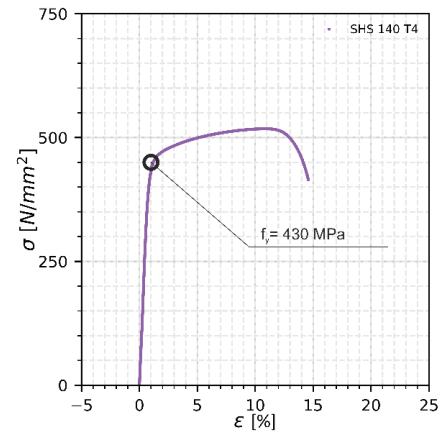
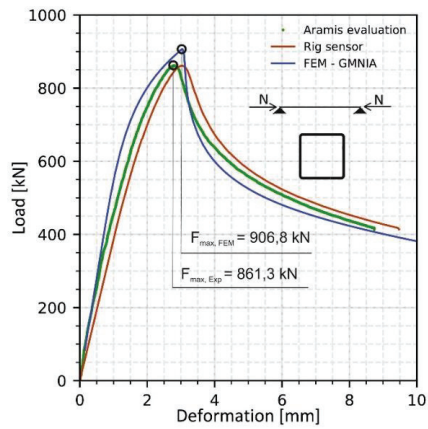
Test No. T1-1

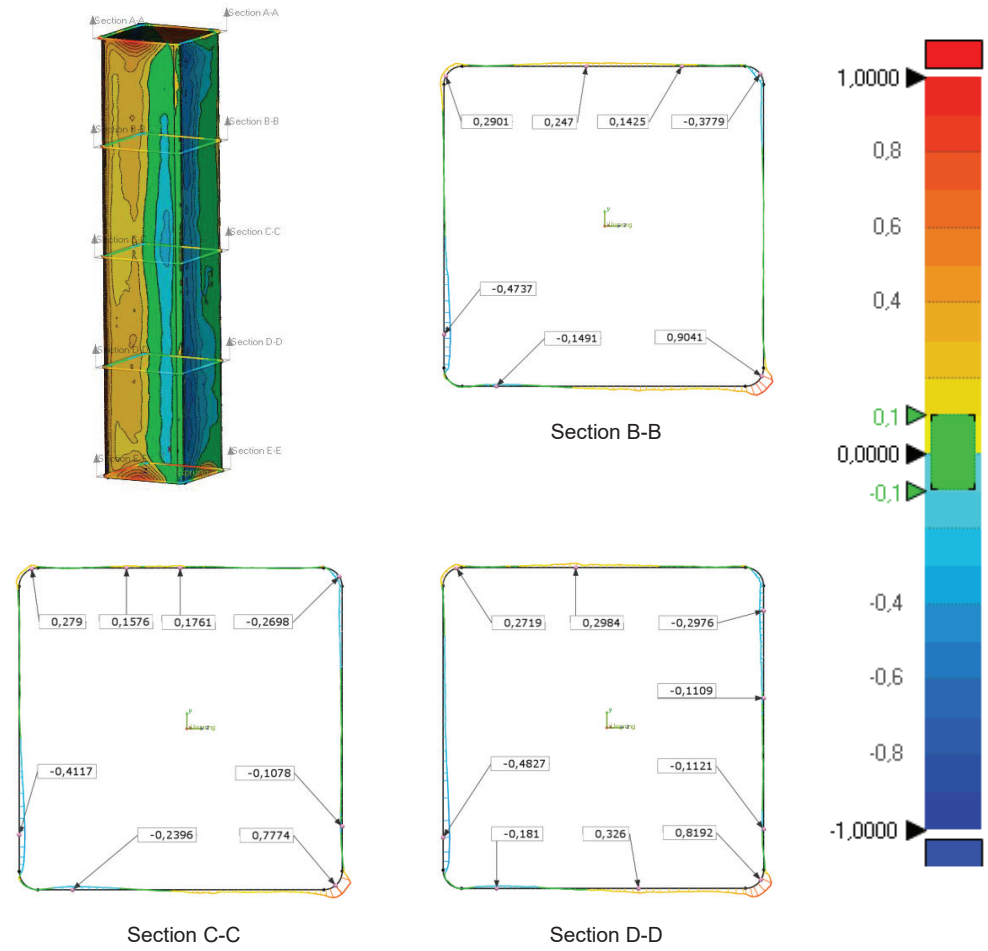
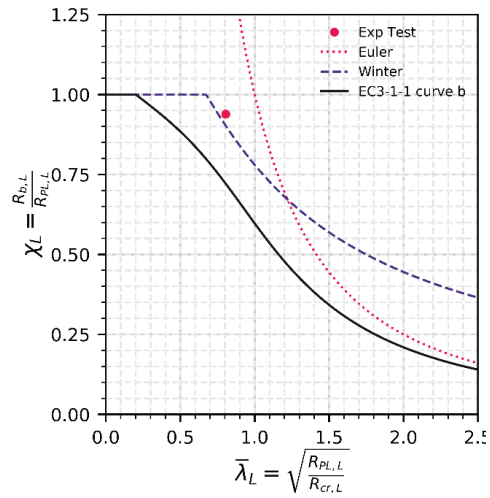
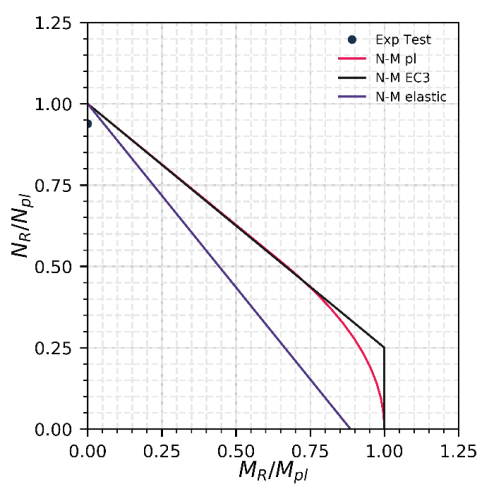
SHS 140/140/4.0

S355 - EN10219

Test type T1

e = 0 mm

t_{MEAS} = 4.0 mmF_{Max, Exp} = 861,3 kNF_{Max, FEM} = 906,8 kN



Test T2-1

SHS 140/140/4.0

S355 - EN10219

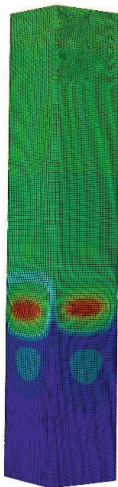
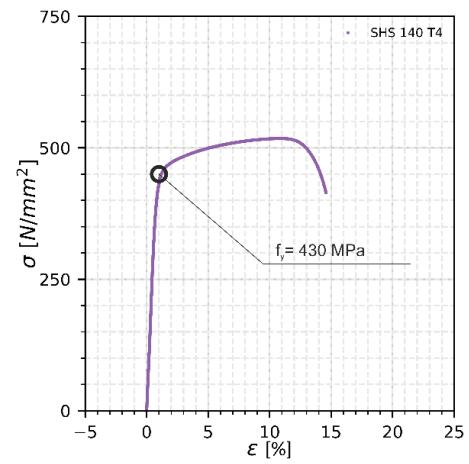
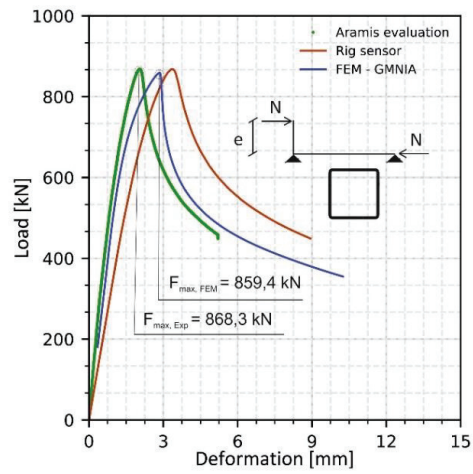
Test type T2

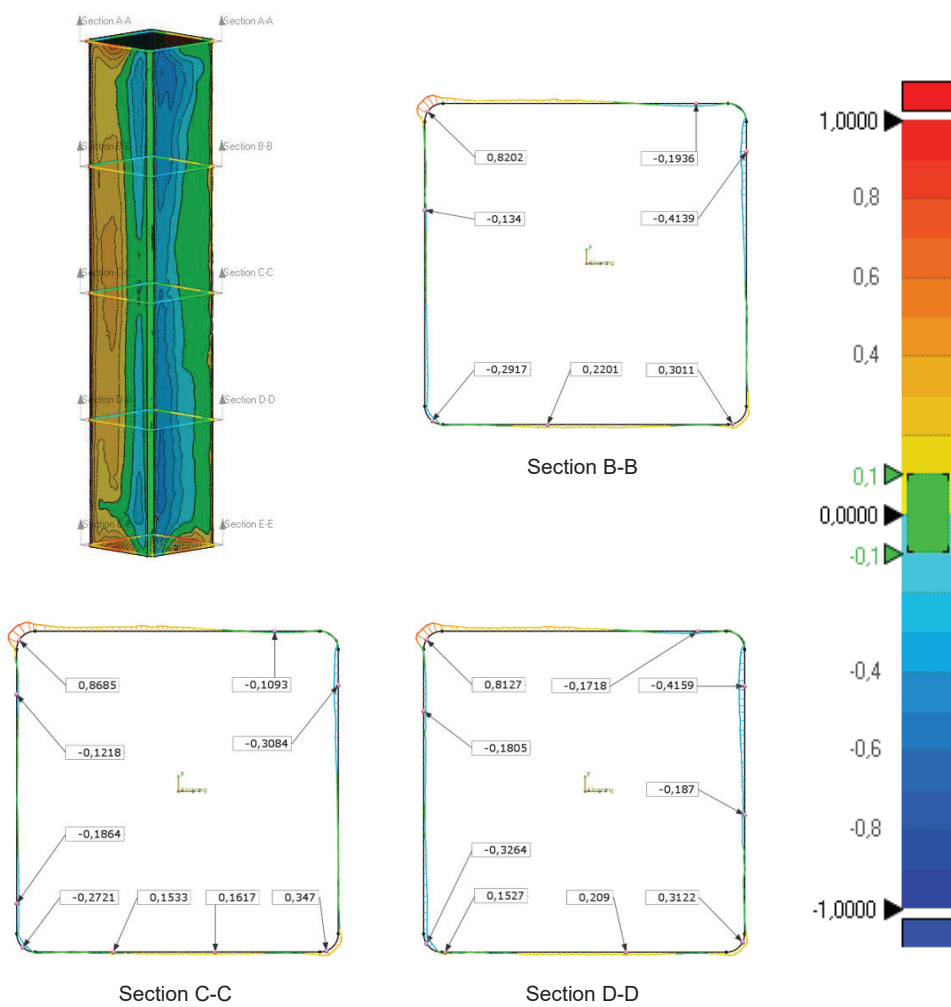
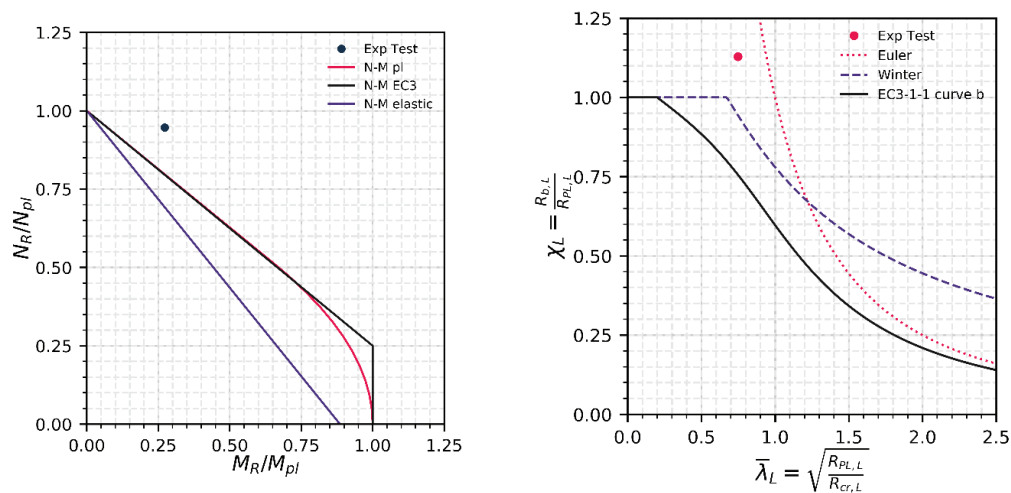
$e = 15 \text{ mm}$

$t_{\text{MEAS}} = 4.0 \text{ mm}$

$F_{\text{Max, Exp}} = 868,3 \text{ kN}$

$F_{\text{Max, FEM}} = 859,4 \text{ kN}$





Test T3-1

SHS 140/140/4.0

S355 - EN10219

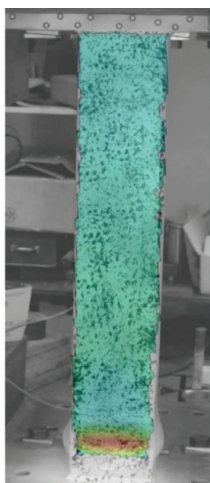
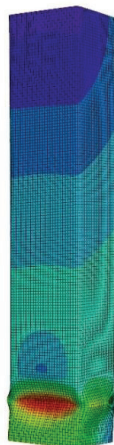
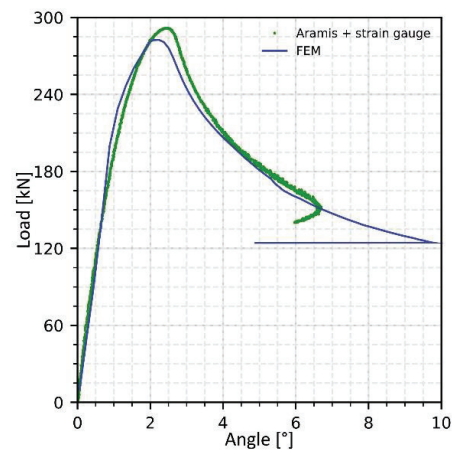
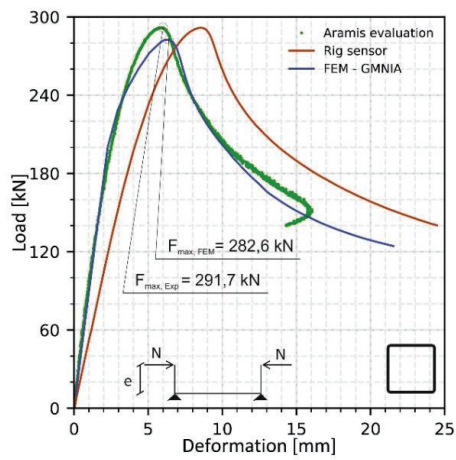
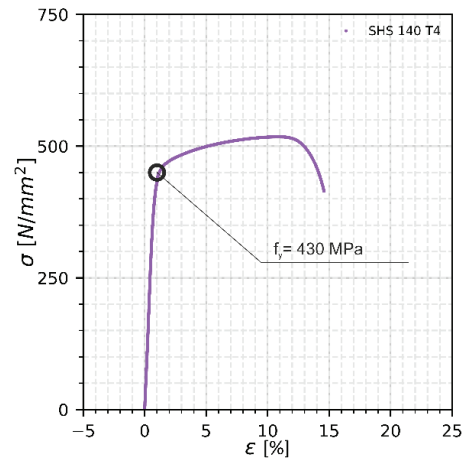
Test type T3

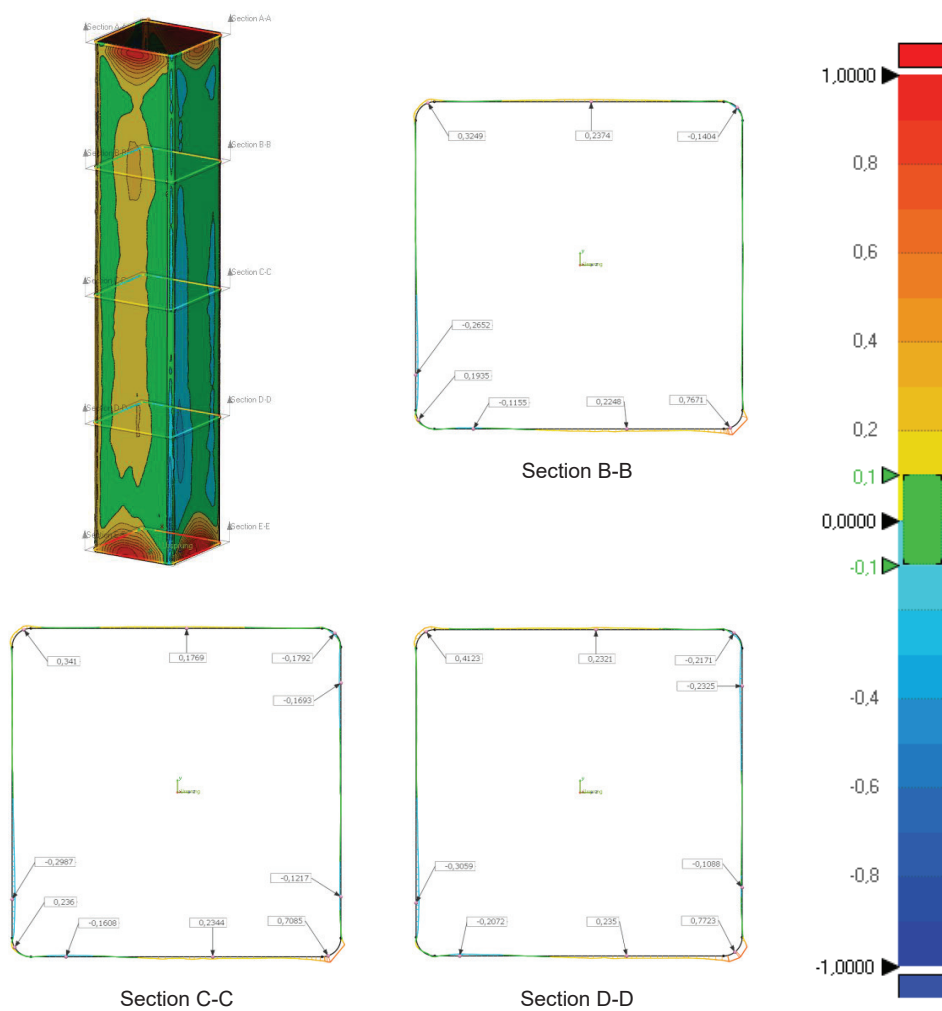
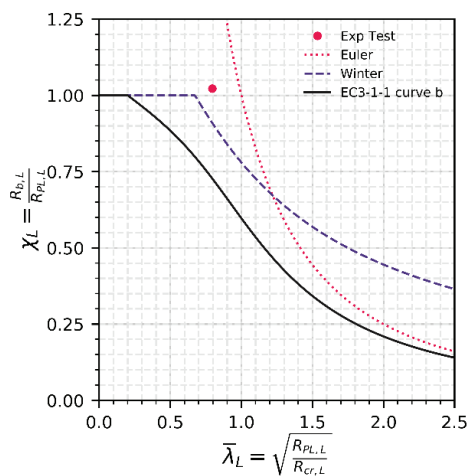
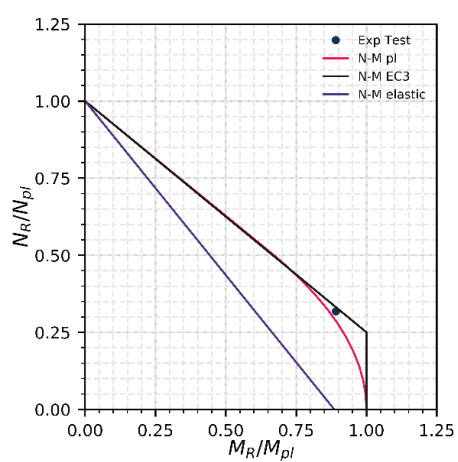
$e = 137 \text{ mm}$

$t_{MEAS} = 4.0 \text{ mm}$

$F_{Max, Exp} = 291,7 \text{ kN}$

$F_{Max, FEM} = 282,6 \text{ kN}$





Test T4-1

SHS 140/140/4.0

S355 - EN10219

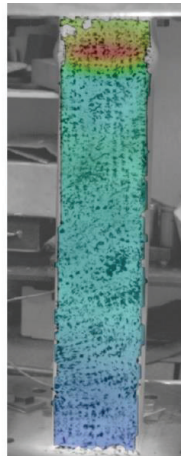
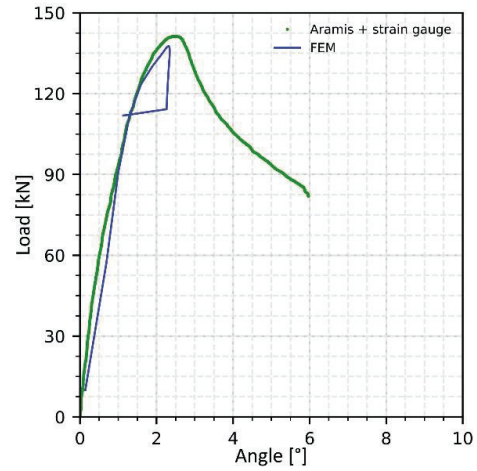
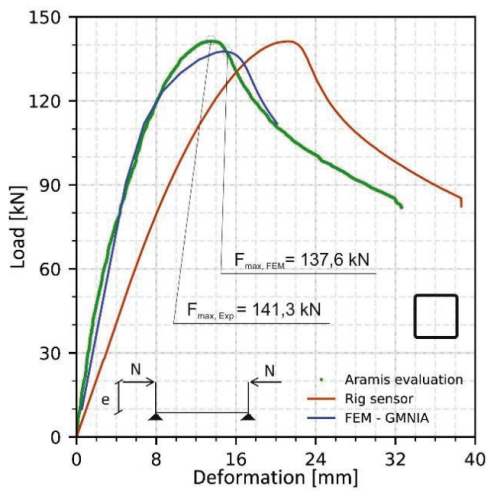
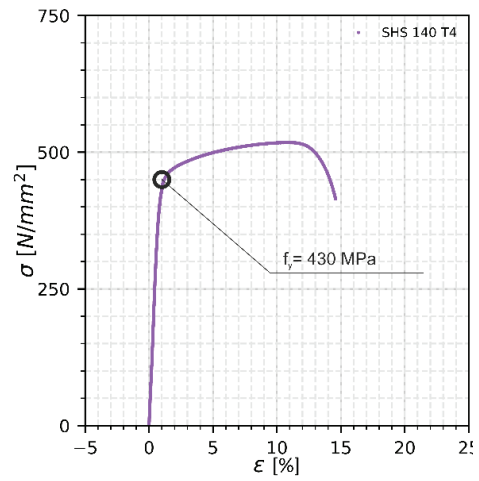
Test type T4

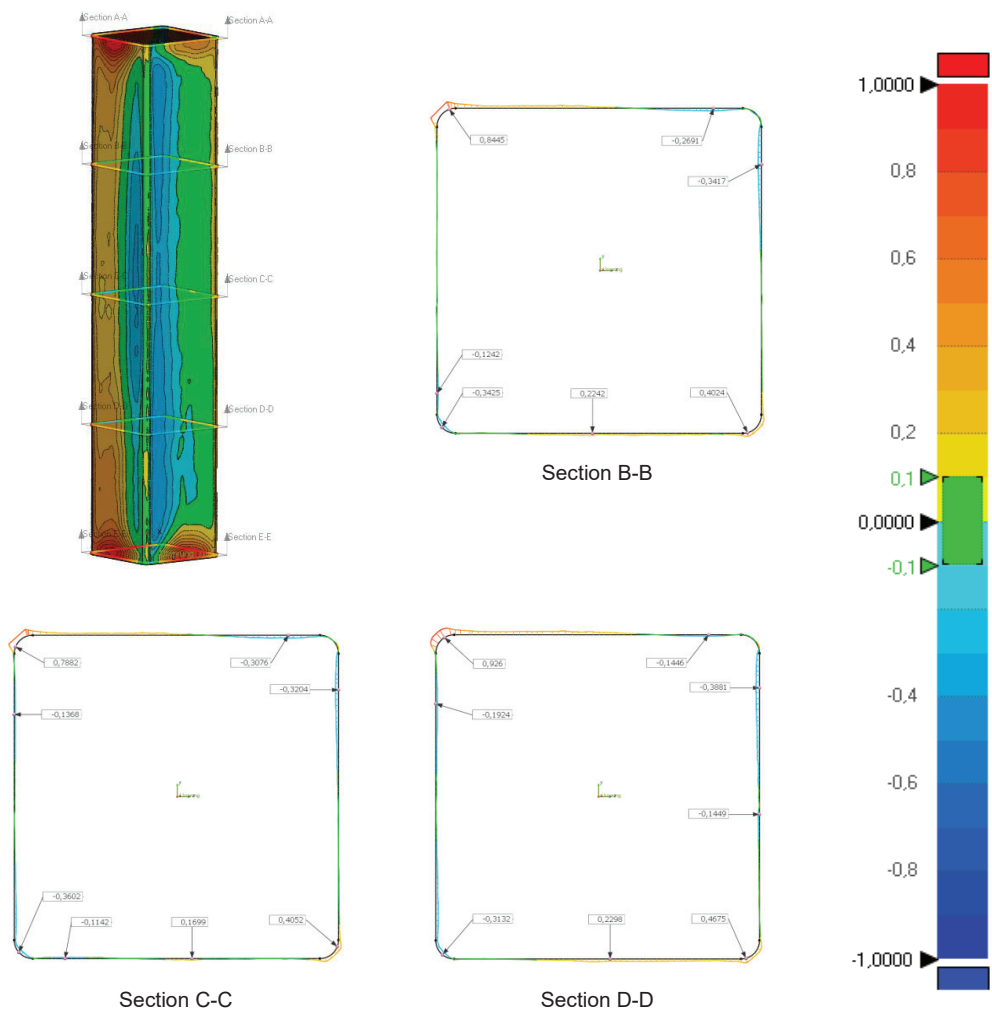
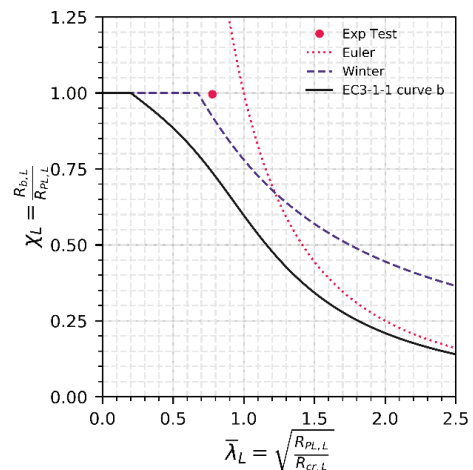
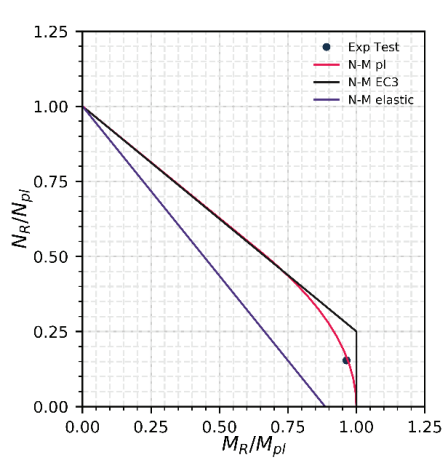
$e = 312 \text{ mm}$

$t_{MEAS} = 4.0 \text{ mm}$

$F_{Max, Exp} = 141,3 \text{ kN}$

$F_{Max, FEM} = 137,6 \text{ kN}$





Test T5-1

SHS 140/140/4.0

S355 - EN10219

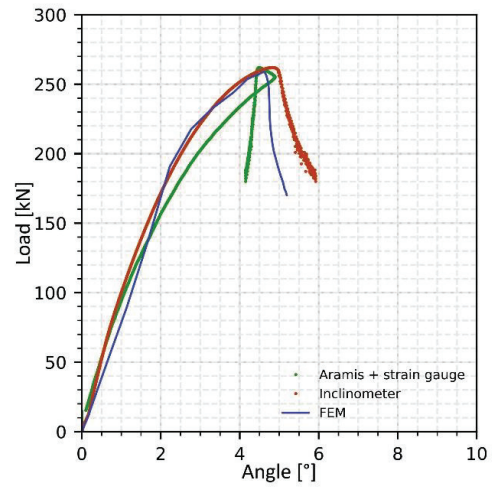
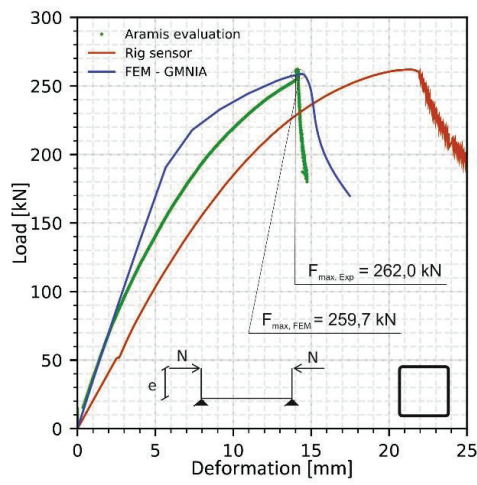
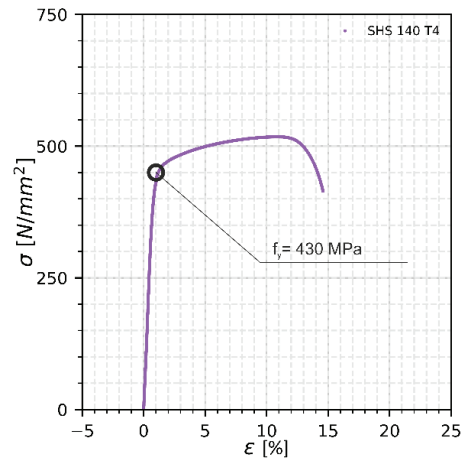
Test type T5

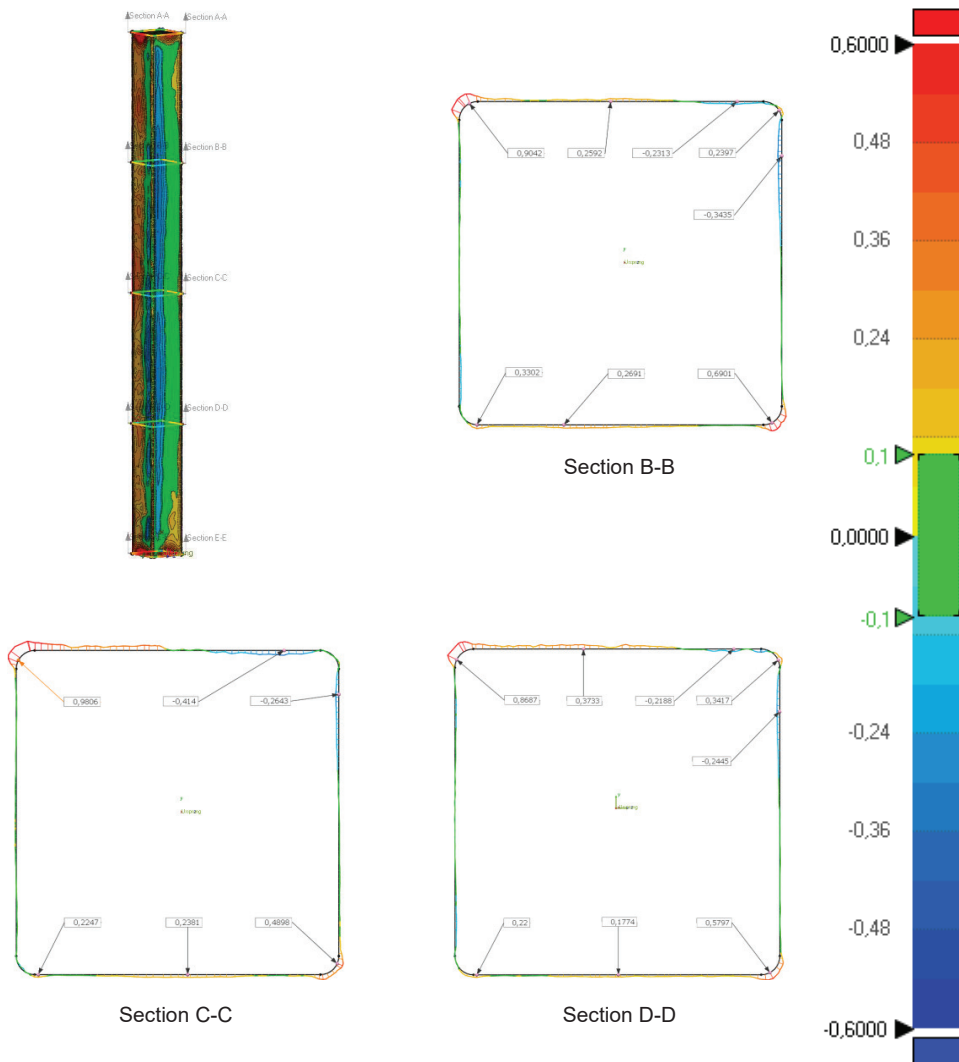
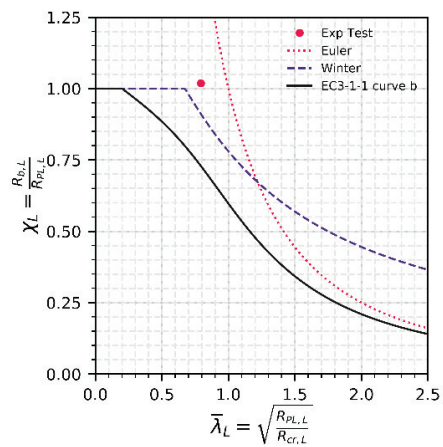
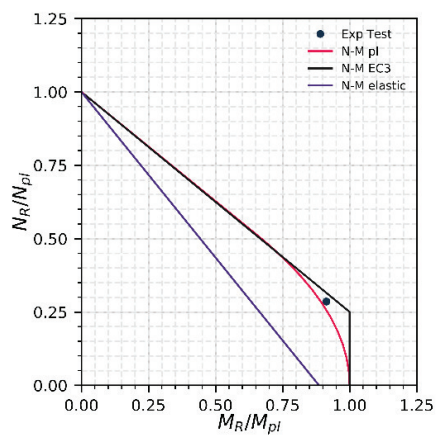
$e = 137 \text{ mm}$

$t_{MEAS} = 4.0 \text{ mm}$

$F_{Max, Exp} = 262,0 \text{ kN}$

$F_{Max, FEM} = 259,7 \text{ kN}$





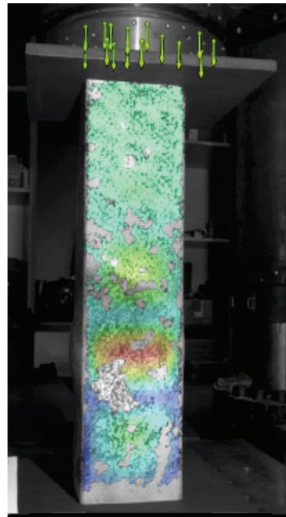
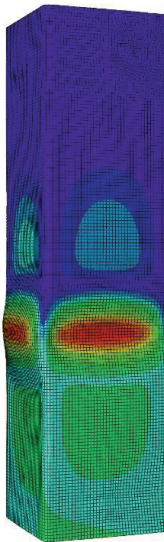
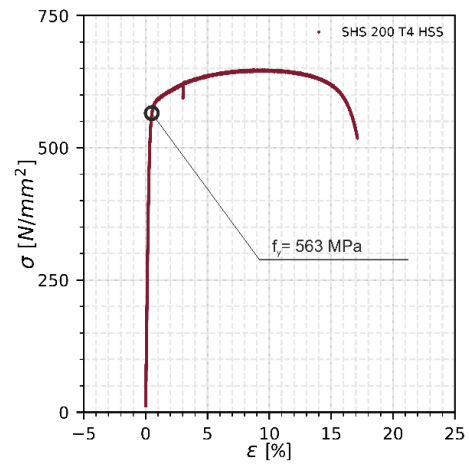
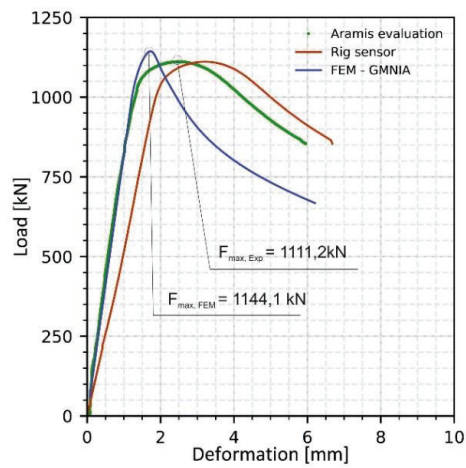
Test No. T1-4

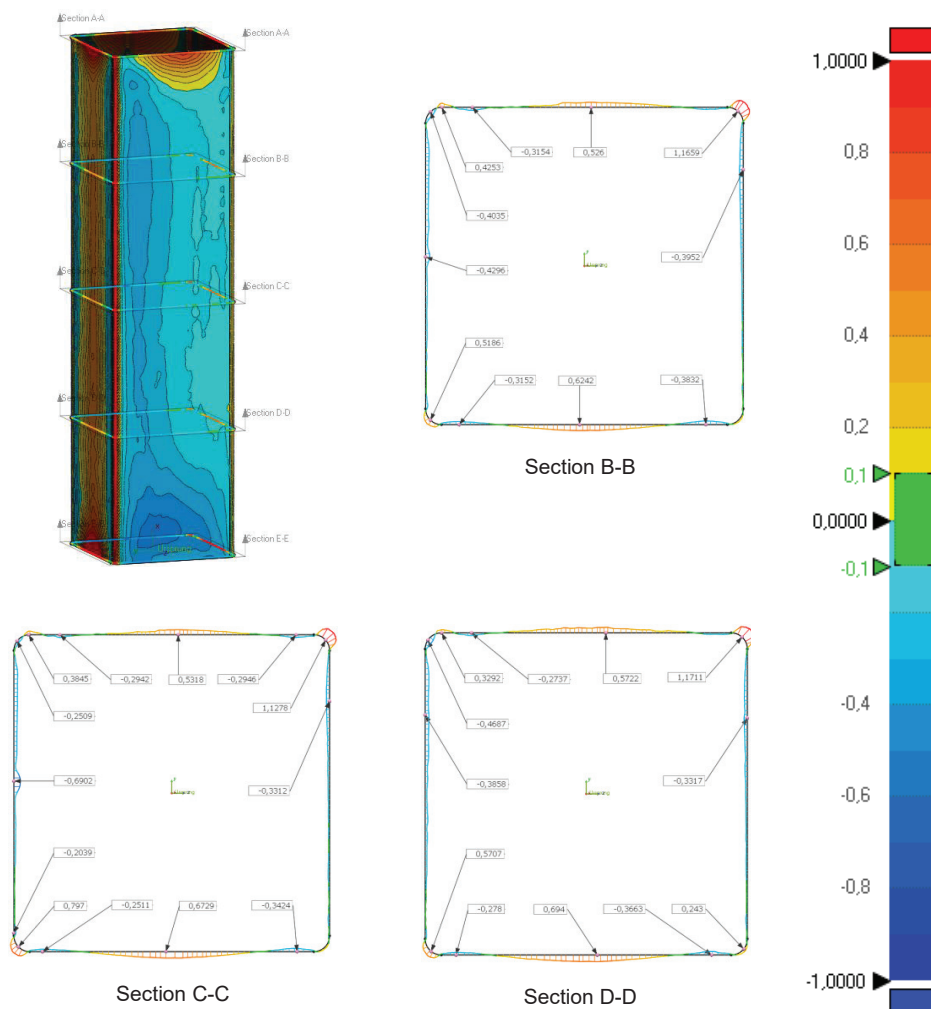
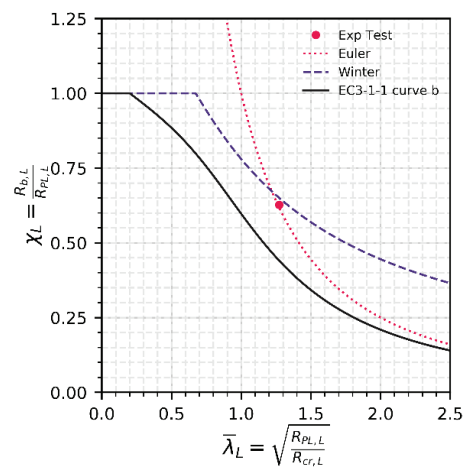
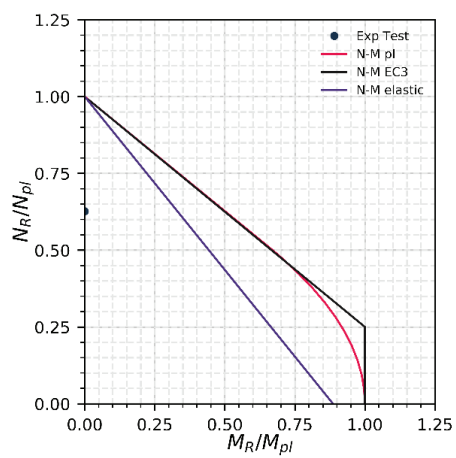
SHS 200/200/4

S500 - EN10219

Test type T1

e = 0 mm

 $t_{MEAS} = 4.1$ mm $F_{Max, Exp} = 1111,2$ kN $F_{Max, FEM} = 1144,1$ kN



Test T2-4

SHS 200/200/4

S500 - EN10219

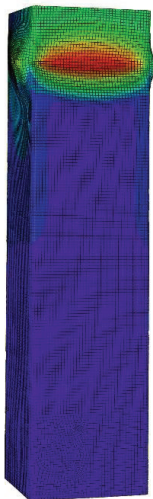
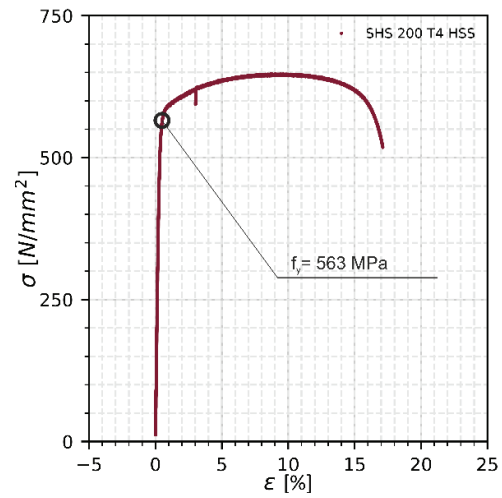
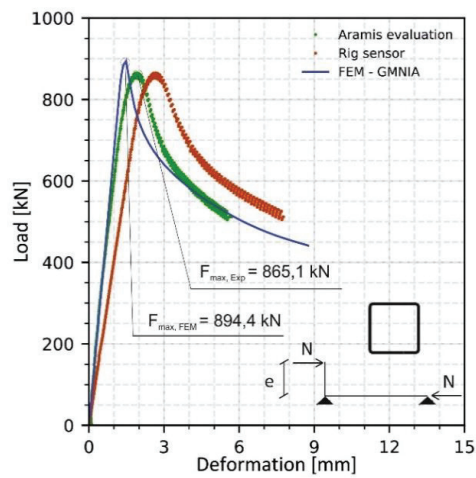
Test type T2

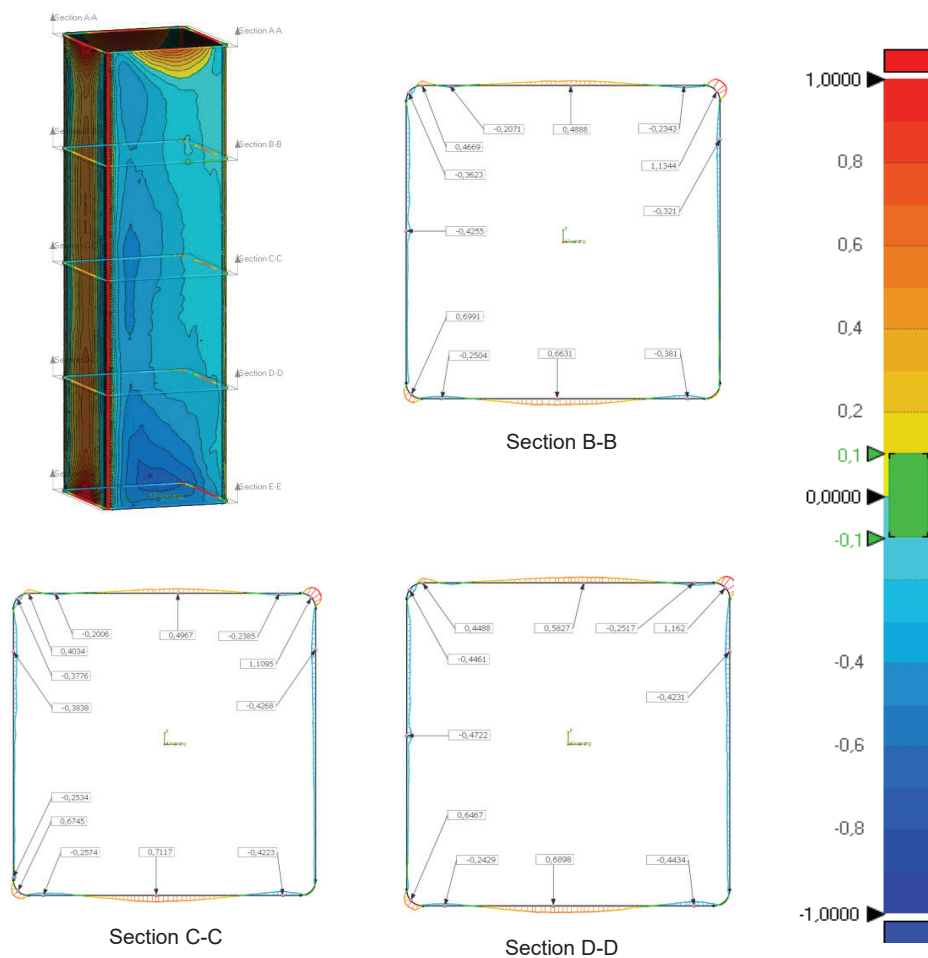
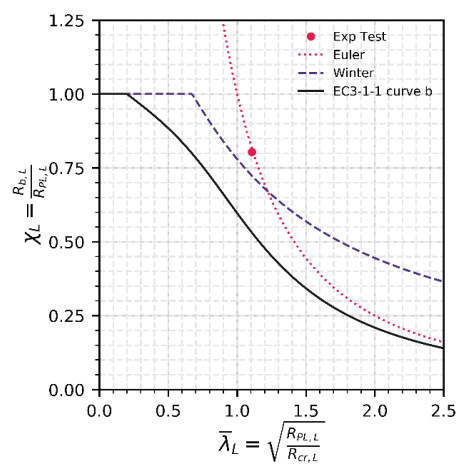
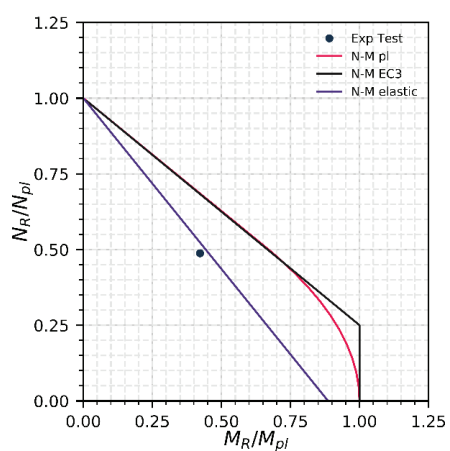
$e = 63 \text{ mm}$

$t_{\text{MEAS}} = 4.1 \text{ mm}$

$F_{\text{Max, Exp}} = 865,1 \text{ kN}$

$F_{\text{Max, FEM}} = 894,4 \text{ kN}$





Test T3-4

SHS 200/200/4
S500 - EN10219

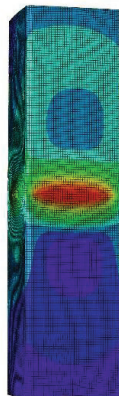
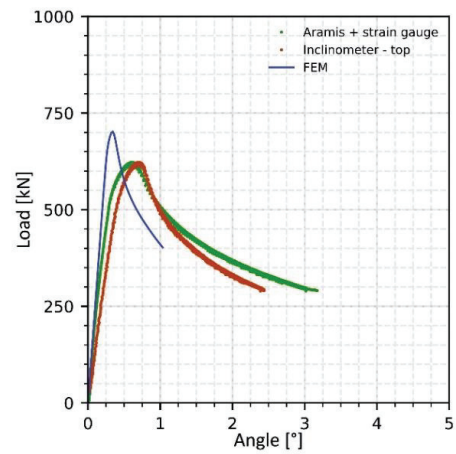
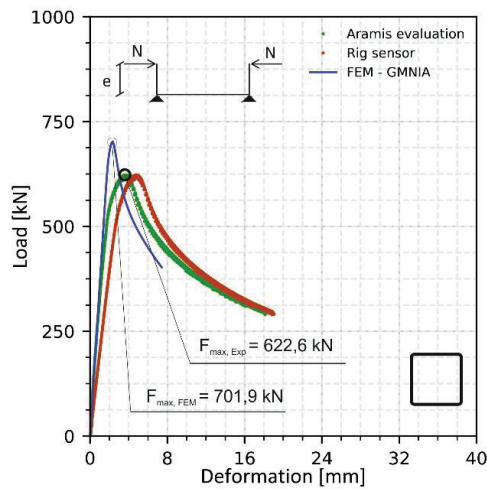
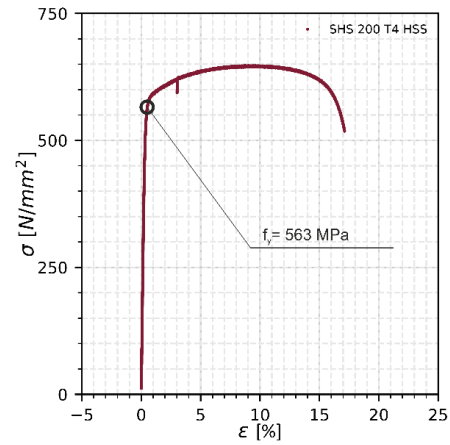
Test type T3

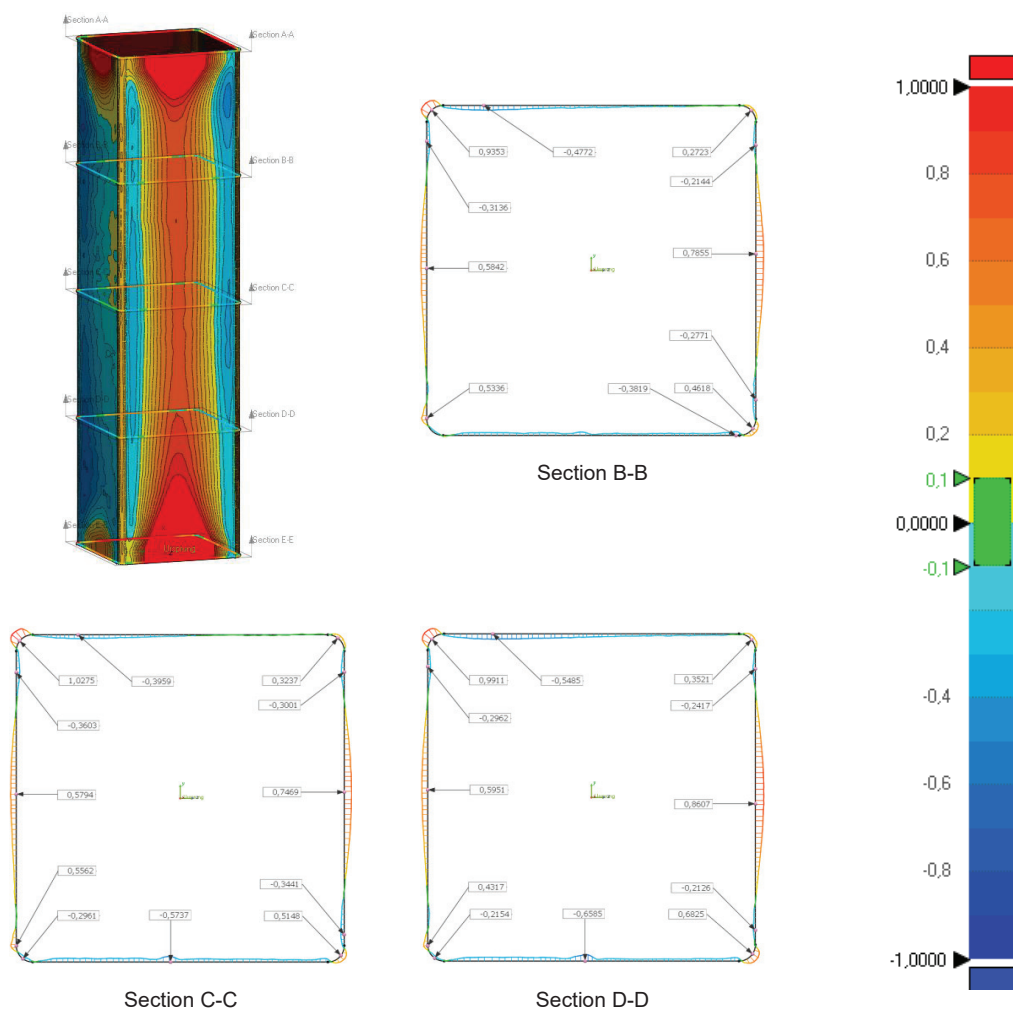
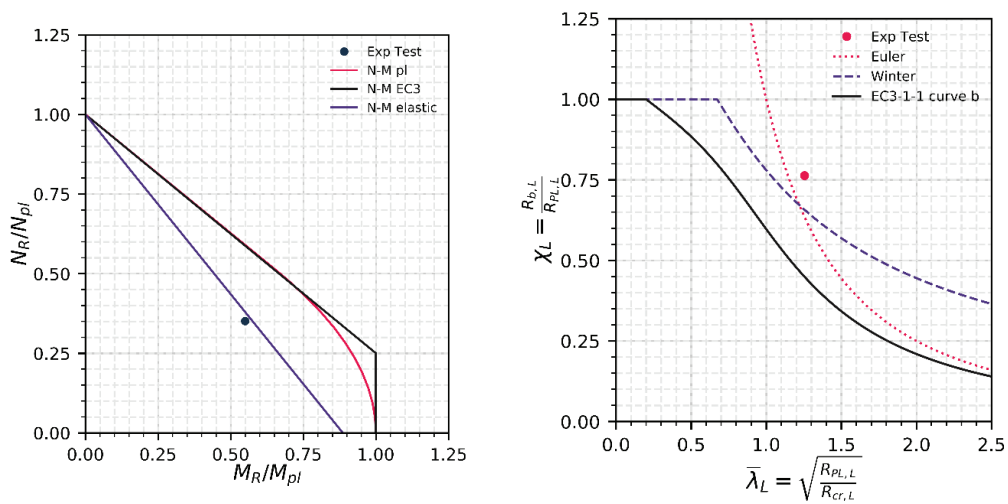
$e = 107 \text{ mm}$

$t_{MEAS} = 4.1 \text{ mm}$

$F_{Max, Exp} = 622,6 \text{ kN}$

$F_{Max, FEM} = 701,9 \text{ kN}$





Test T4-4

SHS 200/200/4

S500 - EN10219

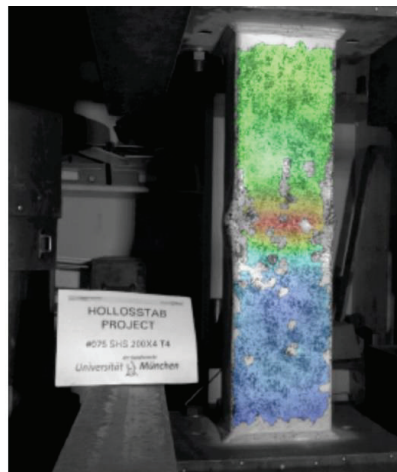
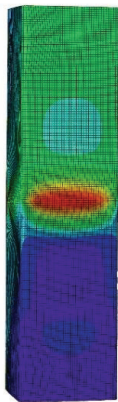
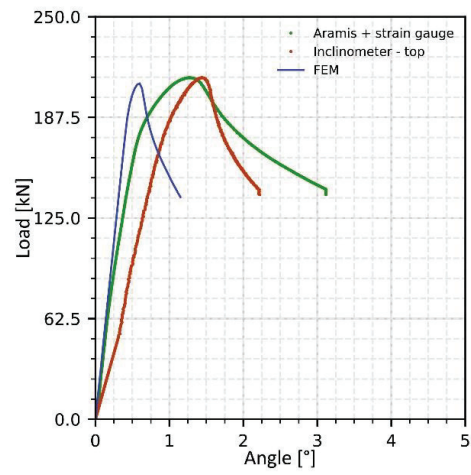
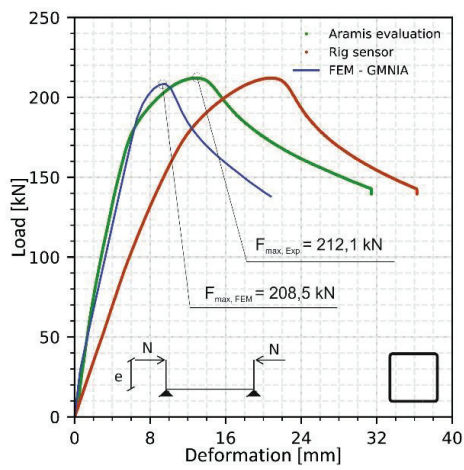
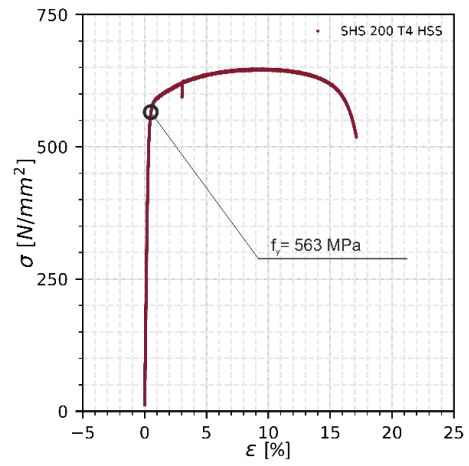
Test type T4

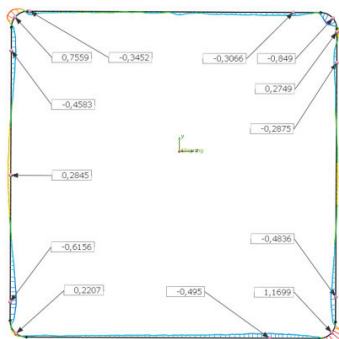
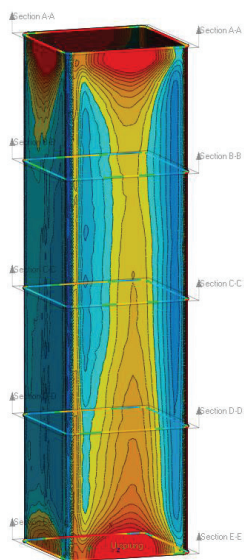
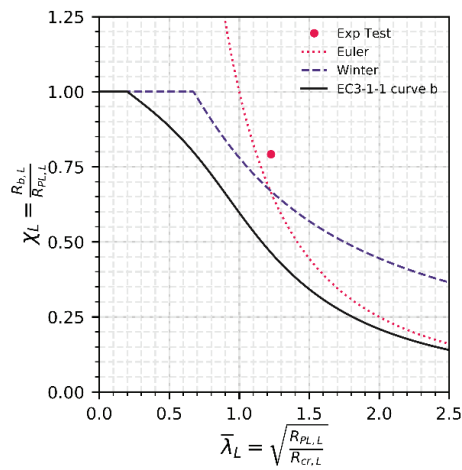
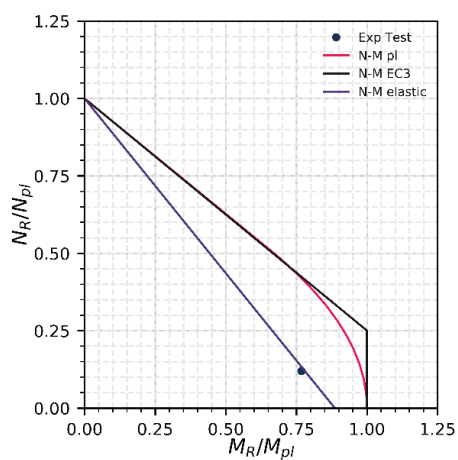
$e = 457 \text{ mm}$

$t_{MEAS} = 4.1 \text{ mm}$

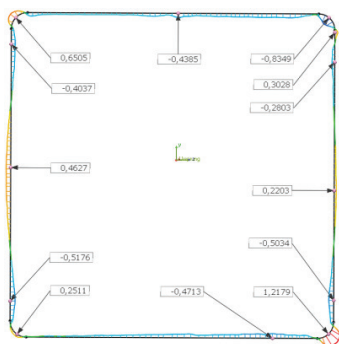
$F_{Max, Exp} = 212,1 \text{ kN}$

$F_{Max, FEM} = 208,5 \text{ kN}$

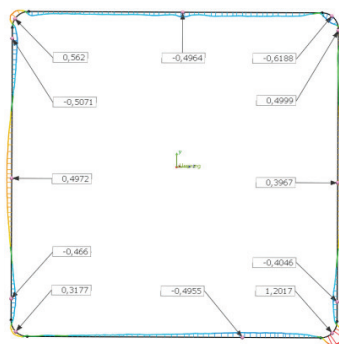




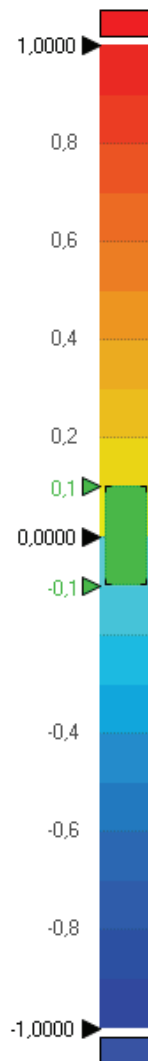
Section B-B



Section C-C



Section D-D



Test T5-4

RHS 300/150/6

S355 - EN10219

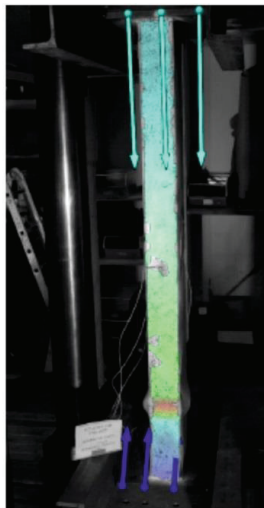
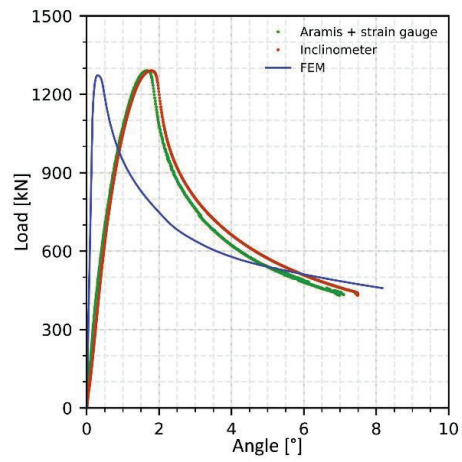
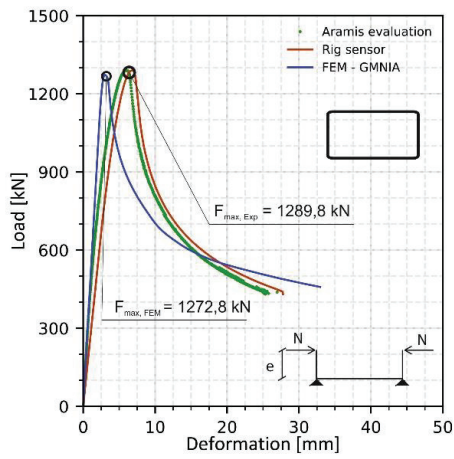
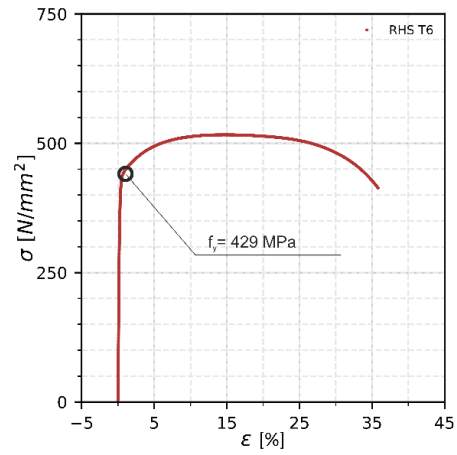
Test type T5

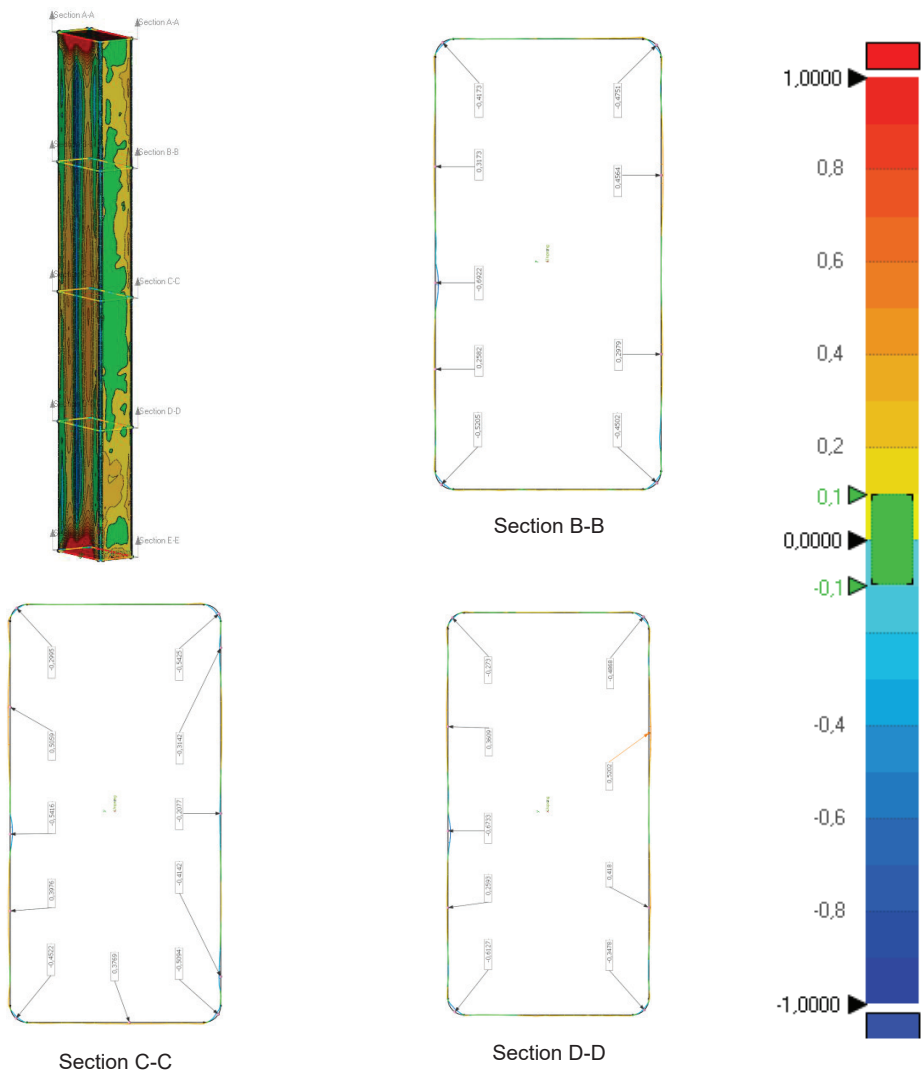
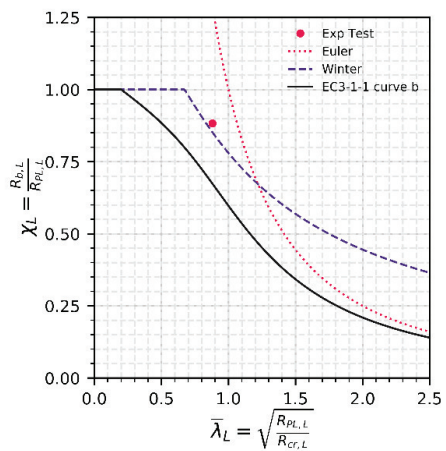
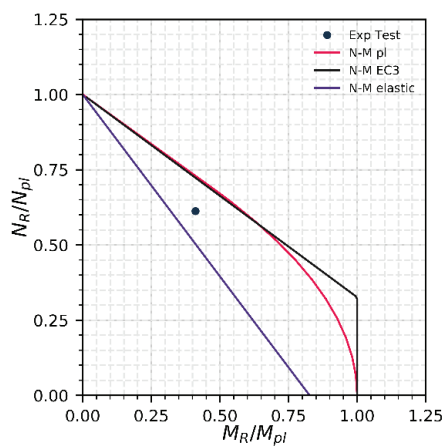
$e = 57 \text{ mm}$

$t_{MEAS} = 5.7 \text{ mm}$

$F_{Max, Exp} = 1289,8 \text{ kN}$

$F_{Max, FEM} = 1272,8 \text{ kN}$





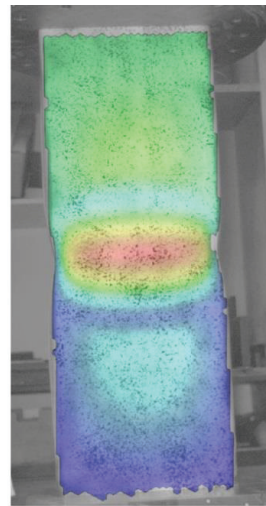
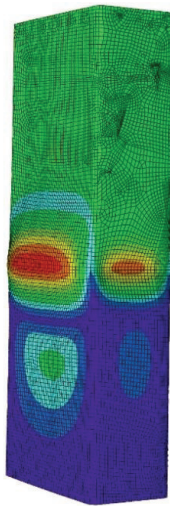
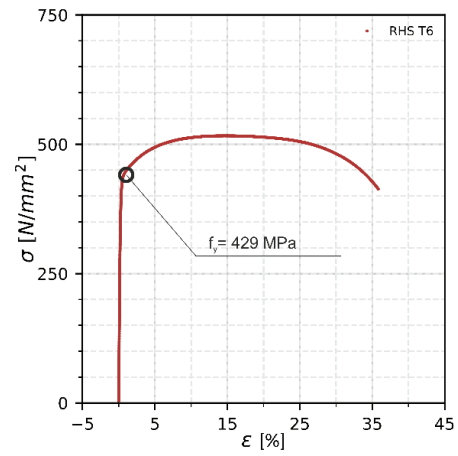
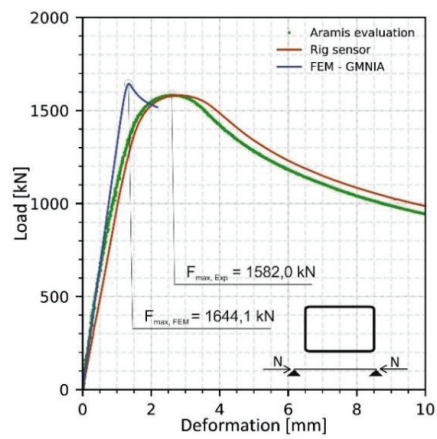
Test No. T1-6

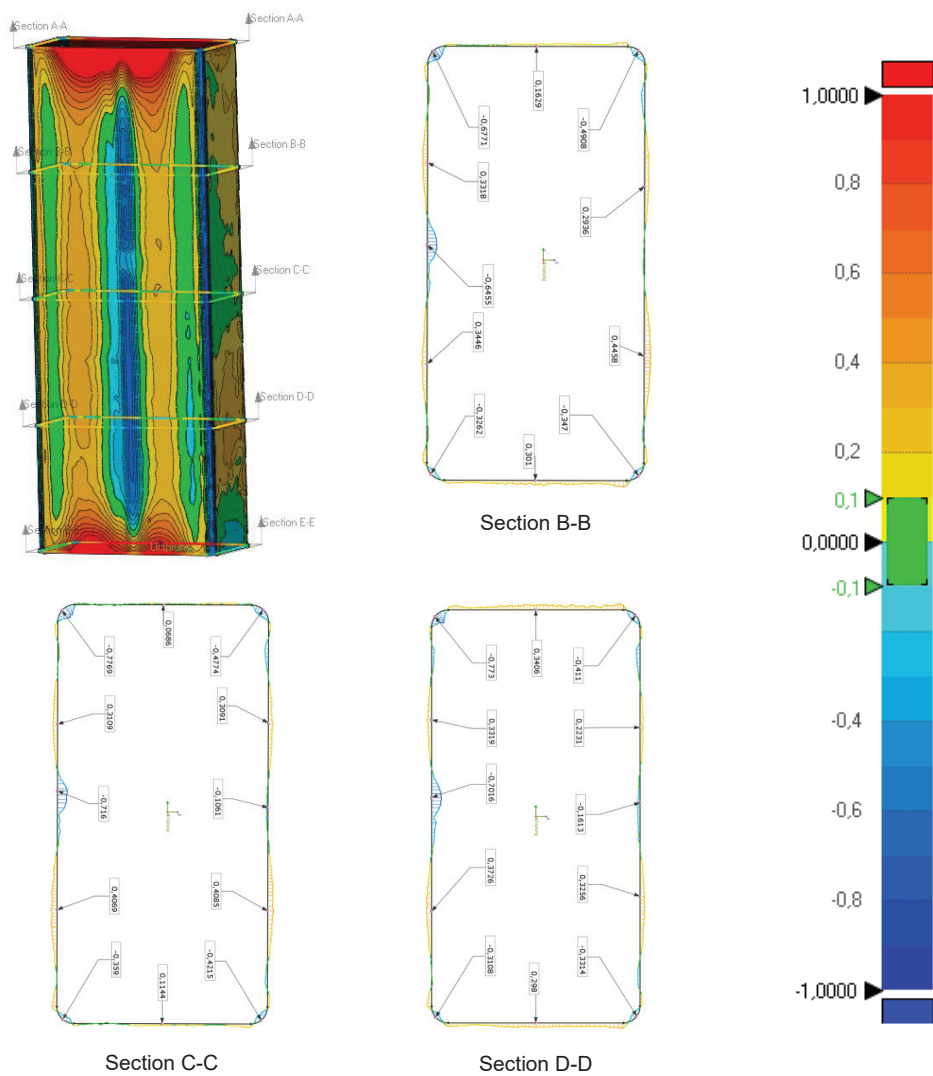
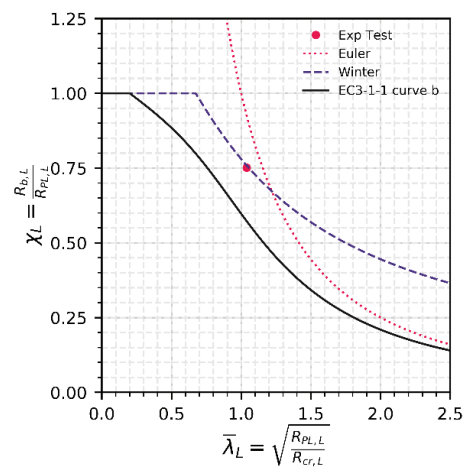
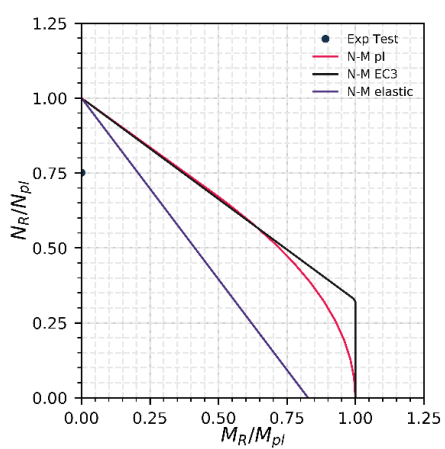
RHS 300/150/6

S355 - EN10219

Test type T1

e = 0 mm

 $t_{MEAS} = 5.7$ mm $F_{Max, Exp} = 1582,0$ kN $F_{Max, FEM} = 1644,1$ kN



Test T2-6

RHS 300/150/6

S355 - EN10219

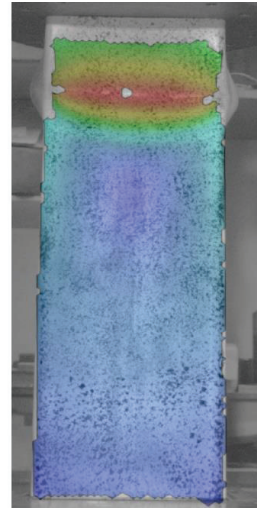
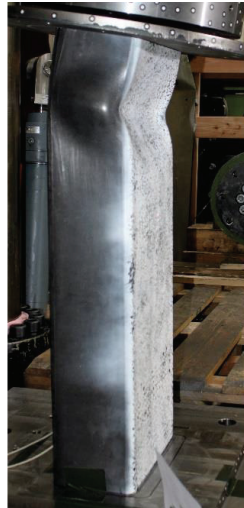
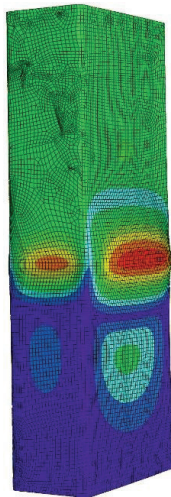
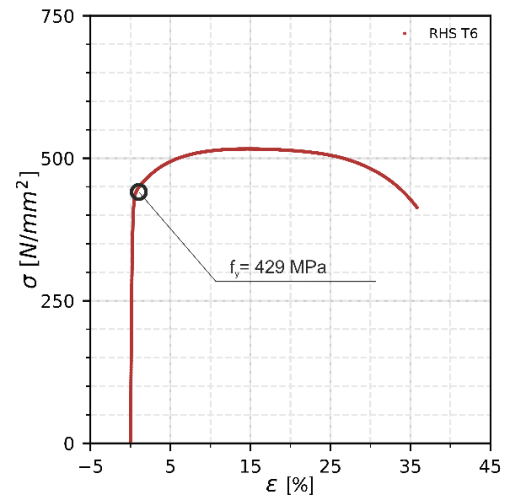
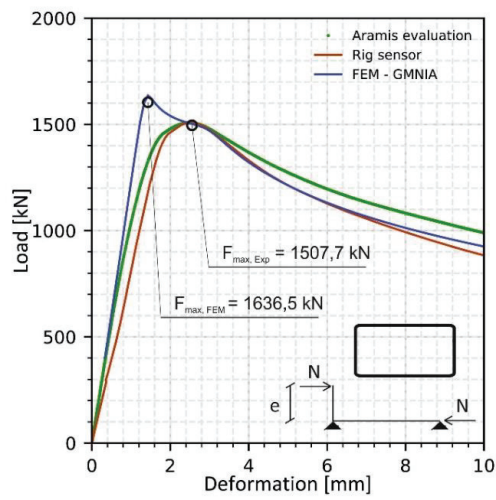
Test type T2

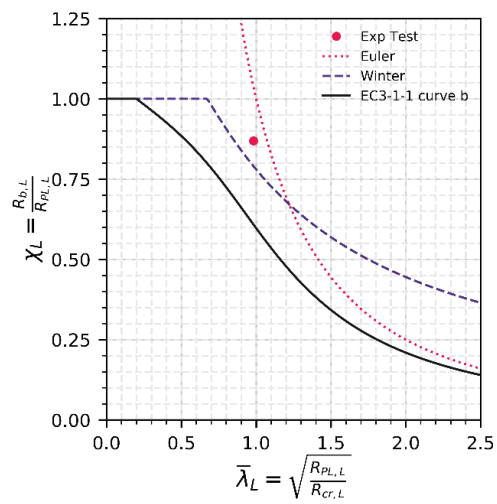
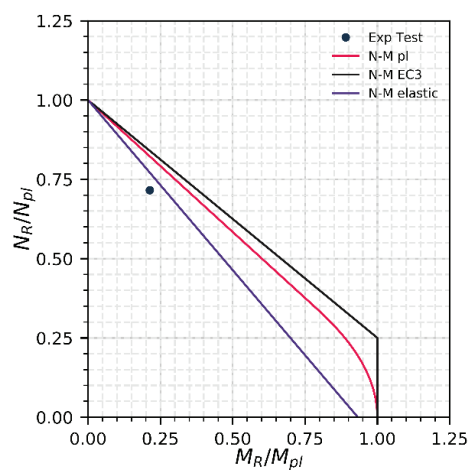
$e = 18 \text{ mm}$

$t_{\text{MEAS}} = 5.7 \text{ mm}$

$F_{\text{Max, Exp}} = 1507,7 \text{ kN}$

$F_{\text{Max, FEM}} = 1636,5 \text{ kN}$





Test T3-6

RHS 300/150/6

S355 - EN10219

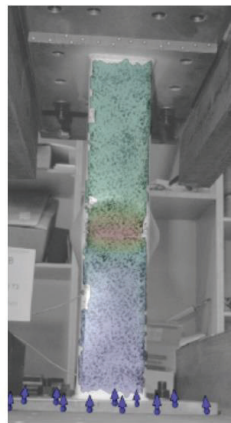
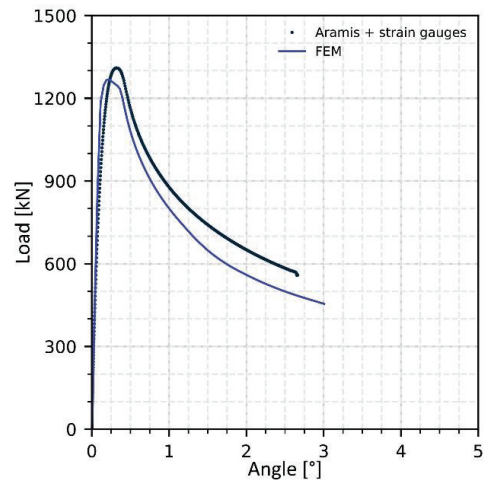
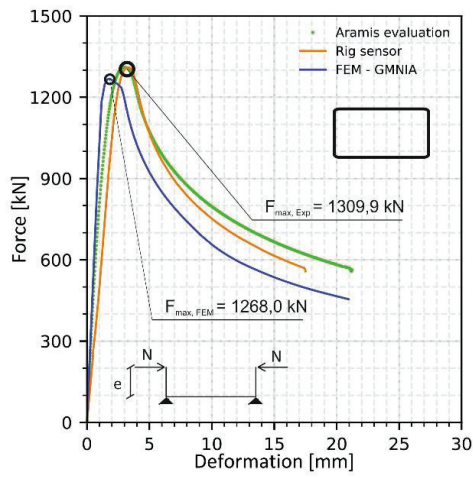
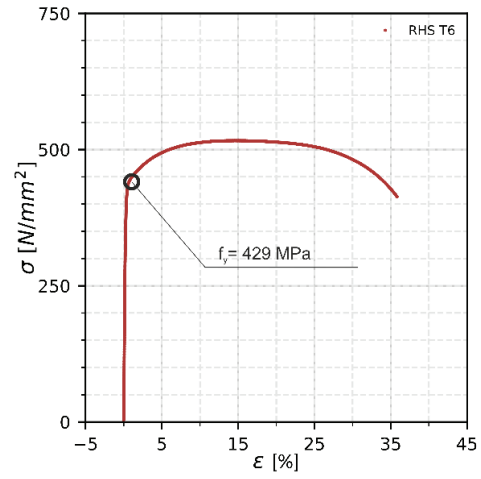
Test type T3

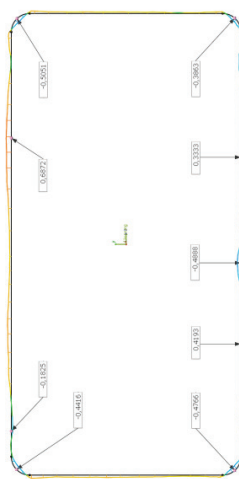
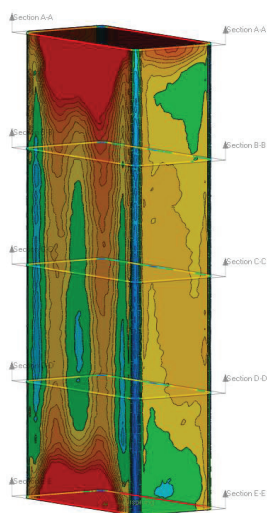
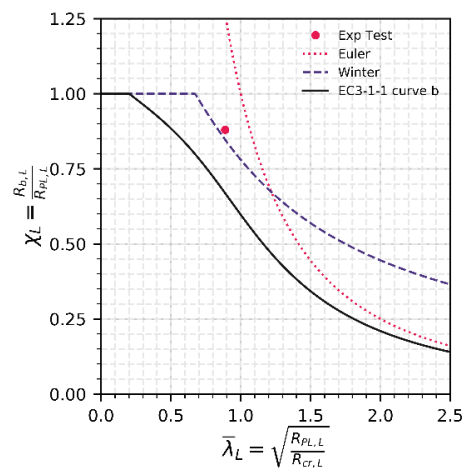
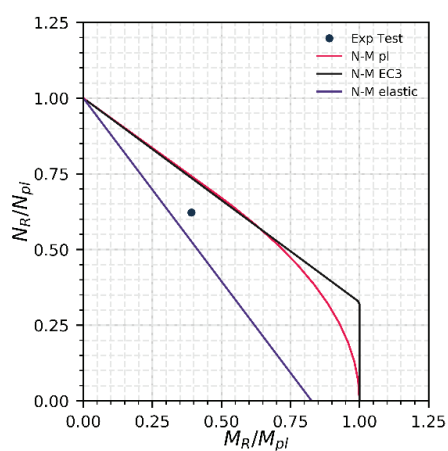
$e = 57 \text{ mm}$

$t_{MEAS} = 5.7 \text{ mm}$

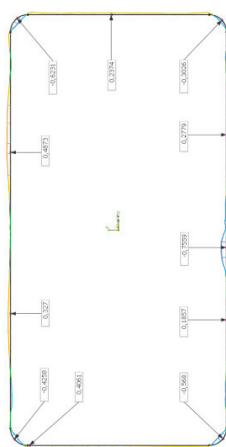
$F_{Max, Exp} = 1309,9 \text{ kN}$

$F_{Max, FEM} = 1268,0 \text{ kN}$

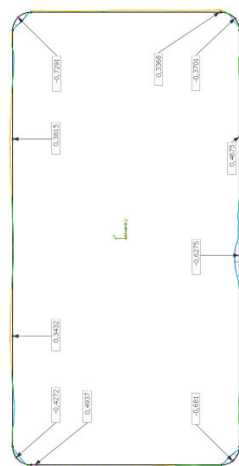




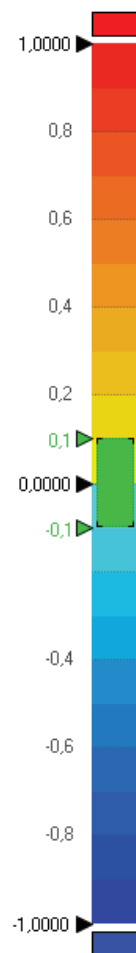
Section B-B



Section C-C



Section D-D



Test T4-6

RHS 300/150/6

S355 - EN10219

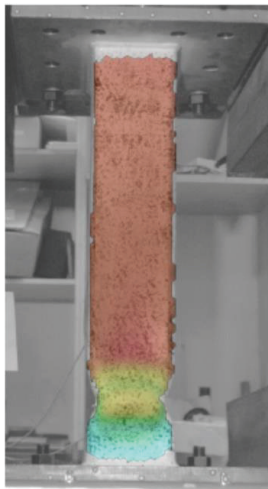
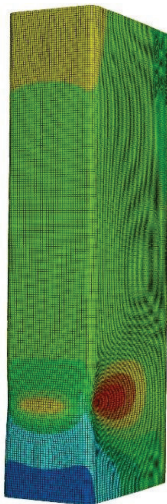
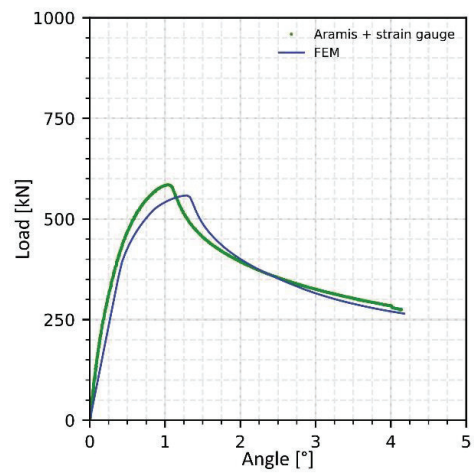
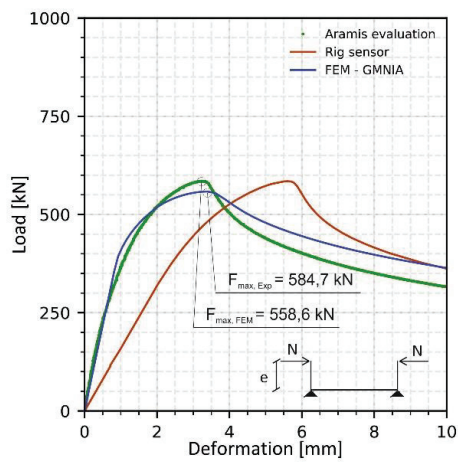
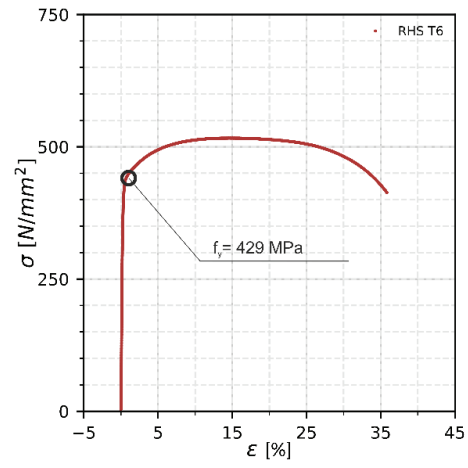
Test type T4

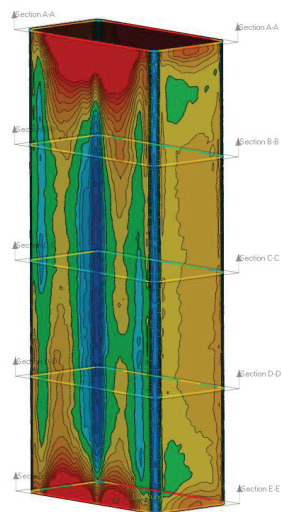
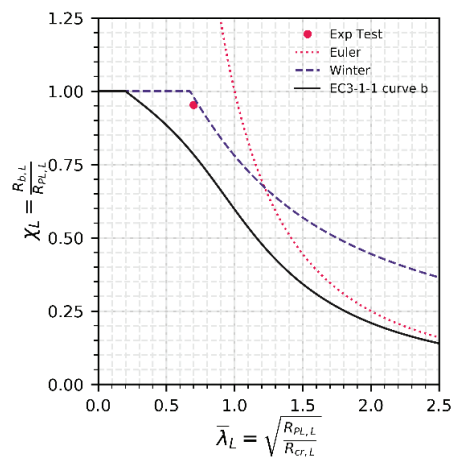
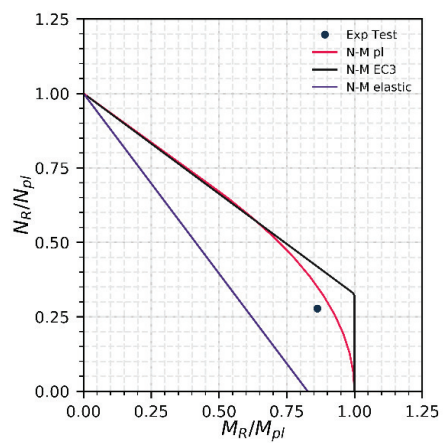
$e = 297 \text{ mm}$

$t_{MEAS} = 5.7 \text{ mm}$

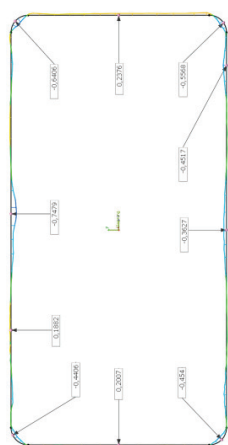
$F_{Max, Exp} = 584.7 \text{ kN}$

$F_{Max, FEM} = 558.6 \text{ kN}$

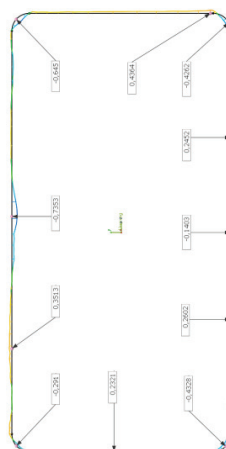




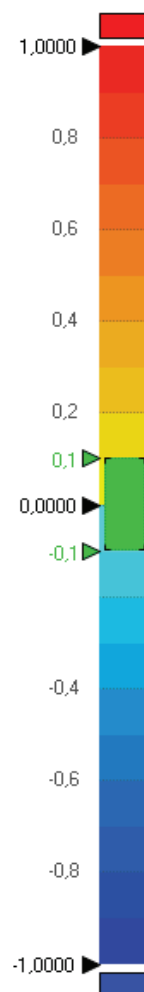
Section B-B



Section C-C



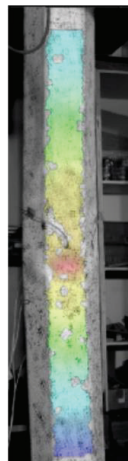
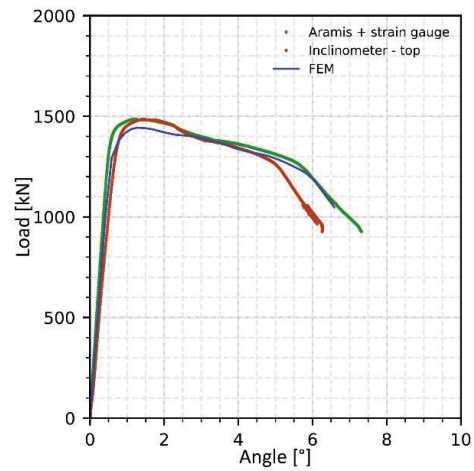
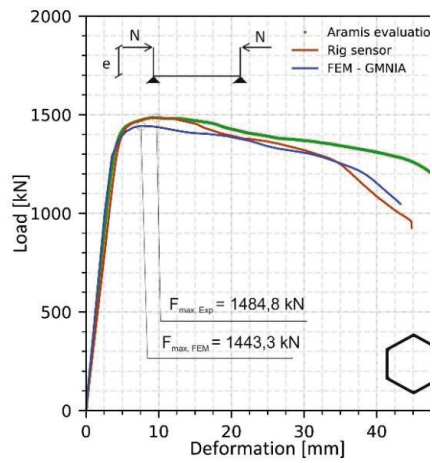
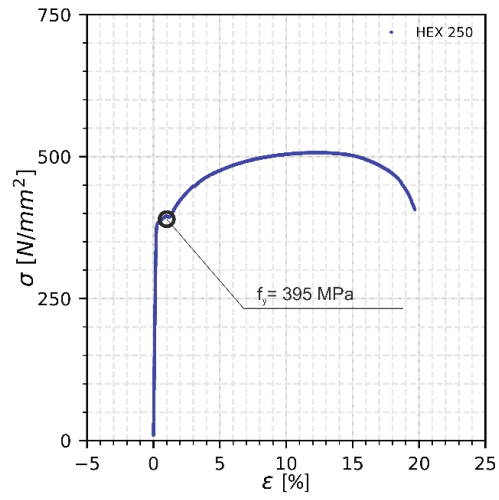
Section D-D

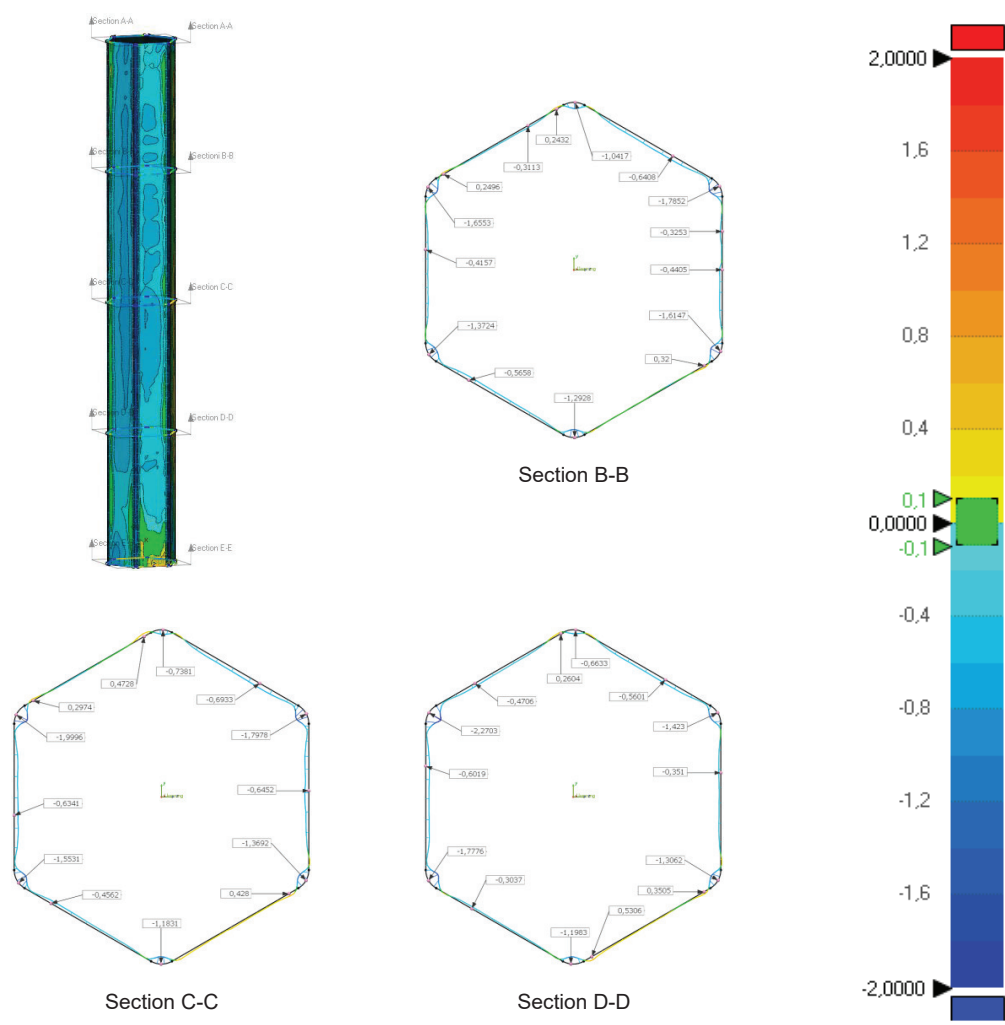
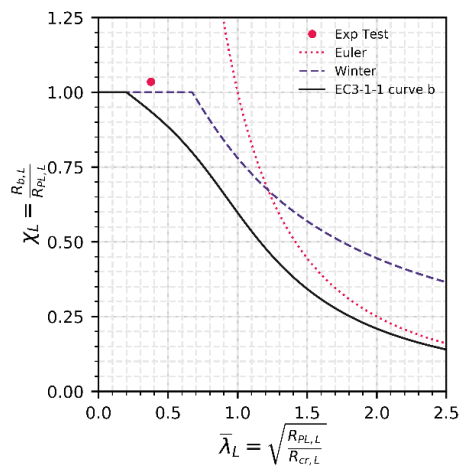
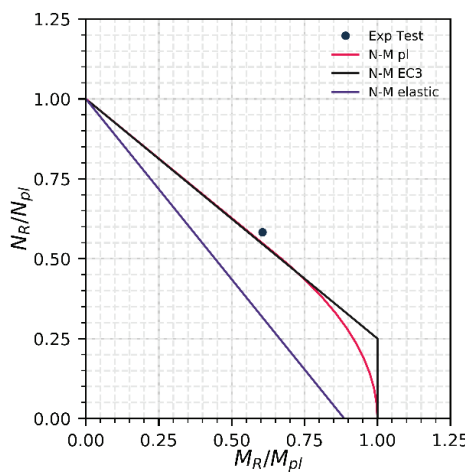


Test T5-6

HEX 250/8.5
 S355 - EN10210
 Test type T5
 $e = 76 \text{ mm}$
 $t_{MEAS} = 8.5 \text{ mm}$

$F_{Max, Exp} = 1484,8 \text{ kN}$
 $F_{Max, FEM} = 1443,3 \text{ kN}$





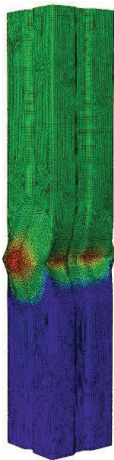
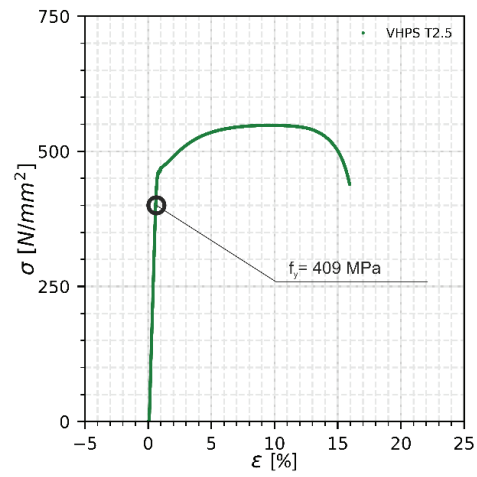
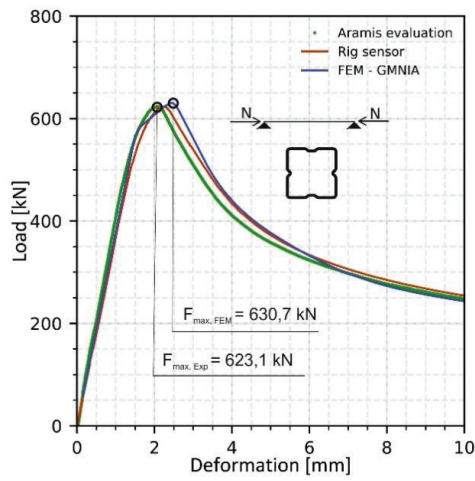
Test No. T1-8

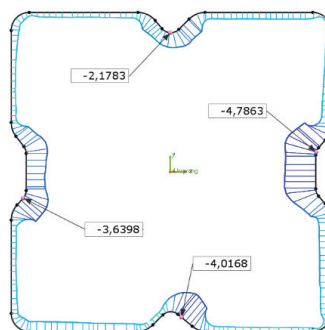
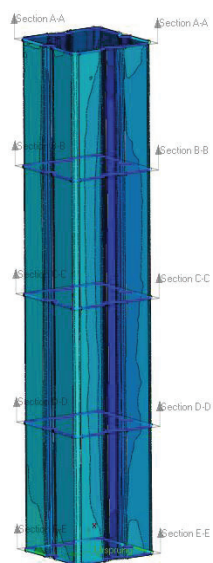
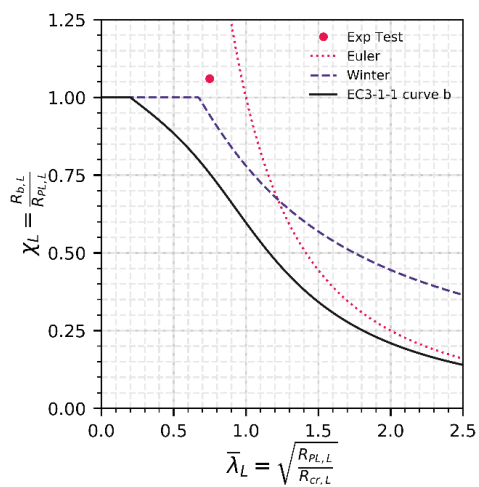
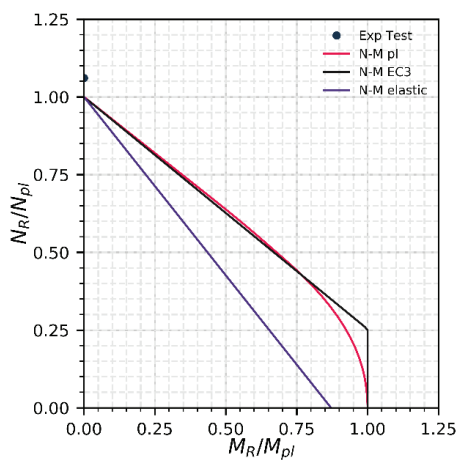
VHPS 140/140/2.5

S355 - EN10219

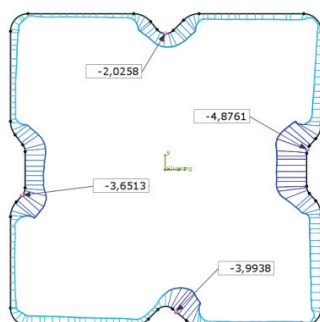
Test type T1

e = 0 mm

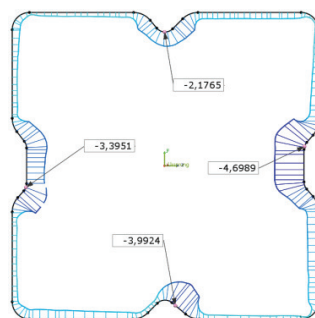
 $t_{MEAS} = 2.5$ mm $F_{Max, Exp} = 623,1$ kN $F_{Max, FEM} = 630,7$ kN



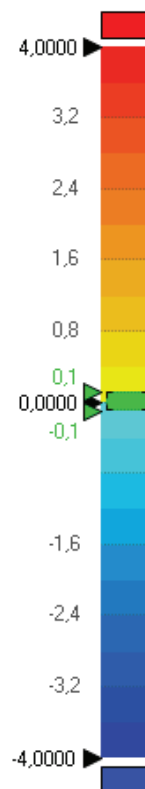
Section B-B



Section C-C



Section D-D



Test T2-8

VHPS 140/140/2.5

S355 - EN10219

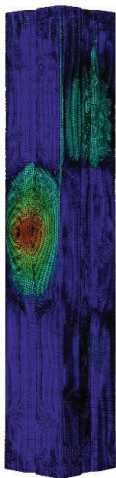
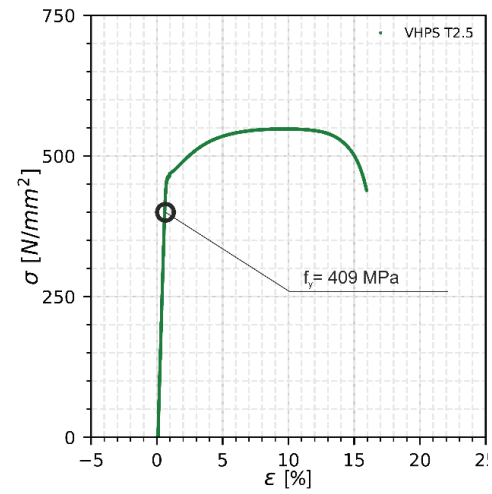
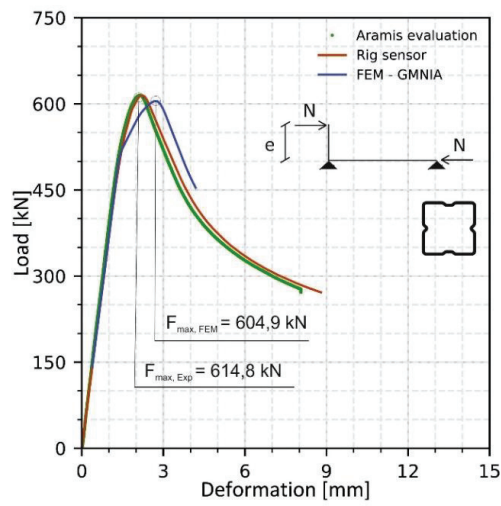
Test type T2

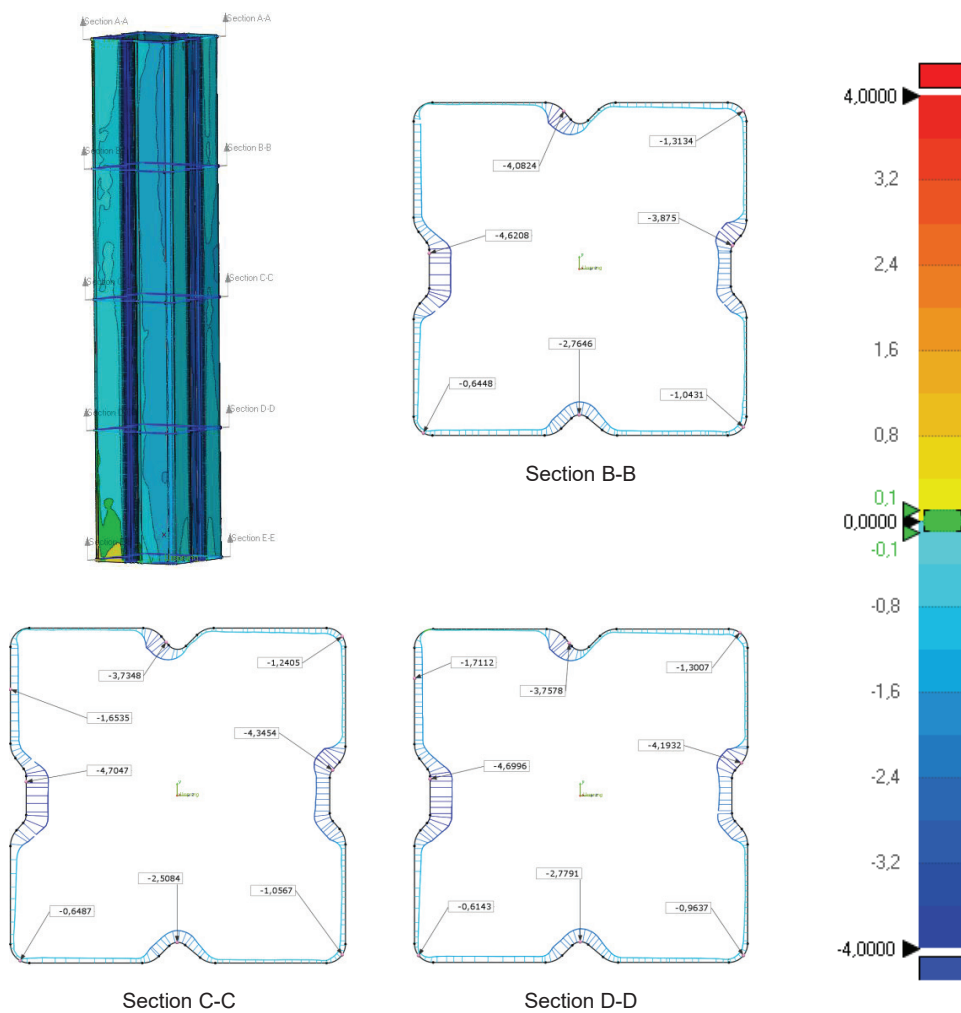
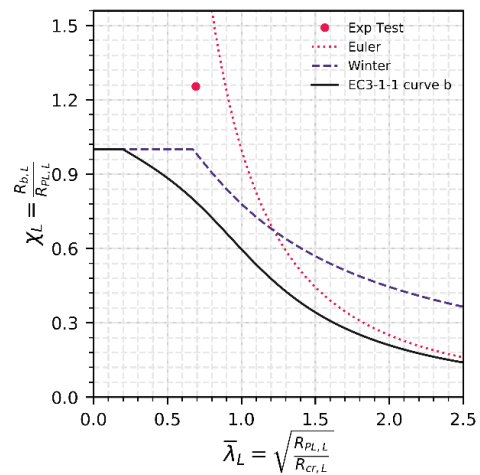
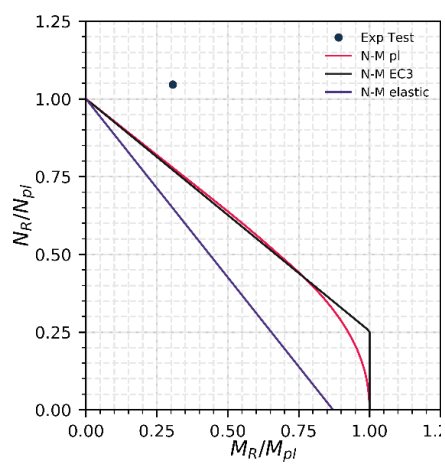
$e = 0$ mm

$t_{MEAS} = 2.5$ mm

$F_{Max, Exp} = 614,8$ kN

$F_{Max, FEM} = 604,9$ kN





Test T3-8

VHPS 140/140/2.5

S355 - EN10219

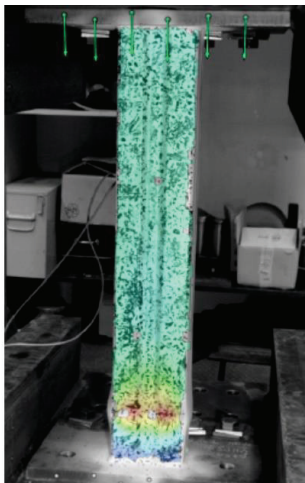
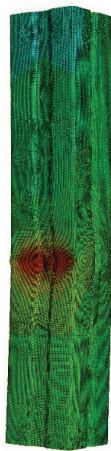
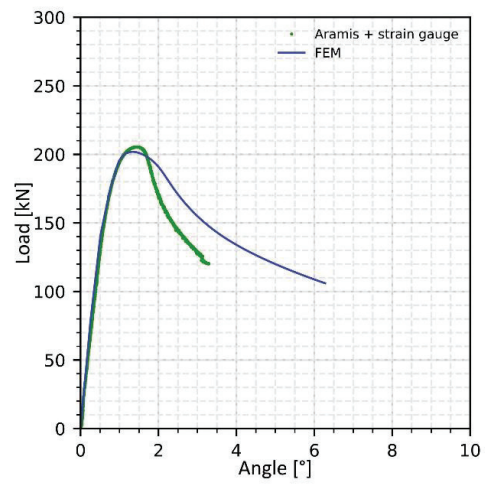
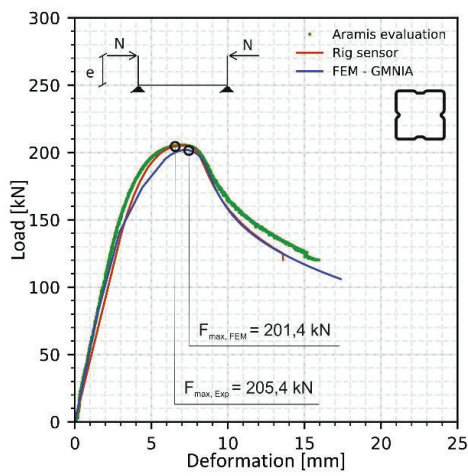
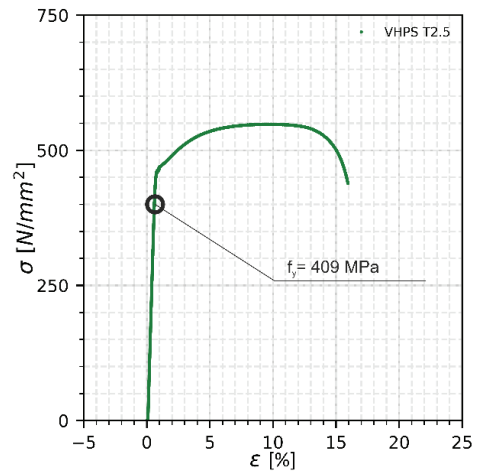
Test type T3

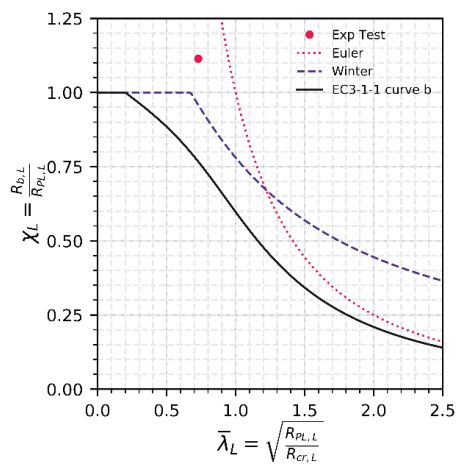
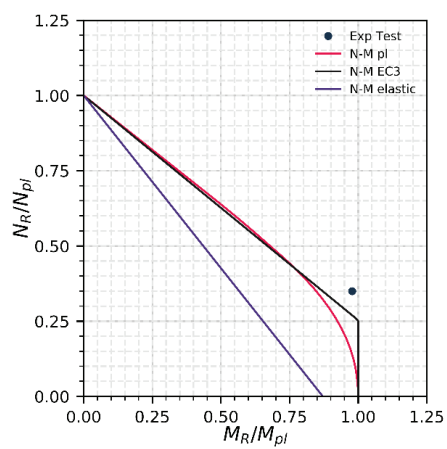
e = 138 mm

t_{MEAS} = 2.5 mm

F_{Max, Exp} = 205,4 kN

F_{Max, FEM} = 201,4 kN





Test T4-8

VHPS 140/140/2.5

S355 - EN10219

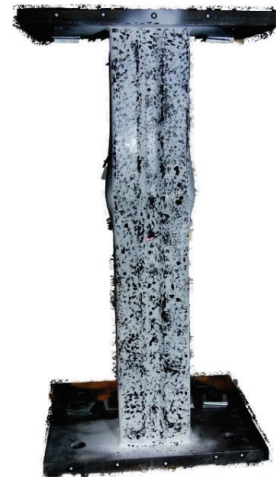
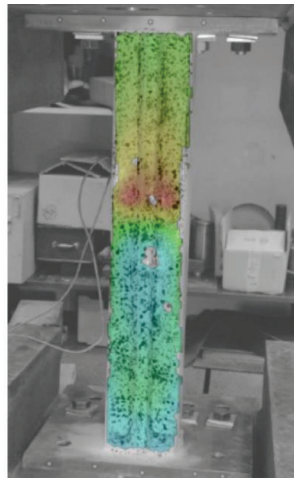
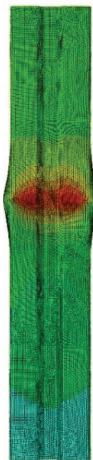
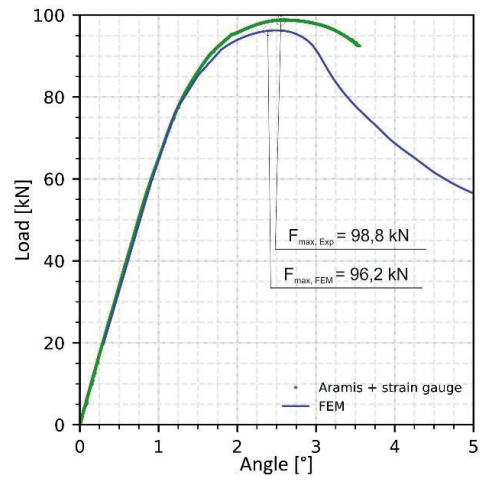
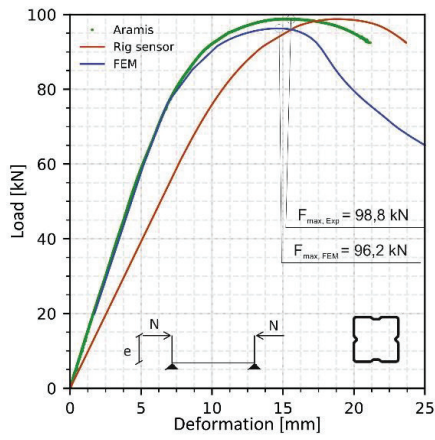
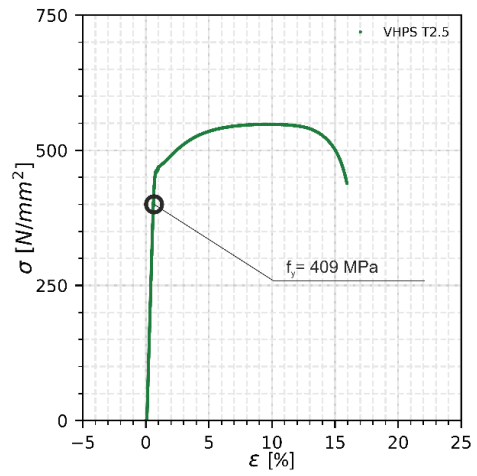
Test type T4

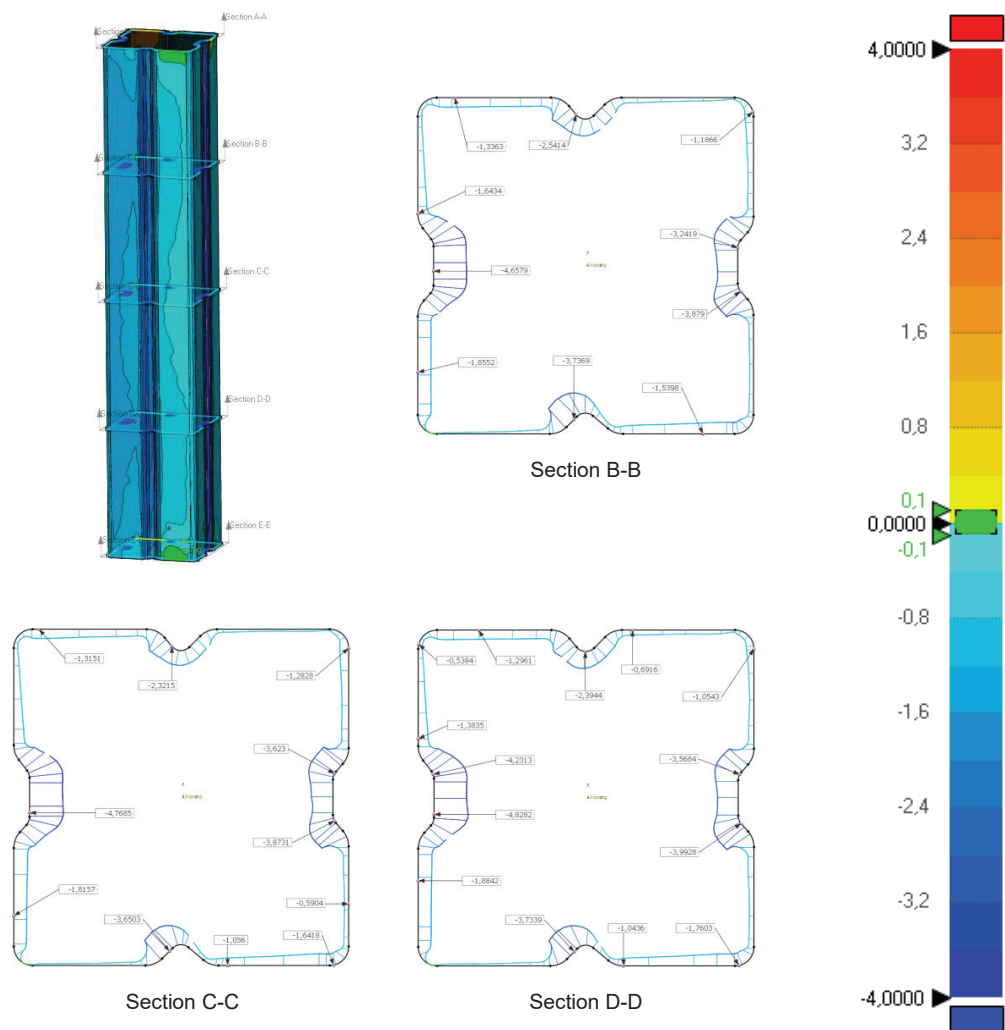
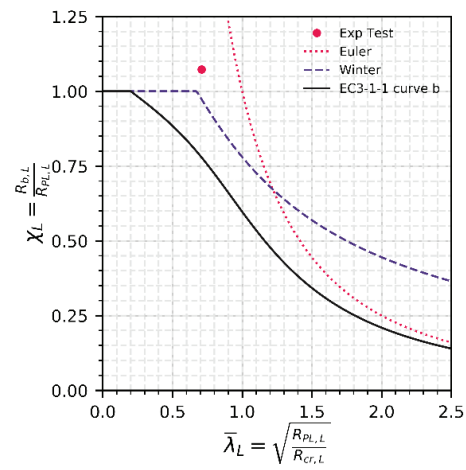
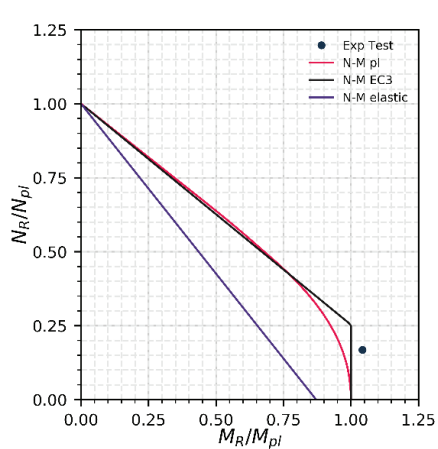
$e = 312 \text{ mm}$

$t_{MEAS} = 2.5 \text{ mm}$

$F_{Max, Exp} = 98,8 \text{ kN}$

$F_{Max, FEM} = 96,2 \text{ kN}$



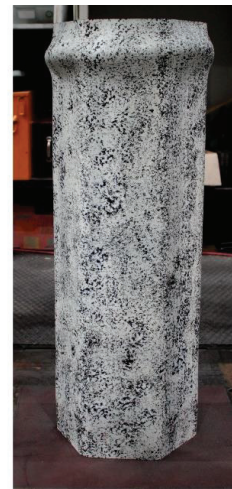
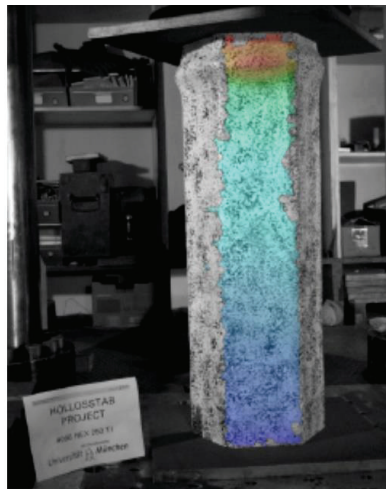
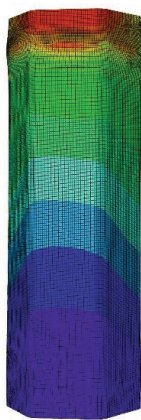
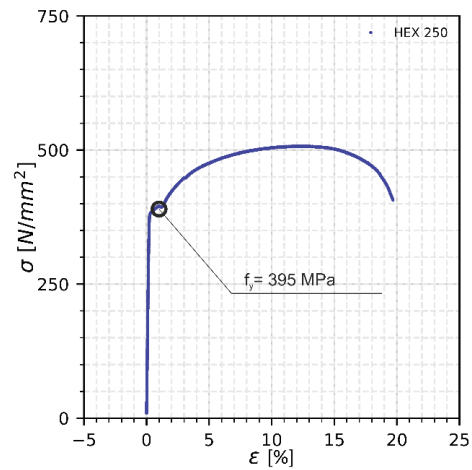
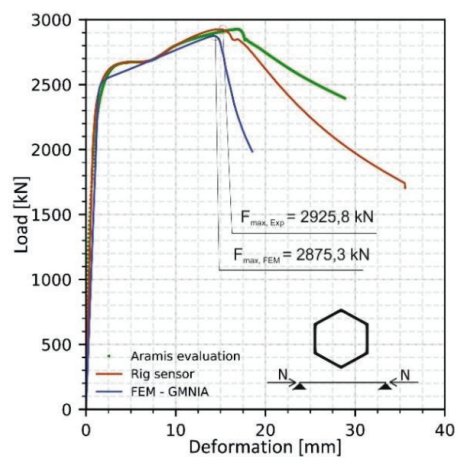


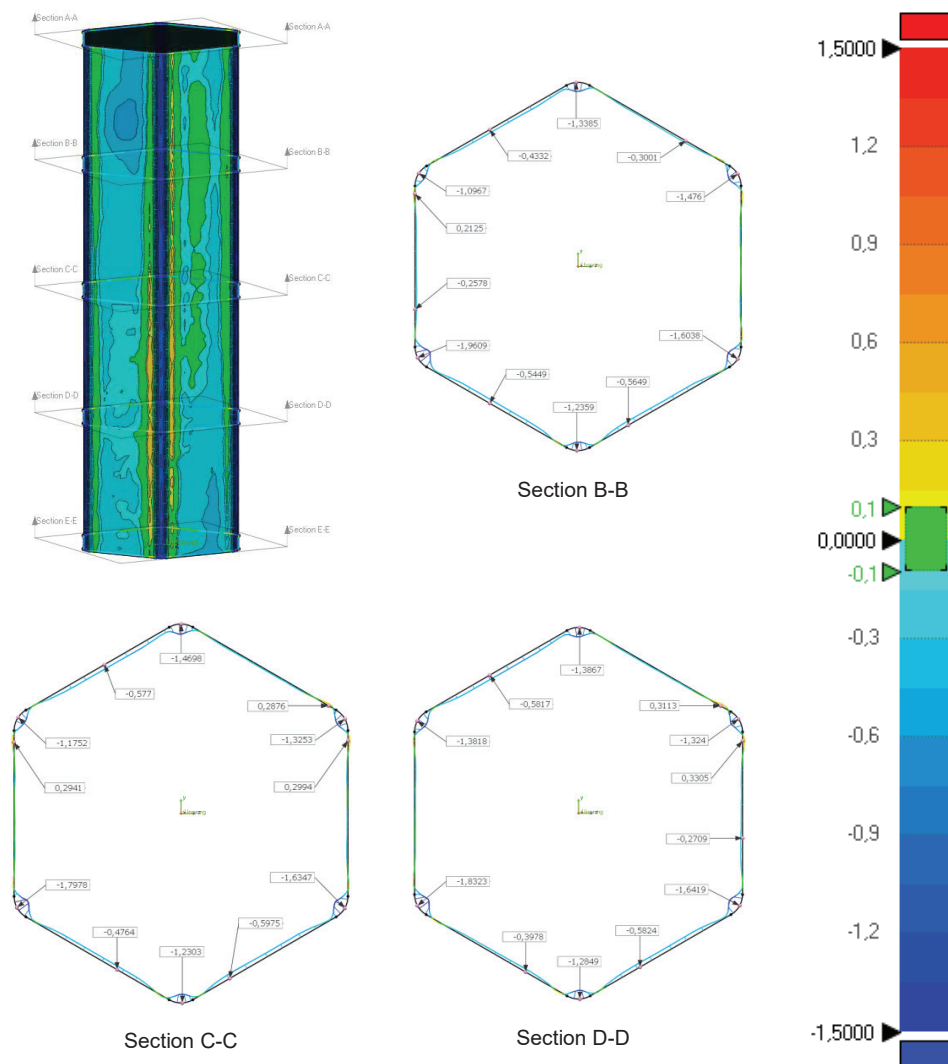
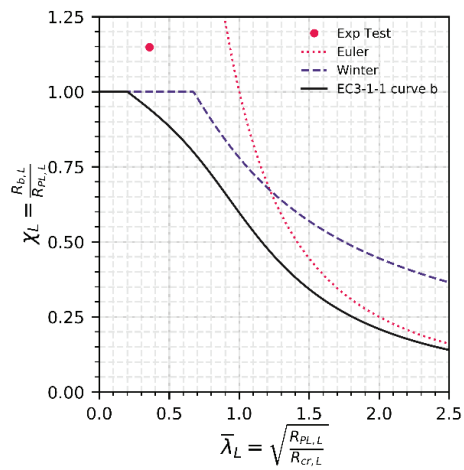
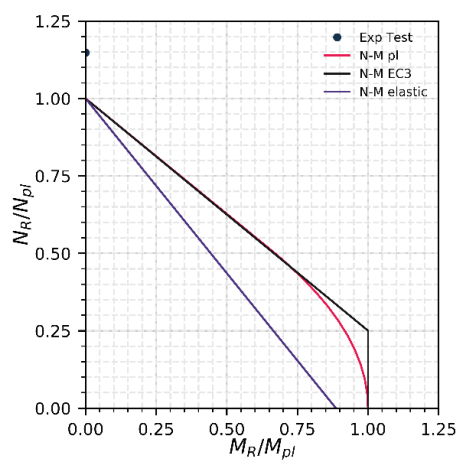
Test No. T1-10

HEX 250/8.5

S355 - EN10210

Test type T1

 $e = 0$ mm $t_{MEAS} = 8.5$ mm $F_{Max, Exp} = 2925,8$ kN $F_{Max, FEM} = 2875,3$ kN



Test T2-10

HEX 250/8.5

S355 - EN10210

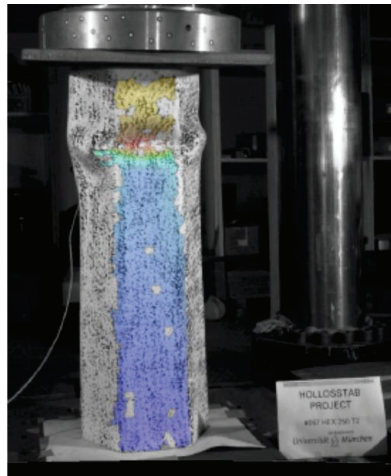
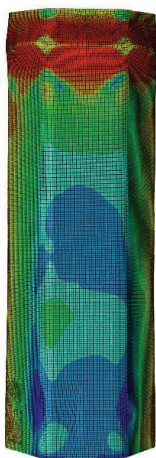
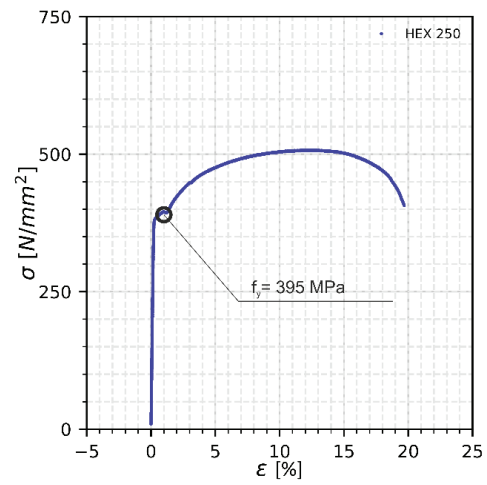
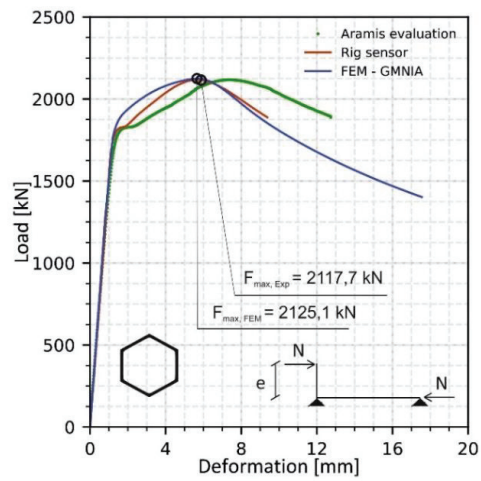
Test type T2

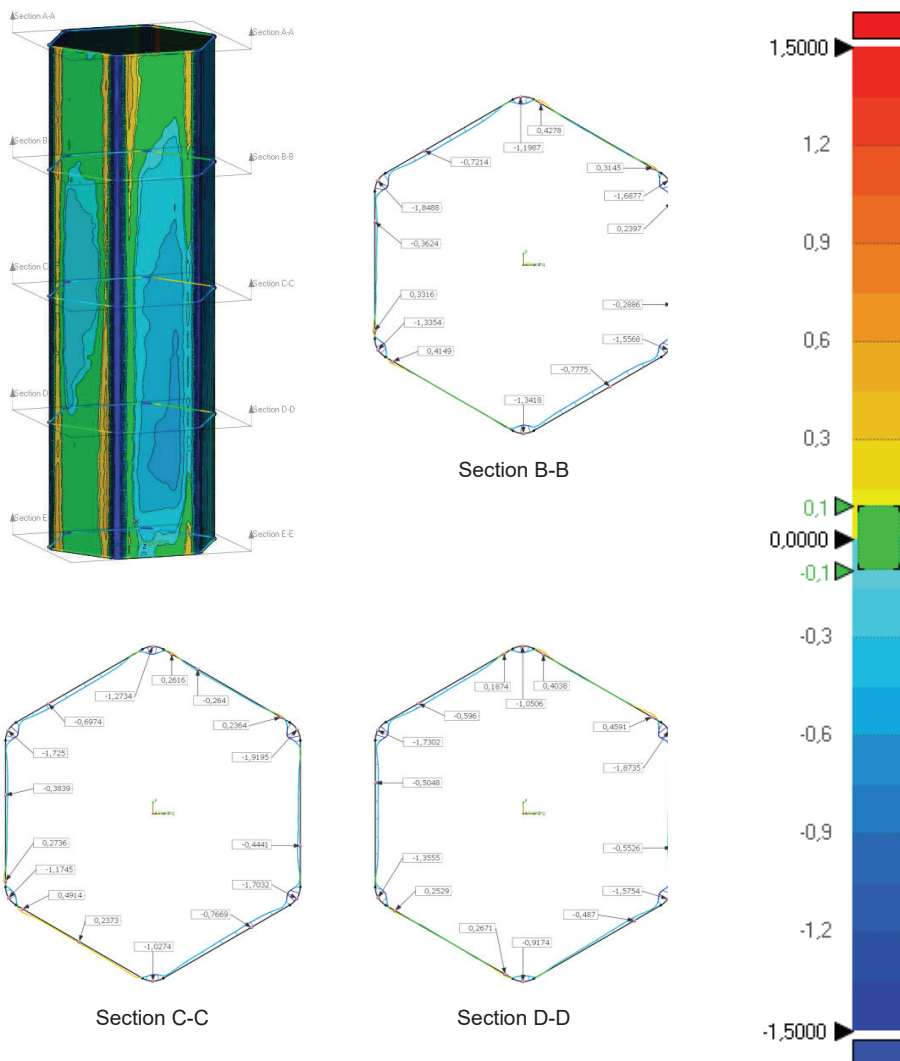
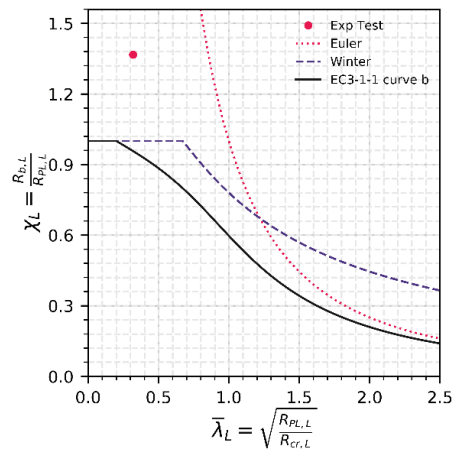
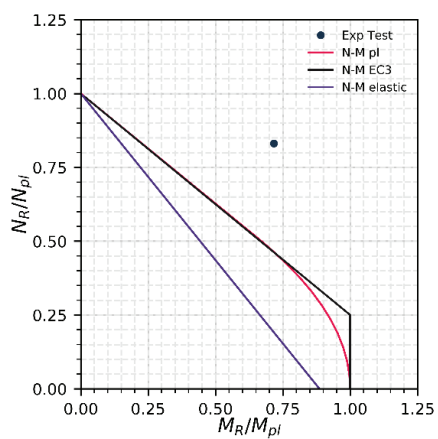
$e = 63 \text{ mm}$

$t_{\text{MEAS}} = 8.5 \text{ mm}$

$F_{\text{Max, Exp}} = 2117,7 \text{ kN}$

$F_{\text{Max, FEM}} = 2125,1 \text{ kN}$





Test T3-10

HEX 250/8.5

S355 - EN10210

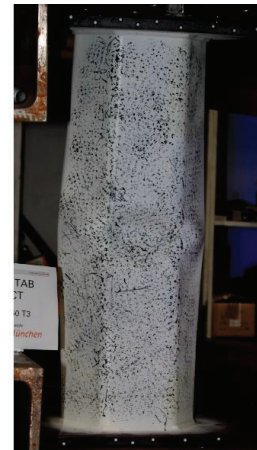
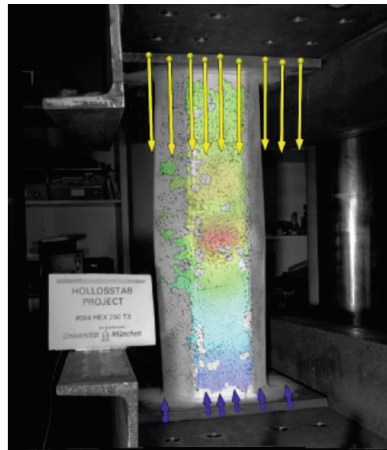
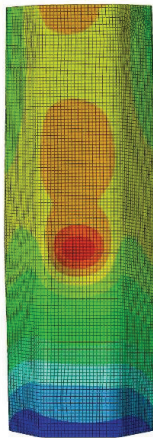
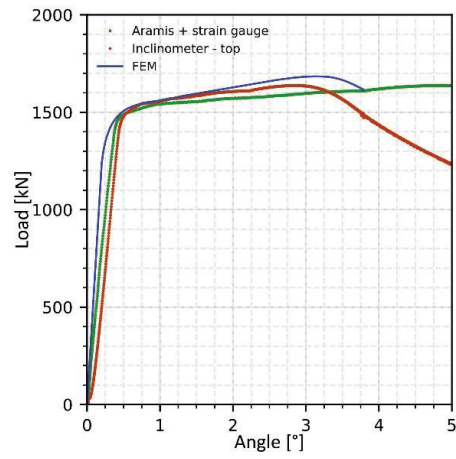
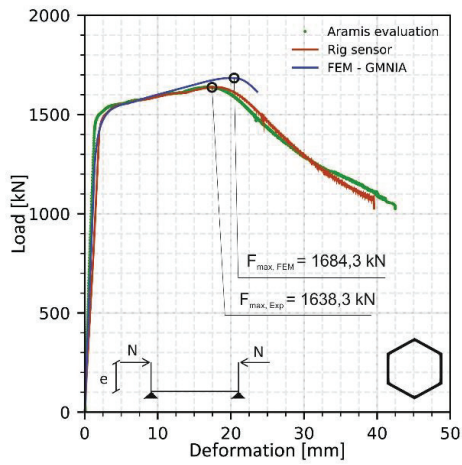
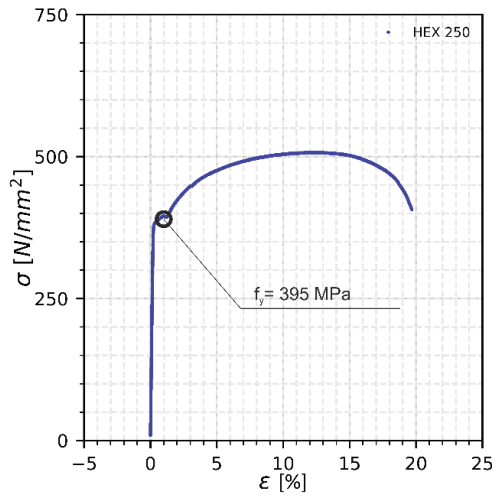
Test type T3

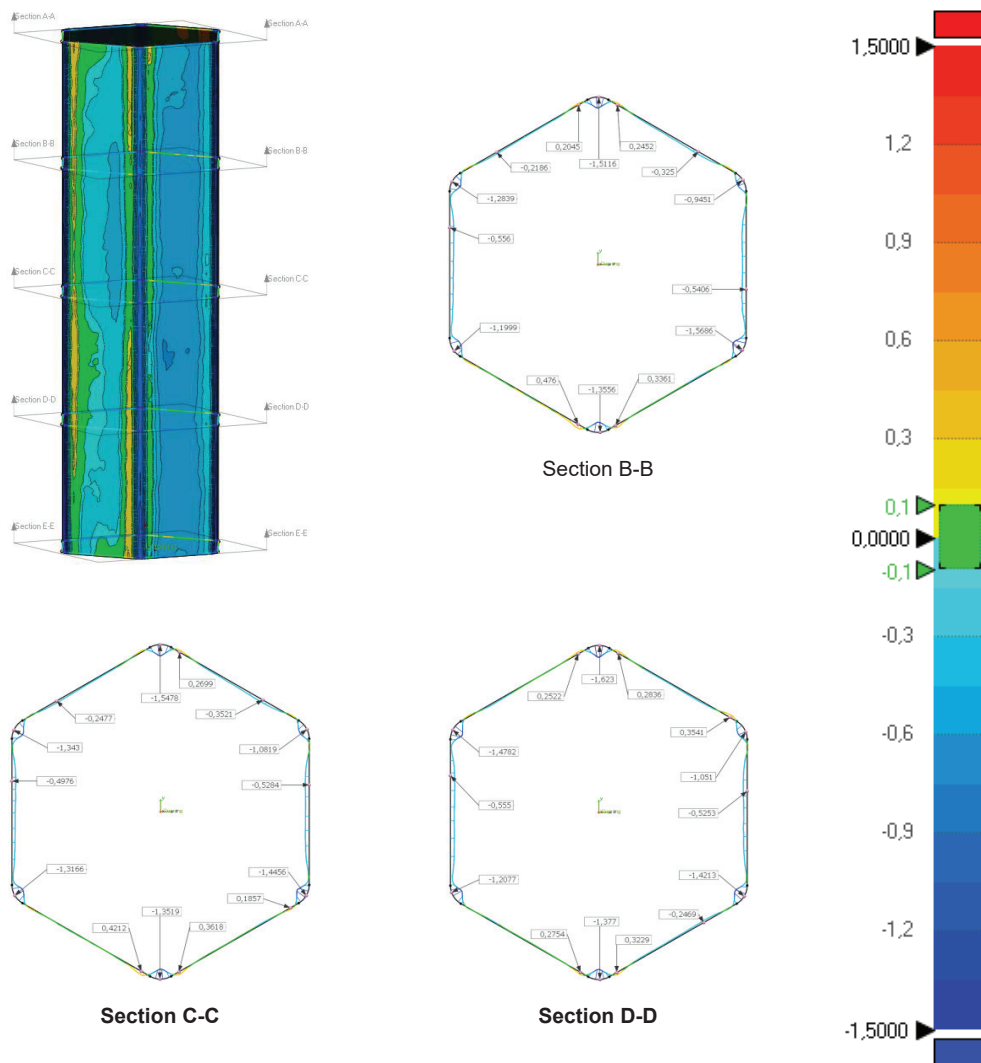
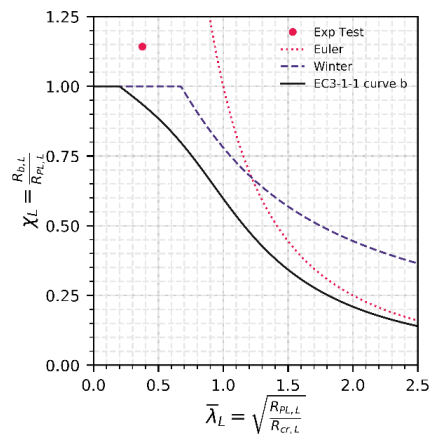
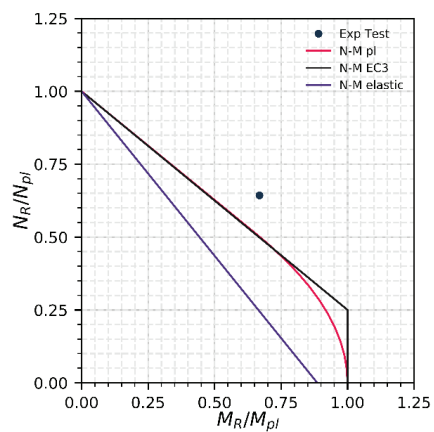
$e = 76 \text{ mm}$

$t_{MEAS} = 8.5 \text{ mm}$

$F_{Max, Exp} = 1638,3 \text{ kN}$

$F_{Max, FEM} = 1684,3 \text{ kN}$

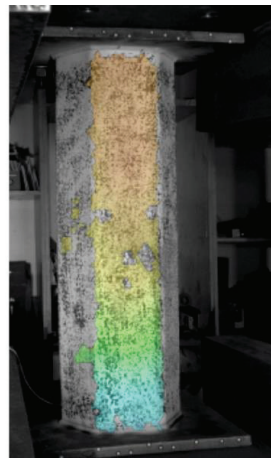
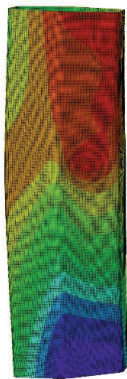
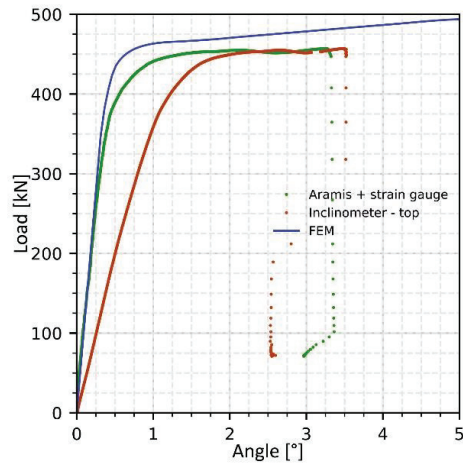
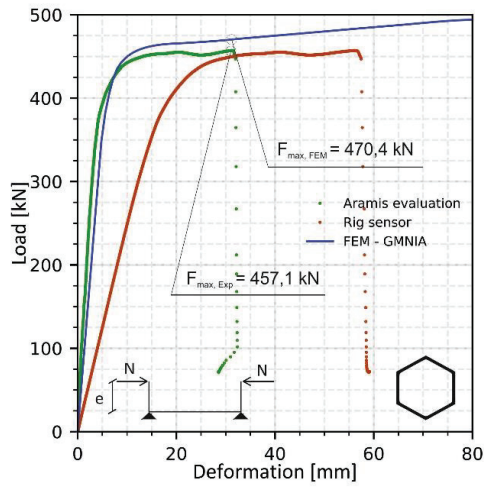
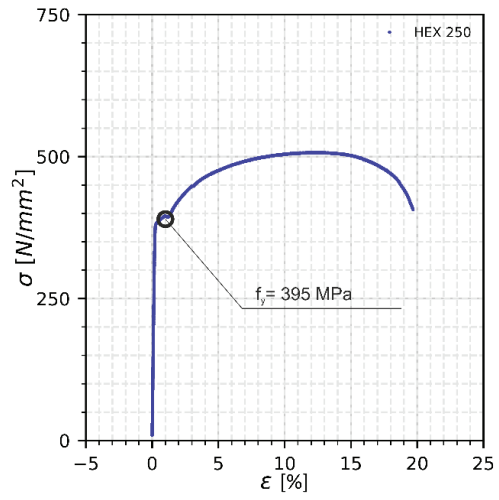


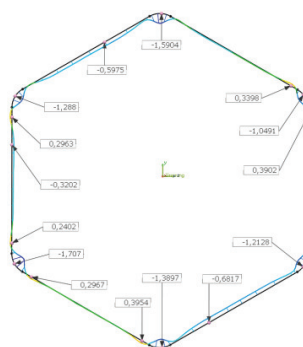
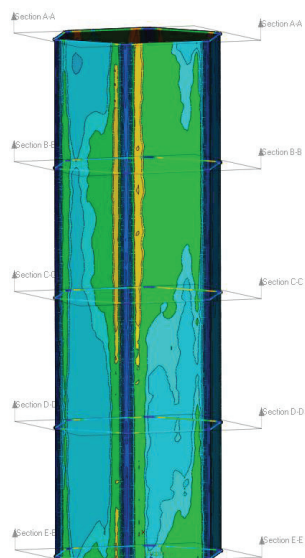
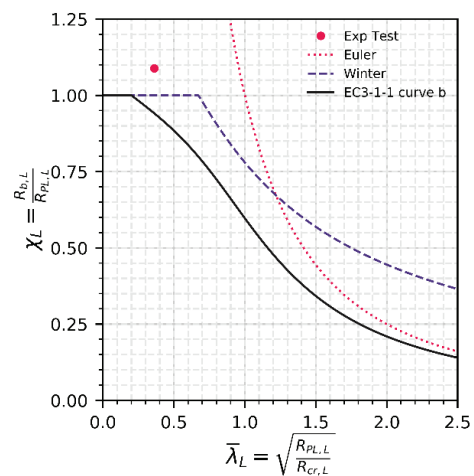
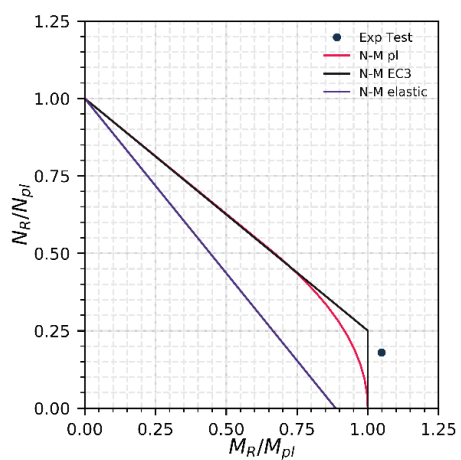


Test T4-10

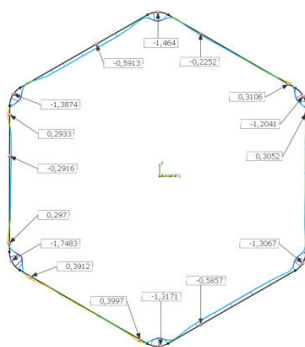
HEX 250/8.5
 S355 - EN10210
 Test type T4
 $e = 426 \text{ mm}$
 $t_{MEAS} = 8.5 \text{ mm}$

$F_{Max, Exp} = 457,1 \text{ kN}$
 $F_{Max, FEM} = 470,4 \text{ kN}$

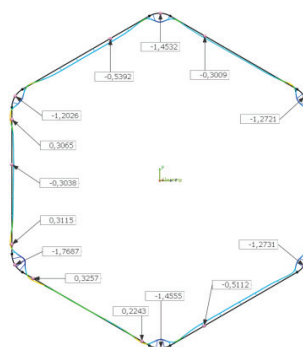




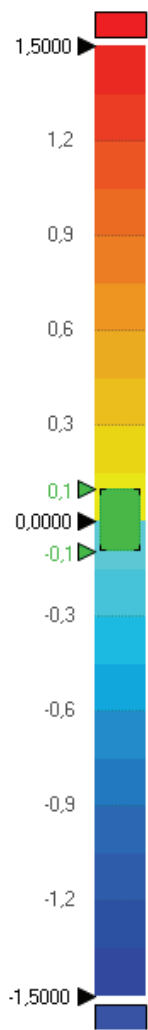
Section B-B



Section C-C



Section D-D



Test No. T1-11

VHPT 140/140/2.5

S355 - EN10219

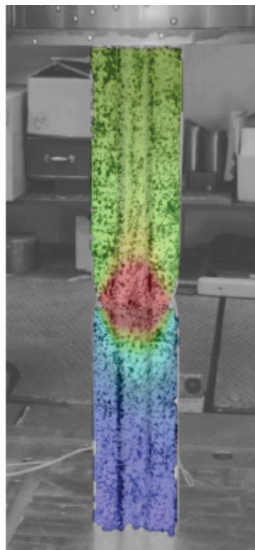
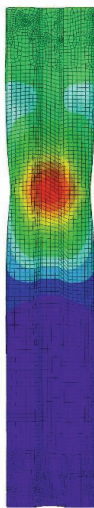
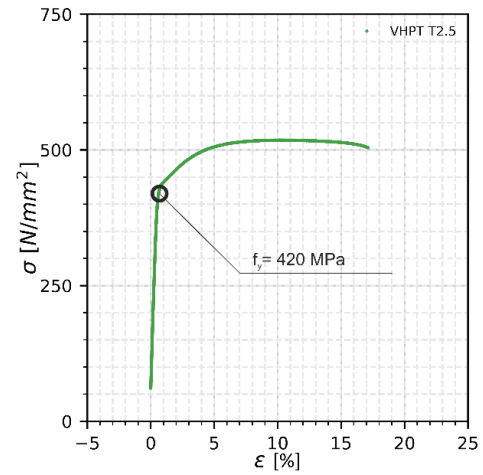
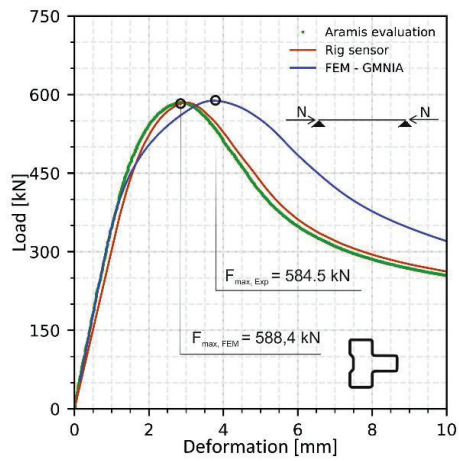
Test type T1

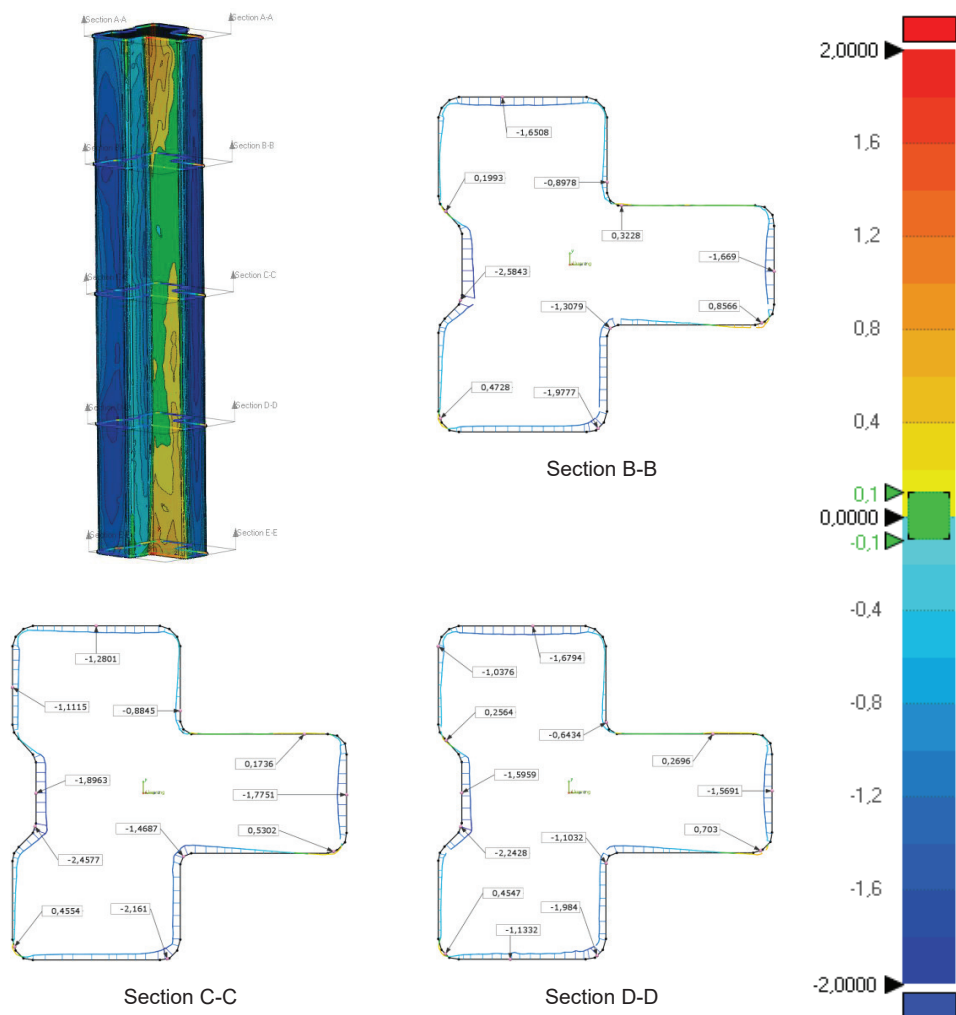
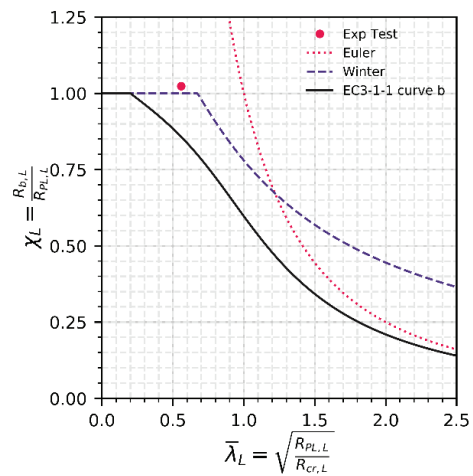
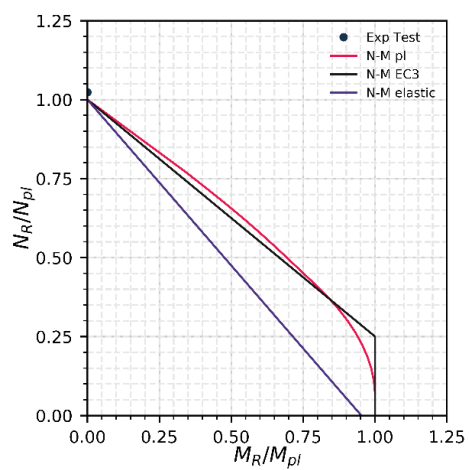
$e = 0$ mm

$t_{MEAS} = 2.5$ mm

$F_{Max, Exp} = 584,5$ kN

$F_{Max, FEM} = 588,4$ kN





Test T2-11

VHPT 140/140/2.5

S355 - EN10219

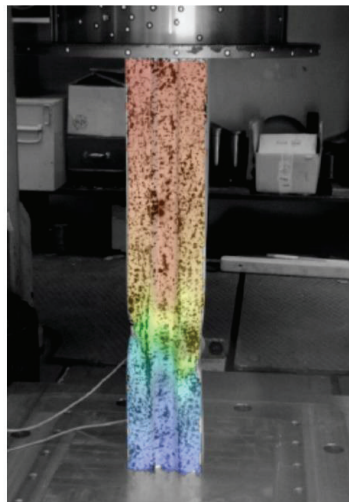
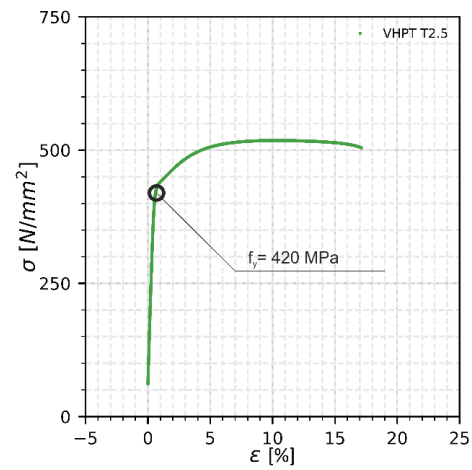
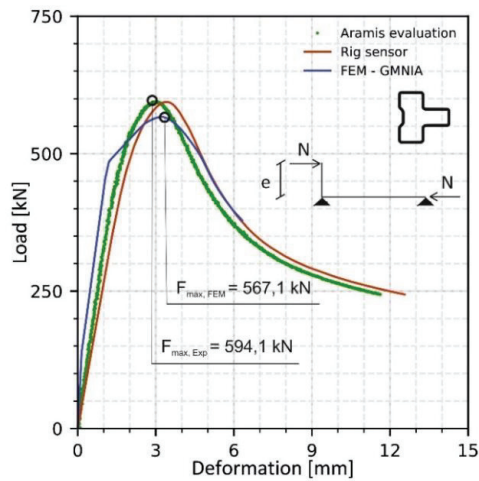
Test type T2

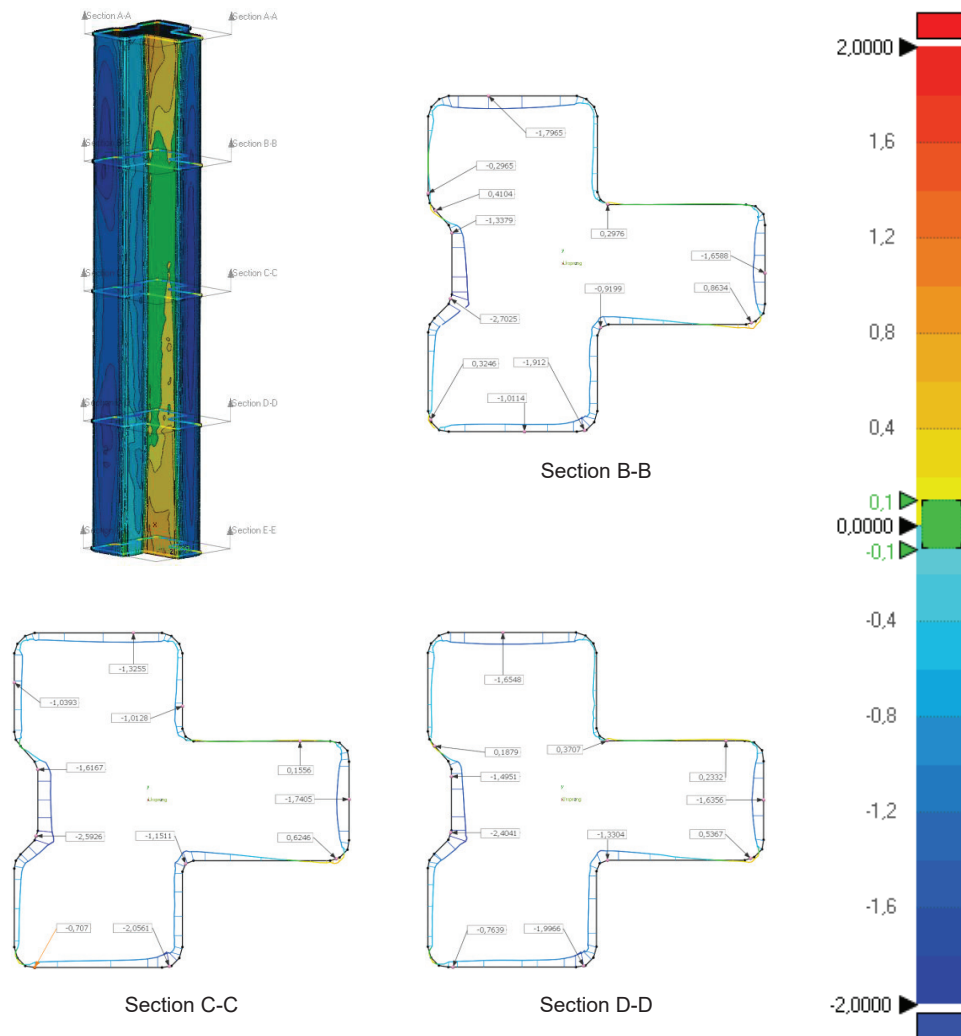
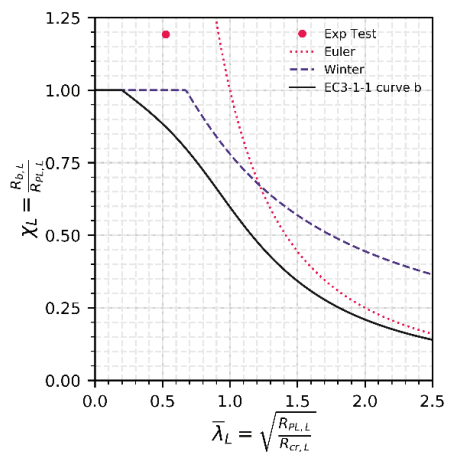
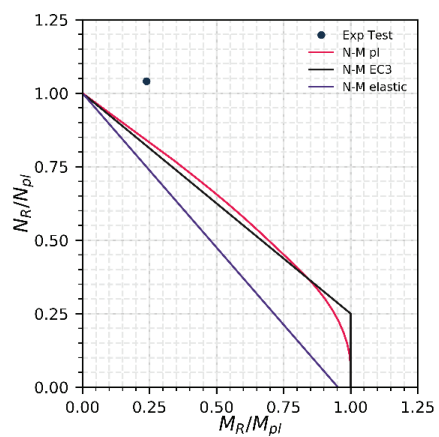
$e = 10 \text{ mm}$

$t_{\text{MEAS}} = 2.5 \text{ mm}$

$F_{\text{Max, Exp}} = 594,1 \text{ kN}$

$F_{\text{Max, FEM}} = 567,1 \text{ kN}$





Test T3-11

VHPT 140/140/2.5

S355 - EN10219

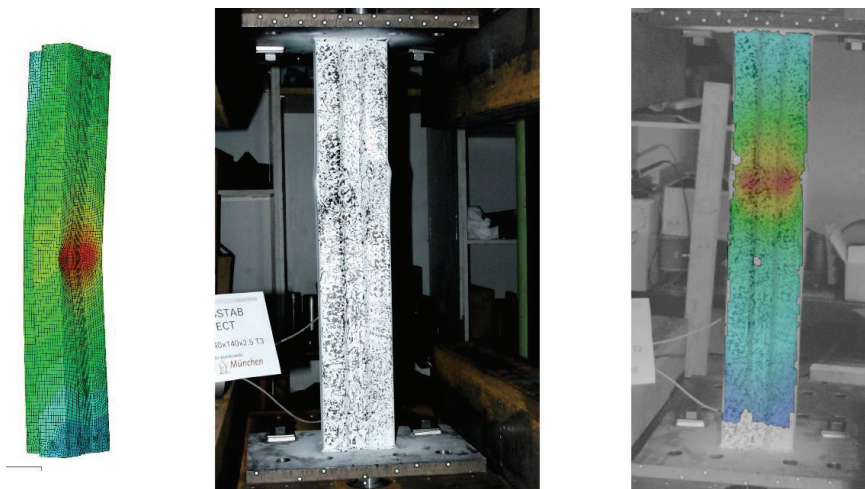
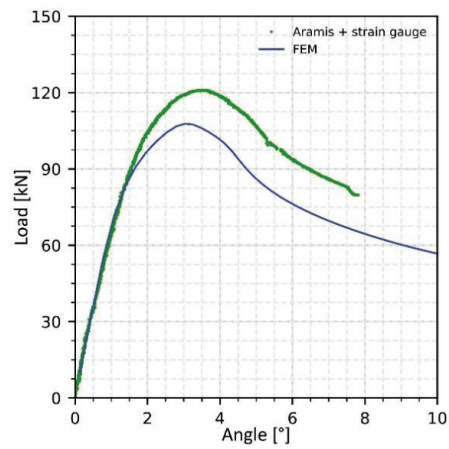
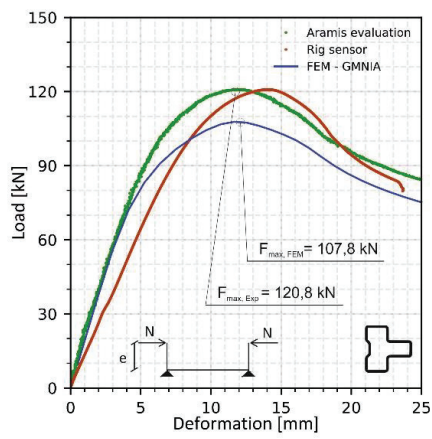
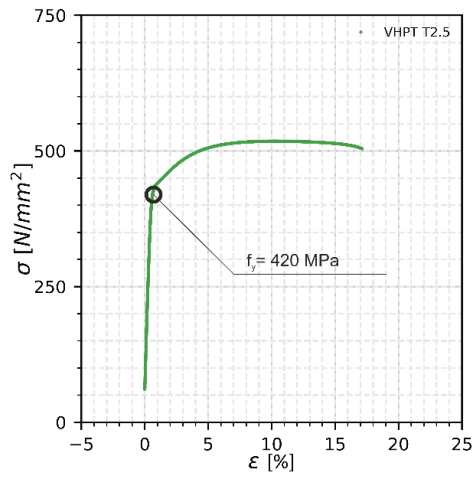
Test type T3

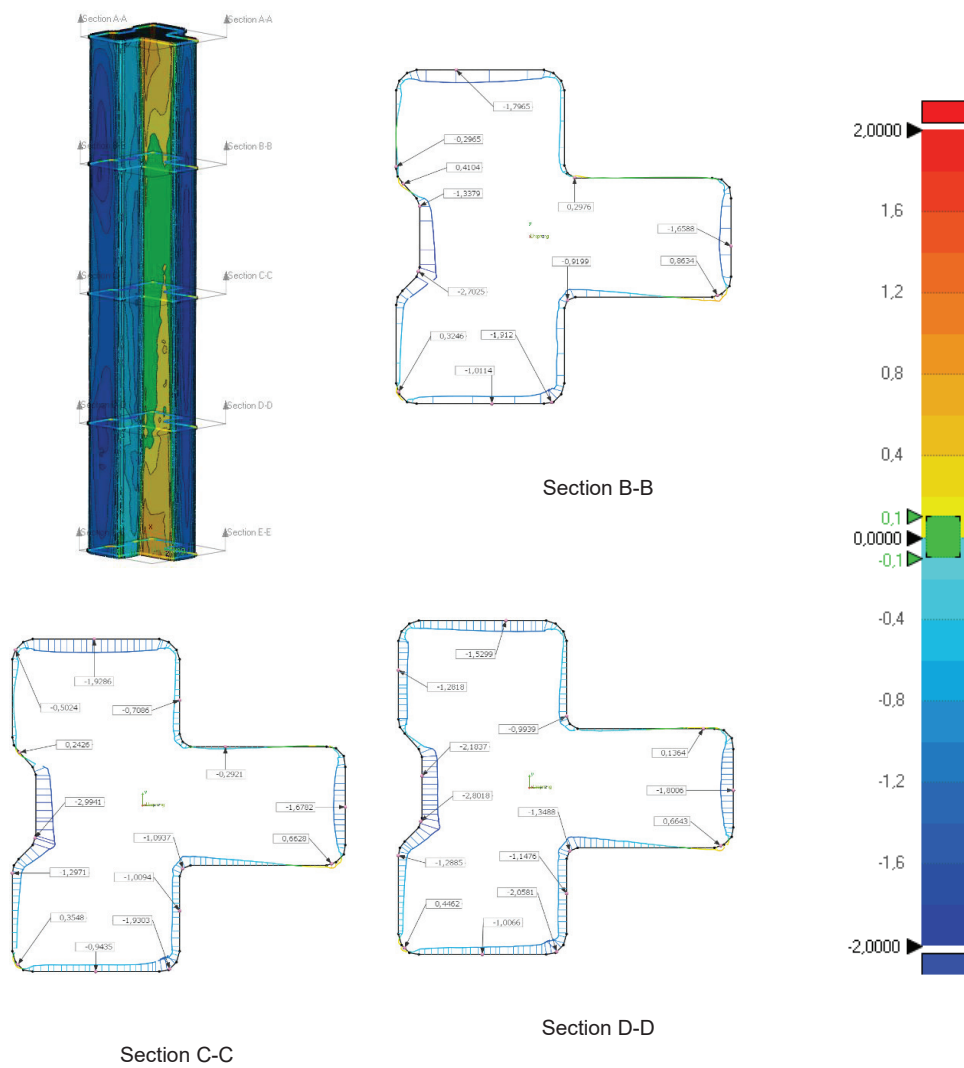
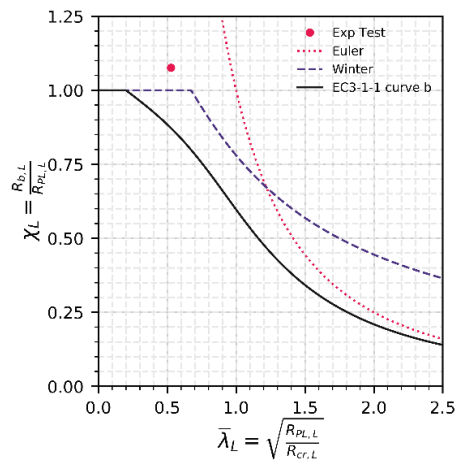
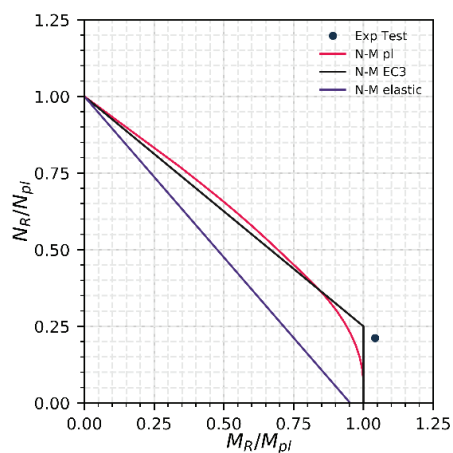
$e = 196 \text{ mm}$

$t_{MEAS} = 2.5 \text{ mm}$

$F_{Max, Exp} = 63.2 \text{ kN}$

$F_{Max, FEM} = 59.9 \text{ kN}$





Test T4-11

VHPT 140/140/2.5

S355 - EN10219

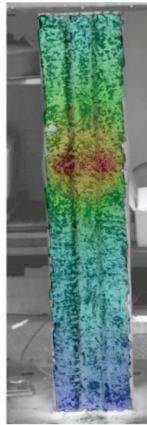
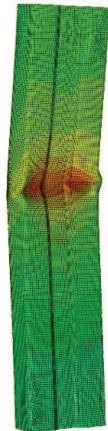
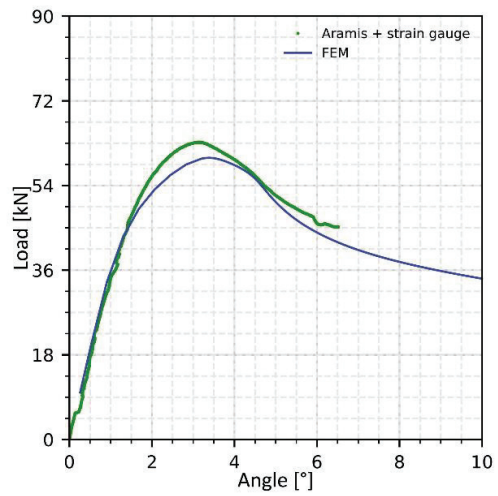
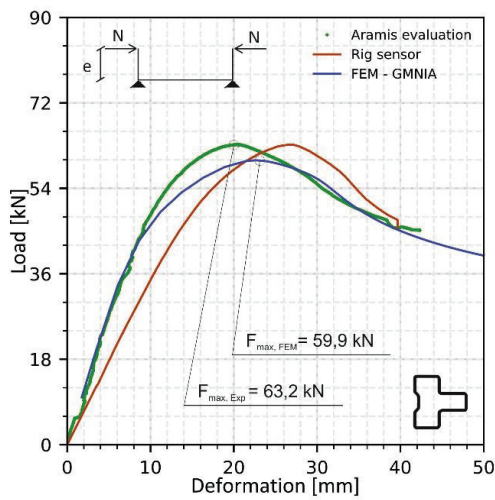
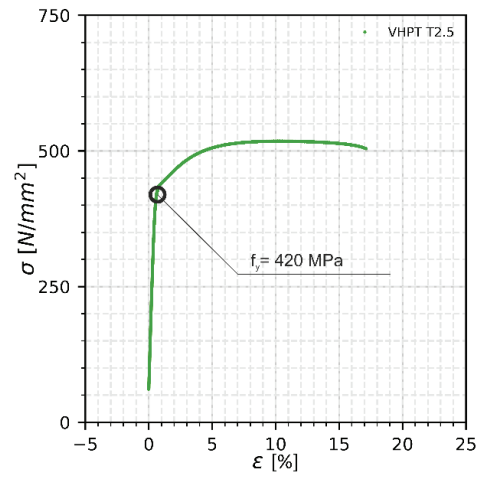
Test type T4

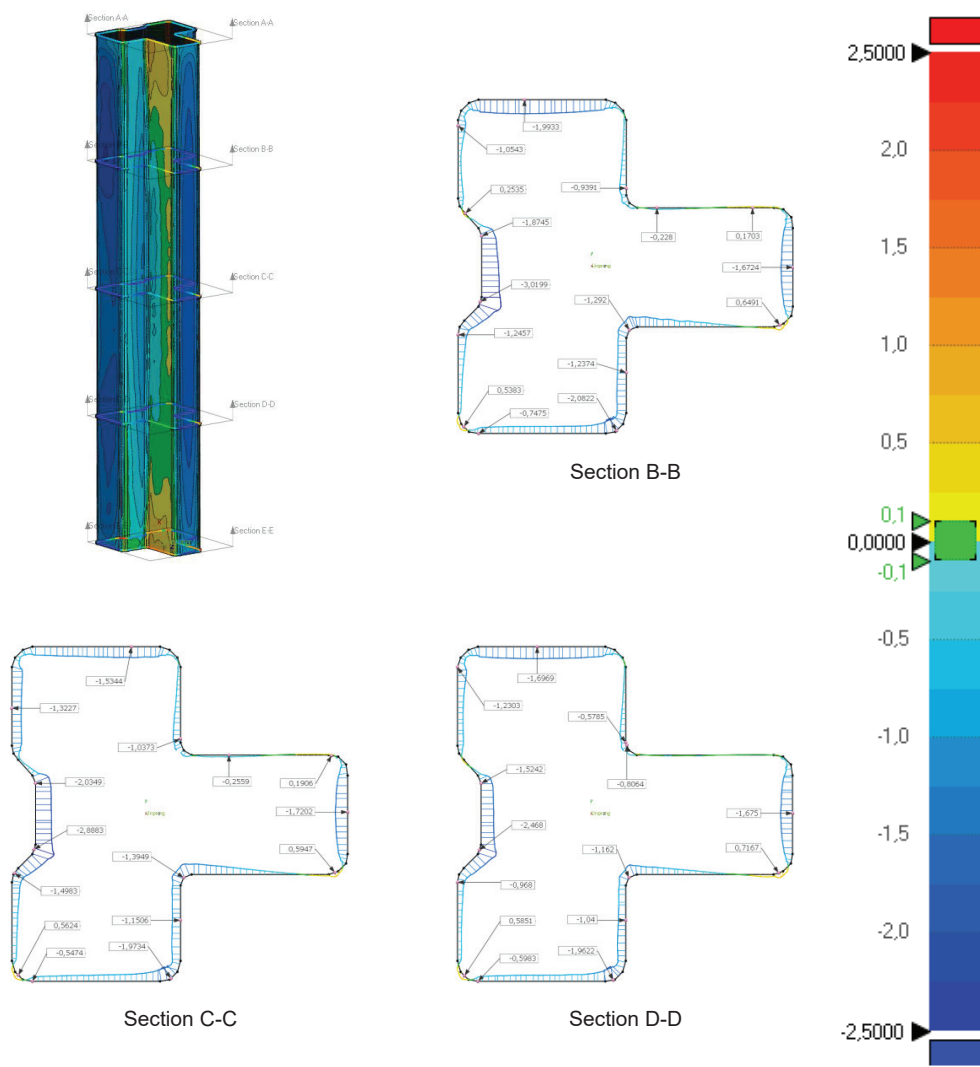
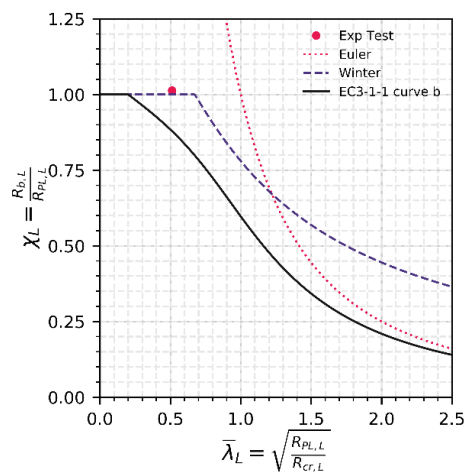
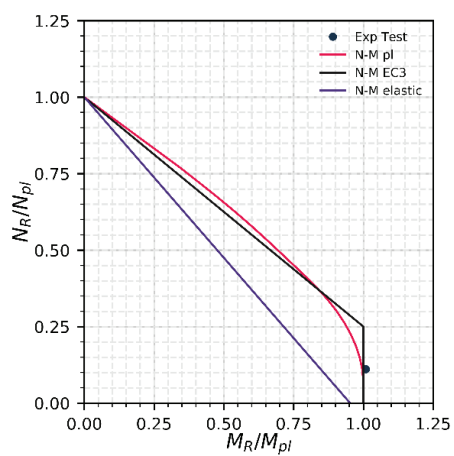
$e = 371 \text{ mm}$

$t_{MEAS} = 2.5 \text{ mm}$

$F_{Max, Exp} = 63,2 \text{ kN}$

$F_{Max, FEM} = 59,9 \text{ kN}$





Appendix C

Sample Abaqus input file for GMNIA

```
*HEADING
**GMNIA INP FILE
***** Parameters for the calculation
*PARAMETER
ecc_My = 0.
ecc_Mz = 0.
H = 120
B = 180
t = 6.3
nu = 0.3
E = 210000.
fy = 355.0
fu = 470.0
L = 554.6500480036693
bound = 4
imperfection_factor = B/400.0
*****
***** GEOMETRY INPUTS
r_0 = 15.75
r_i = 9.45
r_m = (r_0+r_i)/2
bi = B-t-2*r_m
hi = H-t-2*r_m
Bi = B-t
```

```

Hi = H-t
n_arc = 5
n_arc_tot = 16
n_ang = 180-360/n_arc_tot
bi05 = bi*0.5
hi05 = hi*0.5
Bi05 = Bi*0.5
Hi05 = Hi*0.5
*****
***** LOAD INPUTS
**n = 1.3093073414159544
**my = 0.7559289460184545
**mz = 1.3093073414159542
N_pl = 1237160.5336378017
M_y_pl = 55805226.20597269
M_z_pl = 73636939.21510673
N = 1619823.3692020534
M_y = 42184785.82820237
M_z = 96413385.11373961
*****
*****
*NODE
1000021,0,<bi05>,-<hi05>
1000046,0,<bi05>,<hi05>
1000071,0,-<bi05>,<hi05>
1000096,0.,-<bi05>,-<hi05>
11 , 0., 0., 0.
21 , <L>, 0., 0.
*****
**top-left
1001001,0.,-<bi05>,-<Hi05>
*****
**top-right_1
1001021,0.,<bi05>,-<Hi05>
**top-right_2
1001026,0.,<Bi05>,-<hi05>

```

```

*****
**bottom-right 1
1001046,0.,<Bi05>,<hi05>
**bottom-right_2
1001051,0.,<bi05>,<Hi05>
*****
**bottom-left_1
1001071,0.,-<bi05>,<Hi05>
**bottom-left_2
1001076,0.,-<Bi05>,<hi05>
*****
**top-left_1
1001096,0.,-<Bi05>,-<hi05>
**top-left_2
1001101,0.,-<bi05>,-<Hi05>
*****
*****Creation of reference lines*****
*NGEN,,NSET=Ntop
1001001,1001021,1
*NGEN,LINE=C, NSET=Ntop_right
1001021,1001026,1,1000021,0,<bi05>,-<hi05>,1,0,0
*NGEN,,NSET=Nright
1001026,1001046,1
*NGEN,LINE=C, NSET=Nbottom_right
1001046,1001051,1,1000046,0,<bi05>,<hi05>,1,0,0
*NGEN,,NSET=Nbottom
1001051,1001071,1
*NGEN,LINE=C, NSET=Nbottom_left
1001071,1001076,1,1000071,0,-<bi05>,<hi05>,1,0,0
*NGEN,,NSET=Nleft
1001076,1001096,1
*NGEN,LINE=C, NSET=Ntop_left
1001096,1001101,1,1000096,0,-<bi05>,-<hi05>,1,0,0
*****
*Nset, nset=Bottom, GENERATE
1001001,1001101,1

```



```

*Nset, nset=Middle, GENERATE
1101001,1101101,1
*ncopy,new set=Top,old set=Bottom,shift,change number=200000
<L>, 0, 0
0.0,0.0,0.0,0.0,0.0,0.0,0.0
*NFILL,NSET=Ntop
Bottom,Top,200,1000
*Element, type=S4R
1001001,1001001,1001002,1002002,1002001
*elgen,elset=arc_top_right
1001001,100,1,1,200,1000,1000
*****
*NSET, nset=top_left_1, GENERATE
1002001,1200001,1000
*NSET, nset=top_left_2, GENERATE
1002101,1200101,1000
*Nset, nset=ref_11
11
*Surface, type=NODE, name=surface_section_bottom
Bottom,1
*Nset, nset=ref_21
21
*Surface, type=NODE, name=surface_section_top
Top,1
*****
*****SECTION*****
*Shell Section, elset=arc_top_right, material=STEEL
<t>, 5
*****
*****MPC BEAM*****
*MPC
BEAM, Bottom, 11
*MPC
BEAM, Top, 21
*****
*****MPC TIE*****

```

```
*MPC
TIE,top_left_2,top_left_1
*****
*****MATERIAL*****
*MATERIAL,NAME=STEEL
*ELASTIC
<E>,<nu>
*PLASTIC
112.8000000000001,0
122.2,8.31730871333038e-07
131.6,1.428666989394204e-06
141.0,2.3640820241577903e-06
150.4,3.7867987320426176e-06
159.8,5.894859734312057e-06
169.2000000000002,8.947168922409298e-06
178.6,1.327692911544517e-05
188.0,1.9307023179544313e-05
197.4,2.7567488444156692e-05
206.8,3.8715236772490867e-05
216.2000000000002,5.355617507129943e-05
225.6000000000002,7.306988336743393e-05
235.0,9.843700984192225e-05
244.4,0.00013106954440296708
253.8,0.00017264413450263322
263.2,0.00022513860896293254
272.6,0.0002908718775797589
282.0,0.0003725473762215654
291.4000000000003,0.0004733002290372181
300.8,0.0005967483012372403
310.2,0.0007470473177174975
319.6,0.0009289502245568211
329.0,0.0011478709721424755
338.4000000000003,0.001409952900361915
347.8,0.0017221419079477848
357.2,0.0017784728490239244
366.6,0.002210734432717389
```

```

376.0,0.00291558797062788
385.40000000000003,0.004263300205066824
394.8,0.006720486165804696
404.2,0.010832302281732185
413.6,0.01721202705165437
423.0,0.026533953035916585
432.40000000000003,0.039528127108269896
441.8,0.05697625143553327
451.20000000000005,0.07970837119118655
460.6,0.10860012511684931
470.0,0.1445704154002026
112.80000000000001,0.1447149858156028
*****
*****BOUNDARY*****
*BOUNDARY
21, 2, 3
**bottom boundary conditions; according to test setup.
11, 1, <bound>
*****
*****GMNIA*****
*IMPERFECTION,FILE=LBA_H120_B180_t6.3_L0.15_fy355.0_phiy0.52359_phiz0.78539, Step = 1
1,<imperfection_factor>
*Step, name=GMNIA, nlgeom=YES
GMNIA
*Static
0.1, 1.,0.000025,0.4
*****
*****LOAD*****
*Cload
21,1,-<N>,
21,5,<M_y>,
21,6,<M_z>,
11,5,-<M_y>
11,6,-<M_z>
*****
*****OUTPUT*****

```

```
** OUTPUT REQUESTS
*Restart, write, frequency=0
** FIELD OUTPUT: F-Output-1
*Output, field, variable=PRESELECT
** HISTORY OUTPUT: H-Output-1
*Output, history, variable=PRESELECT
*NODE PRINT, FREQ=1, NSET=Middle
U2,U3
*NODE PRINT, FREQ=1, NSET=ref_11
U
*NODE PRINT, FREQ=1, NSET=ref_11
RF
*NODE PRINT, FREQ=1, NSET=ref_21
U
*NODE PRINT, FREQ=1, NSET=ref_21
RF
*End Ste
```